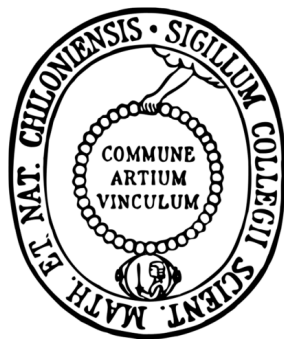

Energetic particles in the heliosphere

New measurements from Chang'E-4/LND and Solar Orbiter



DISSERTATION

zur Erlangung des Doktorgrades
der Mathematisch-Naturwissenschaftlichen Fakultät
der Christian-Albrechts-Universität zu Kiel

vorgelegt von
Zigong Xu

– Kiel, June 2023 –

Zigong Xu:
Energetic particles in the heliosphere
New measurements from Chang'E-4/LND and Solar Orbiter
© June 2023

ERSTER GUTACHTER (SUPERVISOR):
Prof. Dr. Robert F. Wimmer-Schweingruber

ZWEITER GUTACHTER :
Prof. Dr. Wolfgang J. Duschl

TAG DER MÜNDLICHEN PRÜFUNG:
July 24, 2023

ZUM DRUCK GENEHMIGT:
Nov 17, 2023

ABSTRACT

Energetic particles including solar energetic particles (SEPs), galactic cosmic rays (GCRs) and anomalous cosmic rays (ACRs), play a crucial role in shaping the local space environment. Understanding how these energetic particles spread throughout the heliosphere, considering different particle sources and periodically varying solar modulations and their impact on radiation environments, are still subjects of ongoing debate in the scientific community. To address these questions and advance our understanding, we need new instruments that are essential to provide new measurements of energetic particles from unique perspectives.

The Lunar Lander Neutron and Dosimetry Experiment (LND) aboard the Chang'E - 4 lander and the High Energy Telescope (HET) onboard the Solar Orbiter (SolO) are two new state-of-the-art high-energy particle telescopes that provide invaluable insights into the nature of local space environment. LND is the first such instrument operating on the far-side surface of the Moon. SolO enables precious observations of energetic particles when the satellite orbits the Sun between 0.3 - 1 au.

In the first part of this thesis, we present new measurements obtained from LND on the lunar surface, including observations of SEPs, GCRs, and albedo protons which are a subclass of secondary particles generated by the interaction between GCRs and the lunar regolith. Notably, we report the first SEP event ever observed on the lunar far-side surface. Using both in-situ measurements and remote sensing observations, we investigate the solar origin of these particles and discuss the potential transport mechanisms of protons and electrons for distributing these particles over a wide range of longitudes in the heliosphere. We also determine the flux of GCRs and albedo protons that were observed by LND during the recent solar activity minimum between 2019 - 2020. Through comparison with observations from other instruments we find the GCR proton spectra and the albedo proton flux from LND are consistent with the corresponding measurements from other instruments. In particular, below 50 MeV, the albedo proton flux exceeds the (primary) GCR proton flux. Throughout this section, attention is also devoted to the calibration of data, the validation of the instrument performance, and the generation of reliable scientific data products.

The second part of this thesis focuses on the new measurements from HET. Firstly, the quiet time spectra of ions between 2020.02 - 2021.01 are reported. These spectra are averaged between 0.5 - 1 au and clearly show GCRs, ACRs, and the very low energy part of the spectrum. Lastly, we present preliminary results regarding the observation of ACRs and radial gradient of ACR helium between 2020.02 and 2022.10, which is approximately 20%/au within the energy range of 10 - 50 MeV/nuc. Overall, the findings are consistent with measurements from the Parker Solar Probe (PSP) within uncertainties of HET and PSP. Besides, the radial gradient's energy dependency and time variation are also discussed. It is worth noting that, at the moment, the results of the ACR radial gradients are still

preliminary, and some peculiar features of ACRs in this solar cycle are not well understood.

ZUSAMMENFASSUNG

Energieriche Teilchen, darunter solare energieriche Teilchen (SEPs), galaktische kosmische Starhlung (GCRs) und anomale kosmische Strahlung (ACRs), spielen eine entscheidende Rolle für die lokale Weltraumumgebung. Die Frage, wie sich diese energiereichen Teilchen in der Heliosphäre ausbreiten, wobei verschiedene Teilchenquellen und periodisch variierende solare Modulationen sowie deren Auswirkungen auf die Strahlungsumgebung zu berücksichtigen sind, wird in der wissenschaftlichen Gemeinschaft immer noch diskutiert. Um diese Fragen anzugehen und unser Verständnis zu verbessern, benötigen wir moderne Instrumente, die neue Messungen von energetischen Teilchen aus einzigartigen Perspektiven ermöglichen.

Das Lunar Lander Neutron and Dosimetry Experiment (LND) an Bord des Chang'E - 4 Landers und das High Energy Telescope (HET) an Bord des Solar Orbiter (SolO) sind zwei solche hochmodernen Hochenergieteilchenteleskope, die unschätzbare Einblicke in die Natur der lokalen Weltraumumgebung liefern. LND ist das erste Instrument dieser Art, das auf der Rückseite des Mondes betrieben wird. SolO ermöglicht wertvolle Beobachtungen von energetischen Teilchen, während der Satellit die Sonne zwischen 0,3 und 1 AU umkreist.

Im ersten Teil dieser Arbeit stellen wir die neuen Messungen von LND auf der Mondoberfläche vor, einschließlich Beobachtungen von SEPs, GCRs und Albedo-Protonen, einer Unterkategorie von Sekundärteilchen, die durch die Wechselwirkung zwischen GCRs und dem Mondregolith entstehen. Insbesondere berichten wir über das erste SEP-Ereignis, das jemals auf der mondfernen Oberfläche beobachtet wurde. Anhand von In-situ-Messungen und Fernerkundungsbeobachtungen untersuchen wir den solaren Ursprung dieser Teilchen und erörtern die möglichen Transportmechanismen von Protonen und Elektronen, die bei 1 AU beobachteten breite longitudinale Verteilung ermöglichen könnten. Wir bestimmen auch den Fluss von GCRs und Albedo-Protonen, die von LND während des jüngsten solaren Aktivitätsminimums zwischen 2019 und 2020 beobachtet wurden. Durch den Vergleich mit Beobachtungen von anderen Instrumenten sowie mit Vorhersagen von Modellen stellen wir fest, dass die GCR-Protonenspektren und der Albedo-Protonenfluss konsistent sind. Insbesondere unterhalb von 50 MeV übersteigt der Albedo-Protonenfluss den (primären) GCR-Protonenfluss. In diesem Abschnitt wird auch auf die Kalibrierung der Daten, die Validierung der Messeigenschaften des Instruments und die Erzeugung zuverlässiger wissenschaftlicher Datenprodukte eingegangen.

Der zweite Teil dieser Arbeit konzentriert sich auf die neuen Messungen von HET. Zunächst wird über die Spektren während ruhiger Zeiten von Ionen zwischen 2020,2 und 2021,1 berichtet. Diese Spektren sind zwischen 0,5 - 1 AU gemittelt und zeigen deutlich die Existenz von GCRs, ACRs sowie den untersten Energiebereich des Spektrums. Schließlich präsentieren wir vorläufige Ergebnisse bezüglich der Beobachtung von ACRs und des radialen Gradienten von ACR

Helium zwischen 2020.2 und 2022.10, der etwa 20% /AU im Energiebereich von 10 - 50 MeV/nuc beträgt. Insgesamt stimmen die Ergebnisse mit den Messungen von Parker Solar Probe (PSP) innerhalb der Unsicherheiten überein. Außerdem werden die Energieabhängigkeit des radialen Gradienten und seine zeitliche Variation diskutiert. Es ist erwähnenswert, dass die Ergebnisse zu den radialen Gradienten im Moment noch vorläufig sind und einige besondere Eigenschaften der ACRs in diesem Sonnenzyklus noch nicht gut verstanden sind.

PUBLICATIONS

The following four peer-reviewed publications are relevant in the main context of this thesis and are included therein. The full list of the publications that I have contributed during my phd is given in Appendix C.

FIRST SOLAR ENERGETIC PARTICLES MEASURED ON THE LUNAR FAR-SIDE

Xu, Z., J. Guo, R. F. Wimmer-Schweingruber, J. L. Freiherr von Forstner, Y. Wang, N. Dresing, H. Lohf, S. Zhang, B. Heber, and M. Yang, *The Astrophysical Journal Letter*, 902, 2, page L30 (2020), doi: 10.3847/2041-8213/abbccc

Own contribution: 80%

PRIMARY AND ALBEDO PROTONS DETECTED BY THE LUNAR LANDER NEUTRON AND DOSIMETRY EXPERIMENT ON THE LUNAR FAR SIDE

Xu, Z., J. Guo, R. F. Wimmer-Schweingruber, M. I. Dobynede, P. Kühl, S. Khaksarighiri, and S. Zhang, *Frontiers in Astronomy and Space Sciences*, 9, page 974946 (2022), doi: 10.3389/fspas.2022.974946

Own contribution: 80%

QUIET-TIME LOW ENERGY ION SPECTRA OBSERVED ON SOLAR ORBITER DURING SOLAR MINIMUM

Mason, G. M., G. C. Ho, R. C. Allen, **Z. G. Xu**, N. P. Janitzek, J. L. Freiherr von Forstner, A. Kohllhoff, D. Pacheco, J. Rodríguez-Pacheco, R. F. Wimmer-Schweingruber, G. Bruce Andrews, C. E. Schlemm, H. Seifert, K. Tyagi, W. J. Lees, J. Hayes, R. Gómez-Herrero, M. Prieto, S. Sánchez-Prieto, F. Espinosa Lara, I. Cernuda, P. Parra Espada, O. Rodríguez Polo, A. Martínez Hellín, C. Martin, S. Böttcher, L. Berger, J. C. Terasa, S. Boden, S. R. Kulkarni, A. Ravanbakhsh, M. Yedla, S. Eldrum, R. Elftmann, and P. Kühl, *Astronomy & Astrophysics*, 656, page L5 (2021), doi: 10.1051/0004-6361/202140540

Own contribution: 25%

SOLAR ORBITER EPD MEASUREMENTS OF ANOMALOUS COSMIC RAY IN THE INNER HELIOSPHERE FROM 0.3 AU TO 1 AU

Xu, Z., R. F. Wimmer-Schweingruber, P. Kühl, D. Pacheco, A. Kollhoff, L. Berger, L. Yang, S. Fleth, R. Gomez-Herrero, J. Rodriguez-Pacheco, G. C. Ho, S. I. Boettcher, and G. M. Mason, (2023), manuscript in preparation.

Own Contribution 80%

CONTENTS

1	INTRODUCTION AND MOTIVATION	1
1.1	Energetic particles in the heliosphere	1
1.2	Motivation	3
2	OBSERVATION AND THEORETICAL BACKGROUND OF ENERGETIC PARTICLES	7
2.1	Solar energetic particles	7
2.2	Galactic cosmic rays	12
2.3	Anomalous Cosmic Ray	16
2.4	Radiation hazard of energetic particles	19
3	INSTRUMENTATION	23
3.1	Chang'E-4 and Lunar Lander Neutron and Dosimetry (LND)Experiment	23
3.2	Solar orbiter and High energy telescope	32
4	FIRST SOLAR ENERGETIC PARTICLES MEASURED ON THE LUNAR FAR-SIDE	37
4.1	Introduction	40
4.2	Observations	41
4.3	Summary and Discussion	44
4.4	Appendix	46
4.5	References	47
5	PRIMARY AND ALBEDO PROTONS DETECTED BY THE LUNAR LANDER NEUTRON AND DOSIMETRY EXPERIMENT ON THE LUNAR FAR SIDE	49
5.1	Introduction	51
5.2	Preparation of LND data	54
5.3	Measurements and comparison with model	59
5.4	Summary, discussion and conclusion	62
5.5	References	63
5.6	Supplement material	65
6	QUIET-TIME LOW ENERGY ION SPECTRA OBSERVED ON SOLAR ORBITER DURING SOLAR MINIMUM	69
6.1	Introduction	71
6.2	Observations	72
6.3	Discussion and conclusion	73
6.4	References	74
6.5	Appendix	75
7	OBSERVATION OF ANOMALOUS COSMIC RAYS IN THE INNER HELIOSPHERE	77
7.1	Introduction	77
7.2	Instruments and data employed in this study	79
7.3	Overview of observations between 2020 and 2022 and the cross-calibration between four instruments	82
7.4	Averaged helium intensity profile between 2020 and 2022	86
7.5	Radial gradient of ACR helium	88
7.6	Summary and discussion	93
8	CONCLUSION AND OUTLOOK	97
	BIBLIOGRAPHY	101

A LND INSTRUMENT	113
B SEPS LIST OF HET AND EPHIN MEASUREMENTS	121
C LIST OF PUBLICATIONS	125

LIST OF FIGURES

Figure 1	Energy spectra of oxygen ions in near-Earth space	2
Figure 2	Two types of Solar energetic particle (SEP) event	8
Figure 3	The first wide-spread solar energetic particle event on Nov 29, 2020	10
Figure 4	The cosmic-ray spectrum of all particles at 1 au	12
Figure 5	Sunspot number and Neutron monitor count data	14
Figure 6	The global drift pattern of positively charged particles in different polarity	15
Figure 7	Long term variation of anomalous cosmic ray (ACR) oxygen and neutron monitor count rate	18
Figure 8	The long-term radiation dose rates on the Martian surface	20
Figure 9	The proton spectra in two solar energetic particle (SEP) events indicating the possible radiation energy	21
Figure 10	A photograph of the Lunar Lander Neutron and Dosimetry Experiment (LND)	23
Figure 11	The inner structure of LND sensor head (SH)	24
Figure 12	LND Boehm plot of stopping particles based on the simulated data	28
Figure 13	LND Xmas plot from measurements	30
Figure 14	The orbit of Solar Orbiter (SolO) between 2020-2030	33
Figure 15	The energy coverage of different Energetic Particle Detector (EPD) sensors	34
Figure 16	Cut view of High Energy Telescope (HET) sensor head	34
Figure 17	The orbit variation of SolO in Carrington coordinate system	80
Figure 18	Orbit track of SolO	81
Figure 19	The quiet time spectra of helium, carbon, nitrogen, and oxygen between 2020 and 2022	84
Figure 20	The helium spectra when SolO was between 0.95 and 1 au	84
Figure 21	Overview of helium intensities measured by different instruments	85
Figure 22	The multiple detector counters of HET	87
Figure 23	The proton intensity profile observed by Electron Proton Helium Instrument (EPHIN)	87
Figure 24	The averaged helium flux in four energy channels between 10 and 50 MeV/nuc	89
Figure 25	11.1 - 19.4 MeV/nuc HET helium flux vs the radial distance of SolO	90
Figure 26	Ratio of helium intensity between HET and EPHIN and helium radial gradient in different energy range	91
Figure 27	Energy dependency of the helium radial gradient	92
Figure 28	The time variation of the ACR helium radial gradients	93

Figure 29	The sketch of LND sensor head	114
Figure 30	The overview of the proton, helium flux and Total Ionizing Dose (TID) measured by LND	115
Figure 31	LND temperature, bias current, and bias voltage variations	119

LIST OF TABLES

Table 1	Two classes of SEP events	9
Table 2	Time periods when Solar Orbiter (SolO) closed to 1 au	86
Table 3	Table of helium radial gradient	90
Table 4	Table of helium radial gradient with extra mask	95
Table 5	LND SEP events lists	116
Table 6	SEP events list and duration from SolO/HET	121
Table 7	SEP event list and duration from SOHO/EPHIN	122

ACRONYMS

ACE	Advanced Composition Explorer
ACR	anomalous cosmic ray
ARS	Acute Radiation Syndrome
Bepi	BepiColombo
BGO	bismuth germanium oxide
CAD	computer-aided design
CIR	corotating interaction region
CME	coronal mass ejection
CRIS	Cosmic Ray Isotope Spectrometer
CRI	Cutaneous Radiation Injuries
CRaTER	Cosmic Ray Telescope for the Effects of Radiation (onboard LRO)
DSCOVR	Deep Space Climate Observatory
DNA	Deoxyribonucleic Acid
dps	data product scheduler
EB	electroninc box
EPD	Energetic Particle Detector (onboard SolO)
EPHIN	Electron Proton Helium Instrument (onboard SOHO)
EPAM	Electron, Proton, and Alpha Monitor
EPT	Electron Proton Telescope (part of EPD onboard SolO)
EUV	Extreme ultraviolet
ESA	European Space Agency
FD	Forbush decrease
FFS	Force-field Solution
FOV	field of view
GCR	galactic cosmic ray
Geant4	Geometry and Tracking 4 (simulation toolkit, Agostinelli et al., 2003)
GLE	ground level enhancement
HCS	Heliospheric Current Sheet
HEE	Heliocentric Earth Ecliptic (coordinate system)
HET	High Energy Telescope (part of EPD onboard SolO, or onboard STEREO)
HSS	high speed stream

HMF	Heliospheric Magnetic Field
ICME	interplanetary coronal mass ejection
IMF	interplanetary magnetic field
IMP	Interplanetary Monitoring Platform
ISM	interstellar medium
ICME	interplanetary coronal mass ejection
LASCO	Large Angle and Spectrometric Coronagraph Experiment (onboard SOHO)
LET	linear energy transfer
LET	Low-Energy Telescope
L1	the first Lagrange point
LIS	Local Interstellar Spectra
VLISM	Very Local Interstellar Medium
LND	Lunar Lander Neutron and Dosimetry Experiment
LRO	Lunar Reconnaissance Orbiter
MAVEN	Mars Atmosphere and Volatile Evolution
NASA	National Aeronautics and Space Administration
MIP	minimally ionizing particle
NMDB	Neutron Monitor Database
NSSC	National Space Science Center of the Chinese Academy of Sciences
MSL	Mars Science Laboratory
NOAA	National Oceanic and Atmospheric Administration
PCB	printed circuit board
PSP	Parker Solar Probe
RTG	Radioisotope Thermoelectric Generator
RHU	Radioisotope Heater Unit
RAD	Radiation Assessment Detector(onboard MSL)
REDMoon	Radiation Environment and Dose at the Moon
SDO	Solar Dynamics Observatory
SEP	solar energetic particle
SC	Solar Cycle
SIR	stream interaction region
SIS	Solar Isotope Spectrometer onboard ACE
SIS	Suprathermal Ion Spectrograph (part of EPD onboard SolO)
SOHO	Solar and Heliospheric Observatory

SolO	Solar Orbiter
SSD	solid state detector
SEE	single event event
SH	sensor head
STEP	Suprathermal Electrons and Protons (part of EPD onboard SolO)
STEREO	Solar Terrestrial Relations Observatory
TID	Total Ionizing Dose
TPE	transport equation
UV	ultraviolet
3DP	3D Plasma and Energetic Particle Investigation

INTRODUCTION AND MOTIVATION

1.1 ENERGETIC PARTICLES IN THE HELIOSPHERE

The heliosphere is a vast, bubble-like region in space that envelops the Sun. This region is moving with respect to the interstellar medium (ISM) with a speed of about 25 km/s (McComas et al., 2015). The heliosphere can also be regarded as a plasma cavity. This cavity is created by the Sun and is governed by the solar wind and its embedding magnetic field. It is filled by particles with various origins. The particle populations are identified from Fig.1 which is adapted from Mewaldt et al. (2001). Based on the accumulated measurements of oxygen by the Advanced Composition Explorer (ACE) between 1997 and 2000 at 1 au, the oxygen fluence spectrum, which spans over more than seven orders of magnitude from keV/nuc to GeV/nuc provides clear insight into the lower energy particles including the slow solar wind, the fast solar wind, the suprathermal tails, and high energetic particles composed of solar energetic particles (SEPs), anomalous cosmic rays (ACRs), and the extremely high energetic galactic cosmic rays (GCRs).

The solar wind is a stream of charged particles released from the solar corona, the upper atmosphere of the Sun. This plasma consists mainly of protons and electrons that continuously flow outward and expand to about ~ 100 au (depending on the direction and the phase of the solar activity cycle). The typical energy range of the solar wind is between 0.5 keV and 4.5 keV. Depending on the locations that produce the solar wind, the speed and density of the solar wind might be different. For instance, the fast solar wind with a typical speed between 500 and 800 kilometers per second is emitted from the coronal holes, which are funnel-like regions of open field lines in the magnetic field and usually appear at the north and south poles of the Sun (Sakao et al., 2007; Tu et al., 2005; Hundhausen et al., 1968). Therefore, the fast solar wind dominates the high latitude regions during the solar activity minimum. On the other hand, the slow solar wind is observed to have a velocity of about 300 - 500 kilometers per second and is believed to originate from the equatorial region. Some may also come from the boundaries of coronal holes. The slow solar wind is more likely to be observed in the low latitude regions.

Suprathermal particles are ions and electrons that move about two to hundreds of times faster than solar wind particles. In the spectrum shown in Fig.1, the suprathermal particles are beyond the tails of the fast solar wind and are the dominant particle population between a few keV to few Mev. The source of the suprathermal particles might be the accelerated solar wind and the remnants of previous solar eruptions and SEP events (Gloeckler et al., 1995). Suprathermal particles are suspected to play an important role as seed particles for SEP events (Kahler and Ling, 2019).

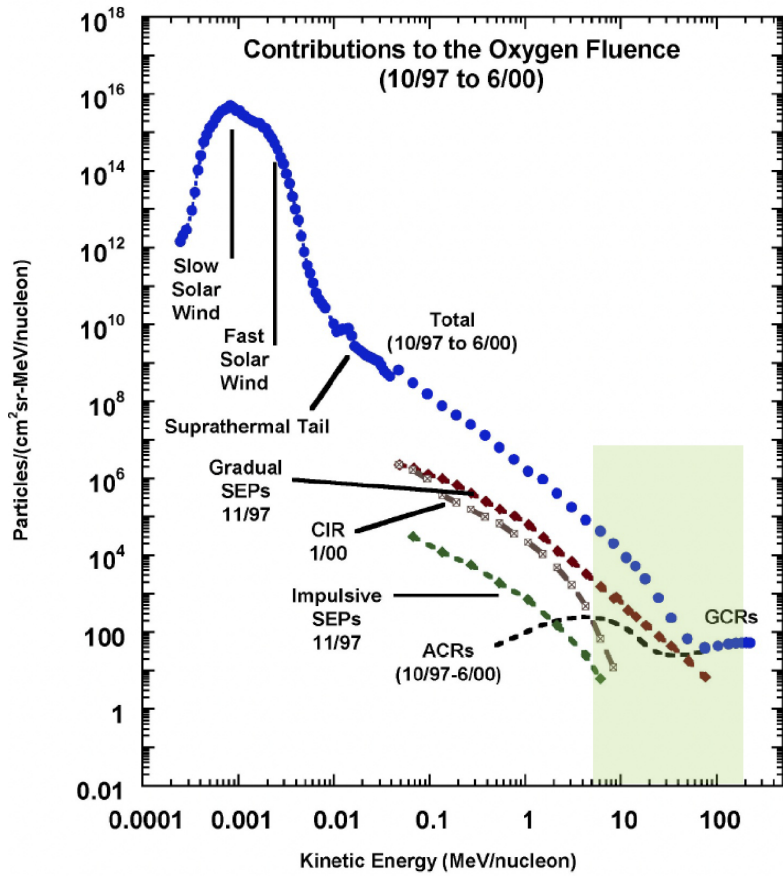


Figure 1: The typical oxygen spectra in the interplanetary space near Earth, indicating the contributions of different particle populations, particularly in the energy range between few MeV/nuc and few hundred MeV/nuc (green shaded region), where SEP, ACR and GCR coexist. The spectra of other particle species, such as, helium and protons, have a similar shape but a different flux level in the corresponding energy regime. The figure is adapted from Mewaldt et al. (2001)

Above the energy of suprathermal particles is the energy range that we are interested in in this thesis, especially the energy range between a few MeV/nuc and a few hundred MeV/nuc where the dominant particles are SEPs (not limited to this energy range), ACRs (up to ~ 100 MeV/nuc) and lower energy GCRs. The measurements we used in this study are from this energy range.

SEPs are high-energetic particles with energies ranging from a few keV up to \sim GeV. They are emitted from the Sun and accelerated by solar flares and coronal mass ejection (CME)-driven shocks. SEP events are intermittent, short-term, and typically intensive, compared with cosmic rays (Reames, 1999). Different types of SEP events persist for different time scales from a few hours to a few days.

ACRs are believed to be the high energy interstellar pick-up ions (Giacalone et al., 2022). Pick-up ions are born from neutral interstellar atoms getting ionized by solar UV radiation and charge exchange process with solar wind after the neutral atoms flow into the heliosphere. Those ionized particles are then carried

by the expanding solar wind to the outer heliosphere, where they are accelerated somewhere near the termination shock to higher energy and then redirected inwards (Russell et al., 2016). The exact accelerated site is still unclear. The typical ACR species that have been observed are protons, helium, oxygen, nitrogen, neon, and argon.

GCRs are fully ionized particles that are accelerated at so-called supernova remnants (Blasi, 2013) outside of the solar system. Those energetic particles bombard Earth constantly. The complete spectrum of GCRs covers the energy from a typical few MeV (Potgieter, 2013) to TeV, which is even larger than the energy range in Fig. 1. GCRs are comprised of about 99% ions and 1% electrons.

After entering the heliosphere, the transport of both ACRs and GCRs are controlled by the Heliospheric Magnetic Field (HMF). Hence ACR's and GCR's temporal variation is highly related to the solar activity and so-called solar modulation. More details of the solar modulation will be discussed in Section 2.2.

1.2 MOTIVATION

So, why do we choose energetic particles in the tens to hundreds of MeV/nuc range as the central topic of this thesis? First, it is worth noting that charged particles within this energy range exhibit complicated properties and consist of three distinct particle populations, varying depending on time, energy range, and particle species. Disentangling the specific particle types within this energy range is exceptionally challenging, particularly when the Sun is active. By investigating these charged particles, we have the opportunity to gain insights into the origin, acceleration, and transport mechanisms of SEPs, ACRs, and GCRs. In this thesis, we focus on the questions that we bring up below.

Furthermore, as space exploration advances, energetic particles are recognized as one of the most dangerous radiations in space, especially those of hundreds of MeV energy. They pose potential threats to astronaut health and have a significant possibility of causing direct radiation damage such as nausea and vomiting and after-effects like cancer. They could also fail the functioning of electronic devices (Reames, 2021; McKenna-Lawlor et al., 2015; Armstrong et al., 2014). The secondary particles generated on the lunar surface from the interaction between cosmic rays and the lunar regolith can also reach such high energy and contribute significant radiation dose rate on the lunar surface (Schwadron et al., 2016), which are particularly important for crewed missions to the Moon. Therefore, understanding the variations and distribution of those energetic particles or even higher energy particles in space and on the lunar surface is particularly important for future human space exploration.

Lastly, another compelling reason for the investigation of the particles of interest here is the data from two new instruments. The instruments are the Lunar Lander Neutron and Dosimetry Experiment (LND) on board Chang'E - 4 and the High Energy Telescope (HET) on board the Solar Orbiter (SolO), which were developed by the extraterrestrial physics department at Kiel University and measure charged particles within this energy range. Chang'E-4 was the first mission that was ever launched to the far-side surface of the Moon. It serves as a monitor of the

radiation environment and a charged particle telescope. Meanwhile, HET provides an excellent opportunity to measure energetic particles within one au. We have the opportunity to study many questions using the new measurement of tens of MeV/nuc energetic particles (Wimmer-Schweingruber et al., 2020; Rodríguez-Pacheco et al., 2020), such as the questions we ask below. Consequently, those studies can advance our understanding of particles in space and the radiation environment on the lunar surfaces.

There are numerous intriguing questions regarding those energetic particles within the heliosphere. In this thesis, we mainly focus on the following questions:

Scientific questions - SEPs

S1: What is the source of those tens of MeV particles?

S2: How do those tens of MeV particles arrive at distant longitudes?

Scientific questions - cosmic rays

C1: How do the ACRs and GCR behave during the most recent solar activity minimum and the onset phase of solar cycle 25?

C2: What is the difference between the current solar cycle and the previous one?

C3: How does solar modulation affect the intensity of cosmic rays?

C4: How do the cosmic rays distribute within the inner heliosphere?

C5: How do those secondary particles induced by those cosmic rays affect the radiation environment on the lunar surface?

SEPs are the product of multiple processes that fill the heliosphere and are observed at different locations. With limited satellite observations from few locations in space, it is hard to figure out different processes involved in the generation and transport of SEPs. In the new space era, more and more spacecraft and instruments are deployed in space at different locations. Those significant observations allow us to study the SEPs from different perspectives. A case study of SEPs is given in section 4 of this thesis.

Meanwhile, the recent solar activity minimum ended in 2020, before the starting of the new Solar Cycle (SC) 25. Notably, this solar cycle has exhibited unusual properties compared to the previous solar cycle. For example, observations have indicated historically high levels of GCR flux during this period, exceeding the space-age records (Fu et al., 2021; Xu et al., 2022), but ACR intensities have not reached the same record-setting levels (Strauss et al., 2023). In addition, solar activities increased rapidly during the onset of SC 25, suggesting that this solar cycle could be the strongest since records began (Nagovitsyn and Ivanov, 2023). The peak of the SC might arrive one year earlier than anticipated (Prasad et al.,

2023; McIntosh et al., 2020). We discuss those questions regarding the cosmic rays during the new solar cycle in Xu et al. (2022) and Mason et al. (2021b) and the fourth part below, where we report the observations of ACR helium.

The structure of the thesis is as follows: After the introduction in this section, we give the observational and theoretical background of SEPs, GCRs, and ACRs in the heliosphere in Sec. 2. In Sec. 3, we briefly introduce the two new instruments - LND and SolO/HET - and the data that we use in this thesis. In the next chapters, we report our findings of the first SEP observed on the lunar far-side surface. In Sec. 5 we report GCRs and secondary protons measured on the lunar surface. In Sec. 6 we report the latest quiet time spectra of energetic particles measured by SolO in the inner heliosphere. And in Sec. 7, we report the ACR helium radial gradients based on the newest measurements from SolO/HET. The summaries and outlooks are given in the last section. In particular, more detailed information on the LND is provided in the Appendix A.

OBSERVATION AND THEORETICAL BACKGROUND OF ENERGETIC PARTICLES

2.1 SOLAR ENERGETIC PARTICLES

Two types of SEPs

The first observation of solar energetic particle (SEP) event was made during a magnetic storm on March 1, 1942, (Lange and Forbush, 1942; Forbush and Lange, 1942), during which three unusual increases in the cosmic-ray intensity were observed in ground-based ionization chambers and neutron monitors. Those increases appeared simultaneously with solar flare eruptions. Later, Forbush (1946) attributed such increases to the charged particles emitted from the Sun with sufficient energy to penetrate the Earth's atmosphere. Nowdays, such events are called ground level enhancement (GLE) events. The particle energies in these events exceed ~ 400 MeV/nuc and pose a major threat for astronauts health (Meyer et al., 1956; Shea and Smart, 2012; Gopalswamy et al., 2013; Thakur et al., 2014; Reames, 2013; Miroshnichenko et al., 2013).

During the first few decades after the discovery of SEP, it was commonly believed that the generation of SEPs were highly related to solar flares because they appeared simultaneously. This is the so-called "solar flare myth" as discussed in Gosling (1993). The important role of coronal mass ejections (CMEs) and the CME-driven shocks that are capable of accelerating particles up to energies of few GeV had been largely underestimated, although a considerable amount of studies focused on the characteristics of such SEPs like the duration, longitudinal distribution, the abundance of the typical elements and their association with radio burst had already indicated the existence of two types of distinct events - impulsive and gradual SEP events (Kahler et al., 1978, 1984; Cliver et al., 1982; Cane et al., 1986; Reames, 1988). Currently, scientists have established a classic two-class paradigm (See, Fig. 2 and Tab. 1), which has been widely accepted by the science community (Kallenrode, 2003; Reames, 2013; Desai and Giacalone, 2016; Reames, 2021). Both the acceleration mechanisms and the source locations are different for the two types of SEPs.

Fig. 2 illustrates the established scenario of gradual (left) and impulsive (right) SEPs. The gradual events are diffusively accelerated by the CME-driven coronal and interplanetary (IP) shocks. Generally, a complete gradual SEP event usually consists of a sharp increase phase as the start, a long-lasting plateau, and a flux peak at lower energy, which indicates the arrival of the CME at the detector. The event finishes with a decay phase, and the flux returns to the quiet-time level. The whole process might persist from one day to several days. Gradual SEPs are always accompanied by type II radio bursts, which are generated when the shock wave propagates out from the corona to 1 au (Gopalswamy, 2006). Shocks mainly

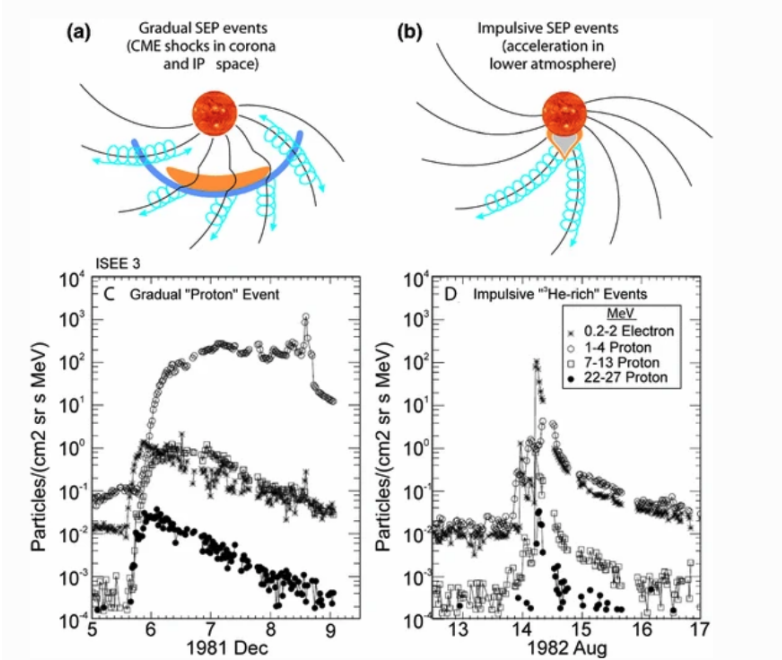


Figure 2: Two classes of SEP events. (a) The gradual SEP events that are associated with CME driven shocks in the corona or in the interplanetary space. The particles populate the interplanetary magnetic field (IMF) lines over a wide range of longitudes. (b) The impulsive SEP events that are associated with solar flares. Here, the particles only populate a limited range of the open IMF lines that are well-connected to the flare site. Plots (c) and (d) are the corresponding typical proton and electron time profiles of the large gradual and small impulsive SEP events. The figure is reproduced from Desai and Giacalone (2016).

accelerate protons and heavy ions, but not electrons with the same efficiency, causing a smaller electron-to-proton ratio compared to impulsive SEP. Besides, gradual SEPs events spread widely in the IP since CMEs have broader longitudinal extents and can be measured by multiple detectors even if they are far away from each other. The appearance frequency of gradual SEPs during the solar activity maximum is about ~ 100 per year.

On the other hand, a solar flare that erupts from the solar active region is considered as the source of an impulsive SEP event. The strong magnetic reconnection during the flare eruption can accelerate particles, especially electrons, up to tens of MeV. Therefore, the electrons are the dominant particles in such an event. Besides, in this scenario, the particles escape from the open magnetic field and arrive at the Earth along the spiral magnetic field. i.e. the Parker spiral (Parker, 1958), that is shaped by the expanding solar wind. From the Earth's point of view, the impulsive SEPs are typically located in a narrow region in the western hemisphere of the Sun. Type III radio bursts usually appear with impulsive events rather than CMEs. The appearance frequency of impulsive SEPs during the solar activity maximum is about $\sim 10^3$ per year. The typical duration of impulsive SEP is less than days.

It is worth noting that Cane et al. (2003) proposed a type of mixed event that have flare particles as seed population and later, those particles are reaccelerated

by the shocks. Such intensive SEPs have two components related to both flare and shocks.

In Tab. 1, we summarized the general properties of the two types of SEP events.

Table 1: Two-class paradigm of SEP event, adapted from Kallenrode (2003), Desai and Giacalone (2016), and Wang (2009).

Property	Gradual SEP (Large SEP)	Impulsive SEP (Electron/ ${}^3\text{He}$ -rich SEP)
Dominant particle	protons	electrons
Electron/proton ration	50 - 100	$10^2 - 10^4$
${}^3\text{He}/{}^4\text{He}$ ratio	4×10^{-4}	1
Fe/O	~ 0.1	~ 1
H/He	~ 100	~ 10
Q_{Fe}	~ 14	~ 20
Duration	\sim Days	\sim hours
Longitude cone	$> 100^\circ$	$< 30^\circ$
Seed particles	Ambient Corona or Solar wind	Heated corona
Radio burst type	Type II/IV	Type III
X-ray duration	\sim hours	\sim minutes - 1h
CME association	Yes (fast)	No
Frequency(at solar activity maximum)	~ 10	~ 1000

Wide-spread SEP and multi-instruments observation

In this part, we briefly introduce the multiple observations of the wide-spread SEPs. Figure 3 shows the first widespread SEP of the Solar Cycle (SC) 25 happened on 2020 November 29 that was observed by SolO and also by PSP, STEREO, ACE and SOHO near the Earth, with a shift in the onset time (Kollhoff et al., 2021; Kouloumvakos et al., 2022; Palmerio et al., 2022). Both relativistic electrons and higher energy protons with energy >50 MeV were observed. The particles in this event spread over a region at 1 au spanning more than 230° in longitude. This SEP was associated with an M4.4 class flare accompanied by a CME, Extreme ultraviolet (EUV) waves, and type II/III radio bursts. The black arrow in the central panel indicates the location of the active region and the possible location of the central meridian of the CME. Depending on the magnetic connection between the CME-driven shock and the instrument at different locations, as indicated by colored lines in the central panel, the time profiles of particles recorded by different observers have different shapes. For instance, both PSP and STEREO connect to the neighboring source region of the flare eruption region. Hence, their intensity profile shapes are similar to the SEP we showed in Fig. 2, i.e., abruptly increase with a later peak when the shock reached the spacecraft location. While

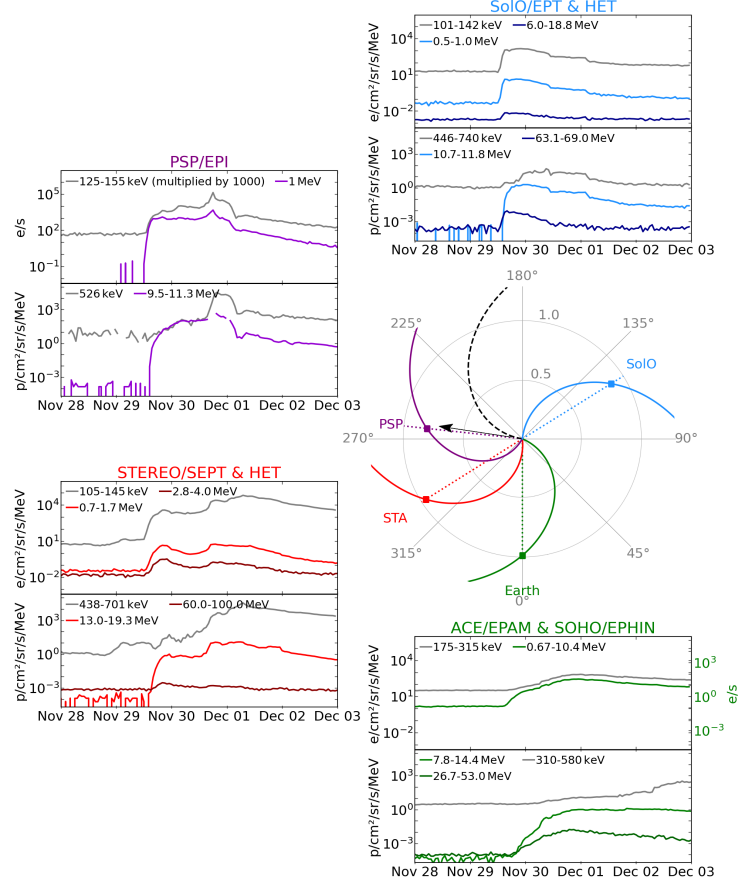


Figure 3: The first wide-spread solar energetic particle event on Nov 29, 2020. The central panel illustrates the locations of different spacecraft and their magnetic connections to the Sun. Both proton and electron observations from Solar Orbiter (SolO) (top), Parker Solar Probe (PSP) (top left), Solar Terrestrial Relations Observatory (STEREO)-A (bottom left), and the Earth including Advanced Composition Explorer (ACE) and Solar and Heliospheric Observatory (SOHO) are given. (Figure reproduced from Kollhoff et al. (2021))

Earth is about 166° away from the active region and is connected to the western limb of the source, the intensity of the event slowly increases before they peak.

Recently, a comprehensive study of the second widespread SEP of SC 25 that occurred on 2021 April 17 has been carried out by Dresing, N. et al. (2023). The particles were detected over a region of more than 210° longitude at six locations between 0.42 au and 1.62 au, including the four used in the previous study, BepiColombo (Bepi) and the energetic particle instrument near Mars, though the Mars observation only provides an observational constrain. Dresing, N. et al. (2023) argued that the distinct SEP injections, which cover a wide range of longitudes, should be the reason for this widespread SEP event.

As indicated in the above two examples, the widespread SEP event is a subclass of events with particles being spread over a range of longitude more than 200° , though the minimum requirement of the longitudinal separation has not been well defined (Dresing, 2014). The shape of particle's temporal profiles at different locations, especially if they are far away from each other, varies a lot, which

indicate possibly completely different transport effects and source of particles. Therefore, one of the most essential questions about widespread SEP is how the energetic particles spread through the heliosphere in such large longitudinal regions. Many ideas have been proposed to explain the longitudinal property (Richardson et al., 2014; Dresing et al., 2012; Desai and Giacalone, 2016; Reames, 2021). The possible mechanisms of the large-spread SEPs include:

- Magnetic connection to an expanding coronal and IP shock (Cliver et al., 1995; Torsti et al., 1999; Reames, 1999; Cane et al., 2003; Richardson et al., 2014; Kouloumvakos et al., 2019): The widespread energetic protons and heavier ions are accelerated by the shocks and are released from different shock fronts. These particles are observed when shock fronts are intersected by and connected to the magnetic footprint of the observer. Hence, the SEP distribution depends on the extent of the shock in the inner heliosphere.
- Cross-field diffusion (Dresing et al., 2012): The particles are transported perpendicular to the average IMF direction in the solar wind, which is a slow process compared with parallel transport along the magnetic field lines.
- Coronal transport (Reinhard and Wibberenz, 1974; Newkirk and Wentzel, 1978): This process spreads energetic particles from the source region i.e., a flare or an active region, to the remote longitudes in the corona via a divergent magnetic field.
- Multiple particle injections from different sources (Dresing, N. et al., 2023): The distinct SEP injections covering a wide range of longitudes might be responsible for the widespread SEP event.
- EUV waves (Rouillard et al., 2012; Park et al., 2013): EUV waves are large scale disturbances in EUV images. Those waves encounter the magnetic foot point on the solar surface when they are propagating and expanding outward, which might be used to account for the widespread SEP events.
- Meandering magnetic field lines (Laitinen et al., 2016, 2023): The meandering walk of magnetic field lines is associated with turbulence in the solar wind and causes efficient particle movement across the magnetic field lines.
- Particle transport to remote longitudes by large-scale magnetic loops (Klassen et al., 2018; Schrijver et al., 2013) and along the heliospheric current sheet (Battarbee et al., 2018).
- Mixture of the processes above.

To further clarify the processes leading to widespread events, multi-spacecraft observations are essential for determining the properties of widespread SEP events (Kollhoff et al., 2021). Previously, major contributions to understanding these events have been made by the combined measurements of STEREO mission with its two spacecraft and the remote-sensing and in-situ measurements near the first Lagrange point (L1). Nowadays, with the new era of spacecraft, including Parker Solar Probe (Fox et al., 2016), Solar Orbiter (Müller et al., 2020), and

the Lunar Lander Neutron and Dosimetry Experiment (Wimmer-Schweingruber et al., 2020) we have a better opportunity to investigate the spectral variation, acceleration, transport processes and other aspects of widespread SEP events in more detail.

We had to admit that the SEP is a very broad topic, and we can not include every aspect of SEPs here due to the limitation of length. More details can be found in review papers (Reames, 2013; Desai and Giacalone, 2016; Reames, 2021).

2.2 GALACTIC COSMIC RAYS

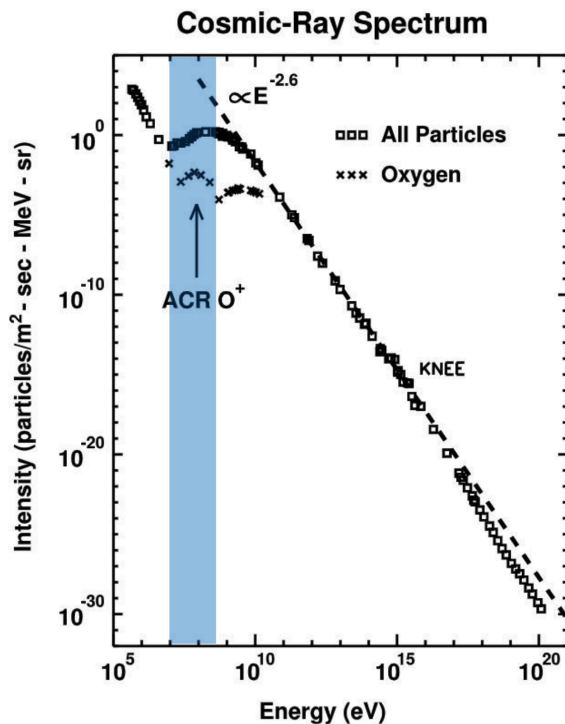


Figure 4: The cosmic-ray spectrum of all particles and anomalous cosmic ray (ACR) oxygen observed at 1 au. This figure is reproduced from Giacalone et al. (2022, 2012), which is originally from Jokipii (1990). The spectrum shows more than 15 orders of magnitude on the energy scale and about 30 orders of magnitude on the intensity scale. In particular, it extends the high energy end of Fig.1. The blue shaded region indicateds the energy range that we are interested in this thesis.

The first discovery of galactic cosmic rays (GCRs) was made by Victor Hess in 1912 when he carried out a balloon experiment. The initial purpose of the experiment was to find the source of ionizing radiation in Earth's atmosphere using an electroscope. However, as the balloon climbed up during the experiment, he found that the ionization rate measured in the electroscope showed a less significant decrease than anticipated. Such a discrepancy was attributed to the existence of cosmic rays, which increase the radiation in the atmosphere. Later

Millikan and Cameron (1928) for the first time coined the term "cosmic ray" after they carried on a similar balloon experiment over Texas.

Figure 4 shows the spectrum of cosmic ray particles that can be observed at 1 au. This spectrum includes both the ACR and GCR components. The GCRs are indicated as empty squares. In the right half of the spectra with energy above 1 GeV, the spectrum could be simply fitted by power law spectrum with an index of about -2.6. The higher energy knee in the GCR spectrum is around few PeV energy and reflects the dominant contribution of hypernovae (Sveshnikova, 2003; Hörandel, 2003). The lower energy spectrum below 1 GeV is shown as a "turnover" structure which is more complicated and could not be simply fitted by a power law spectrum.

GCRs consists of multiple energetic particle species spanning a wide range of energy, which are mostly simple protons, about 89%, and the remains are shared by 9% helium nuclei, a small fraction of nuclei of heavier elements (1%) and 1% electrons. Abundances may vary with time. It is believed that GCRs mainly originate from the supernova remnants which are at distant locations away from the Sun (Blasi, 2013; Bhattacharjee, 2000; Fermi, 1949). Particles obtain the energy from the shock waves that are generated during the explosion of supernova (Blandford and Ostriker, 1978).

GCRs have an isotropic and constant intensity profile before entering the heliosphere. Their energy spectra are called the Local Interstellar Spectra (LIS) or the heliopause spectra, which are observed by the Voyager missions after the space-craft crossed the boundary of the solar system and entered the interstellar medium (Stone et al., 2013; Cummings et al., 2016; Stone et al., 2019). When propagating in the heliosphere, cosmic rays are modulated periodically by the solar wind emitted from the Sun and the magnetic field embedded in it. The relevant process of the solar modulation can be described by a basic transport equation (TPE), which was first derived by Parker (1965). The same equation was also derived by Gleeson and Axford (1967) in a more rigorous way. This equation is based on the motion of charged particles in the frequently changing magnetic field and averaged over the pitch angle of particles moving in the magnetic field. The precondition of this equation is the reasonable assumption of the isotropically distributed GCRs. In Potgieter (2013), the heliospheric TPE is rewritten in the following form:

$$\underbrace{\frac{\partial f}{\partial t}}_a = -(\underbrace{V}_b + \underbrace{\langle v_d \rangle}_c) \cdot \nabla f + \underbrace{\nabla \cdot (K_s \cdot \nabla f)}_d + \underbrace{\frac{1}{3} (\nabla \cdot V) \frac{\partial f}{\partial \ln P}}_e \quad (1)$$

s

where $f(r, P, t)$ is the cosmic ray distribution as a function of time, t, particle rigidity, P , and 3-dimensional position in space. Compared with the ~ 11 and 22 years solar activity cycle, the periodic solar rotation (~ 27 days) and the time of the solar wind traveling to the edge of the heliosphere ($\gtrsim 1$ years) are short-term variations. Hence, the steady-state solution with $\frac{\partial f}{\partial t} = 0$ (part a of Eq.1) is a reasonable assumption and considered when we study the solar modulation of cosmic rays. Terms on the right side of the Equation 1 include four effects that are used to describe the variation of the cosmic rays: (b) convection due to the solar wind velocity V ; (c) drift effects caused by the gradient and curvature of

the large-scale Heliospheric Magnetic Field (HMF), which is estimated by a 3D Archimedean spiral (Parker, 1958), $\langle v_d \rangle$ represents the averaged drift velocity; (d) diffusion effects caused by the turbulent magnetic field, with K_s the symmetrical diffusion tensor; (e) adiabatic energy change and deceleration due to the expansion of the solar wind.

TPE is a highly non-linear partial differential equation. A simplified solution of the modulated GCR spectra called Force-field Solution (FFS) was first derived by Gleeson and Axford (1967, 1968). The solution simply depends on the kinetic energy T of particles and the solar modulation potential for the same particle type and the same LIS. Later, reasonable GCR spectra of the particle with energy above 150 MeV were given by Gleeson and Urch (1973). With the development of computer techniques and numerical studies, simulations are becoming more and more important in studying the transport and solar modulation of the cosmic rays (Jokipii and Kopriva, 1979; Le Roux and Potgieter, 1995; Manuel et al., 2011; Potgieter, 2013; Vos and Potgieter, 2015; Vos and Potgieter, 2016; Boschini et al., 2019, 2022; Corti et al., 2019; Shen et al., 2019). Commonly used GCR models like Badhwar-O'Neill (O'Neill, 2006; O'Neill, 2015; Slaba and Whitman, 2020), CREME (Tylka et al., 1997; Weller et al., 2010) and HELMOD (Boschini et al., 2018) with the solar modulation and sunspot number as input attempt to reproduce the GCR intensity and spectra. The model predictions are consistent with the measurements from ACE at 1 au and the Voyager probes in different regions of the heliosphere (Boschini et al., 2019).

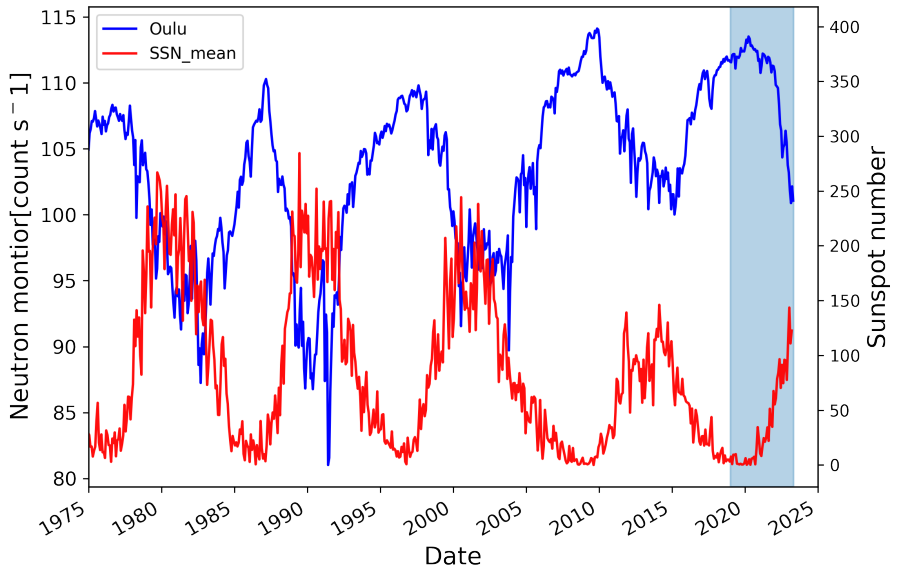


Figure 5: Oulu neutron monitor count rate downloaded from the Neutron Monitor Database (NMDB) measured by the Sodankyla Geophysical Observatory of the University of Oulu, Finland and the monthly averaged sunspot number from Solar Influences Data analysis Center (SIDC), Royal Observatory of Belgium, Brussels. The blue shaded region marks the period that we are interested in.

Figure 5 shows the monthly averaged sunspot number since 1975 in red and the Oulu neutron monitor count rate in blue. The sunspot number is a proxy for solar activity. The neutron monitor count rate reflects the temporal variation of neutrons that are generated during the process of high-energy charged particles penetrating Earth's atmosphere. The overall variation of the neutron monitor count rate is anti-correlated with the averaged sunspot number. The count rate peaks during the solar activity minimum when the sunspot number is minimum and vice versa in the solar activity maximum. The time between two neighboring solar minima is about 11 years, which is the period of the solar activity cycle and is caused by the polarity reversal of the solar magnetic field.

Besides the magnetic field reversal, drift effects play an important role in the 22-year cycle of the cosmic ray intensity (Jokipii et al., 1977). Such effects are clearly observed in the temporal variations in Fig. 5. During the negative polarity (denoted by $A < 0$) cycle, GCRs have a more peaked time profile than the positive polarity (denoted by $A > 0$) cycle, which have a plateau-like profile. This is because in the negative magnetic polarity cycle, the positively (negatively) charged particles drift inwards (outwards) mainly along the equatorial plane in the heliosphere and drift outward (inwards) through the open magnetic field line in the polar region, which results in a sharp change of the intensity. While in the positive polarity cycle, the drift direction of the particles is opposite to that in a negative cycle, which causes the plateau region on the solar minimum. Fig. 6 illustrates the drift effects in the opposite polarity cycles, explicitly depicting the drift directions of positively charged particles such as helium and oxygen.

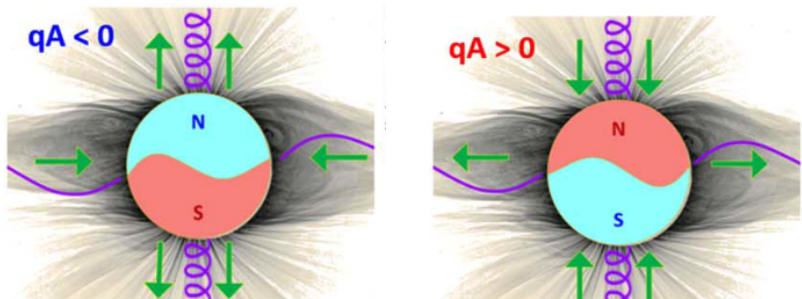


Figure 6: The illustrations of the cosmic ray drift pattern in negative polarity (left) and positive polarity (right). The Sun's north pole has a positive magnetic field, while the south pole has a negative magnetic field during the $A > 0$ cycle. The signs of the magnetic field in the south and north poles are reversed during the $A < 0$ cycle. The green arrows indicate the drift directions of ions, and the wavy lines in purple are the heliosphere current sheets. This figure is adapted from the Fig. 4 of Rankin et al. (2022)

Furthermore, the drift effects, which depend on the charge sign of particles and the magnetic polarity, are also reflected in the spatial gradient of the cosmic rays, including both GCRs and ACRs. In the following, we recap the observation of GCR spatial gradient with energy above hundreds MeV/nuc, although those observations are not the focus of this thesis. The details of the ACR component are discussed in the next section.

One evidence of GCR latitudinal variation is the observation from Ulysses. Simpson et al. (1995) and Heber et al. (1996a,b) determined positive variations with an upper limit of 0.25 % /° in the A > 0 solar cycle. When the polarity changes to the negative sign, the latitudinal gradient was found to change the sign accordingly and decrease to a very small value with a maximum of -0.1 %/° (de Simone et al., 2011; Gieseler and Heber, 2016). It was also found that the solar modulation conditions in the same solar polarity but different solar cycles could affect the latitudinal gradient (Gieseler and Heber, 2016; Vos and Potgieter, 2016). Moreover, the latitudinal gradient of electrons was first determined by Heber et al. (2008), which was about 0.2 % /° and agreed with the proton gradient.

Recently, by revisiting GCR proton data from Helios E6, Marquardt and Heber (2019) found that the radial gradient in the inner heliosphere (0.3 - 1 au) is about 6.6 ± 4 % /au, compared with the previous results of 2.5 ± 0.5 % /au between 2 and 28 au (Webber and Lockwood, 1981). Such a discrepancy indicates that the radial gradients in the inner heliosphere have different behavior than those in the outer heliosphere.

2.3 ANOMALOUS COSMIC RAY

ACRs are mostly the singly charged energetic particles dominantly in the energy range between a few MeV/nuc and ~ 100 MeV/nuc. ACRs were first discovered with Interplanetary Monitoring Platform (IMP) 7 and 8 missions, which date back to the 1970s (Garcia-Munoz et al., 1973; Hovestadt et al., 1973; McDonald et al., 1974). By analyzing the low energy spectra of cosmic rays, scientists found "unusual" enhancements of the flux of helium below 50 MeV/nuc, oxygen and nitrogen below 20 MeV/nuc. The intensity of lower energy oxygen does not decrease as the energy decreases from hundred MeV/nuc to MeV/nuc, as expected from our understanding of the GCR spectrum, but increases instead. The anomalous oxygen spectrum is pointed out by an arrow in Figure 4. Due to their anomalous behaviors in the cosmic spectrum, these were called anomalous cosmic rays. ACR elements include helium, nitrogen, oxygen, and neon that have been discovered in the inner heliosphere, and Ar and possibly protons that have been found in the outer region of heliosphere (Klecker, 1995).

One of the key characteristics of ACRs is their singly charged nature (Klecker et al., 1980; Adams et al., 1991; Klecker et al., 1995). This property suggests a distinct source for ACRs and separates it from GCR and SEPs, as well as limits the travel time of ACRs in the space. Direct measurement of the charge states of tens of MeV/nuc particles is challenging with the current measurement techniques. Therefore, in the early stage, most studies relied on the propagation model to infer the charge states. For example, Klecker et al. (1980) reported that the ACR oxygen has lower charge states of < 3 by observing the phase leg effect. Later, a clever approach using the Earth's magnetic field as the magnetic spectrometer was employed to determine the charge states. Adams et al. (1991) and Klecker et al. (1995) both confirmed the charge states of oxygen, nitrogen, and neons at energies in the range of tens of MeV/nuc, which were found to be equal to 1.

It is widely believed that ACRs are the high energy interstellar pick-up ions that are accelerated in the termination shock region of the heliosphere (Fisk et al., 1974). These pick-up ions originate from interstellar neutral atoms, which are ionized by the solar ultraviolet (UV) and charge exchange with the solar wind when those atoms stream into the heliosphere. Once ionized, the solar wind picks them up and transports them to the outer heliosphere, where pick-up ions are accelerated by the blunt termination shock (McComas and Schwadron, 2006) and acquire energies of several tens of MeV/nuc. The flank of termination shock as the origin of ACR is one of the most accepted theories and is supported by observations of various instruments (McComas et al., 2019; Cummings et al., 2019).

As aforementioned and explained, the transport of cosmic rays in the heliosphere can be described by the TPE equation. Various processes are modeled in that equation, including diffusion driven by the HMF fluctuation, adiabatic energy loss, convection in the expanding solar wind, and the drift effects in the large-scale HMF, which have already been successfully modeled (Parker, 1965; Jokipii et al., 1977; Jokipii and Thomas, 1981).

At 1 AU, similar to GCRs, the intensities of ACRs are heavily modulated as they traverse the solar wind and global HMF. Figure 7 illustrates the comparison between the ACR oxygen intensity and the Newark neutron monitor count rate, which serves as a proxy of the GCRs variation in the deep space. The ACRs intensities show clearly the peaked and plateau-shaped profiles, which depend on the magnetic polarity over the last two and a half solar cycles. In particular, during periods of negative magnetic polarity, ions drift into the heliosphere near the equatorial region along the Heliospheric Current Sheet (HCS) but drift outward from the region near the south and north pole. The opposite behavior occurs during the positive polarity Solar Cycle.

As discussed previously, the spatial distribution of ACRs along the radial and latitudinal direction contains valuable insight into how the particles are transported and accelerated throughout the heliosphere (Rankin et al., 2021). By quantifying the magnitude of this gradient, we can estimate and reconstruct the transport processes involving drift and diffusion of ACRs in the heliosphere. The following general equation is used to model the radial and latitudinal gradients (Vos and Potgieter, 2016):

$$\ln\left(\frac{f_M}{f_E}\right) = G_r \Delta R + G_\theta \Delta \theta + C \quad (2)$$

where f_M is the particle flux measured by spacecraft located away from 1 au and the equatorial plane, like SolO, PSP. On the other hand, f_E is the flux measured at 1 AU by space missions like SOHO, ACE; G_r and G_θ are the radial and latitudinal gradients, respectively. C is a constant term to account for any additional contributions.

As predicted by the cosmic ray transport model, the latitudinal gradient changes signs from positive to negative or vice versa during different polarity SC. Evidences of the change-sign nature of latitudinal gradient in the outer heliosphere were first determined by the two Pioneer and Voyager missions (McKibben et al., 1979; Cummings et al., 1987; Christon et al., 1986). They found that latitudinal gradients of 15 Mev/nuc ACR helium during SC of $A > 0$ range from 2.1 to 3.1% /°.

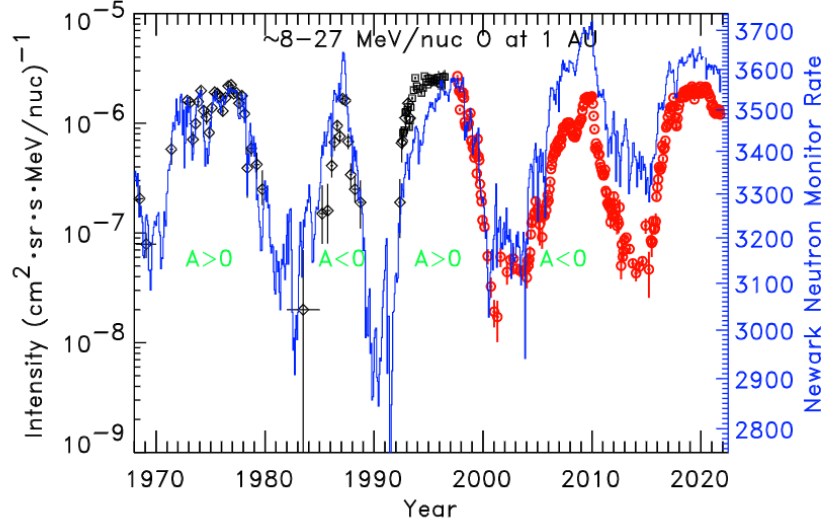


Figure 7: ACR oxygen intensity variation with energy between 8 and 27 MeV/nuc at 1 AU measured by ACE/SIS instrument (red) and count rate of Newark Neutron monitor (blue). The black data points are from the earlier measurements by Mewaldt et al. (1993). (Figure reproduced from Figure 6 of Giacalone et al. (2022))

In contrast, during $A < 0$ SC the gradients varied between -2.2 and -1.6 % /°. Moreover, ACR oxygen exhibited an even larger latitudinal gradient ranging from -3.7 to -2.9% /° (Cummings et al., 1987).

The Ulysses mission, operating in the inner heliosphere (within 5 au), significantly expanded our understanding of cosmic rays by providing the polar region measurements, thus covering a wider latitude region up to 80°. Lanzerotti and MacLennan (1995) and Heber et al. (1998) conducted studies during the positive polarity period and found the latitudinal gradients to vary between 0.39% /° and 2.12% /°. However, during the opposite solar polarity period, the respective gradients were reduced by approximately five times to about -0.3 - 0.4 % /°, which is consistent with zero. Cummings et al. (2009) concluded that particles could not drift into the inner heliosphere along the HCS in this solar cycle. In addition, a north-south asymmetry of cosmic rays was reported by Simpson et al. (1996).

Studies investigating the radial gradients of ACRs are still ongoing, and discrepancies have been found between the recent measurements in the inner heliosphere and the previous studies (Webber and Lockwood, 1981; Marsden et al., 1999) for the outer heliosphere. Recent studies by Rankin et al. (2021, 2022) and Marquardt et al. (2018), utilizing different measurements from Helios and PSP, have reported a consistent ACR oxygen radial gradient of about 45% /au during $A > 0$ solar cycle for the inner heliosphere. However, this gradient is approximately three times higher than the measurement reported by Webber and Lockwood (1981). Moreover, Rankin et al. (2022) reported the radial gradient of ACR helium with energies between 4 - 45 MeV/nuc during the last solar activity minimum (2018-2020), which was estimated to be approximately $25 \pm 5\%$ /au. Those values are also

higher than the prior observations from Pioneer, Voyager, and Ulysses mission (McDonald et al., 2001; Webber and Lockwood, 1981; McKibben, 1989; McDonald and Lal, 1986; Cummings et al., 1987, 1995). The discrepancies observed in the radial gradient of ACRs are still worth further investigation, particularly with the new measurements from SolO and PSP, which are operating below 1 au.

2.4 RADIATION HAZARD OF ENERGETIC PARTICLES

High-energy particles pose a significant threat to the human body and electronic hardwares in deep space and on the surfaces of solar system bodies, such as Mars and the Moon, where effective protection from the atmosphere and an inner magnetic field is absent. These particles can damage the Deoxyribonucleic Acid (DNA) in our cells when they penetrate tissue or organs. In this case, the possibility of cancer is largely increased when damaged cells are badly repaired. It is even worse if too many cells are killed by the abruptly increased radiation dose in a short time. High doses of radiations caused by high-energy charged particles or neutral particles result in Acute Radiation Syndrome (ARS) or Cutaneous Radiation Injuries (CRI), which are rapid whole-body responses¹. Furthermore, prolonged exposure to the radiation environment can further increase the risk of cancer, even after the mission is completed.

In addition to the health risks for astronauts, high-energy particles can also cause degradation and damage to instruments and the electronic systems onboard the satellite in space. One of the primary reasons for the instrument failure is due to the so-called single event events (SEEs), which is the change of state of a memory cell or transistor in electronic devices induced by ionizing particles, particularly heavy ions. SEEs can result in permanent or temporary failure of the electronic systems, potentially leading to the loss of mission.

The radiation hazard posed by energetic particles, based on their source, can be separated into two types: short-term but intense radiation caused by SEPs, and prolonged but lower intensity radiation mainly caused by GCRs. Exposure to intense radiation can lead to ARS, such as nausea and vomiting. Chronic exposure to the GCR radiation environment, although not fatal immediately, can increase the risk of late-term consequences, such as cancer, damage to the central nervous system, and many other side effects (Guo et al., 2021; Cucinotta and Durante, 2006; Kennedy, 2014; Iancu et al., 2018).

Fig. 8 illustrates the variations in radiation dose rate on the surface of Mars over the last ten years. Several large SEPs with sufficient energy penetrated the atmosphere of Mars, resulting in an increased dose rate up to a few times higher than the pre-event background. Apart from those abrupt enhancements, the overall dose calculated by the Mars Science Laboratory (MSL)/Radiation Assessment Detector (RAD) shows an increasing trend from the solar activity maximum to the solar activity minimum during the SC 24. This long-term trend is due to the solar modulation of the GCR intensity. Therefore, understanding the variations in radiation dose rates is crucial for the assessment of potential health risks and to properly schedule human activities in outer space.

¹ <https://www.nrc.gov/about-nrc/radiation/health-effects/high-rad-doses.html>

Fig. 9 illustrates the spectra of two famous SEP events that happened in April 1998 and September 1989. The colored regions indicate the proton energies that pose threats to human activities. Protons with energy above 150 MeV (red) are considered as hard radiation, which can penetrate $20\text{g}/\text{cm}^2$ of aluminum. Soft protons are categorized as particles with energies above 50 MeV (shown in yellow), which are capable of penetrating spacesuits and the skin of spacecraft (Reames, 2021).

In addition to the radiation we discussed earlier, secondary particles such as protons and neutrals generated from the interaction between energetic particles and lunar regolith are another significant contribution to the radiation dose. Secondary protons possess enough energy to penetrate space suits and cause radiation hazards (Xu et al., 2022). Secondary neutrals are even more detrimental than charged particles due to their high penetrating ability and high biological effectiveness despite their lower intensity. Spence et al. (2013) estimated the amount of radiation hazard caused by GCRs and secondary particles on the lunar surface by conducting simulations and found that secondary particles account for 8.6% of the overall radiation dose.

In the future, potential human missions may require longer stays of astronauts on the surface of solar system bodies or in space while traveling to their destination. As a result, the probability of exposure to intense radiation and the risk of exposure to chronic radiation are considerably increased. Properly estimating and understanding the radiation hazard in different situations and locations is crucial for preparing for future human missions.

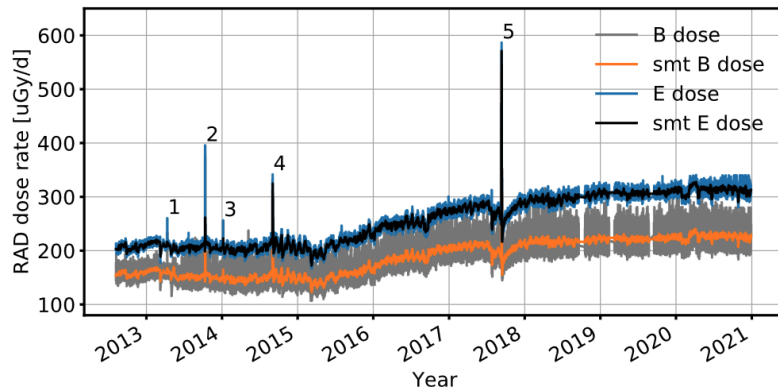


Figure 8: The radiation dose rates on the Martian surface, measured by RAD in the silicon detector B (grey) and plastic detector E (blue). The daily averaged dose rates of B (smt B dose, orange) and E (smt E dose, grey) overlay the original measurements. Apart from five prominent SEPs (1-5), the long-term trend of the dose rate is correlated with the GCR variation. (Figure reproduced from Guo et al. (2021))

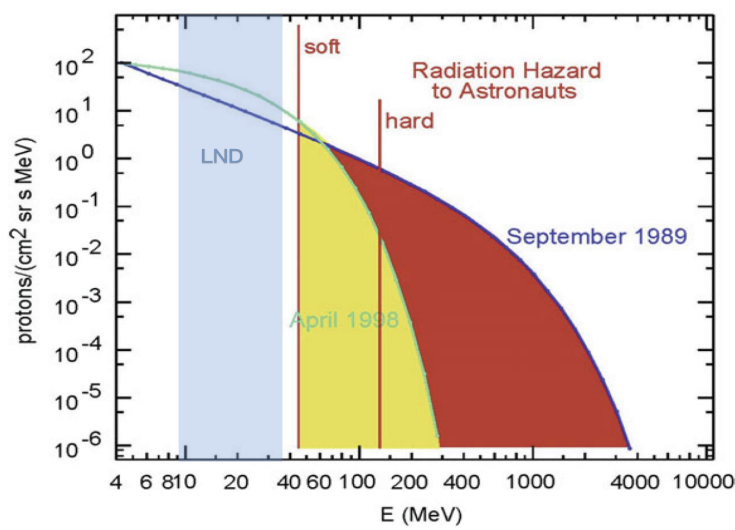


Figure 9: The proton spectra of two famous SEP events. The yellow and red colored regions indicate the energy region with protons harmful to instruments and the human body. Both "hard" and "soft" spectra threaten human activities. The blue-colored region indicates the energy coverage of LND stopping particles in the energy range of 8 - 35 MeV. (Figure reproduced and adapted from Reames (2021))

INSTRUMENTATION

This chapter describes the current status, the measurement principle, and the latest updates of the Lunar Lander Neutron and Dosimetry Experiment (LND) onboard the lander of Chang'E - 4 mission and the High Energy Telescope (HET) onboard Solar Orbiter (Solo).

3.1 CHANG'E-4 AND LUNAR LANDER NEUTRON AND DOSIMETRY (LND) EXPERIMENT

Overview and current status (2019 - 2022)

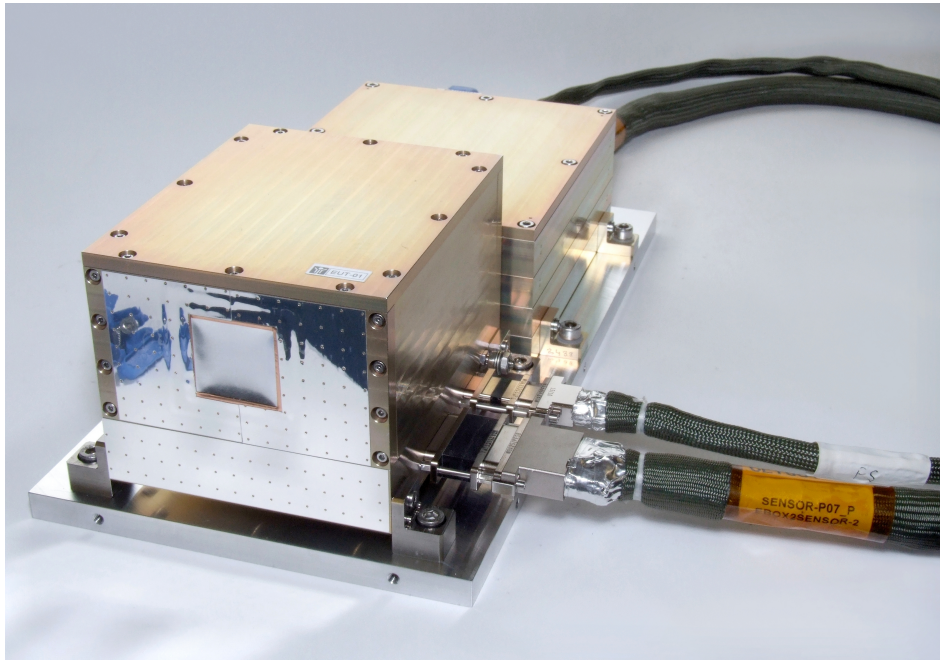


Figure 10: A photograph of the LND, including the sensor head (SH) in the front, electronic box (EB) in the rear, and 1-meters data and power harness that connects the SH and EB. The figure was adapted from Wimmer-Schweingruber et al. (2020) and shows the flight spare model of LND and was taken on 2018.11.23.

Chang'E-4 is a robotic spacecraft mission of China exploring the lunar far-side surface, which is also the first soft-landing mission on the lunar far-side surface (Li et al., 2021). The whole mission consists of a lander, a rover named Yutu-2, and a relay satellite named Queqiao, which works on a halo orbit around the Earth-Moon L2 Lagrangian point and enables communication between the lunar far-side surface and the ground. The mission was launched on December 8, 2018, and successfully landed on the Von Kàrmàn crater near the south pole of the Moon on

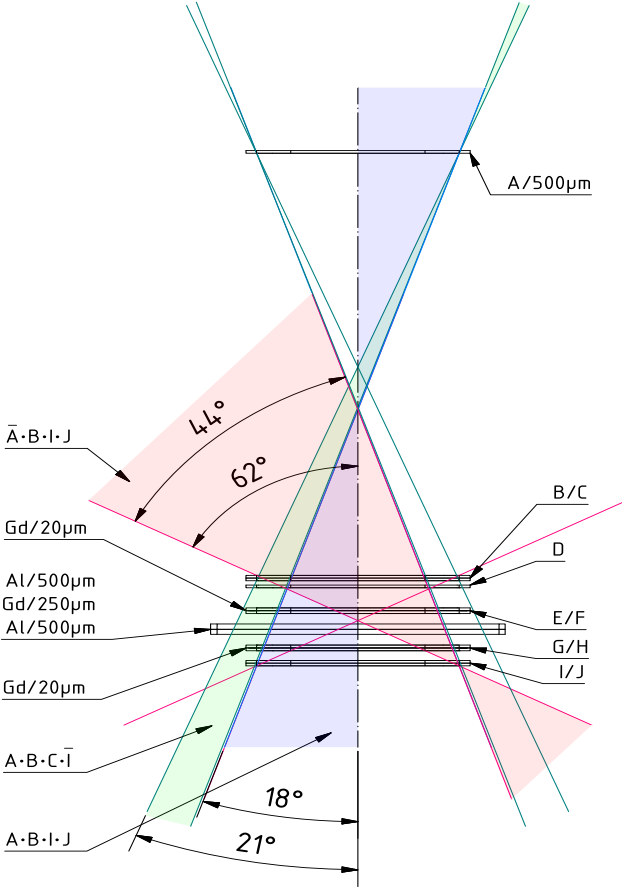


Figure 11: A sketch of the inner structure of the LND SH. Ten $500\text{ }\mu\text{m}$ Si solid state detectors (SSDs) are assembled in order. The different colored regions indicate the field of view (FOV) of different measurement combinations. The figure was reproduced from Wimmer-Schweingruber et al. (2020), and more details could be found in the instrument paper.

January 3, 2019 (Wu et al., 2019). In order to cope with the significant temperature variations on the lunar surface, the rover, lander, and scientific payloads onboard enter a hibernation state during the approximately two-week-long lunar night to avoid possible damage caused by the unexpected cold temperature (down to -190 degrees Celsius according to the result from Chang'E-4) on the lunar far-side surface. After the extended 'sleep' night, the probe and the instruments onboard wake up autonomously after they detect the sunlight and start regular operation during the lunar daytime. The initial design lifetime of the mission was set at a minimum of one year. Obviously, this target has been successfully surpassed, and the scientific instruments onboard are continuing to perform impressive measurements. According to the search results from NASA/ADS, more than 50 papers that are related to Chang'E-4 mission have been published, and the number is still increasing.

As an integral part of the Chang'E-4 mission's international scientific payload, Lunar Lander Neutron and Dosimetry Experiment is designed by the Kiel University in Germany. An image of the flight spare model of LND is displayed in Fig. 10. The initial design purpose of LND is to provide the first active dosimetric mea-

surements on the lunar surface and monitor the radiation environment caused by charged and neutral (neutrons and γ -ray) particles in preparation of future human exploration of the Moon and the solar system. Therefore, the main scientific objects of the LND, as indicated in the instrument paper (Wimmer-Schweingruber et al., 2020), are "Dosimetry for human exploration of the Moon" which is based on temporal variations of the dose rate and the linear energy transfer (LET) spectra, and "Contribution to the heliospheric science" which based on the measurement of charged particles. The dose rate is the amount of radiation energy deposited in the detector per hour and per mass. LET is the energy that an ionizing particle transfers to the material per unit path length. Besides, LND also has two technological demonstration objects, which are "Determine the subsurface water content in the South-Pole Aitken Basin" and "Determine the FeO content in the South-Pole Aitken Basin" (Wimmer-Schweingruber et al., 2020).

As of May 2023, LND has been successfully working on the lunar far-side surface for more than four years, which corresponds to approximately 50 Lunar days since January 3, 2019. It has largely surpassed its designed lifetime. One of the simplest ways to check whether LND is working or not is to look up during the night and check the Moon's phase. If you can see a new moon or the Moon is in the last/first quarter phase, it indicates that the Moon is moving out of the Earth's shadow and that the far-side surface of the Moon is facing the Sun, enabling LND to work.

Based on the operations and experiment schedule established from the ground, LND has been entirely or partly (more than half a lunar day) switched off on the 6th, 44th, and 45th lunar days since the start of the mission. As of the finalization of this thesis in May 2023, we have received 46 lunar days' data from January 2019 to the end of November 2022, which are stored on the servers of Kiel University. The data have officially been published in the Lunar and Planetary Data release system¹, where currently the data is available until the end of December 2022. The alternative downloading options include National Aeronautics and Space Administration (NASA)'s Space Science Data Coordinated Archive and European Space Agency (ESA)'s archive ESDC (ESAC Science Data Center), which are still being assessed. The instrument will continue its operation on the lunar far side, and we anticipate receiving more intriguing data in the future with increasing solar activities.

LND as Charged particle telescope

LND has a specially designed sensor head that enables it to be used as a dosimeter, neutral particles telescope, and charged particle telescope. Here, we put our focus on the charged particle telescope in this section, and a brief introduction to the other two components is given in the next section. For a comprehensive overview of LND's capability, see Wimmer-Schweingruber et al. (2020).

The flight spare model of LND, which is an exact replica of the flight model currently deployed on the Moon, is displayed in Fig.10. The instrument is composed of two separate parts, the sensor head in the front and the electronic

¹ moon.bao.ac.cn

box at the rear. SH and EB are connected by two 1-meter cables, which serve to provide power and transfer data. The SH is comprised of ten segmented Si SSD of nominal $500 \mu\text{m}$ thickness. They are labeled from A to J and assembled in a charged-particle telescope configuration as illustrated in Fig. 11.

The structure of the telescope can be further divided into two parts. The upper half consists of four detectors (A, B, C, D), with A placed 80.5 mm away from B. Detector A is crucial for the function of LND as a charged particle telescope since only particles that trigger detector A will be counted. B/C/D are assembled as close in space as possible, with zero space between B and C and 0.5 mm between C and D, enabling the anti-coincidence measurements in the inner C segment. Such a detector arrangement is similar to the Flight Radiation Environment Detector (FRED) (Möller et al., 2013a,b). The lower half consists of three detector pairs (E/F, G/H, I/J) and an Al-Gd-Al absorber. The detector pairs are closely packed together, and the absorber is designed for the detection of thermal neutrons. 20 μm thick Gd foils are inserted between E/F and G/H, creating sandwich-like structures to detect thermal neutrons. This charged particle telescope is completed by the last detector pair I/J.

By measuring the energy deposition in different SSDs and using the $dE/dX - E$ or $dE/dX - dE/dX$ methods, which depend on the primary energy of particles, LND can easily identify the energies and species of particles. The averaged energy loss of the charged particle along the travel path depends on the nuclear charge Z_1 (equal to atomic number) and the incident velocity v . Such a relationship can be expressed by the well-known Bethe-Bloch formula (Bethe, 1930; Bloch, 1933):

$$\frac{dE}{dx} = -\frac{Z_1^2 e^4 n_e}{4\pi \cdot \epsilon_0^2 \beta^2 c^2 m_e} \cdot \left[\ln \left(\frac{2m_e \beta^2 c^2}{E_B} \right) - \ln(1 - \beta^2) - \beta^2 \right], \quad (3)$$

Where c is the speed of light, $\beta = v/c$, E_B is the ionization energy of the medium that particles pass, n_e is the electron density in the medium, m_e is the electron mass, and constant ϵ_0 is the permittivity of free space. E is the kinetic energy of the particle, and x is the travel length of the particle in the medium.

The expression in the square brackets simplifies to $\ln(\beta^2)$ plus an extra constant. Because $\ln(\beta^2)$ is nearly constant and slowly changes in the energy range covered by LND, the above equation could be further simplified to:

$$E_A \propto \frac{Z_1^2 m_1}{E_{tot}}, \quad (4)$$

where E_A is the energy loss in the detector A, E_{tot} is in principle the primary kinetic energy of particles. The product of E_A and E_{tot} is proportional to the square of nuclear charge, Z_1^2 , and the mass of elements, m_1 . The nuclear charge of particles equals the atomic number. Both Z_1^2 and m_1 depend on the particle species. Hence, by checking the values of the product of E_A and E_{tot} , we can distinguish the species of particles that LND measured. It is worth noting that LND has the capability to discriminate between the isotopes of elements, such as helium-3 and helium-4, despite the limited resolution and larger uncertainty. See appendix of chapter 5 for more details.

Once the charged particle enters the sensor head of LND, they can be further categorized into two groups: stopping particles and penetrating particles. Stopping

particles have a primary energy range between ~ 8 MeV/nuc and ~ 35 MeV/nuc, stopping within any of the detectors B-I. Penetrating particles possess energy above this range and have the capability to penetrate through all the detectors. In Fig. 12, a plot generated by the large counting statistic Geometry and Tracking 4 (Geant4) (Agostinelli et al., 2003) simulation illustrates how the stopping particles are separated by using $E_{tot} * E_A$ as the y-axis and E_{tot} / E_A as the x-axis. Note that due to the thick absorbers in the middle of the detector stack, the total energies of particles that stop in detectors F to I are unknown. Therefore, we use the summation of energy deposition in detectors A to D as the E_{tot} above (See table 5 of Wimmer-Schweingruber et al. (2020)). The data points are simulated in Geant4 based on a carefully constructed LND instrument model. This model takes into account all the inner structures within the sensor head, including the printed circuit board (PCB) next to the detector stacks and the outer shell of the sensor head. However, we must note that a completed model including the surrounding material of LND is unavailable since we lack the structure information of the Chang'E-4 lander. A screenshot of the LND model is provided in the appendix A, presenting the detailed structure of the LND sensor head.

Penetrating particles have a primary energy above approximately 35 MeV/nuc, and as the name suggests, can penetrate through detectors A to I and stop in J or continue to penetrate J with more energy. The majority of the penetrating particles are fully penetrating particles, which means we can not directly measure their total energy. Since the total energy of particles is unavailable, it is not possible to create a plot similar to Fig. 12. Instead, we change the formula of the x-axis and y-axis to E_I / E_A and dE , respectively. The E_I is the energy deposit in the last detector I. The dE is the energy deposition summed from the B, C, and D.

It is worth noting that the incident direction of particles i.e. whether they come from above or beneath the detector, can be inferred from the penetrating data for a small fraction of the penetrating particles which have enough energy to penetrate all detectors but are not minimally ionizing particles (MIPs). From the Bethe-Bloch formula, we figure out that the energy loss of those particles decreases with the increase of the incident energy. Therefore, the particle that incidents from above deposits less energy in the front detector A than the bottom detector I, and the ratio E_I / E_A tends to be larger than 1. While the particle entering from beneath deposits more energy in detector A than detector I, the ratio of E_I to E_A tends to be less than 1. By analyzing the distributions and patterns in the histogram, we can identify the albedo protons from the 2-D histogram of penetrating particles, corresponding to columns 248 - 264 of Fig. 13. A detailed understanding of the derivations and analysis of albedo protons is given in the chapter. 5

LND as dosimeter and neutral telescope

LND measures the Total Ionizing Dose (TID) in the inner B segment utilizing the energy deposition and corresponding energy spectrum. The inner segment of C, which is surrounded by the B, D, and C outer segments and in anti-coincidence with all other detector segments, is used to measure the neutral dose rate caused by both fast neutrons and γ -rays. The above two measurements are the primary

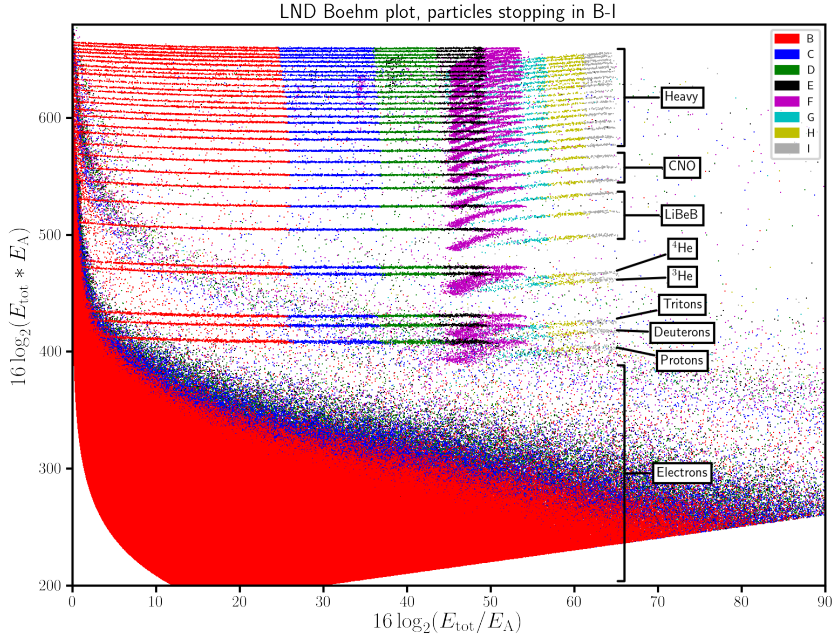


Figure 12: The different particle species are well discriminated in this LND Boehm plot, which is a scatter plot of the LND simulation data generated by the Geant4 tools (Agostinelli et al., 2003). During the simulation, an isotropic source is positioned above detector A.

data products of LND. TID and dose in C play important roles in assessing the radiation environment on the lunar surface.

LND employs the E/F, G/H pairs which clamp a Gd-foil, to measure the thermal neutron flux. The Gd-foil has a large cross-section for thermal neutrons, resulting in a high probability of interaction with neutrons (Wimmer-Schweingruber et al., 2020). After the capture of thermal neutrons in the Gd-foil, X-rays with energies of 43 keV and electrons with energies of 71 keV, 131 keV, and 173 keV are emitted and then detected by detectors closed to the foil. In the calibration experiment, LND successfully measured neutrons by calculating the energy spectrum discrepancy between E (G) and F (H) for neutrons coming from the front (back). However, in actual measurements, the quality of the thermal neutron data is unexpectedly low due to various factors. The most prominent factors are the neutron background emitted from the Radioisotope Thermoelectric Generator (RTG) and the Radioisotope Heater Unit (RHU). These radioactive sources generate heat to protect the lander and payload from the frozen night. But they also contribute significantly to the neutron background (Zhang et al., 2020). Unfortunately, the direct measurement of the radiation sources had never been done, and only an experimental and empirical estimation of the contamination from the background on the data was conducted by Hou et al. (2020). Based on data from laboratory experiments and Monte Carlo simulations, Hou et al. (2020) confirmed the non-negligible background interference and estimated the dose rate background.

Another factor that affects the neutron measurements is the unanticipated noise increase in neutral channels F₂ and H₂. In those two channels, the single detector counter rates increased from about a few thousand count/min to 10^6 count/min,

and the energy spectra of noise channels indicate that the dominant energy of noise is below 300 keV. The high energy noise obscures the x-ray line at 43 keV and electron lines at 71 keV, 131 keV, and 173 keV, which are used to determine the thermal neutrons flux and make it more challenging to derive the accurate thermal neutron flux of lower intensity. Furthermore, the larger count rates in those thermal neutron channels increase the dead time of counters. The dead time is the time during which the system is not able to record another event after one valid event (Leo, 1994). The increasing dead time of counters leads to the loss of valid events that can be registered by the detector. In LND, thermal neutrons measurement and the neutron dose in C share the same counter buffer. Therefore, the dead time caused by H₂ and F₂ counters also impacts neutron dose in C, which is one of the primary data products of LND.

The unexpected noise signals of H₂ appeared since the third lunar day after the malfunction of the front lid (see Sec. 3.1 and further discussion in chapter 5). The increased noise level of the F₂ channel first appeared on the 17th lunar day. It was soon back to normal after a few hours. But, in the last few lunar days, the situation has worsened, and the noisy period of F₂ can account for up to half of one lunar day. The impact of F₂ noise on the neutral dose in C is becoming significant. In order to mitigate the dead time issue, we need to raise the corresponding threshold of noise detectors to avoid this extra dead time issue. The energy threshold of the H₂ channel has been raised to 300 keV since the 9th lunar day (Xu et al., 2022). But we haven't fixed the F₂ channel yet.

The remaining data products related to dosimetric quantities that LND provides are the LET spectra. There are three types of LET spectra in LND's normal data products - \bar{ABC}_I , \bar{ABIJ} and $ABIJ$. Those LET spectra can be used to derive the quality factor (Q), which is a dimensionless modifier used in converting absorbed dose to dose equivalent, which is used to account for the biological effectiveness of different kinds of radiation (Kerr, 1988).

The first scientific results of LND regarding the radiation environment on the lunar surface are reported by Zhang et al. (2020). These initial findings present the TID, neutron dose, and LET spectra of the first two lunar days. This represents the first-ever dynamic measurements of the radiation variation on the lunar surface. The average total absorbed dose rate in silicon is about $13.59 \pm 1.01 \mu\text{Gy}/\text{hour}$. Amongst this total dose rate, the contribution from neutral particles is estimated to be $3.10 \pm 0.43 \mu\text{Gy}/\text{hour}$. These values are consistent with the measurements from the Cosmic Ray Telescope for the Effects of Radiation (CRaTER) on Lunar Reconnaissance Orbiter (LRO).

Primary data products: Xmas plots

Fig. 13 is the so-called "Xmas plot" ² of the LND. The Xmas plot is an image of LND's memory space shaped in a 274×64 matrix, where each pixel in the Xmas plot serves as a counter. The counters are incremented based on the deposited energy of particles in different detectors. Rules to determine which counter should

² It was used as the front cover of the Xmas card of IEAP group in 2017. Hence, we named it Xmas plot

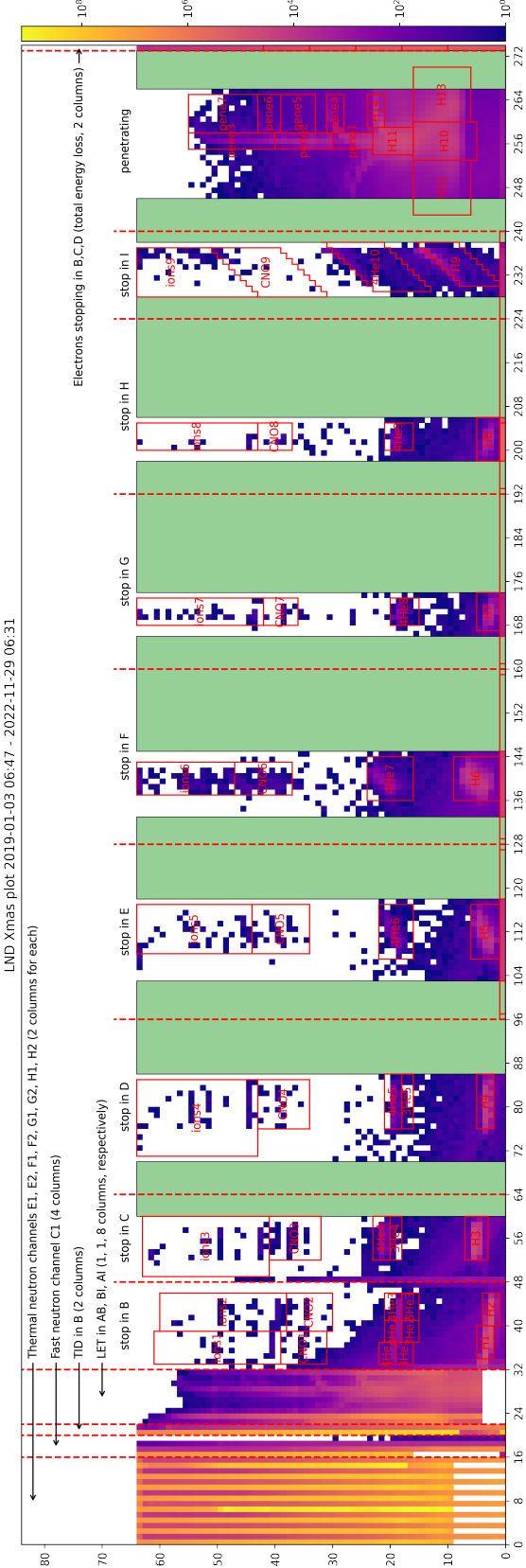


Figure 13: The completed Xmas plot (274×64) of LND based on the measurements between 2019.1.3 and 2022.11.29. All the data products could be found in this matrix, including neutrals, LET spectra, TID, stopping and penetrating charged particles, including electrons, protons, helium nuclei, and heavy ions. The corresponding simulation version can be found in Wimmer-Scheingruber et al. (2020).

be incremented are given in Wimmer-Schweingruber et al. (2020), and data products of LND are then extracted from this matrix. LND provides multiple data products, including charged and neutral particle dose rates measured in silicon detectors, LET spectra and neutral spectra, count rates of thermal neutrons, ion and electron flux variation, and their energy spectra.

Unlike the simulated plot in Wimmer-Schweingruber et al. (2020), here we showcase a Xmas plot from the actual measurements between 2019.1.3 to 2022.11.29, encompassing all the data accumulated since the first lunar day observed by LND. The green rows are the memory spaces that are not transmitted to the ground in order to save telemetry bandwidth. For a more detailed explanation of the format of the Xmas plot, see Wimmer-Schweingruber et al. (2020).

Configuration changes of LND

It is important to highlight that several configuration changes have been made after LND was delivered and launched. Those configuration changes are reflected in 14 extra commands, which are uploaded to the control unit of LND every morning of the lunar day, fixing software issues and malfunction issues. One of the software issues arises from errors in the software pipeline where the control unit uses the wrong channels to determine particle energies. Another one is due to the mistakes we made in simulations when designing data products, causing the location of the data product scheduler (dps) boxes to shift in the X-mas plot, which is a matrix storing LND data products (See below and Wimmer-Schweingruber et al. (2020) for more details about the X-mas plot). Nevertheless, the impact of the second problem on the data products is minor.

The significant changes in the data products are mainly caused by raising the thresholds of channels, which have turned noisy due to unforeseen thermal stresses, as well as the fact that we had to disable the A2 channel. A2 represents the outer segment of the front detector A (see Appendix in chapter 5 for more details of the changes). These changes are motivated by high observed noise levels in detectors A, H, I, and J, which appeared coincidentally with the malfunction of the front lid. The front lid of LND is a part of the lander and is designed to protect the fragile detectors inside the SH. The lid should be opened up to allow unobstructed measurements of the particles during lunar days and should be closed immediately after the instrument is switched off, protecting the detectors from the extreme temperature decrease on the lunar surface and the lunar night.

However, on the 3rd and 4th lunar days, the lid was opened, and LND was only switched on several hours afterward. This led to the detectors getting much colder than anticipated, causing irreversible deformation of carriers and the attached detectors, particularly the detectors A and I/J on the front side and the bottom side. Such deformation increased the thermal stresses, which have not been overcome after the malfunction. As a result, before the malfunction, the energies of most noise signals are below 20 keV. But afterward, the noise level increased significantly to hundreds of keV.

By implementing the changes mentioned above, we have successfully reduced the influence of these additional noise and mitigated their impact on the primary

data products such as LET spectra. However, it is worth noting that these changes still resulted in significant consequences for several other data products. For instance, we partly lose the measurement of MIPs, whose mean energy loss in the detectors is close to the minimum, after the increment of the threshold of the I detector; the geometry factors of two LET spectra and penetrating particle are reduced dramatically after disabling the A₂ channel, which plays a key role in LND's measurement. For a better understanding of the configuration changes and their impact on the data products, see the appendix of chapter 5.

3.2 SOLAR ORBITER AND HIGH ENERGY TELESCOPE

Successfully launched on February 10, 2020, the SolO mission (Müller et al., 2020) is an international mission in cooperation between ESA and NASA with the aim to understand the Sun and how it controls the heliosphere. As indicated in the mission paper, the following scientific questions will be answered and further studied: (a). What drives the solar wind, and where does the coronal magnetic field originate from? (b). How do solar transients drive heliospheric variability? (c). How do solar eruptions produce the energetic particle radiation that fills the heliosphere? (d). How does the solar dynamo work and drive connections between the Sun and the heliosphere?

SolO has an elliptic heliocentric orbit with the closest perihelion of 0.29 AU (about 42×10^6 km). Using several gravity assist maneuvers (Venus flybys and the Earth flybys), the orbit of SolO will gradually tilt away from the ecliptic plane and, at the end of the nominal mission, will be 24 degrees above the Sun's equator. As of May 2023, SolO is following an elliptical orbit circling the Sun, with a maximum solar latitude of 8.66 degrees. SolO has finished five perihelia with the closest distance of 0.292 AU on September 3, 2022, and has started its 6th orbit, moving away from the Sun. Benefiting from the unique position of SolO during this trip, the multiple scientific instruments onboard the SolO can further advance our understanding of the Sun and its effects on the heliosphere. The evolution of the distance of SolO to the Sun and solar latitude of SolO from 2020 to 2023 are given in Fig. 14.

The Energetic Particle Detector (EPD) (Rodríguez-Pacheco et al., 2020) is part of the scientific payload onboard SolO, measuring energetic particles over a large scale from few keV to GeV. The spectra, composition, time variations and directional distributions can be obtained and derived. EPD is comprises of four different sensors, the Suprathermal Ion Spectrograph (SIS), the Suprathermal Electrons and Protons (STEP), the Electron Proton Telescope (EPT) and the High Energy Telescope. SIS is a time-of-flight mass spectrometer that measures ion composition from ~ 0.1 - few MeV nucleon⁻¹. STEP measures electrons and ions with lower energies between 4 keV and 80 keV. The special design of STEP allows it to have high pitch-angle resolution. EPT and HET share the same electronics, and they are composed of two identical sensor units that are mounted perpendicularly on SolO. This configuration enables the detection of the particle incident from four different directions. EPT is designed to measure medium-energy electrons (ions)within an energy range of 25 keV - 400 keV (25keV - ~ 6000 keV), while HET

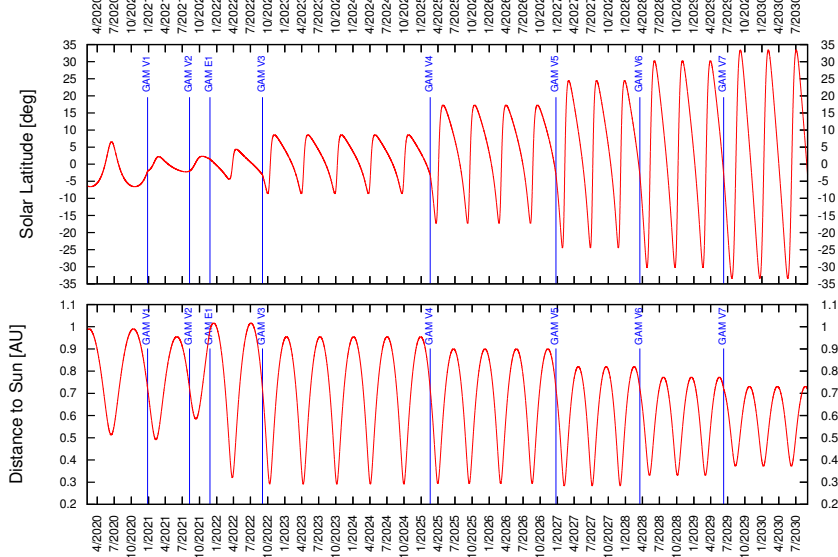


Figure 14: The orbit of SolO from 2020 to 2023. The figure is reproduced from Müller et al. (2020).

completes the higher energy end, measuring electrons from 300 keV to 30 MeV and ions from 6.8 MeV/nuc to \sim 100 MeV/nuc in the nominal data products. Notably, the penetrating data products of HET extend the energy coverage of HET up to \sim 2 GeV/nuc (Elftmann, 2020). The full energy range of those four instruments for different particle species is given in Fig. 15. In this section, we provide a brief introduction of HET, which is the focus of the study in chapter 7. More detailed information on the other components can be found in the instrument paper (Rodríguez-Pacheco et al., 2020) and the first years' overview paper of EPD (Wimmer-Schweingruber et al., 2021).

High Energy Telescope (HET)

A cut view of the HET sensor head is depicted in Fig. 16. HET is a double-ended telescope. The sensor head of HET consists of four $300\text{ }\mu\text{m}$ silicon SSD stacks, with two on each side (A₁, B₁ on the front side and A₂, B₂ on the back side) and a 2-cm thick bismuth germanium oxide (BGO) ($\text{Bi}_4\text{Ge}_3\text{O}_{12}$) scintillator which is named as detector C in the center. The sensor head setup is similar to the configuration of the Radiation Assessment Detector (RAD) (Hassler et al., 2012), another instrument developed by Kiel University, which is currently operating on the Martian surface.

HET uses the $dE/dX - E$ technique to discriminate different particle species of different energy. This method is the same as the measurement principle of LND that has been well explained before. The particle species that HET can discriminate include electrons, protons, helium nuclei, and all heavy ions such as carbon, nitrogen, oxygen, and iron.

Once the charged particles hit and penetrate the A detector (A₁ or A₂), they can be split into stopping particles and penetrating particles, depending on their

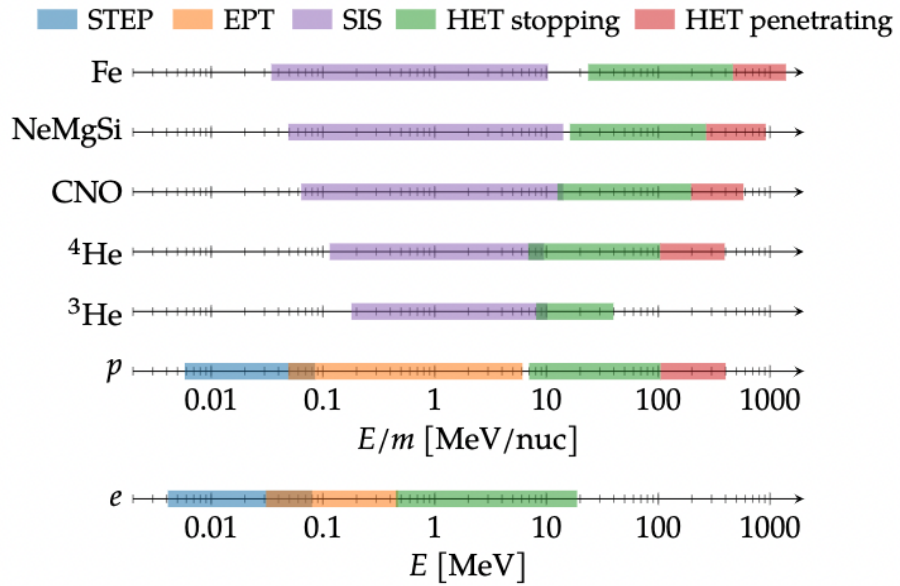


Figure 15: The energy coverage of different EPD sensors for different particle species. This figure is an updated energy coverage plot made by Forstner (2020), based on a similar plot from Rodríguez-Pacheco et al. (2020). The HET measurements are split into stopping and penetrating parts, and the latter one considerably extends HET's capability (Elftmann, 2020).

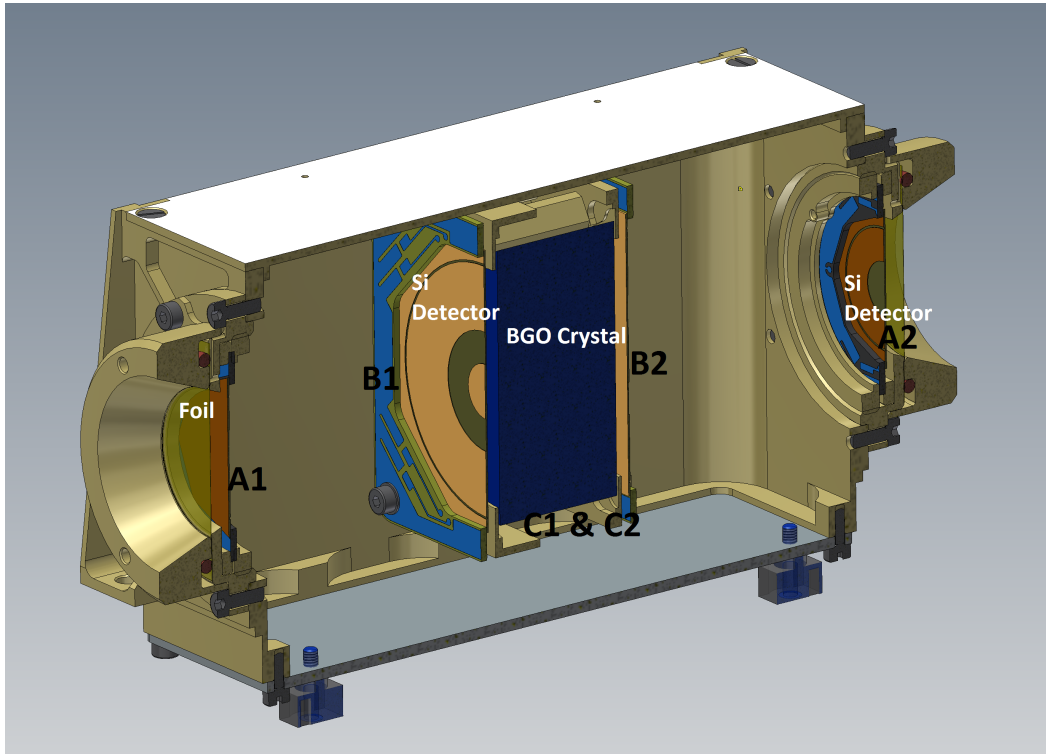


Figure 16: Cut view of HET sensor head. The corresponding detector names are labeled. This figure is reproduced from Rodríguez-Pacheco et al. (2020).

energy and whether they stop in detector B/C. As given in Table 22 of Rodríguez-Pacheco et al. (2020), the corresponding nominal data products are ABnC, which corresponds to ions stopping in B with the energy of 6.5 - 9.5 MeV/nuc, ABC, which register ions stopping in C with an energy range of \sim 10 - \sim 100 MeV/nuc, and penetrating detector C with energy above 100 MeV/nuc up to \sim 2 GeV.

In addition to the nominal charged particle data products, we must emphasize the significant contribution of housekeeping data in our studies. Housekeeping data include temperature, voltage, current, and single/multiple detector count rate. They have the highest priority for downlinking to the Earth and are used to monitor the instrument status and health. Here, what we emphasize is mainly the single detector count rate. Although the single detector count rates are not designed for scientific purposes, they still provide valuable insight into the instrument performance, and their contributions to the scientific studies is impressive (Wimmer-Schweingruber et al., 2021), especially the counter rate from the BGO scintillator crystal (C detector).

This counter does not require any coincidence condition and responds to particles from all directions and types. The sole requirement is that the deposited energy exceeds the threshold of the C detector. Due to its large geometry factor, this counter exhibits excellent counting statistics and can be used to detect minor disturbances in the galactic cosmic ray (GCR) background. For example, Forstner et al. (2021) use this counter to study a Forbush decrease (FD) with an amplitude of 3% when a coronal mass ejection (CME) passed SolO on April 19, 2020. In addition, Allen et al. (2021a) found an \sim 5% drop in the count rates during the first Venus flyby. This drop is due to the blockage by the planetary body on FOV of HET.

For more details on the inner structure and parameters of the HET, as well as the most updated status of HET, one could refer to Elftmann (2020), Rodríguez-Pacheco et al. (2020), and Wimmer-Schweingruber et al. (2021).

FIRST SOLAR ENERGETIC PARTICLES MEASURED ON THE LUNAR FAR-SIDE

The Chang'E-4 mission, launched on 7 December 2018, coincided with a period of solar activity minimum characterized by a scarcity of solar energetic particle (SEP) events. However, as the Sun entered the new Solar Cycle in 2022, the solar activities soon began to increase. Consequently, a growing number of SEP events, including prolonged-duration and high-intensity ones, were observed to reach the lunar surface and were detected by the Lunar Lander Neutron and Dosimetry Experiment (LND) on the lunar far-side surface. For example, Guo et al. (2023) recently reported the first ground level enhancement (GLE) of Solar Cycle (SC) 25, which was concurrently detected by instruments deployed on the Moon, Earth, Mars and also by Solar Orbiter (SolO) as well as Parker Solar Probe (PSP) (Papaioannou et al., 2022; Martucci et al., 2023; Chertok, 2022). It is noteworthy that LND was switched on after the initial phase of the event and hence did not cover the whole event. Even so, it still advances our understanding of potential radiation risks that are caused by these extreme SEP events on the surface of solar system bodies. In the appendix section of this thesis, a comprehensive list of SEP events detected by LND on the lunar far-side surface between 2019 and 2023 is provided, further emphasizing LND's contribution to the study of SEP.

The SEP event on May 6, 2019, is the first SEP event that has ever been detected on the lunar surface. This SEP event ch is located in the eastern hemisphere and is associated with an M-class flare originating from a solar active region (AR12470) more than 110 degrees away from the Earth's magnetic footpoint on the solar surface. The remote-sensing observations conducted by the Solar and Heliospheric Observatory (SOHO)/Large Angle and Spectrometric Coronagraph Experiment (LASCO) and the Solar Terrestrial Relations Observatory (STEREO) revealed the presence of a slow, narrow, and westward-moving coronal mass ejection (CME). Though the SEPs from this event cause negligible radiation dose due to its weak intensity and lower peak energy, it is still an exciting event that is worth studying for the following reasons. The primary objective of this study is to utilize the first SEP event observed by LND to validate the data products produced during SEP occurrences and assess the instrument's performance under such conditions. By cross-calibrating the proton measurements between LND and other already existed particle instruments at the first Lagrange point (L_1), such as the Electron Proton Helium Instrument (EPHIN) onboard SOHO and the Electron, Proton, and Alpha Monitor (EPAM) onboard Advanced Composition Explorer (ACE), we conclude that LND provides reliable solar energetic proton measurement with a good time resolution of one minute. In addition, we investigate the extensive spatial distributions of this SEP by using both in-situ and remote-sensing measurements. Unlike the typical widespread SEP events, which persist for a few days and are accompanied by broad CME, the temporal profile

of this event and remote-sensing observation imply that it is an impulsive event that has good magnetic connections. Several mechanisms could be involved in the process of the particle traversal across considerable distance in the so-called wide spread SEP.

Short Overview of the publication

First, we check and analyze the in-situ data from May 3, 2019 to May 8, 2019 in detail from different viewpoints and different detectors. Proton and electron flux, solar wind parameters, and local magnetic field measured at L1 are given. Though STEREO-A had a better magnetic connection, the background on STEREO-A is dominated by particles from a pre-existing SEP and is therefore not included here in the analysis. Then, we determine the onset time based on the combined data from LND, EPHIN, EPAM, and 3DP. A Poisson-CUSUM method (Huttunen-Heikinmaa et al., 2005; Palmroos et al., 2022), which refers to a cumulative sum method for variables that follow Poisson distribution, is applied to tackle the lower statistic measurements. By fitting the velocity dispersion, we derived the release time of protons and electrons. Besides, the proton integral spectra of the SEP event are also derived. At the end of the observation section, we analyze the remote-sensing observation, including X-ray flux, radio observation CME, and EUV waves observations. This work attempts to answer two questions that we brought up in Sec. 1.2: "What is the source of those tens of MeV particles?" and "How do those tens of MeV particles arrive at distant longitudes?"

The key observations of the publication are:

- LND has consistent measurements with other L1 instruments during the first SEP events, including the consistent onset time and spectra.
- Protons and electrons show clearly velocity dispersion and are beam-like structures. The release time of electrons is an hour earlier than that of protons.
- The magnetic footprint of Earth is about 113° away from the flare location. The accompanied CME is slow and narrow. We found no evidence of the arrival of an EUV wave at the magnetic footprint of Earth.
- The more than 100-degree longitudinal separation is hard to explain in an impulsive SEP event. Possible reasons include the expanding coronal shock, irregular magnetic field, magnetic field line random walk, or a mixture of the above three. Besides, the release mechanism of electrons and protons might be different due to their distinct behaviors.

The following article is reproduced from Xu et al. (2020) by permission of the AAS:

FIRST SOLAR ENERGETIC PARTICLES MEASURED ON THE LUNAR FAR-SIDE

Xu, Z., J. Guo, R. F. Wimmer-Schweingruber, J. L. Freiherr von Forstner, Y. Wang, N. Dresing, H. Lohf, S. Zhang, B. Heber, and M. Yang, *The Astrophysical Journal*



First Solar Energetic Particles Measured on the Lunar Far-side

Zigong Xu¹, Jingnan Guo^{2,3,1}, Robert F. Wimmer-Schweingruber^{1,4}, Johan L. Freiherr von Forstner¹, Yuming Wang^{2,3}, Nina Dresing¹, Henning Lohf¹, Shenyi Zhang^{4,5,6}, Bernd Heber¹, and Mei Yang⁷

¹ Institute of Experimental and Applied Physics, Kiel University, D-24118 Kiel, Germany; xu@physik.uni-kiel.de,

² CAS Key Laboratory of Geospace Environment, University of Science and Technology of China, Hefei 230026, People's Republic of China; jnguo@ustc.edu.cn

³ CAS Center for Excellence in Comparative Planetology, Hefei 230026, People's Republic of China

⁴ National Space Science Center, Chinese Academy of Sciences, Beijing, People's Republic of China

⁵ Beijing Key Laboratory of Space Environment Exploration, Beijing, People's Republic of China

⁶ University of Chinese Academy of Science, Beijing, People's Republic of China

⁷ Beijing Institute of Spacecraft System Engineering, Beijing, People's Republic of China

Received 2020 August 8; revised 2020 September 26; accepted 2020 September 29; published 2020 October 16

Abstract

On 2019 May 6 the Lunar Lander Neutron & Dosimetry (LND) Experiment on board the Chang'E-4 lander on the far-side of the Moon detected its first solar energetic particle (SEP) event with proton energies up to 21 MeV. Combined proton energy spectra are studied based on the LND, SOHO/EPHIN, and ACE/EPAM measurements, which show that LND could provide a complementary data set from a special location on the Moon, contributing to our existing observations and understanding of space environment. We applied velocity dispersion analysis to the impulsive electron event and weak proton enhancement and show that electrons are released only 22 minutes after the flare onset and \sim 15 minutes after the type II radio burst, while protons are released more than one hour after the electron release. The beam-like in situ electrons and clear velocity dispersion indicate a good magnetic connection between the source and Earth. This is remarkable because stereoscopic remote-sensing observations from Earth and STEREO-A suggest that the SEPs are associated with an active region nearly 113° away from the magnetic footpoint of Earth. This suggests that these SEPs did not propagate along the nominal Parker spiral normally assumed for ballistic mapping and that the release and propagation mechanism of electrons and protons are likely to differ significantly for this event.

Unified Astronomy Thesaurus concepts: Solar energetic particles (1491); Interplanetary physics (827); Lunar surface (974); Solar active regions (1974); Solar coronal mass ejection shocks (1997); Solar physics (1476); Space weather (2037); Solar active region magnetic fields (1975); Solar instruments (1499)

1. Introduction

The Chang'E-4 mission, which consists of a lander, a rover, and a relay satellite, is the first mission to land on the far side of the Moon. It landed in the von Kármán Crater on 2019 January 3, 02:26 UTC. The Lunar Lander Neutron and Dosimetry experiment (LND) (Wimmer-Schweingruber et al. 2020) on board the lander of Chang'E-4 is designed to take active dosimetry measurements on the surface of the Moon as its chief scientific goal. Apart from the primary objective of LND, which is to measure the radiation level on the lunar far-side preparing for astronaut missions (Zhang et al. 2020), the charged particle telescope also provides high-quality data of energetic particles and contributes to heliophysics. For example, LND provides proton and Helium-4 spectra between 9 and 35 MeV nuc $^{-1}$.

During the first year of the mission (2019), solar activity was minimal and LND detected only two small solar energetic particle (SEP) events on 2019 May 4 and 6, of which the second had sufficient counting statistics for protons between 9.0 and 21.0 MeV to allow a meaningful analysis. This event was related to an active region located at E50, nearly 113° away from the Earth's nominal coronal magnetic footpoint, where an M1.0 class flare erupted before the SEPs onset and a narrow and slow coronal mass ejection (CME) appeared later. Combining remote-sensing observations of the solar source with in situ particle measurements

from multiple spacecraft, we analyze and discuss the possible particle release and transport processes.

2. Observations

2.1. In Situ Measurements

Chang'E 4 landed on the far side of the Moon and can only operate during its local daytime because it is too cold at night. Therefore, LND only provides measurements ahead of the Earth's bow shock. It measures the energy that a particle deposits in its 10 detectors. LND can stop and thus identify the species and energy of charged particles up to 30 MeV nuc $^{-1}$. In order to better understand the temporal variation of protons and electrons at other energies during the event, we also include observations from the Electron Proton Helium Instrument (EPHIN, Müller-Mellin et al. 1995) on board the Solar and Heliospheric Observatory (SOHO), the Electron Proton Alpha Monitor (EPAM, Gold et al. 1998) on board the Advanced Composition Explorer (ACE), and the 3D Plasma and Energetic Particle Investigation (3DP, Lin et al. 1995) on board Wind. Those data are presented in the top panel of Figure 1 and are discussed from top to bottom in the following paragraph.

After the flare eruption at 04:56 on May 6 (Table 1, more details in Section 2.4), which is marked as a red vertical dashed line in Figure 1, LND detected the arrival of SEPs as shown in panel (a) of Figure 1. The proton channel 9.0–21.0 MeV shown here is the combination of the first five channels of LND's 1 minute proton data, which are provided in the Appendix. Due to the low intensity of the event and poor counting statistics in

Original content from this work may be used under the terms of the [Creative Commons Attribution 3.0 licence](#). Any further distribution of this work must maintain attribution to the author(s) and the title of the work, journal citation and DOI.

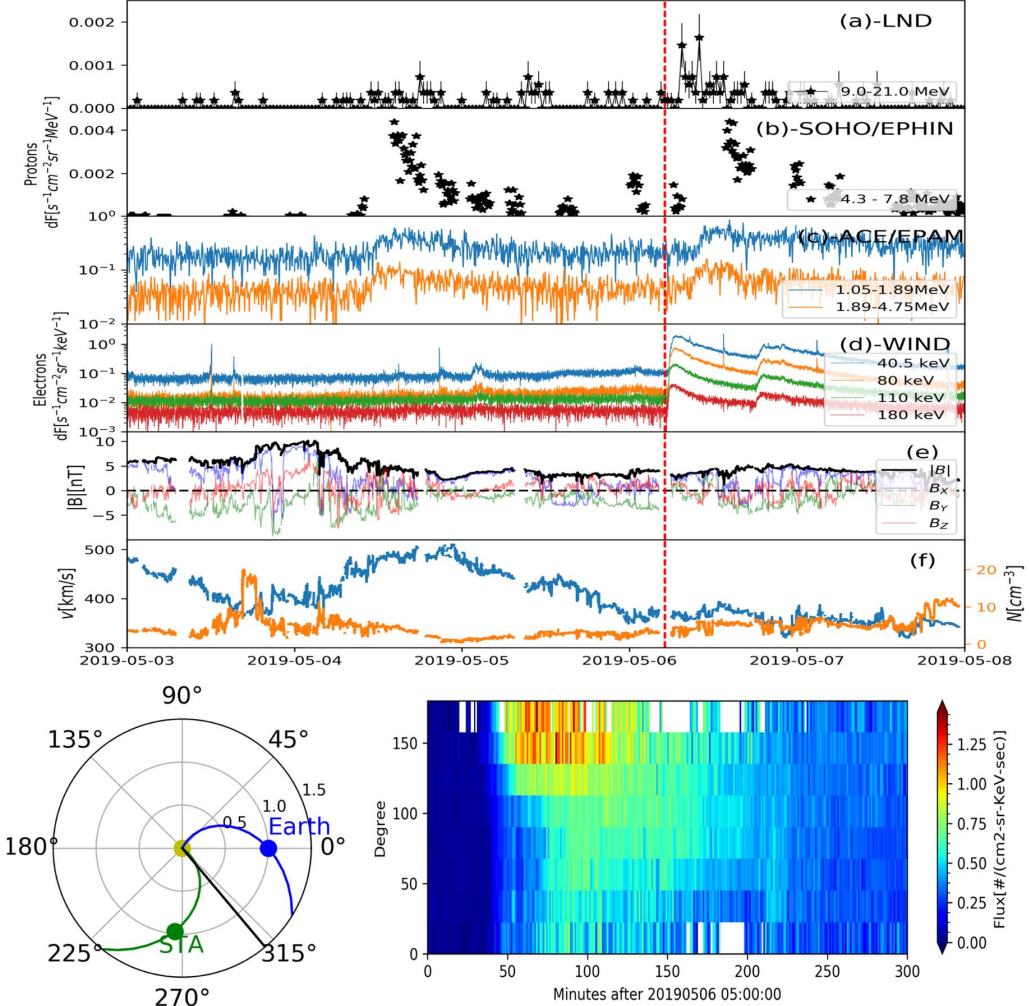


Figure 1. In situ measurements near Earth, including (a) proton intensity at 9.0–21.0 MeV by LND, (b) proton intensity at 4.3–7.8 MeV by SOHO/EPHIN, (c) ion intensity in 1.05–4.75 MeV by LEMS120 of ACE/EPAM, (d) electron intensity in 40.5 keV–180 keV by Wind/3DP, (e) magnetic field magnitude and three components in the GSE coordinates, (f) solar wind velocity and plasma density from OMNI. The red line indicates the eruption time of solar flare on May 6. The radial direction of the active region as well as the nominal Parker spirals for Earth and STA are plotted in the HEEQ coordinate in the bottom left panel. The pitch angle distribution of electrons measured by Wind after 05:00:00 on May 6 is given in the bottom right panel. Electrons are flowing outwards toward the observer at 180 degrees.

the data, the flux is averaged over 30 minutes for this figure. The analysis described below will be performed using the highest possible time resolution. In panel (b) we display the 4.3–7.8 MeV proton intensity profile measured by SOHO/EPHIN. However, the EPHIN measurements have data gaps due to limited telemetry during a SOHO roll maneuver on May 6. Thus, LND becomes the only instrument that observed the complete duration of this event at these energies.

Both y-axes in panels (a) and (b) are plotted in linear scale in order to better show the SEP enhancement. Panel (c) shows the ion flux averaged over each 30 minutes for two energy channels between 1 and 4.75 MeV detected by the LEMS30 (Low-Energy Magnetic Spectrometer) detector, one of the telescopes of ACE/EPAM. The intensity profile shows clear velocity dispersion of ions that are mostly attributed to protons.

Finally the electron profile observed by Wind between 40 and 180 keV is plotted in panel (d), which clearly shows

electrons starting to arrive at around 5:30 on May 6, slightly earlier than the energetic protons. Different energy channels show different onset times with higher energy electrons arriving earlier. This velocity dispersion feature is studied using a velocity dispersion analysis (VDA) method as discussed below. The second increase later that day is associated with another solar eruption, which is not considered in this study.

The remaining panels of Figure 1 show the local solar wind plasma data from 1 minute Near-Earth Heliosphere Data (OMNI), including the magnetic field, solar wind speed, and proton density. The near-Earth space is rather calm around the time of the SEP event of interest, with no indication of transient interplanetary coronal mass ejections (ICMEs), shocks or stream interaction regions (SIR), which could otherwise contribute to possible local acceleration of particles around the onset of the SEP event. A preceding SIR on May 3/4 is

Table 1
Time Line of the SEP Event on 2019 May 6

Time (UT)	Event	Characteristics	Refer to
2019.05.06 04:56:00	Eruption of Flare and start of SXR	AR 12740@50° E; M1.0 $D_E = 113^\circ$; $D_{STA} = 7^\circ$	
04:57:23	Type III radio burst	SSRT, Wind/WAVES, STA/SWAVES	
05:00:22	EUV wave propagating toward west	AIA 193 Å; $V \approx 500 \text{ km s}^{-1}$	Figure 4
05:03:30	Type II radio burst	@230 MHz–90 MHz, Last for 6 minutes	
05:18:24	Electron release	VDA, IMF $\sim 1.18 \text{ au}$, beam-like	Figure 2
05:28:00	CME first appears at SOHO/LASCO C2	376 km s ⁻¹ ^a , 326 km s ⁻¹ ^b	Figure 4
05:30:59	310 keV electron onset	Wind	Figure 2
05:31:00	CME at STA COR2	AW $\sim 20^\circ$, deflect to west	Figure 4
06:27:00	10.7–12.7 MeV proton release	LND; TSA	Figure 2
06:29:42	Proton release	VDA, IMF $\sim 1.33 \text{ au}$	Figure 2
07:32:00	10.7–12.7 MeV proton onset	LND, Poisson-CUSUM (Lucas 1985)	Appendix

Notes. The 8.3 minute light travel time has been subtracted from all the times in this table. D_E is the longitudinal distance between active region and magnetic footpoint of the Earth; D_{STA} is the distance to the STA footpoint; SSRT = Siberian Solar Radio Telescope; AW = angular width; GOES = Geostationary Operational Environmental Satellite; VDA = velocity dispersion analysis; IMF = interplanetary magnetic field; TSA = Time shifted analysis.

^a Velocity from Cactus catalog.

^b Velocity from GCS fitting.

indicated by the increase of magnetic fields, enhanced proton density and the slow rise of solar wind speed and was followed by a high-speed stream on May 4/5. We do not expect this preceding structure to have any influence on the SEP event reported here.

As shown in the bottom left panel of Figure 1, at the time of the SEP event under study, the longitudinal separation between the active region and the magnetic footpoint of STA using ballistic back mapping is only 7°, which suggests that STA would be a perfect observer for these energetic particles. However, STA was already experiencing an ongoing SEP event at the time of the flare and no impulsive contribution is seen at STA. Thus all we can state is that the impulsive event reported here was too small to be seen above the background of the preceding event at STA.

2.2. Determination of Onset and Release Times

The small intensity of the SEP event along with the limited geometry factor of LND require careful analysis of the data and limit the accuracy of the determination of the event onset times. Therefore, we apply the Poisson-CUSUM method (Lucas 1985) and follow the procedure in Huttunen-Heikinmaa et al. (2005) to derive the onset time of each energy channel using LND’s highest time resolution of 1 minute. In the Appendix, we present the Poisson-CUSUM analysis on the different LND energy channels in more detail.

The onset times of the 9.0–10.6 and 10.7–12.7 MeV channels are $08:00 \pm 7$ and $07:32 \pm 21$ minutes. The calculation of the uncertainties is explained in the Appendix. Assuming protons traveling scatter-free along a 1.2 au interplanetary magnetic field (IMF) line, which is calculated from the solar wind speed averaged over 8 hr before the SEP event, we derive that the 10.7–12.7 MeV protons need about 63 minutes to arrive at Earth and the release time is around $06:29 \pm 21$ minutes. The onset times for ACE/EPAM and Wind/3DP are determined as the time when the flux exceeds 3σ of the background signal. The latter is defined as the flux an hour before the SEP onset.

In Figure 2, the onset times t_{onset} of different channels are plotted versus $1/\beta$ that is c/v , where c is the speed of light and

v is the speed of particles with different energies. The uncertainties of the onset times at ACE and Wind are computed as the difference between the onset times using a 1σ threshold and a 3σ threshold. The error bar in the $1/\beta$ direction is calculated from the width of the energy channels. Both ACE/EPAM and Wind/3DP onset times of electrons are plotted in the left panel of Figure 2. Proton onset times are plotted in the right panel with the ACE/EPAM LEMS30 channels shown as filled squares, LEMS120 as empty squares and high-energy LND channels are shown as filled circles. Because only two channels of LEMS30 are available, two additional channels from LEMS120 with lower energy are also used here.

We apply the VDA method using the measured onset times in different energy channels to determine the particle release time, t_0 and the length of the IMF spiral, L , along which particles propagated. We fit the measured onset times t_{onset} and inverse velocities, $1/v$, with the function $t_{\text{onset}} = t_0 + L/v$ using orthogonal distance regression to account for uncertainties in both the x and y directions. The underlying assumption is that the particles that arrive earliest have undergone little scattering. The linear VDA fits are plotted as solid lines in the left and right panels of Figure 2 for electrons and protons, respectively, and 95% confidence intervals are given as shaded regions. The fitting result based on protons from the LND and LEMS30 measurements is given in orange, while the result using all data is given in blue. The two fit results are consistent. The results for t_0 and L are also given in Table 1.

The results of the fits suggest that electrons are released 22 ± 3 minutes after the flare eruption and that protons are released about 75 ± 12 minutes after the electron release. The IMF length inferred from electrons is $L_e = 1.18 \pm 0.18$ au, which is consistent with the Parker spiral derived from the in situ solar wind speed, $L = 1.2$ au. For protons we obtain a length $L_p = 1.34 \pm 0.10$ au. L_e and L_p are consistent with each other and weighting them with their inverse errors we find an average $L = 1.28 \pm 0.15$ au.

The VDA method assumes that all particles stream along the same IMF, which may become invalid in a realistic condition. In order to assess the reliability of this assumption for this SEP event, we also checked the pitch-angle measurement by Wind.

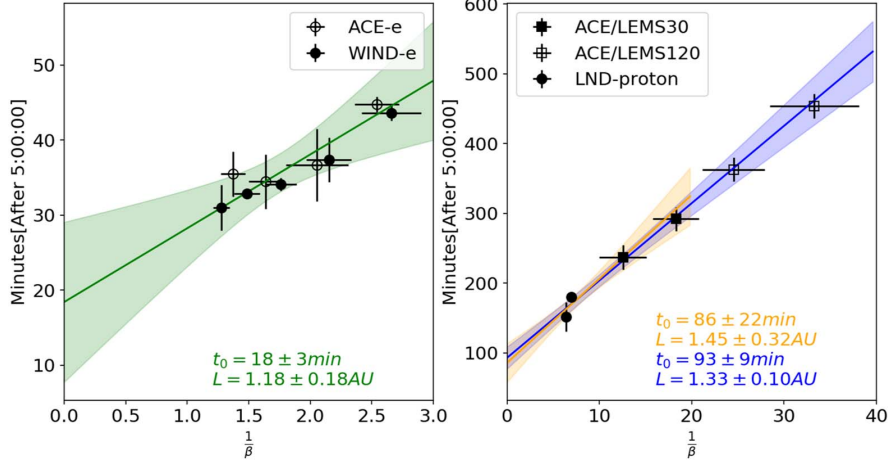


Figure 2. Velocity dispersion analysis of the SEPs (electrons shown in the left and protons shown in the right panel) on 2019 May 6. Wind and ACE electron data are used to determine the electron release time. LND proton, ACE/EPAM LEMS30 and LEMS120 ion data are used to determine the proton release time. The linear fits and the fitted parameters of the VDA analysis with 95% confidence interval are marked in the plots. More details can be found in the text of Section 2.2.

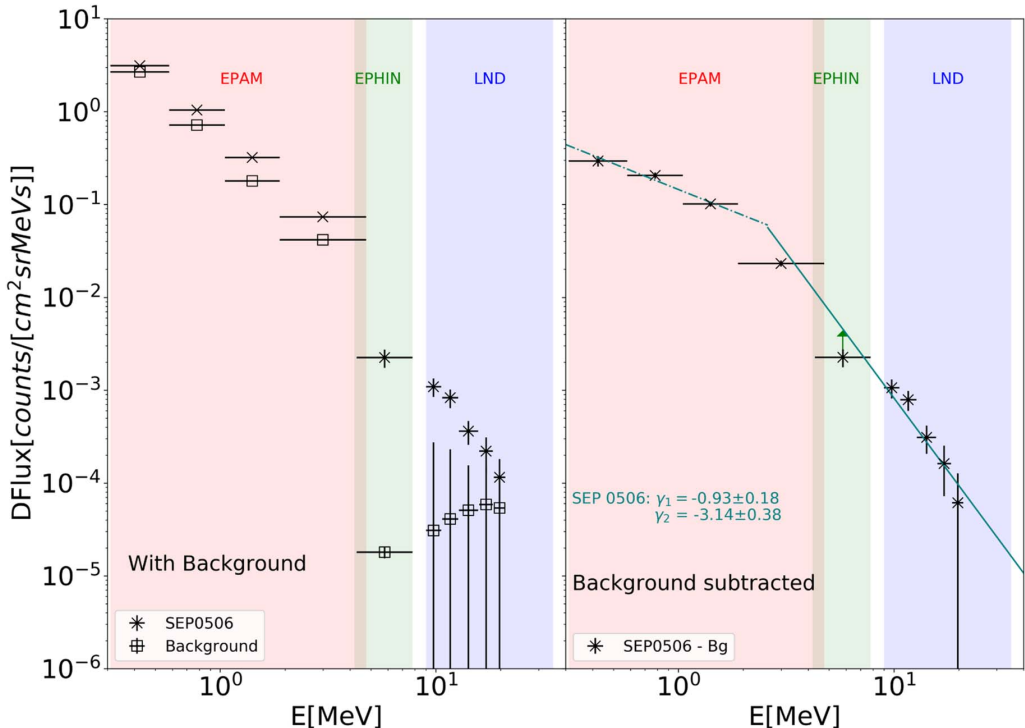


Figure 3. Proton spectra of the SEPs on 2019 May 6 and the background spectra which are averaged between April 29 and May 3. The left panel shows the spectra including the background and the right panel shows the SEP spectra with background subtracted. Different shaded areas indicate the energy ranges covered by the different instruments from ~ 300 keV to ~ 30 MeV. More details can be found in the text of Section 2.3.

At the beginning of the SEP event, electrons show a clear anisotropy (enhanced intensity at $\sim 180^\circ$ pitch angle, bottom right panels of Figure 1) suggesting that electrons first arrived along the IMF (Table 1). Consequently, these particles experienced little scattering, in agreement with the requirement of the VDA method. Unfortunately, proton observations with much smaller statistics make it difficult to identify a significant anisotropy of protons from Wind.

2.3. Energy Spectra

Combining the proton measurement by SOHO/EPHIN as shown in panel (b) of Figure 1 and the ions registered by ACE/EPAM in panel (c), which are dominated by lower energy protons and also those of LND, we plot the proton spectra integrated between 06:00 and 17:00 on 2019 May 6 in the left panel of Figure 3. The areas shaded in blue, green, and pink are

the energy coverage of LND (9–35 MeV), SOHO/EPHIN (4.3–7.8 MeV), and ACE/EPAM (0.310–4.75 MeV), respectively. The background spectra are also plotted and they are averaged between April 29 and May 3 (LND started working on April 29 for its fifth lunar day measurement). The energetic proton spectra during the event are well above the background as shown in the left panel of Figure 3, despite the large uncertainty in the LND data due to the low number of counts. The right panel of the figure shows the SEP spectra where the background spectrum has been subtracted. Because of the EPHIN data gaps during the impulsive phase of the SEP event as shown in Figure 1, the flux of the SEP event measured by EPHIN is likely to be larger than the derived one, as pointed out by the upward-pointing green arrow in the right panel.

Despite this event being of a more impulsive nature, we use a classic double power-law spectrum to fit the data. As can be seen in Figure 3, there is a break in the spectral slopes around 2.5 MeV, a fit using a double power law gives power-law indices of -0.93 ± 0.18 and -3.14 ± 0.38 for the spectra below and above this break energy, respectively. Interestingly, the break energy falls right between the values for large gradual events (Mewaldt et al. 2012) and those determined for very small events by Joyce et al. (2020) using data from the Parker Solar Probe (Fox et al. 2016).

2.4. Remote-sensing Observations

On 2019 May 6, an impulsive M1.0 flare erupted from active region (AR) 12470 located at N08E50. The soft X-ray (SXR) flare had an onset at 04:56:00⁸ and lasted for ~ 8 minutes as detected by the solar X-ray Imager on the GOES satellite. Since this is the only visible eruptive source on the Sun seen from Earth before the onset of the SEPs, we believe this is the solar counterpart of the SEPs measured in situ near the Earth and Moon. At nearly the same time as the SXR emission, a broadband type III radio burst starting from 240 MHz was observed by not only the ground radio observatory Solar Radio Telescope (SSRT)⁹ on Earth but also by the WAVES instrument on board the Wind spacecraft at Earth L1 point as well as by WAVES on board STEREO-A (STA). A type II radio burst between 230 and 90 MHz indicating the existence of a coronal shock was reported by the SSRT during 05:03:30–05:09:30. The timeline of this event is given in Table 1.

At 05:00:20, an asymmetric EUV wave (500 km s^{-1}) started propagating toward the northwestern hemisphere from the source as observed in the 193 Å band of the Atmospheric Imaging Assembly (AIA) on board the Solar Dynamics Observatory. The outer edges of the wave front at different times, i.e., at 05:00, 05:02, 05:07, 05:12, 05:17, and 05:22 on May 6, are marked as colored dashed lines in the top panel of Figure 4, which is explained in more detail below. After 05:22, the wave continued expanding across the solar surface as a rather faint structure that does not contain a clear wave front.

About half an hour after the flare eruption, at 05:28, a CME first appeared in the field of view of the Large Angle and Spectrometric Coronagraph Experiment (LASCO) C2 of SOHO with a projected (plane of the sky) speed of 376 km s^{-1} and an angular width of 20° , as reported in the

CACTUS CME catalog.¹⁰ Simultaneously, STA COR2 also captured the same structure. We applied the Graduated Cylindrical Shell (GCS) model (Thernisien 2011) to the coronagraph observations from two directions to obtain the velocity and propagation direction of the CME. In the bottom panel of Figure 4, we give the CME observation and outline the fitted CME structure in green at 05:46 on May 6. The fitting results show that the linear speed of the CME front was about 326 km s^{-1} and the CME was deflected by about 10 degrees away from the location of the flare to the west, consistent with the direction of the EUV wave propagation.

In the top panel of Figure 4, we show a magnetogram (in gray shades) on which the results of a potential field source-surface (PFSS) model for this Carrington rotation 2217 have been overlaid.¹¹ Open magnetic field lines (here with positive polarity shown in green and negative polarity shown in red) that connect the photosphere and the PFSS source surface for the solar wind are generally considered to be the main channels for SEP propagation in the solar corona. The polarity inversion line is shown in blue. The abovementioned active region AR 12470 is in the right part of the plot and marked by a white arrow. The radial projection points of STA and Earth on the solar surface on May 6 are plotted as open circles in black and blue, respectively. The magnetic footpoints based on the ballistic back mapping of the solar wind propagating at an average solar wind speed (about 360 km s^{-1} as observed in situ at Earth) are marked as filled circles. We note that the magnetic footpoint of STA is only 7° away from the location of AR 12470, which suggests STA is well connected to this active region. On the other hand, the longitudinal separation between the flare and Earth's footprint is about 113° as displayed in Figure 4. Also, the wave does not appear to persist to the Earth's footprint.

3. Summary and Discussion

On 2019 May 6, an SEP event was observed by LND on the far-side surface of the Moon. While it had only a low intensity, this is nevertheless the first SEP event with enough counting statistics that is detected by LND. This event was also detected by SOHO/EPHIN, which unfortunately only registered its decay phase, and also by Wind and ACE. The only possible solar source is a flare and its accompanying CME at AR 12470 located on the east hemisphere ($E50^\circ$). The type II radio burst indicates the existence of a shock in the lower corona and the CME speed was fitted as 326 km s^{-1} by the GCS model.

The time profiles of electrons and protons clearly show velocity dispersion. According to the VDA analysis, which assumes that all particles propagate along the same IMF line arriving at Earth and based on the combined data of LND, Wind, and ACE, electrons were released about 22 ± 3 minutes after the flare and type III radio burst and about 8 minutes after the high frequency type II radio burst, while protons were released at least 70 minutes later. The in situ velocity dispersion and anisotropy of electrons suggest that a direct magnetic connection from the source to Earth was established for these electrons. However, the separation between the flare location and the magnetic footpoint of Earth derived from the standard ballistic mapping is as large as 113° . This wide separation is remarkable. In the classical scenario of particle transport during

⁸ The time for remote-sensing measurements in this study has subtracted the ~ 8.3 minute light travel time over 1 au distance.

⁹ <http://www.e-callisto.org/>

¹⁰ <http://sidc.oma.be/cactus/>

¹¹ Source: Global Oscillation Network Group (GONG, <https://gong.nso.edu>).

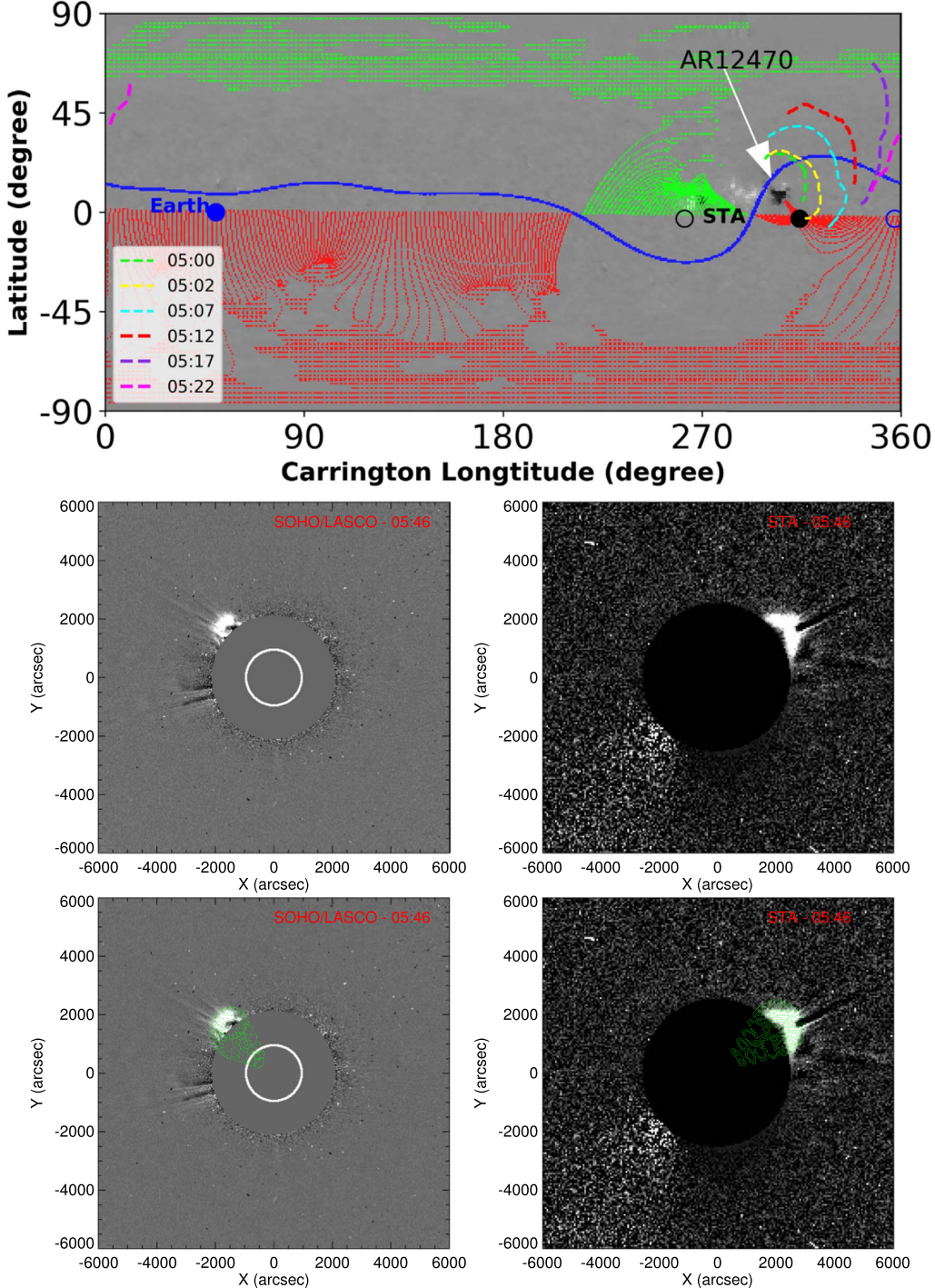


Figure 4. Top: the synoptic ecliptic-plane field plot for Carrington rotation 2217. The projected locations of STEREO-A (STA) and Earth are added as open circles and their magnetic footpoints mapped back to 2.5 solar radii based on the ballistic model are shown as filled circles. The outer edges of an EUV wave front at different times, i.e., at 05:00, 05:02, 05:07, 05:12, 05:17, and 05:22 on May 6, are marked as colored dashed lines. Bottom: CME observation of SOHO/LASCO (left) and STA/Cor2 (right) at 05:46 on 2019 May 6. The green mesh outlines the GCS reconstruction of the CME geometry. A more in-depth description of this figure can be found in Section 2.4.

impulsive events (Reames 1999) accelerated particles stream along an open IMF connecting the source and the observer with high-energy particles arriving earlier than lower energy ones. The in situ electron observation of this event at Earth (impulsive, velocity dispersion, and beam-like distribution) suggests a good connection to the flare, while the remote-sensing observation contradicts this explanation.

A possible explanation could be that particles are accelerated by the coronal shock, which deviated westwards and reached the magnetic footpoint of Earth. For example, Rouillard et al. (2012) have found an association between EUV waves that track the lateral shock expansion (Veronig et al. 2010) and particle release in wide-spread SEPs. As shown in the top panel of Figure 4, the EUV waves marked as colored dashed lines are propagating westward. The GCS fitting of the CME also indicates a nonradial and westward-deflected propagation toward the location of the Earth footpoint. However, the deflection of the CME is only about 10° and the EUV wave became rather faint after 05:25 suggesting that the shock was unlikely to reach Earth's footpoint around the particle release time. Therefore, it is difficult to conclude that a deflected shock should be responsible for the initial particle acceleration and release processes.

Klassen et al. (2018) proposed another scenario in which electrons accelerated by a flare can reach a distant magnetic footpoint (90° in their example found with STA) through an irregular magnetic field at the solar source. The PFSS extrapolation of the magnetic field (top panel of Figure 4) before this eruption does not show any direct connection between the flare and the location of Earth's footpoint. The PFSS model, however, assumes a current-free field by definition, and is an idealized consideration of the solar corona, so the real magnetic configuration might be drastically different. Furthermore, solar eruptions often rearrange the solar magnetic fields through, e.g., magnetic reconnection, and might have created a path for the particles to propagate over a large distance in heliolongitude. Unfortunately, the available observations do not show any evidence of a rearrangement of the solar magnetic field due to eruptions.

Moreover, the Parker spiral model is also an oversimplified, nondisturbed IMF condition and some researchers suggest the meandering and *random walk* of IMF would affect the particle propagation in the heliosphere (e.g., Mazur et al. 2000; Laitinen et al. 2016). In addition, the cross-field transport due to pitch-angle scattering and diffusion also causes particles to propagate in longitude and be observed on field lines with footpoints far away from the center of the solar eruption (e.g., Wibberenz & Cane 2006). This means that one could observe particle events on poorly connected field lines. However, the beam-like nature of the first electrons to arrive does not support such a cross-field transport model for this event.

Another observation about this event is the long delay between the electron and proton release times as derived from the VDA model, which indicates that different acceleration processes and/or release locations might be responsible for protons and electrons. As protons are released much later, they may be more likely accelerated by the shock that, however, cannot be confirmed to have reached Earth's magnetic footpoint. This explanation would also be difficult to reconcile with the common path lengths of electrons and protons, L_e and L_p . In their study of the delay between the electron and proton onset times at STA, STB, and L1 for wide-spread events,

Richardson et al. (2014) found that this time delay and the longitudinal separation between the flare location and back-mapped spacecraft footpoint were correlated. In Table 1 we report a delay between the electron and protons release times that may contribute to the Richardson et al. (2014) results. Such delays are not uncommon.

To summarize, we have presented various observations related to the first SEP event ever detected on the Lunar far-side surface. (1) The energy spectra of LND are consistent with observations from other spacecraft, though this is a weak event requiring large background subtractions. (2) The proton onset time of LND is also consistent with observations from other spacecraft, suggesting that the instrument response appears to be consistent with expectations. (3) The observations show clear velocity dispersion. (4) The SEP event was associated with a widely separated ($\sim 113^\circ$) flare at $E50^\circ$ relative to Earth.

The Lunar Lander Neutron and Dosimetry (LND) instrument is supported by the German Space Agency, DLR, and its Space Administration under grant 50 JR 1604 to the Christian-Albrechts-University (CAU) Kiel and supported by Beijing Municipal Science and Technology Commission, grant No. Z181100002918003 and National Natural Science Foundation of China Grant: 41941001 to the National Space Science Center (NSSC). The scientific data are provided by China National Space Administration. J.G. and Y.W. are supported by the Strategic Priority Program of the Chinese Academy of Sciences (grant Nos. XDB41000000 and XDA15017300), and the CNSA preresearch Project on Civil Aerospace Technologies (grant No. D020104). N.D. was supported under grant 500C1302 by the Federal Ministry of Economics and Technology on the basis of a decision by the German Bundestag. We also would like to express our very great appreciation to Patrick Kühl, Lars Berger, Andreas Klassen, and an anonymous referee for their valuable suggestions on this work.

Appendix

LND Measurement and Poisson-CUSUM Analysis

The charged particle telescope of LND measures protons in 1 minute time resolution between 9.0 and 35 MeV and the explicit energy bins are given in Table 6 of Wimmer-Schweingruber et al. (2020). Here, we present the 1 minute proton count rates at 9.0–10.6 MeV and 10.7–12.7 MeV during May 4 and 8 in Figure 5. The blue curves are the LND measurement in 1 minute time resolution. Most of the time, zero count is registered by LND, even during the SEP event. One reason is the small intensity of the SEP event and the other is the small geometry factor of LND. Both of them cause the poor statistics.

In order to calculate the event onset time, the Poisson-CUSUM method is applied and the results are plotted in an orange line for each channel. Cumulative sum (CUSUM) control schemes are widely used in industrial applications because they are designed to give an indication of when there is a change in a process (Page 1954). In our case, the change is when the SEPs rise above the background. The traditional CUSUM schemes are applied to a normally distributed quantity. When the variable has a Poisson distribution, a Poisson-CUSUM should be used. In the measurement of LND, the number of counts in a fixed interval, for example, 1 minute, obey a Poisson distribution. Hence, the Poisson-CUSUM will

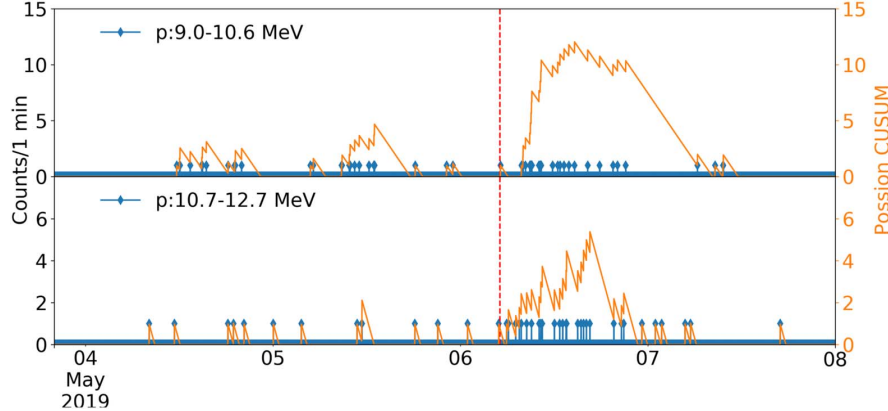


Figure 5. LND proton count rate in 1 minute time resolution (blue) and Poisson-CUSUM analysis (orange) based on 1 minute data.

be used to determine the onset time of the SEP event. By the definition of control schemes (Lucas 1985), the difference between the observed value Y_i and a reference value k are accumulated as a systematic change, which is:

$$S_i = \max(0, Y_i - k + S_{i-1}). \quad (\text{A1})$$

The start value is $S_0 = 0$ in standard CUSUM.

The reference value k is determined below:

$$k = \frac{\mu_d - \mu_a}{\ln(\mu_d) - \ln(\mu_a)}, \quad (\text{A2})$$

where μ_a is the mean number of counts estimated for each channel during the pre-event background and μ_d is selected by a two σ -shift criterion (Huttunen-Heikinmaa et al. 2005):

$$\mu_d = \mu_a + 2\sigma_a, \quad (\text{A3})$$

where σ_a is the standard deviation of the pre-event background. In order to have a nonzero background, the pre-event background is integrated from April 29 to May 2.

When the systematic change S_i exceeds the decision value h , then the onset of the SEP event is determined. Here we give a small decision value $h = 1$ according to the table in Lucas (1985). In order to reduce the false alarms due to the small h , we apply the following criterion: once an S_i exceeds the h , then the following 60 data points are checked as well. If all of them are larger than h , then the first signal is defined as the onset time of the SEP event.

We then apply the Poisson-CUSUM method for the one-minute data and the systematic changes are plotted as orange lines in Figure 5. The red dashed vertical line marks the eruption time of the flare at 04:56 on May 6. The increases of the orange lines during the SEP are very clear and the onset time can be easily determined. The onset time of the 9.0–10.6 MeV and 10.7–12.7 MeV channels are at 08:00 and 07:32, respectively.

We calculated the uncertainty of the Poisson-CUSUM method by determining the average time differences between the Poisson-CUSUM onset time and the times of the closest two neighboring nonzero data points.

The Poisson-CUSUM profiles, especially the one in 9.0–10.6 MeV, indicate the existence of energetic particles registered by LND during May 4 and 6, which are not

explicitly shown in Figure 1(a). The corresponding lower energy protons are also detected by SOHO/EPHIN and ACE/EPAM. Those particles may have the same solar origin as that of the gradual SEP event detected by STA starting on May 4 and lasting until May 8, i.e., the ongoing event that we mentioned in Section 2.1 during May 6.

ORCID iDs

- Zigong Xu <https://orcid.org/0000-0002-9246-996X>
- Jingnan Guo <https://orcid.org/0000-0002-6957-3355>
- Robert F. Wimmer-Schweingruber <https://orcid.org/0000-0002-7388-173X>
- Johan L. Freiherr von Forstner <https://orcid.org/0000-0002-1390-4776>
- Yuming Wang <https://orcid.org/0000-0002-8887-3919>
- Nina Dresing <https://orcid.org/0000-0003-3903-4649>
- Bernd Heber <https://orcid.org/0000-0003-0960-5658>

References

- Fox, N. J., Velli, M. C., Bale, S. D., et al. 2016, *SSRv*, **204**, 7
- Gold, R. E., Krimigis, S. M., Hawkins, S. E., III, et al. 1998, *SSRv*, **86**, 541
- Huttunen-Heikinmaa, K., Valtonen, E., & Laitinen, T. 2005, *A&A*, **442**, 673
- Joyce, C. J., McCormac, D. J., Christian, E. R., et al. 2020, *ApJS*, **246**, 41
- Klassen, A., Dresing, N., Gómez-Herrero, R., Heber, B., & Veronig, A. 2018, *A&A*, **614**, A61
- Laitinen, T., Kopp, A., Effenberger, F., Dalla, S., & Marsh, M. S. 2016, *A&A*, **591**, A18
- Lin, R., Anderson, K., Ashford, S., et al. 1995, *SSRv*, **71**, 125
- Lucas, J. M. 1985, *Technometrics*, **27**, 129
- Mazur, J. E., Mason, G. M., Dwyer, J. R., et al. 2000, *ApJL*, **532**, L79
- Mewaldt, R.,Looper, M., Cohen, C., et al. 2012, *SSRv*, **171**, 97
- Müller-Mellin, R., Kunow, H., Fleißner, V., et al. 1995, *SoPh*, **162**, 483
- Page, E. S. 1954, *Biometrika*, **41**, 100
- Reames, D. V. 1999, *SSRv*, **90**, 413
- Richardson, I. G., von Rosenvinge, T. T., Cane, H. V., et al. 2014, *SoPh*, **289**, 3059
- Rouillard, A. P., Sheeley, N. R., Tylka, A., et al. 2012, *ApJ*, **752**, 44
- Thernisien, A. 2011, *ApJS*, **194**, 33
- Veronig, A. M., Muhr, N., Kienreich, I. W., Temmer, M., & Vršnak, B. 2010, *ApJL*, **716**, L57
- Wibberenz, G., & Cane, H. V. 2006, *ApJ*, **650**, 1199
- Wimmer-Schweingruber, R. F., Yu, J., Böttcher, S. I., et al. 2020, *SSRv*, **216**, 104
- Zhang, S., Wimmer-Schweingruber, R. F., Yu, J., et al. 2020, *SciA*, **6**, eaaz1334

PRIMARY AND ALBEDO PROTONS DETECTED BY THE LUNAR LANDER NEUTRON AND DOSIMETRY EXPERIMENT ON THE LUNAR FAR SIDE

In addition to solar energetic particles (SEPs), extremely high-energy galactic cosmic rays (GCRs) dominated by protons and albedo particles generated through the interaction between GCRs and the lunar regolith are two other crucial components of the plasma environment that cause radiation hazard on the lunar surfaces. Unlike Earth, the Moon has no thick atmosphere and global magnetosphere acting as energy cutoffs for energetic particles and filters of the radiation hazard, which protects its surface. As a result, it is well known that the GCR flux of energy above a few MeV on the lunar surface is identical to that in deep space.

However, during the recent solar minimum period over July 2019 - July 2020, solar eruptions were rare, and so were SEPs. According to the measurement from Lunar Lander Neutron and Dosimetry Experiment (LND), no SEP events with energy exceeding ten MeV arrive at the lunar surface during its operation time. Therefore, it is an excellent opportunity to study the variation of GCR during this unusually quiet solar activity minimum (Fu et al., 2021) without the interference of SEPs. We can also validate the new instrument's performance and response to those high energetic particles.

Furthermore, albedo protons, which are generated in the lunar regolith by the interaction with GCRs and move upward, represent a significant contribution to the radiation hazard on the lunar surface and can potentially be used to detect the hydrogen material in the lunar regolith since the flux of albedo proton depends on the regolith composition and the GCR flux (Schwadron et al., 2016). Below 50 MeV, the flux of albedo proton surpasses that of GCR protons on the lunar surface (Dobynde and Guo, 2021; Wimmer-Schweingruber et al., 2020), and their energy can reach hundreds of MeV, posing a risk to biological tissue and electronic devices.

Benefiting from the advanced structure of LND's charged particle telescope, we have designed data products based on the Xmas plot (See instrument chapter and the following content for details) and successfully obtained the first measurement of albedo proton flux in the energy range between 65 and 75 MeV on the lunar surface.

Short overview of the publication

We first give a detailed explanation of the instrument's inner structure and measurement principle. Configuration changes during the first year of the mission are explained. The simulation set-up and the Xmas plot, which summarizes primary data products, are the basis of the study and are described. With the help of the Geometry and Tracking 4 (Geant4) simulation and the GCR model,

we carefully calibrate the data products and remove the background noise due to the contamination by other particles. As a result, we obtain a spectrum of GCR protons and flux of albedo protons on the lunar surface. Finally, we compare the measurements with the predictions from the Radiation Environment and Dose at the Moon (REDMoon) model and the measurements from other instruments and discuss the possible implications of our measurement. This work attempts to discuss the following questions that we brought up in Sec. 1.2: How do the anomalous cosmic rays (ACRs) and GCR behave during the most recent solar activity minimum and the onset phase of solar cycle 25? What is the difference between the current solar cycle and the previous one? How does solar modulation affect the intensity of cosmic rays? How do those secondary particles induced by those cosmic rays affect the radiation environment on the lunar surface?

- In this paper, the new primary protons products, based on the penetrating protons, are presented for the first time. They extend the proton data coverage to a few hundred MeV and measure the lower energy GCR protons. The flux of the albedo protons with an energy of approximately 70 MeV is measured for the first time on the lunar surface. Possible instrumental contamination and background noise are properly removed.
- The LND GCR spectrum is consistent with Solar and Heliospheric Observatory (SOHO)/Electron Proton Helium Instrument (EPHIN) measurement between 10 - 50 MeV. Predictions from CREME96 (Tylka et al., 1997) GCR model are approximately 50 % lower than measurements during solar activity minimum periods.
- The albedo proton flux agrees with the Lunar Reconnaissance Orbiter (LRO)/Cosmic Ray Telescope for the Effects of Radiation (CRaTER) measurement between 50 - 150 MeV and is consistent with the model prediction by the REDMoon model.
- We derived the ratio of albedo to primary protons flux at the same energy from observation and simulation. We found that the ratio peaks at 20 MeV with a value exceeding 2. The ratio decreases quickly with increasing energy.

The following article is reproduced from Xu et al. (2022), which is an open-access article reproduced under the terms of the CC-BY license. The supplement material including the configuration changes of LND up to now and the data we used in the main content is attached afterward.

PRIMARY AND ALBEDO PROTONS DETECTED BY THE LUNAR LANDER NEUTRON AND DOSIMETRY EXPERIMENT ON THE LUNAR FAR SIDE

Xu, Z., J. Guo, R. F. Wimmer-Schweingruber, M. I. Dobynede, P. Kühl, S. Khak sarighiri, and S. Zhang, *Frontiers in Astronomy and Space Sciences*, 9, page 974946 (2022), DOI: 10.3389/fspas.2022.974946

Own contribution: 80%

**OPEN ACCESS****EDITED BY**

Robert C. Allen,
Johns Hopkins University, United States

REVIEWED BY

Elias Roussos,
Max Planck Institute for Solar System
Research, Germany
Piers Jiggens,
European Space Agency (ESA), France

***CORRESPONDENCE**

Zigong Xu,
xu@physik.uni-kiel.de
Robert F. Wimmer-Schweingruber,
wimmer@physik.uni-kiel.de

SPECIALTY SECTION

This article was submitted to Space
Physics,
a section of the journal
Frontiers in Astronomy and Space
Sciences

RECEIVED 21 June 2022

ACCEPTED 22 August 2022

PUBLISHED 26 September 2022

CITATION

Xu Z, Guo J, Wimmer-Schweingruber RF, Dobynde MI, Kühl P, Khaksarighiri S and Zhang S (2022). Primary and albedo protons detected by the Lunar Lander Neutron and Dosimetry experiment on the lunar farside. *Front. Astron. Space Sci.* 9:974946. doi: 10.3389/fspas.2022.974946

COPYRIGHT

© 2022 Xu, Guo, Wimmer-Schweingruber, Dobynde, Kühl, Khaksarighiri and Zhang. This is an open-access article distributed under the terms of the [Creative Commons Attribution License \(CC BY\)](#). The use, distribution or reproduction in other forums is permitted, provided the original author(s) and the copyright owner(s) are credited and that the original publication in this journal is cited, in accordance with accepted academic practice. No use, distribution or reproduction is permitted which does not comply with these terms.

Primary and albedo protons detected by the Lunar Lander Neutron and Dosimetry experiment on the lunar farside

Zigong Xu^{1*}, Jingnan Guo^{2,3}, Robert F. Wimmer-Schweingruber^{1,4*}, Mikhail I. Dobynde², Patrick Kühl¹, Salman Khaksarighiri¹ and Shenyi Zhang^{4,5,6}

¹Institute of Experimental and Applied Physics, Kiel University, Kiel, Germany, ²School of Earth and Space Sciences, University of Science and Technology of China, Hefei, China, ³CAS Center for Excellence in Comparative Planetology, Hefei, China, ⁴National Space Science Center, Beijing, China, ⁵Beijing Key Laboratory of Space Environment Exploration, Beijing, China, ⁶University of Chinese Academy of Science, Beijing, China

The Lunar Lander Neutron and Dosimetry (LND) Experiment aboard the Chang'E-4 Lander on the lunar far-side measures energetic charged and neutral particles and monitors the corresponding radiation levels. During solar quiet times, galactic cosmic rays (GCRs) are the dominating component of charged particles on the lunar surface. Moreover, the interaction of GCRs with the lunar regolith also results in upward-directed albedo protons which are measured by the LND. In this work, we used calibrated LND data to study the GCR primary and albedo protons. We calculate the averaged GCR proton spectrum in the range of 9–368 MeV and the averaged albedo proton flux between 64.7 and 76.7 MeV from June 2019 (the seventh lunar day after Chang'E-4's landing) to July 2020 (the 20th lunar day). We compare the primary proton measurements of LND with the Electron Proton Helium INstrument (EPHIN) on SOHO. The comparison shows a reasonable agreement of the GCR proton spectra among different instruments and illustrates the capability of LND. Likewise, the albedo proton measurements of LND are also comparable with measurements by the Cosmic Ray Telescope for the Effects of Radiation (CRaTER) during solar minimum. Our measurements confirm predictions from the Radiation Environment and Dose at the Moon (REDMoon) model. Finally, we provide the ratio of albedo protons to primary protons for measurements in the energy range of 64.7–76.7 MeV which confirm simulations over a broader energy range.

KEYWORDS

LND, Moon, lunar radiation environment, galactic cosmic rays, lunar albedo protons, data calibration, instrumentation

1 Introduction

The charged particle radiation environment on the lunar surface consists of Galactic Cosmic Rays (GCR), a small contribution from Anomalous Cosmic Rays (ACR), and a highly variable, sporadic contribution from Solar Energetic Particles (SEPs). In addition, secondary albedo particles are created primarily by the GCR interaction with the lunar regolith (Treiman, 1953; Dorman, 2004; Wilson et al., 2012). In this work we focus on measurements by the Lunar Lander Neutron and Dosimetry experiment (LND, Wimmer-Schweingruber et al., 2020) of GCR primary and secondary (albedo) protons and compare them with state-of-art model predictions (Dobynde and Guo, 2021). The space radiation measured by LND is a key concern for human space flight and may pose limits on long-term crewed missions to the Moon or Mars (Cucinotta and Chappell, 2011).

The interaction of high-energy particles with the lunar regolith results in the production of secondary particles. Some of these particles can escape from the soil and can be measured as albedo particles. Obviously, they will also contribute to the radiation exposure of astronauts on the lunar surface, but they also provide information about conditions beneath the lunar surface.

Wilson et al. (2012) first distinguished protons measured by the Cosmic Ray Telescope for the Effects of Radiation (Spence et al., 2010, CRaTER) instrument from different directions and constructed the first albedo proton yield map between 60 and 150 MeV. They found that the ratio of albedo to primary protons is uniformly distributed over the lunar surface within $\sim 10\%$ uncertainty and that the average ratio of upward to downward particle during the minimum between solar cycles 23 and 24 (in 2009–2011) was about 0.38 ± 0.02 . Simulations by Spence et al. (2013) show that such upward albedo particles can contribute a significant amount ($\sim 8.62\%$) to the radiation dose with albedo protons accounting for 3.1% of the total dose rate. Moreover, albedo neutrons have been used to detect and determine the subsurface hydrogen content (Mitrofanov et al., 2016). Likewise, Schwadron et al. (2016) used the CRaTER instrument to detect albedo protons and provided evidence for the existence of hydrated material in the lunar regolith at the polar regions, based on small variations of the proton yield. A follow-up study by Schwadron et al. (2017) analyzed the difference of the lunar albedo protons yield for the lunar sunrise and sunset terminators.

Looper et al. (2013) presented the CRaTER measurements of radiation environment near the lunar surface including GCRs and albedo particles. They also utilized a GEANT4 simulation to model the energy distribution of albedo particles, and the response of different detectors to various particle species that reach the instrument on the 50 km height lunar orbit.

More recently, Dobynde and Guo (2021) developed the Radiation Environment and Dose at the Moon (REDMoon)

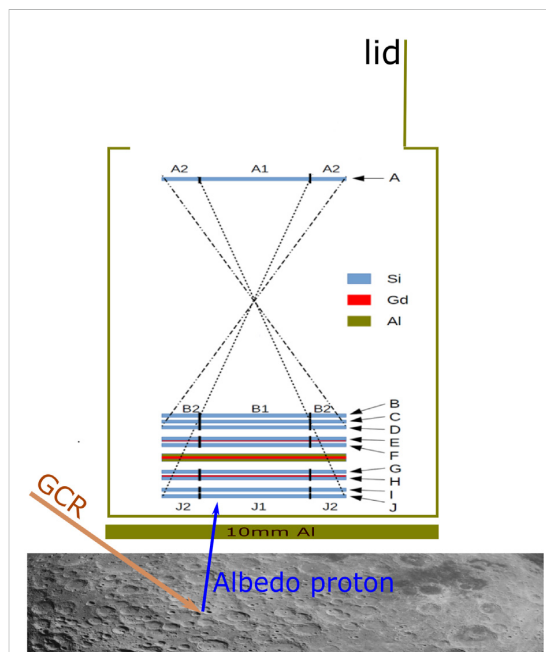


FIGURE 1

Schematic view of the LND sensor head located above the lunar regolith with a 10-mm Al equivalent shielding (olive) between LND and the lunar soil. The LND sensor head consists of 10 segmented 500 μm -thick Si detectors A–J. The Gd (red) and Al (olive) absorbers are designed to detect uncharged particles. The 10-mm Al sheet is added to mimic the shielding by the material between the sensor head and the lunar soil. On the lunar surface, the interaction of high-energy GCR particles (mainly protons) with the soil generates secondary, upward-moving protons. A more detailed description of LND is given in Wimmer-Schweingruber et al. (2020).

model that describes the detailed radiation environment both on the lunar surface and in the lunar soil. In this model, the lunar body is described by concentric spherical layers of different densities and soil composition is based on Apollo 17 drill core results (McKinney et al., 2006). The model is based on the GEANT4 Monte-Carlo particle transport code (Agostinelli et al., 2003) and the FTFP_BERT_HP physics list was used to calculate the GCR-induced radiation environment on and below the lunar surface. Primary GCRs have an isotropic direction (in the upper half-sphere) and the output particle types and energy at each soil depth or zenith angle are recorded. Results from different solar modulation conditions are also derived.

On 3 January 2019, China successfully landed the Chang'E-4 spacecraft on the far side of the Moon inside the von Kärmán Crater. As one of its scientific payloads, Lunar Lander Neutron and Dosimetry experiment (LND, Wimmer-Schweingruber et al., 2020) aboard the Chang'E-4 Lander is a small instrument with the primary objective of monitoring the radiation level on the lunar surface. LND consists of ten

500 μm silicon detectors (labeled A–J) that are assembled as shown in [Figure 1](#). The primary data products of LND include dynamic Total Ionizing Dose rate (TID) and Linear Energy Transfer (LET) spectra. The radiation dose rate is the radiation energy deposited by incoming radiation per unit time and unit mass of the absorber and is often measured in silicon detectors. LET is the energy that an ionizing particle transfers to the material per unit path length. Knowledge of both of these quantities is crucial in preparing for human spaceflight and human exploration of the Moon. Apart from these dosimetric quantities, LND also measures primary charged-particle energy spectra. Using the energy loss in its individual detectors, LND measures the primary energy of particles in the energy range between ~ 10 MeV/nuc and a few hundred MeV/nuc and distinguishes different particle species, including electrons, protons, ^4He , its isotope ^3He , and heavy ions such as carbon, oxygen, nitrogen, and iron. The post-launch performance of LND and its capability of measuring protons have been partially verified through analysis of a weak and impulsive SEP event in May 2019 ([Xu et al., 2020](#)), with proton energy up to ~ 20 MeV. Moreover, LND measures upward-directed albedo particles using the same method as was successfully applied using data from the Radiation Assessment Detector (RAD, [Hassler et al., 2012](#)) on Mars. [Appel et al. \(2018\)](#) determined the flux of albedo particles in the energy range 100–200 MeV on the Martian surface using a two-dimensional count density histogram. Here we use a similar method to distinguish upward proton fluxes from downward ones.

[Zhang et al. \(2020\)](#) displayed the first measurement of TID and LET spectra during the first two lunar days after LND was switched on. During the solar minimum of Solar Cycle (SC) 24/25, the average total absorbed dose rate on the lunar surface reached $13.2 \pm 1 \mu\text{Gy}/\text{h}$. This value is consistent with the radiation dose that is measured by CRaTER in orbit after the conversion to the surface in January 2019. A comparison with the radiation level on the Mars surface shows that the dose rate on the lunar surface is about 15% higher than that on Mars when GCR intensity reached a maximum during the deep solar minimum. Furthermore, the lunar surface dose rate is about two times higher than that measured in the International Space Station (ISS) by the 3D-DOSTEL instrument ([Berger et al., 2020](#)).

More than 3 years into the Chang'E 4 mission, most of LND's detectors are still in good condition and operating well despite the grueling temperature differences between lunar day and night. Nevertheless, since a mishap on the dawn of the third lunar day some segments of four of the 10 detectors in LND have begun to suffer from increased noise levels. We believe that a premature opening of LND's lid led to a severe drop in the temperature of LND's sensor head. The mounting of LND's detectors led to unintended thermo-mechanical stress on the front detector (A) and the three detectors at the end of the particle telescope (H, I, and J). An adjustment of the thresholds of the affected detector segments has led to some changes in the

LND data products compared to those presented in [Wimmer-Schweingruber et al. \(2020\)](#). The changes are described in the appendix.

In this work, we provide a detailed calibration of the GCR proton spectra measured by LND and present the first measurements of the albedo protons by LND. The paper is organized as follows: In [Section 2](#), we briefly describe LND, its measurement principles for primary and albedo protons, data calibration, the processing of LND data, and the simulation set-up used for interpreting the data. In [Section 3](#), we present the LND measurements and compare processed LND data with other available data sets, i.e., the primary GCR measurements by the Electron Proton Helium INstrument (EPHIN, [Müller-Mellin et al., 1995](#)) on-board SOHO and the albedo protons measured by CRaTER onboard LRO ([Wilson et al., 2012; Schwadron et al., 2016](#)). We compare these measurements with the numerical cosmic ray model of Cosmic Ray Effects on Micro-Electronics Code ([Tylka et al., 1997](#), CREME96), Badhwar-O'Neill 2014 model (BON14, [O'Neill et al., 2015](#)) and the lunar radiation model REDMoon as mentioned above. [Section 4](#) gives a summary and discussion. Finally, the appendix gives a detailed description of the current LND configuration and calibration parameters.

2 Preparation of LND data

2.1 Instrument and the simulation set-up

A schematic structure of the LND sensor head is given in [Figure 1](#). It consists of ten silicon detectors, each with a nominal thickness of 500 μm . Detectors are arranged in a charged-particle telescope configuration and labeled A through J from top to bottom. Each detector is segmented into an inner and an outer segment (labeled 1 and 2, respectively), each with approximately the same area. LND uses coincidence measurements to detect the charged particles which requires particles to pass through the uppermost detector A and at least trigger the next detector, B. In the middle of the sensor head, Al and Gd absorbers (shown in olive and red in [Figure 1](#)) are used to detect the upward and downward flux of thermal neutrons (Gd has a very large cross-section for thermal neutrons). These absorbers increase the scattering of particles inside the sensor head and absorb part of the particle energy without providing a measurement thereof.

Above detector A, the front window is covered by a lid that opens when LND operates, allowing particles to arrive at the detector without any obstacles. During lunar nights, the lander closes the lid to keep the sensor head and detectors warm enough for them to survive the cold lunar night. The payload compartment of the Chang'E-4 lander which contains other scientific instruments is located beneath the LND sensor head and thus provides extra shielding for upward albedo particles before they reach LND. However, the details of that shielding are

unknown and an estimation of 10-mm Al shielding equivalent was provided by the Chang'E-4 team. We thus add a 10-mm Al sheet between LND and the lunar soil in our model for estimating the albedo contribution to LND as shown in [Figure 1](#). Consequently, the shielding material raises the lowest energy that albedo protons are required to have in order to arrive at the LND detector. A more detailed description of LND is given in [Wimmer-Schweingruber et al. \(2020\)](#).

We employed the GEANT4 toolkit ([Agostinelli et al., 2003](#)), version 10.4.1, using the QGSP_BERT physics list to simulate the detector response to different particles from different directions at the relevant energies.

To simulate the particles from above, we placed a square-shaped planar source right above the front detector A with a size that is larger than the size of detector A and fully covers the field of view (FOV) of LND, i.e., the inner dashed line of the combination of A1 and B1 in [Figure 1](#). Similarly, a square particle source is placed below the 10 mm-Al sheet when simulating upward particles. The sources are isotropic and the energy spectrum is a power law with index -1, i.e., logarithmically flat, to allow easy scaling to any other spectral index¹, as discussed, e.g., in [Guo et al. \(2019\)](#), but is a standard process. The spectrum is in differential flux units. We then obtain the averaged geometric factors from such a simulation and use them to convert detected counts to flux.

2.2 Xmas plot

The Xmas plot² is the primary data product of LND that is generated onboard and represents the memory space of the LND flight model. All LND measurements are stored in a 274×64 matrix though not all elements of this matrix are transmitted to Earth. The memory space refreshes every hour; hence the time cadence of the Xmas plot is 1 h. The Xmas plot can be divided up column-wise into the following regions (from columns 0–274): thermal neutrons, fast neutrons, TID, LET, and charged particles. More details of the data products can be found in [Wimmer-Schweingruber et al. \(2020, Sec. 4\)](#). In this section, we focus on charged particles and explain the generation of the corresponding two-dimensional density histogram in the Xmas plot which is important to understand the calibration of LND data. Part of the charged particles measurement is displayed in panels (A) and (B) of [Figure 2](#).

The charged particles in the Xmas plot can be further divided up into two parts, stopping and penetrating particles. The

stopping particles have energies between ~ 8 and ~ 35 MeV/nuc. LND thus measures SEPs, ACRs, and lower energy GCRs in this energy range. When arriving at LND on the lunar surface, particles within this energy range can first trigger and penetrate detector A, then pass the following detectors, depositing (part of) their kinetic energy. Depending on their primary energy, some of these particles will stop in one of the detectors between B and I (as indicated by B, C, etc. along the top of panel (A) of [Figure 2](#)) and hence deposit all of their energy. The higher their primary energy, the deeper they get in the detector stack. The upper limit is ~ 35 MeV/nuc for protons and helium nuclei stopping in detector I, but different for heavier ions ([Wimmer-Schweingruber et al., 2020](#)). A small uncertainty in their primary energy remains due to noise in the individual detectors. Particles with energies above 35 MeV/nuc will penetrate detector I and stop in detector J or penetrate it, i.e., all detectors from A to J are triggered. Penetrating particles may come from above or below. Panels (A) and (B) of [Figure 2](#) show those parts of the Xmas plot that belong to stopping and penetrating particles. A precise description of the quantities used to populate the Xmas plot are given in Table 5 of [Wimmer-Schweingruber et al. \(2020\)](#), but a short summary is given here for convenience. For particles stopping between detectors B and H, the values along the x axis are a monotonous function of the ratio E_{total}/E_A . The y axis is ordered according to the product E_{total}/E_A . The ratio and product are mapped to row and column values internally in the instrument. Thus, the column regions marked by B, C, D are similar to traditional $dE/dx - E$ plots, but rotated and compressed into $dE/dx \cdot E_{\text{total}}$ vs. $dE/dx/E_{\text{total}}$ space. In this space the “ $1/E$ ” energy loss appears as a horizontal line and the penetrating particles do not show up because they are detected in the next detector. The horizontal (energy) axis is compressed by the division by E_A . Particles stopping in detectors E, F, etc. are treated somewhat differently, see [Wimmer-Schweingruber et al. \(2020\)](#) for more details. The quantities used for penetrating particles and particles stopping in detector I are similar. The x axis is ordered by E_I/E_A and the y axis is ordered by the sum of energy depositions in detectors B, C, and D (see [Section 2.4.1](#) for the exact definition of penetrating particles). Stopping particles populate columns 32–240, while penetrating particles are between 246 and 266. The data in the empty regions in panel (A) of [Figure 2](#) are not transmitted back to Earth.

The proton channels that are used in this work are outlined by the black boxes in panels (A) and (B) of [Figure 2](#) and further indicated by H1 – H14. We call them DPS boxes, where DPS stands for “data product scheduler”. Count numbers inside DPS boxes are read out from memory every minute. Therefore the cadence of primary proton data is 1 min. These high-time-resolution proton data are important during the onsets of SEP events ([Xu et al., 2020](#)). The pixels with high count rates around row 20 in panel (A) of [Figure 2](#) are ${}^4\text{He}$ counts. Heavier ions would lie at even higher rows.

¹ The “logarithmically flat” spectrum appears “flat” or horizontal when plotted in a log-log plot. Thus, bins are evenly spaced in a logarithmic scale and have the same number of counts per bin

² We call this plot “Xmas plot” because our group in Kiel used a similar plot as our 2017 Xmas card

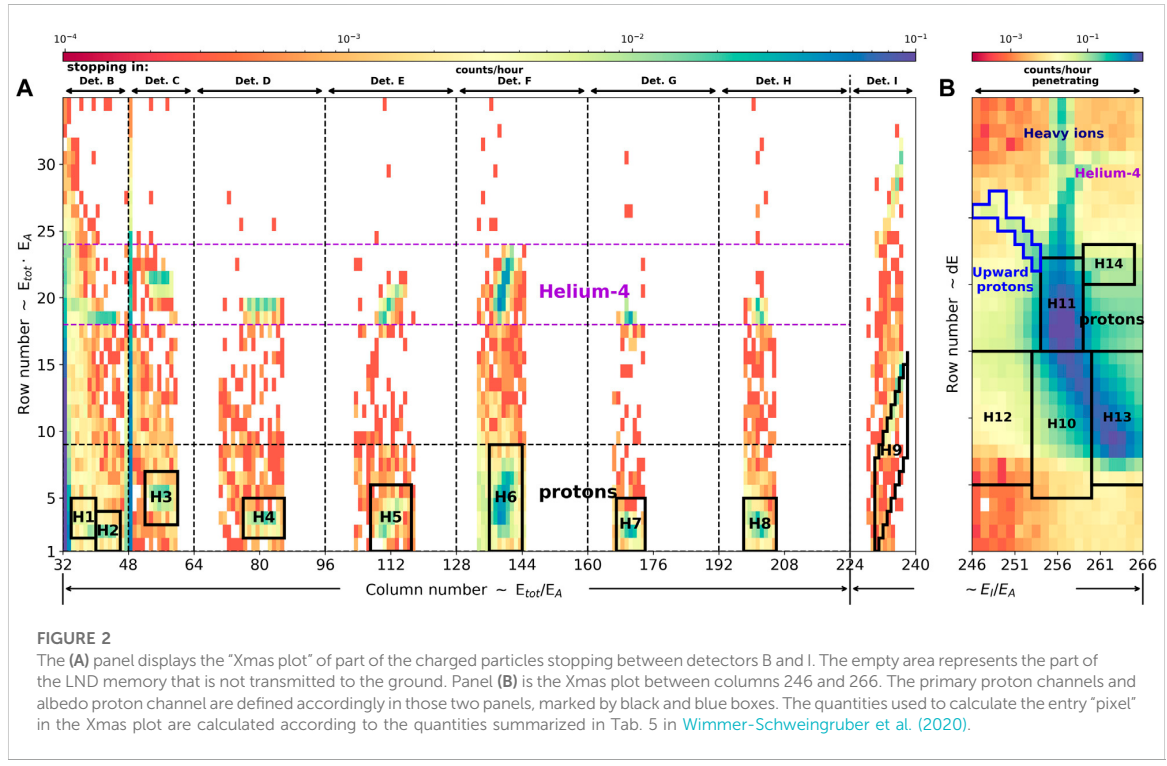


FIGURE 2

The (A) panel displays the “Xmas plot” of part of the charged particles stopping between detectors B and I. The empty area represents the part of the LND memory that is not transmitted to the ground. Panel (B) is the Xmas plot between columns 246 and 266. The primary proton channels and albedo proton channel are defined accordingly in those two panels, marked by black and blue boxes. The quantities used to calculate the entry “pixel” in the Xmas plot are calculated according to the quantities summarized in Tab. 5 in Wimmer-Schweingruber et al. (2020).

One of the advantages of the Xmas plot data product is that one can define one’s own data product. For this work, we defined a mask for upward-moving protons. It is marked by the blue box in panel (B) of Figure 2. The positions of those pixels were determined manually based on simulation results. Because such particles are rare, the 1-h time resolution of the Xmas plot is more than sufficient. In the following sections, we explain this data product in depth.

The Xmas plot in Figure 2 was accumulated between the seventh and the 20th lunar day (from 27 June 2019 to 26 July 2020)³. This was a period in the deep solar minimum between solar cycles 24 and 25. The minimum solar modulation and solar activity during that period led to the highest GCR flux since space age (Fu et al., 2021). It offers the opportunity to validate LND’s performance using GCR data without the interruption by SEPs. As discussed above and in the appendix, the thresholds of several detectors had to be increased, the period we use for this work begins after all these changes have been made.

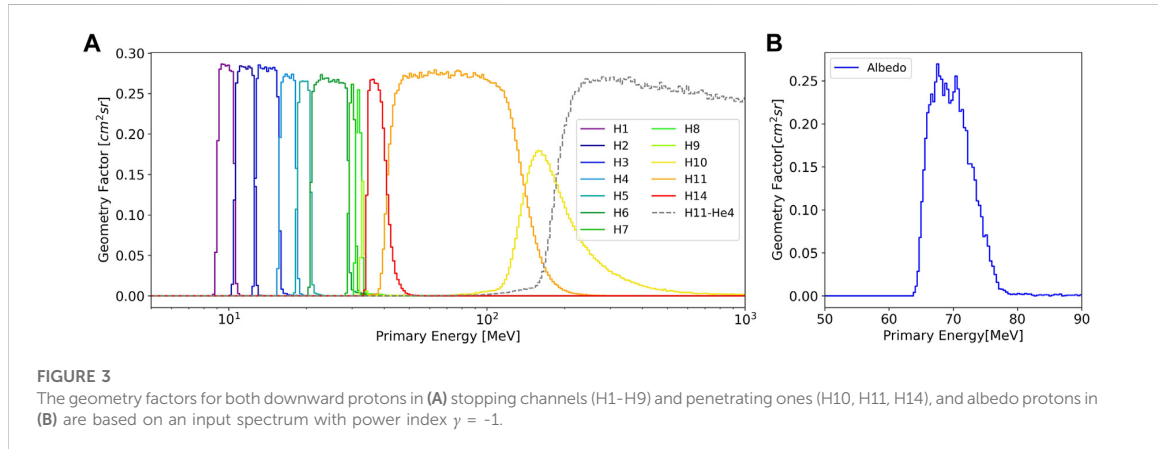
2.3 Detection of downward-moving protons

2.3.1 Stopping and penetrating protons

Stopping and penetrating protons populate DPS boxes H1 - H14, their geometry factors are shown in panel (A) of Figure 3. The DPS boxes H1 - H9 count the protons that stop in detectors B to I⁴. DPS boxes H10 - H14 record penetrating protons with energies above ~ 35 MeV. The energy bins in H10, H11, and H14 are used in this paper for the first time, they extend the measurement capability of LND beyond the energy of stopping particles. Unlike those for stopping particles, the geometry factors of penetrating particles partially overlap, as can be seen in panel (A) of Figure 3. Moreover, the measurement of penetrating channels has a larger uncertainty due to uncertainties in the determination of the background as will be discussed in

³ One lunar day is approximately 28 Earth days long. The periods when LND was on are listed in https://www.ieap.uni-kiel.de/et/change4/data_by_lunar_day/info

⁴ Note that channel H9 has a relatively narrow energy range (bin width) and a smaller geometry factor than the other channels. The reason for this is an error in the definition of the corresponding DPS box (between columns 224 and 240) which does not contain the bulk of the particle population stopping in detector I. As shown in panel(a) of Figure 2, nearly half of the pixels with higher density lie outside of the black box, leading to the reduced geometry factor. This defect was not resolved in time for the flight model and hence the updated geometry factors given in the appendix should be used to make use of this channel



Section 2.3.3. Currently, data from the penetrating channels are not yet publicly available because they still require a better calibration. With the onset of solar activity, we expect this to be achieved with some large SEP events with energies above ~ 35 MeV.

2.3.2 Calculation of fluxes

The differential flux, dF is calculated according to Eq. 1 which is valid for all particle species, including albedo protons,

$$dF = \frac{N}{dE \cdot \bar{G} \cdot dt}, \quad (1)$$

where N is the number of counts in the DPS boxes, dE is the energy bin width determined from the response functions shown in panel (A) of Figure 3, dt is the accumulation time of the whole measurement, and includes possible dead time corrections (Wimmer-Schweingruber et al., 2020), and \bar{G} is the weighted geometry factor of each energy bin. The method that was used to calculate the averaged geometry factors is given in the appendix and their values are given in Table S3. The geometry factors of primary protons and albedo protons as a function of energy are given in panels (A) and (B) of Figure 3.

We note that, despite the intention of the concept of geometry factors, the averaged geometry factors derived via Eq. S1 in the supplementary material do depend on the input spectra. As explained in appendix, the contribution of high-energy particles results in non-negligible contributions in the count rates for low-energy channels. Thus, the spectral shape beyond ~ 100 MeV affects the count rate in the penetrating channels. The stopping channels are less affected, as discussed in the appendix.

In Table S3 we provide the averaged geometry factors derived for two different input spectra; one is a power-law spectrum with index -1 (column 3), where the particles are uniformly

distributed in logarithmic energy space. The other one is the numerical CREME96 GCR model spectrum (Tylka et al., 1997) for the 2019 solar minimum (column 4).

2.3.3 Correction of the contribution from ^4He and heavy ions to the proton flux

Close inspection of panel (A) of Figure 2 shows that ^4He and heavy ions contaminate the proton DPS boxes H1 - H9. While ^4He is well separated from protons (its counts can be seen to populate the Xmas plot around row number 20), the Xmas plot entries between ^4He and protons are clearly populated by a substantial background. This background which mainly affects the low-energy proton DPS boxes is primarily due to high-energy He and heavier ions which create secondary particles after they interacted with detector A. The secondary particles trigger B after which A is read out. Because the geometry factor for interaction with A is large and the flux of high-energy (GCR) ions is also high, this process happens sufficiently often to result in this background.

The penetrating channels shown in panel (B) of Figure 2 are affected by the noisy detector segments A2,I1&I2, and J1. The effect of this malfunction has been accounted for by increasing the thresholds of these detectors and disabling A2 in the LND level-3 data processing logics (see Wimmer-Schweingruber et al., 2020, for a discussion). This results in the asymmetric shape seen in panel (B). In the supplementary material, we give the detailed explanations of this asymmetric structure. Moreover, minimally-ionizing protons are affected more than ^4He because of their smaller energy deposition in the detectors. Thus the detection efficiency for minimally-ionizing protons (measured in H10) is reduced because of the increased thresholds in I and J. The minimally-ionizing protons populate primarily H10, whereas minimally ionizing ^4He populates primarily H11. Thus, as can be seen in panel (A) of Figure 3 the protons measured in H11 are strongly affected by minimally-ionizing ^4He (dashed line in Figure 3).

In order to quantify these different sources of contamination and reduced detection efficiencies, we ran extensive GEANT4 simulations of LND. We used the simulation setup introduced in [Section 2.1](#) to model elements from hydrogen to iron, thus including all relevant GCR species. Instead of calculating the geometry factors for detecting these elements in their instrument channels (i.e., in the appropriate boxes in the Xmas plot), we derived the geometry factors for measuring them in the proton channels (H1 - H14) as a function of energy. These simulation data were then analyzed using the current LND configuration (incl. thresholds). Thus we could estimate the contamination of the H1 - H14 proton channels by high-energy (GCR) helium and - to a lesser extent - heavy ions. Of course, ^4He is rarer than hydrogen, the contribution of GCR ^4He to the stopping proton channels (H1 - H7) is on the order of a few percent, but larger for H8 and H9 (cf. Tab. S3 of supplementary material). Similarly, minimally-ionizing ^4He affects the penetrating, but not minimally-ionizing protons in H11, only 36% of all particles in H11 are protons (see respective entry in Tab. S3 of supplementary material).

To check the influence of different GCR models on the correction factors, we compare the results of the CREME 96 ([Tylka et al., 1997](#)) and BON14 GCR models ([O'Neill et al., 2015](#)). The correction factors are given in columns 5 and 6 of Tab. S3 of supplementary material. Both models have comparable values, except for the factor of channel H1, which measures protons with energy of about 10 MeV. CREME96 suggests that about 95% of particles measured in H1 are protons, while this percentage for the BON14 is about 87%. This discrepancy is likely due to the different spectral shapes for protons below 10 MeV. CREME96 includes low-energy (solar) particles while BON14 only includes GCR protons (and heavier ions). Thus, the ratio of “true” protons in H1 to “background protons” is larger for CREME96 than for BON14.

We note that the contamination from GCR ions discussed above is negligible during SEP events because of the higher fluxes at low energies (softness of the spectra) and the higher proton abundance compared to heavier ions. However, the same contamination processes will affect the measurements, but to a different extent that depends on the exact spectra of the solar particles. Because the GCR-induced background is always present, we can subtract the background which was measured before the SEP event from the measurements taken during the event.

2.4 Detection of albedo protons

2.4.1 Measurement principle and response function

As alluded to in [Section 2.2](#) both downward and upward pointing particles contribute to the “penetrating” channels in the Xmas plot between columns 246 and 266 (panel (B) of [Figure 2](#)).

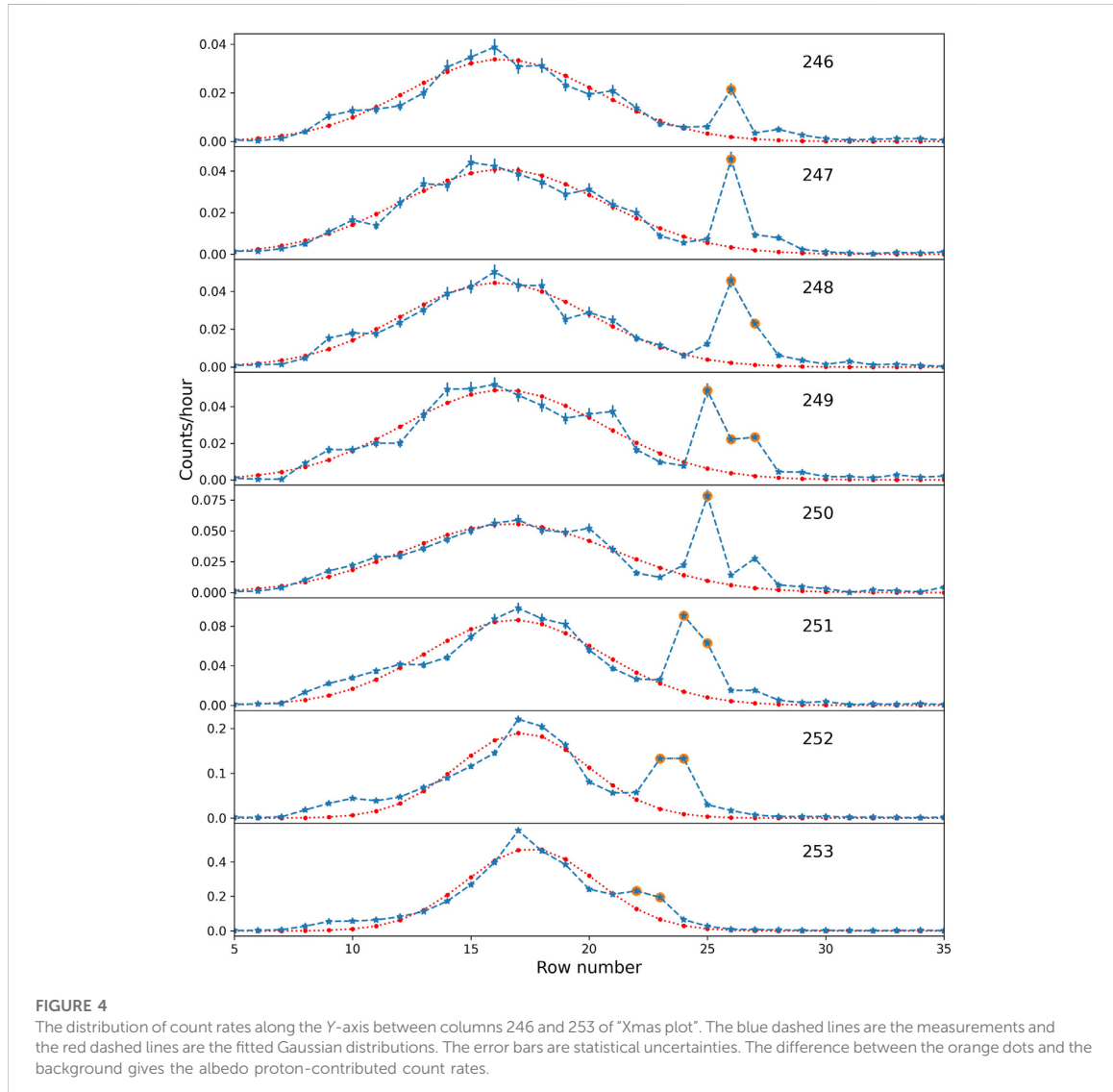
The extent of the y -axis shown covers penetrating protons and ^4He nuclei, heavier nuclei do not contribute to the region shown here.

The x and y axes in panel (B) of [Figure 2](#) are defined as $4 \cdot \log_2 (E_I/E_A) + 16$ and $4 \cdot \log_2 ((E_{B1} + E_C + E_D)/100)$ respectively, where E_I, E_A, E_C, E_D represent the total energy deposited in both the inner and outer segments of the corresponding detectors, and E_{B1} is the energy deposition in the inner segment of detector B. The row number is determined by the total energy deposited by particles in detectors B1, C, and D. The Bethe-Bloch equation ([Bethe, 1930](#); [Bloch, 1933](#)), $dE \propto \frac{Z^2}{ME^2}$, gives the energy deposited by particles in the silicon detectors; high-energy particles tend to deposit less energy than lower-energy particles (E less than ~ 1 GeV) and heavy ions deposit more energy than light elements due to their higher nuclear charge, Z . Therefore, in the Xmas plot, the row number of protons with high primary energy is smaller than the low energy proton, and the protons are at the bottom of the 2D histogram. ^4He and heavy ions are located above them.

The column number of a particle in the Xmas plot depends on the E_I to E_A ratio. Suppose particles in particular the minimum ionizing particles, deposit similar energy in the front detector A and the bottom detector I, i.e. $E_I \sim E_A$, particles will be placed in the middle column of the penetrating histogram, i.e., in column 256. When the particle deposit more energy in detector I than detector A ($E_I > E_A$), the quantities for the x -axis are larger than 256, and those particles will be added to the pixels in the right half of panel (B). On the other hand, if a particle deposits less in detector I than in detector A, it will be placed in the left half of panel (B). In principle, the former corresponds to particles moving downward, since particles first trigger detector A with larger incident energy and trigger I in the end with smaller incident energy after they lose their energy in the previous detectors, and the latter represents particles moving upward. Here we only focus on particles with energies of up to a few tens to a few hundred MeV/nuc and for which their average energy loss in silicon detectors decreases with the increased primary energy.

From simulations we thus determine the region marked in blue in panel (B) of upward-moving protons and calculate the corresponding geometry factor as shown in the panel (B) of [Figure 3](#). The energy range of this albedo proton channel is (64.7–76.7 MeV), with an average geometry factor of $0.18 \text{ cm}^2\text{sr}$ for an $dJ/dE \propto E^{-1}$ spectrum. The energy range is defined by the 10%-of-maximum criterion, and the uncertainty in these limits was estimated at the 5 and 10% of maximum and 90% to 95% of maximum levels. Given the steep flanks of this energy channel, these uncertainties are realistic.

Fortunately, our simulations show that the noise issue and the changes in LND configuration do not affect LND’s response to albedo protons. They are too much away from the affected region in the Xmas plot, as can be seen in panel (B) of [Figure 2](#).



2.4.2 Background subtraction

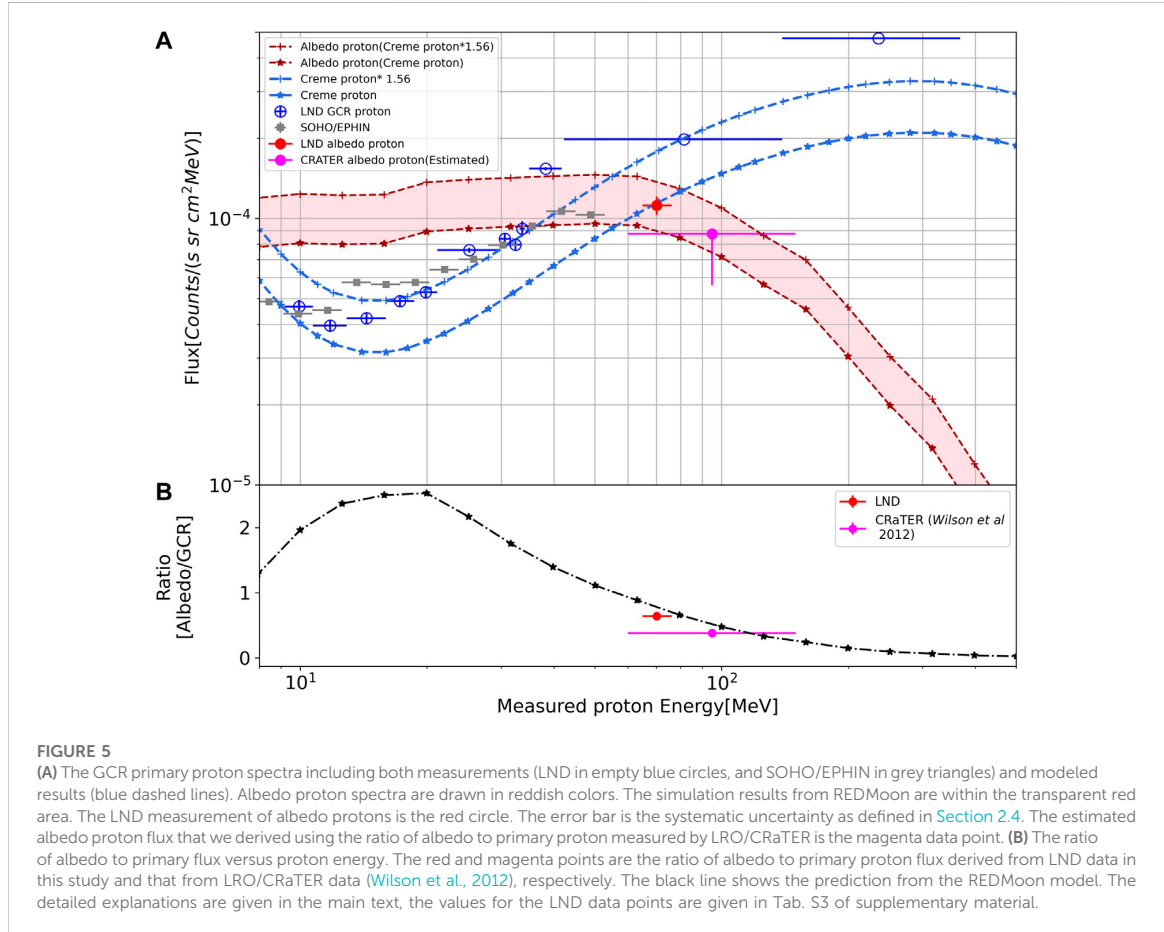
The count rates of albedo protons between 64.7 and 76.7 MeV in the Xmas plots are affected by a background which is caused by high-energy protons from both directions and needs to be subtracted. To better visualize this background, we plot the distributions of the count rates with statistical uncertainties as error bar along the Y-axis from columns 246 to 253 in the different panels of Figure 4. The blue dots are the averaged counts per hour in each pixel, and the orange dots are the count rates of albedo protons in the relevant pixels.

We model the background along the y -axis with a Gaussian distribution. The fitted results are plotted as red dashed lines in

Figure 4. Each panel is fitted separately with different parameters. Finally, the backgrounds of the albedo protons are estimated based on the fitted model and subtracted from the albedo proton data points (shown as orange data points) to determine the flux of albedo protons.

3 Measurements and comparison with model

Following the calibration processes mentioned before, we derived the averaged primary proton spectrum between 8 and



368 MeV and the averaged albedo proton flux between 64.7 and 76.7 MeV for the lunar days between June 2019 and July 2020, i.e., when LND was on. No solar energetic protons were observed by LND on the lunar surface.

3.1 GCR primary proton spectrum

The obtained LND GCR proton differential flux is plotted as empty blue circles in [Figure 5](#). The error bars in the x and y directions correspond to the widths of the energy bins and the flux uncertainty, respectively (The numerical values are also given in the last column of table S3 of appendix). The nine lowest energy channels (H1-H9) are the averages of the 1-min data products of stopping protons in the energy range between 9 and 35 MeV. The rightmost three proton channels (from left to right, H14, H11, H10) show the penetrating proton flux with energy above 35 MeV. The detailed information of

the bins is given in Table S3. We only show the statistical uncertainties of the differential flux. Since each channel accumulated a large number of particles during this 1-year measurement reported here, the statistical errors of each channel are small, especially for the penetrating channels. Hence the error bars of those three channels are almost invisible. Moreover, as we explained in [Section 2.3.3](#), the contamination caused by GCR ions has been subtracted.

Besides the measurements of LND, we also plot SOHO/EPHIN (grey square). SOHO/EPHIN provides measurements of protons with energies between 4.3 and 53 MeV. In this work, we use the EPHIN daily averaged level 3 proton fluxes derived from the PHA data according to the methods developed by [Kühl et al. \(2020\)](#). Those data have 16 energy bins provided by the SOHO/EPHIN team. The periods of EPHIN data are the same as those during which LND operated, i.e., to the times when Chang'E 4 was on during local lunar daytime. One sees that the proton spectrum drops in the energy channels above 50 MeV. As

TABLE 1 The ratio of lunar albedo protons to primary protons.

LND (64.7–76.7 MeV)	CRaTER (60–150 MeV)	simulation (65–76 MeV)	simulation (60–150 MeV)
2019–2020 64% \pm 7	2008–2009 38% \pm 2	2019 80%	2019 33%

explained by the EPHIN team, this change is unexpected and might not reflect the actual proton spectrum in space⁵. As shown in Figure 5, the GCR proton spectrum measured by LND agrees well with that measured by SOHO/EPHIN in the energy range below 40 MeV.

Moreover, we also compare the LND measurement of GCR protons with the CREME96 and BON14 cosmic ray models. CREME96 is a widely-used program that can simulate the ionizing-radiation environment in near-Earth space and predict the cosmic ray flux, based on the semi-empirical model of Nymmik et al. (1992). Their solar quiet model includes GCR, ACR, and a low-energy component below \sim 10 MeV that originates from the Sun and interplanetary space. Likewise, BON14 is based on GCR measurements from particle detectors and can predict the GCR variations related to solar modulation which is an input parameter of the model. In Figure 5, we only plot the CREME96 cosmic ray spectra of 2019 as dashed blue lines since the BON14 predicts a very similar proton flux during solar minimum. The lower curve is the original spectrum generated by the CREME website for this period. Obviously, the GCR model underestimates the proton flux at a few tens of MeV during solar minimum 24/25, and the measurement is about $48 \pm 2\%$ higher than the model spectra. This percentage is the averaged ratio between the measurement and the model. The comparison with BON14 leads to the same conclusion. Therefore, we multiplied the CREME spectrum by a factor of 1.56 for the limited energy range which fits the LND measurement best. This implies that the actual solar modulation during the solar minimum 24/25 may be weaker than the modulation used in numerical models. A similar disagreement between models and experimental data has been reported by Mrigakshi et al. (2012) during the solar minimum 23/24 and further discussed by Matthiä et al. (2013). They discuss that the averaged sunspot number is not an accurate predictor of GCR fluxes during solar minimum and show substantial differences between the GCR ISO model (ISO, 2004) (which is a later version of the Nymmik et al. (1992) model) and the BON model. In fact, solar modulation has been reported to be reduced in 2019–2020 and GCR intensities at 1 AU during this period reached the highest record in the space age (Fu et al., 2021).

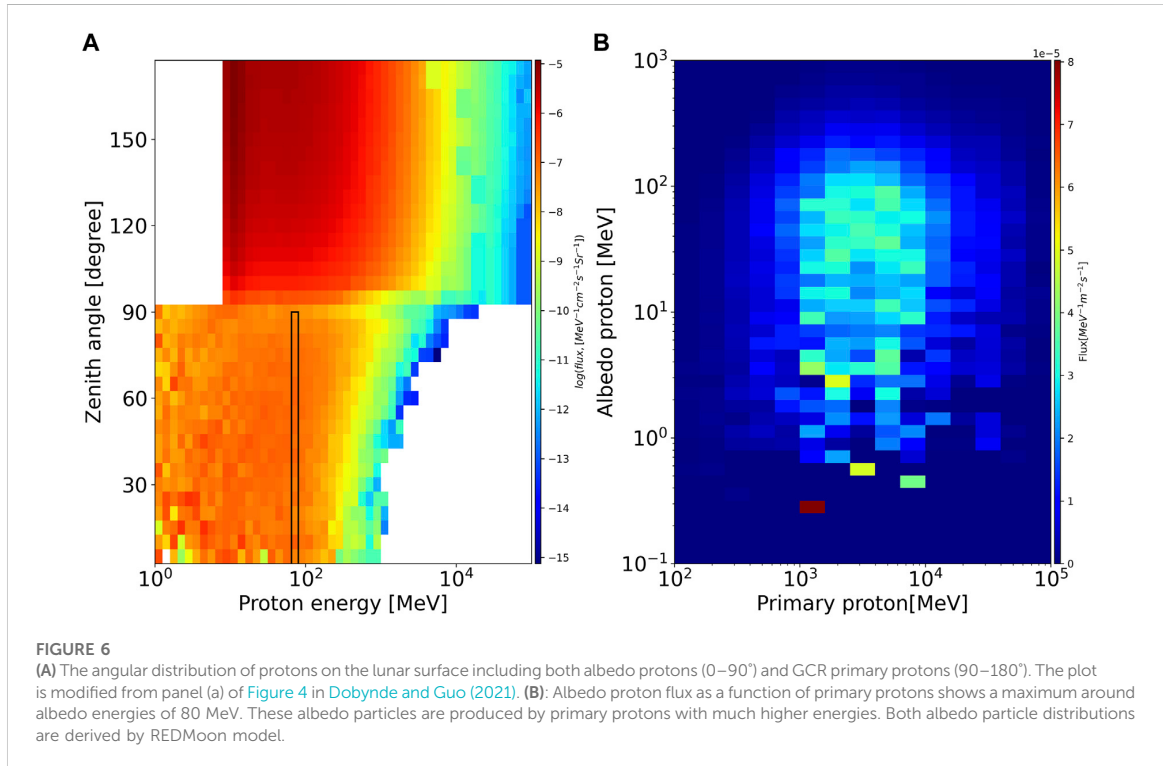
3.2 Albedo protons

As discussed in Section 2.4, LND can resolve albedo protons and determine their flux between 64.7 and 76.7 MeV. This is shown as the red circle in Figure 5 for the same time period as the GCR spectra. The background has been subtracted and the error of the flux is the resulting systematic uncertainty which is larger than the statistical error. The averaged flux at \sim 70.5 MeV is about $1.12 \pm 0.09 \times 10^{-4} (\text{cm}^2 \text{ s sr MeV})^{-1}$ which is remarkably close to the primary GCR proton flux measured by LND in this energy range. Albedo protons are the product of high-energy GCRs which interact with the lunar soil. A small fraction of the reaction products can escape from the soil and thus forms the albedo population. This interaction is modeled by the REDMoon code (Dobynde and Guo, 2021) which then predicts the lunar proton albedo as shown by the red lines in Figure 5 and discussed in the following paragraph.

Here the REDMoon model takes the CREME GCR model as input to calculate the angle- and energy-resolved surface particle flux on the Moon. The result for the time period reported here is given in Figure 6 which shows the isotropically distributed downward flux (zenith angle 90–180 deg) at the lunar surface in the upper half of the figure. The lower half shows the angle- and energy-resolved upward flux of (albedo) protons, the black rectangle marks the energy range which LND measures. The albedo protons are primarily due to GCR protons, but GCR helium and heavier ions contribute a small fraction. The REDMoon results shown as dashed red lines in Figure 5 were calculated with the unscaled CREME model as well as a CREME input spectrum scaled by a constant factor of 1.56, as discussed above. The region between these two model predictions is shaded in pink and represents the upward proton flux that is expected to be measured by LND. The decrease of the albedo protons flux at energy higher than \sim 100 MeV reflects that the generation efficiency of secondary particles drops with energy.

The lower panel of Figure 5 shows the ratio of upward (albedo) to downward (GCR) proton flux as derived by taking the ratio of REDMoon and CREME simulation results. Note that the ratio is the same for the scaled and non-scaled inputs of CREME spectra and that it is computed at the same energy of downward and upward propagating protons. The ratio peaks around 20 MeV, where the albedo protons are more than two times higher than the primary GCR protons in that energy range. Above it, the ratio drops as the GCR flux increases and the albedo flux decreases. The high ratio (> 1) is the consequence of the

⁵ P. Kühl, private communication, 2022



high-energy GCR making the main contribution to the low-energy albedo protons.

We determined the ratio of albedo protons to the primary protons in the energy range between 64.7 and 76.7 MeV, as measured by LND. The average primary proton flux is estimated from the scaled GCR spectrum that fits the LND measurements. We found that the ratio is about 0.64 ± 0.07 which means that the albedo protons are a significant contribution to the particle flux on the lunar surface in this energy range. Thus, about $39 \pm 6\%$ of all protons around 70 MeV are secondary albedo particles emitted from the lunar regolith. The second data point shown in magenta dots is the ratio reported by the CRaTER team ([Wilson et al., 2012](#)). The REDMoon simulation results agree well with the both the LND and CRATER measurements in their energy ranges.

The CRaTER data point was only reported by [Wilson et al. \(2012\)](#) as a ratio of the number of upward (albedo) protons to that of downward protons measured within the same FOV and the same energy range for both particle populations. They found a value of 0.38 ± 0.02 for this ratio which is different from the one reported by LND in this work. It is important to note that the CRaTER measurements are sensitive to a different energy range than LND, i.e., between 60 and 150 MeV (with an average energy higher than the LND-seen albedo protons) and were obtained between 2009 and

2011. This time period also corresponds to a solar minimum and we don't expect the ratio of upward to downward protons to depend strongly on the detailed differences in the two solar minima between solar cycles 23/24 and 24/25.

Primary (GCR) protons interact with the lunar surface and can produce the albedo population reported here. [Schwadron et al. \(2017\)](#) discuss the various generation mechanisms in more detail. The overall shape of the ratio of albedo to primary proton can be understood without sophisticated modeling: Albedo protons necessarily must have lost a significant part of their energy in the uppermost layers of the lunar regolith. Because the primary (GCR) proton flux increases with energy in and beyond the energy range covered by LND, the ratio of albedo/primary proton flux must decrease with energy. This simple explanation is supported by REDMoon model calculations and were also obtained by [Looper et al. \(2013\)](#) in their simulation of the radiation environment on the lunar orbiter of 50 km height. This also explains why the LND observations of the albedo to primary ratio is nearly two times higher than that of LRO/CRaTER. In [Table 1](#), we list the ratios of different cases, including the ratios from LND in 2019, CRaTER in 2009, and the ratio from the simulation averaged over different energy. We always use the GCR spectrum of 2019 as the input spectrum in the simulation. Ignoring the time difference, we can directly compare the simulation with

measurements in the same energy range. The modeled albedo to primary proton ratio averaged between in the LND energy range (65–76 MeV) is 0.8, which is slightly higher than LND's measurement, but the albedo flux falls within the pink shaded band in the upper panel. For CRaTER one needs to average the model over a wider energy range which is given by CRaTER's energy range. Thus folding the model function with the CRaTER energy range, we obtain a value of 0.33, which is comparable with the CRaTER's result.

Wilson et al. (2012) only report the albedo to primary proton ratio, but not the upward proton flux. This can easily be estimated by multiplying the scaled CREME model flux in the appropriate energy range with the reported albedo ratio and is shown as the magenta point in the upper panel of Figure 5. The albedo proton flux that is calculated using the original (unscaled) GCR spectrum can be taken as a lower limit. LND measurements, CRaTER measurements, and the REDMoon simulation are consistent within the reported uncertainties.

4 Summary, discussion and conclusion

We have performed and reported a careful re-analysis of the LND calibration. LND data in the energy range between 9 and 368 MeV agrees well with data from the SOHO/EPHIN instrument. LND data up to 35 MeV are for well-resolved protons stopping in LND's detector stack; the remaining three data points are for penetrating protons.

Furthermore, we compared LND's proton spectrum with the CREME96 GCR model. We find that the CREME96 predictions underestimate the proton flux during reported time period in the solar minimum 24/25. The average ratio between LND measurements and the CREME96 model predictions is $\sim 1.48 \pm 0.02$. This may be due to the much weaker solar modulation during the deep solar minimum 24/25. In fact, GCR intensities at one au during this time period reached the highest recorded fluxes in the space age (Fu et al., 2021).

With its stack of 10 silicon detectors, LND is capable of measuring both the downward as well as the upward proton flux. Such albedo protons are the result of the interaction of high-energy GCR particles with the lunar regolith. The bulk of the albedo particles is created by the high-energy portion of the primary GCR protons, as shown in the right hand panel of Figure 6. This part of the GCR spectrum is less affected by solar modulation than the low-energy part. Therefore, when considering the effect of solar modulation on the ratio of upward to downward particles one needs to consider that this ratio is calculated at the same primary energy of the upward and downward-pointing particles. Because the low-energy part of the GCR

spectrum is strongly affected by solar modulation, the up/down ratio is primarily affected by the low-energy downward flux and much less so by the upward flux which is primarily determined by the high-energy downward-pointing flux, as reported by Wilson et al. (2012). This effect is especially important during solar particle events. Comparing the measured upward to downward differential fluxes we find a ratio of 0.64 ± 0.07 in the energy range between 64.7–76.7 MeV. This ratio is shown as the red data point in the lower panel of Figure 5. Because of the additional shielding from beneath provided by the Chang'E 4 lander, the energy ranges resolved by LND differ for the upward and downward particle populations. Furthermore, we scaled the upward to downward flux ratio reported by the CRaTER team using data prior to solar minimum 23/24 to the time period investigated here. We used the scaled CREME96 downward flux to determine the upward flux expected in the CRaTER energy range. The resulting upward flux (shown as the magenta data point in the lower panel of Figure 5) agrees well with LND's measurement and the REDMoon predictions, despite being valid for a different energy range (60–150 MeV).

As already stated, the REDMoon simulation tool provides the upward (albedo) differential proton flux. We compare the REDMoon model results with the downward flux from the scaled CREME96 model to derive the ratio of upward to downward differential flux shown as the dash-dotted line in the lower panel of Figure 5. At energies below ~ 50 MeV, the ratio is above one and it has a peak value above two near 20 MeV. With increasing energy, the ratio decreases as the generation of albedo protons at this energy decreases. We observe that the modeled energy dependence of the albedo proton flux is confirmed by the combination of the LND and (scaled) CRaTER data.

LND is the first high-energy charged-particles telescope to be working on the lunar surface. We have presented measurements of low-energy cosmic ray protons in conjunction with albedo protons and that the latter contribute significantly to the particle flux on the lunar surface. We also show that the albedo proton flux is energy dependent, and that both primary and albedo proton fluxes are in good agreement with measurements from LRO/CRaTER. Obviously, due to their high flux and relatively low energy, albedo protons are an important contribution to the radiation to which astronauts would be exposed to on the surface of the Moon. Albedo protons are energetic enough to penetrate a space suit and have sufficiently low energy to stop in the body of an astronaut, thus depositing all their energy in the astronaut's tissue. The Sun is now becoming more active and future data from large solar particle events will be critical to understand their effect on the lunar radiation environment and its effect on human exploration of the Moon.

Data availability statement

The original contributions presented in the study are included in the article/supplementary materials, further inquiries can be directed to the corresponding authors.

Author contributions

ZX led the data analysis and paper writing. RW-S and JG advised on the data analysis and improved the paper writing. MD provided the simulation data of the REDMoon model, and PK offered SOHO/EPHIN data. SK and SZ provided valuable information and suggestions. All authors read the paper and approved its submission.

Funding

The Lunar Lander Neutron and Dosimetry (LND) instrument was funded by the German Space Agency, DLR, and its space Administration under grant 50 JR 1604 to the Christian-Albrechts-University (CAU) Kiel as well as the Beijing Municipal Science and Technology Commission (grant no. Z181100002918003) and NSFC (grant no. 41941001). JG and MD are supported by the Strategic Priority Program of the Chinese Academy of Sciences (Grant No. XDB41000000) and the National Natural Science Foundation of China (Grant No. 42074222, 41941001). We acknowledge financial support by Land Schleswig-Holstein within the funding programme Open Access Publikationsfonds.

References

- Agostinelli, S., Allison, J., Amako, K., Apostolakis, J., Araujo, H., Arce, P., et al. (2003). GEANT4 - a simulation toolkit. *Nucl. Instrum. Methods Phys. Res. Sect. A Accel. Spectrom. Detect. Assoc. Equip.* 506, 250–303. doi:10.1016/S0168-9002(03)01368-8
- Appel, J. K., Köehler, J., Guo, J., Ehresmann, B., Zeitlin, C., Matthiä, D., et al. (2018). Detecting upward directed charged particle fluxes in the Mars science laboratory radiation assessment detector. *Earth Space Sci.* 5, 2–18. doi:10.1002/2016EA000240
- Berger, T., Matthiä, D., Burmeister, S., Zeitlin, C., Rios, R., Stoffle, N., et al. (2020). Long term variations of galactic cosmic radiation on board the International Space Station, on the Moon and on the surface of Mars. *J. Space Weather Space Clim.* 10, 34. doi:10.1051/swsc/2020028
- Bethe, H. A. (1930). Zur Theorie des Durchgangs schneller Korpuskularstrahlen durch Materie. *Ann. Phys.* 5, 325–400. doi:10.1002/andp.19303970303
- Bloch, F. (1933). Zur Bremsung rasch bewegter Teilchen beim Durchgang durch Materie. *Ann. Phys.* 16, 285–320. doi:10.1002/andp.19334080303
- Cucinotta, F. A., and Chappell, L. J. (2011). Updates to astronaut radiation limits: Radiation risks for never-smokers. *Radiat. Res.* 176, 102–114. doi:10.1667/RR2540.1
- Dobynne, M. I., and Guo, J. (2021). Radiation environment at the surface and subsurface of the moon: Model development and validation. *JGR Planets* 126, e06930. doi:10.1029/2021JE006930
- Dorman, L. I. (2004). Cosmic rays in the earth's atmosphere and underground. *Cosmic Rays Earth's Atmos. Undergr.* 303. doi:10.1007/978-1-4020-2113-8
- Fu, S., Zhang, X., Zhao, L., and Li, Y. (2021). Variations of the galactic cosmic rays in the recent solar cycles. *Astrophys. J. Suppl. Ser.* 254, 37. doi:10.3847/1538-4365/abf936
- Guo, J., Banjac, S., Röstel, L., Terasa, J. C., Herbst, K., Heber, B., et al. (2019). Implementation and validation of the GEANT4/AtRIS code to model the radiation environment at Mars. *J. Space Weather Space Clim.* 9, A2. doi:10.1051/swsc/2018051
- Hassler, D. M., Zeitlin, C., Wimmer-Schweingruber, R. F., Böttcher, S., Martin, C., Andrews, J., et al. (2012). The radiation assessment detector (RAD) investigation. *Space Sci. Rev.* 170, 503–558. doi:10.1007/s11214-012-9913-1
- ISO, I. (2004). *Space environment (natural and artificial)-galactic cosmic ray model*. Geneva, Switzerland: International Organization for Standardization, 15390.
- Kühl, P., Heber, B., Gómez-Herrero, R., Malandraki, O., Posner, A., and Sierks, H. (2020). The electron proton helium INstrument as an example for a space weather radiation instrument. *J. Space Weather Space Clim.* 10, 53. doi:10.1051/swsc/2020056
- Looper, M. D., Mazur, J. E., Blake, J. B., Spence, H. E., Schwadron, N. A., Golightly, M. J., et al. (2013). The radiation environment near the lunar surface: Crater observations and geant4 simulations. *Space weather.* 11, 142–152. doi:10.1002/swe.20034
- Matthiä, D., Berger, T., Mrigakshi, A. I., and Reitz, G. (2013). A ready-to-use galactic cosmic ray model. *Adv. Space Res.* 51, 329–338. doi:10.1016/j.asr.2012.09.022
- McKinney, G. W., Lawrence, D. J., Prettyman, T. H., Elphic, R. C., Feldman, W. C., and Hagerty, J. J. (2006). MCNPX benchmark for cosmic ray interactions with the Moon. *J. Geophys. Res.* 111, E06004. doi:10.1029/2005JE002551
- Mitrofanov, I. G., Sanin, A. B., and Litvak, M. L. (2016). Water in the Moon's polar areas: Results of LEND neutron telescope mapping. *Dokl. Phys.* 61, 98–101. doi:10.1134/S1028335816020117

Acknowledgments

We thank the two reviewers for their thorough reviews which helped to improve this paper and the many individuals who were involved in conceiving, designing, building, testing, and launching LND and Chang'E 4.

Conflict of interest

The authors declare that the research was conducted in the absence of any commercial or financial relationships that could be construed as a potential conflict of interest.

Publisher's note

All claims expressed in this article are solely those of the authors and do not necessarily represent those of their affiliated organizations, or those of the publisher, the editors and the reviewers. Any product that may be evaluated in this article, or claim that may be made by its manufacturer, is not guaranteed or endorsed by the publisher.

Supplementary Material

The Supplementary Material for this article can be found online at: <https://www.frontiersin.org/articles/10.3389/fspas.2022.974946/full#supplementary-material>

- Mrigakshi, A. I., Matthiä, D., Berger, T., Reitz, G., and Wimmer-Schweingruber, R. F. (2012). Assessment of galactic cosmic ray models. *J. Geophys. Res.* 117, A08109. doi:10.1029/2012JA017611
- Müller-Mellin, R., Kunow, H., Fleißner, V., Pehlke, E., Rode, E., Röschmann, N., et al. (1995). Costep-comprehensive suprathermal and energetic particle analyser. *Sol. Phys.* 162, 483–504. doi:10.1007/bf00733437
- Nyrmik, R., Panasyuk, M., Pervaja, T., and Suslov, A. (1992). A model of galactic cosmic ray fluxes. *Int. J. Radiat. Appl. Instrum. Part D. Nucl. Tracks Radiat. Meas.* 20, 427–429. Special Section Galactic Cosmic Radiation: Constraints on Space Exploration. doi:10.1016/1359-0189(92)90028-T
- O'Neill, P., Golge, S., and Slaba, T. (2015). Badhwar-O'Neill 2014 galactic cosmic ray flux model description. *Tech. Rep.*
- Schwadron, N. A., Wilson, J. K., Jordan, A. P.,Looper, M. D., Zeitlin, C., Townsend, L. W., et al. (2017). Using proton radiation from the moon to search for diurnal variation of regolith hydrogenation. *Planet. Space Sci.* 162, 113–132. doi:10.1016/j.pss.2017.09.012
- Schwadron, N. A., Wilson, J. K.,Looper, M. D., Jordan, A. P., Spence, H. E., Blake, J. B., et al. (2016). Signatures of volatiles in the lunar proton albedo. *Icarus* 273, 25–35. doi:10.1016/j.icarus.2015.12.003
- Spence, H. E., Case, A. W., Golightly, M. J., Heine, T., Larsen, B. A., Blake, J. B., et al. (2010). Crater: The cosmic ray telescope for the effects of radiation experiment on the lunar reconnaissance orbiter mission. *Space Sci. Rev.* 150, 243–284. doi:10.1007/s11214-009-9584-8
- Spence, H. E., Golightly, M. J., Joyce, C. J.,Looper, M. D., Schwadron, N. A., Smith, S. S., et al. (2013). Relative contributions of galactic cosmic rays and lunar proton “albedo” to dose and dose rates near the moon. *Space weather.* 11, 643–650. doi:10.1002/2013SW000995
- Treiman, S. B. (1953). The cosmic-ray albedo. *Phys. Rev.* 91, 957–959. doi:10.1103/PhysRev.91.957
- Tylka, A. J., Adams, J. H., Boberg, R., Brownstein, B., Dietrich, W. F., Flueckiger, E. O., et al. (1997). CREME96: A revision of the cosmic ray effects on micro-electronics code. *IEEE Trans. Nucl. Sci.* 44, 2150–2160. doi:10.1109/23.659030
- Wilson, J. K., Spence, H. E., Kasper, J., Golightly, M., Blake, J. B., Mazur, J. E., et al. (2012). The first cosmic ray albedo proton map of the moon. *J. Geophys. Res.* 117, 1–7. doi:10.1029/2011JE003921
- Wimmer-Schweingruber, R. F., Yu, J., Böttcher, S. I., Zhang, S., Burmeister, S., Lohf, H., et al. (2020). The lunar lander neutron and Dosimetry (LND) experiment on chang'E 4. *Space Sci. Rev.* 216, 104. doi:10.1007/s11214-020-0725-3
- Xu, Z., Guo, J., Wimmer-Schweingruber, R. F., Freiherr von Forstner, J. L., Wang, Y., Dresing, N., et al. (2020). First solar energetic particles measured on the lunar far-side. *Astrophys. J. Lett.* 902, L30. doi:10.3847/2041-8213/abbccc
- Zhang, S., Wimmer-Schweingruber, R. F., Yu, J., Wang, C., Fu, Q., Zou, Y., et al. (2020). First measurements of the radiation dose on the lunar surface. *Sci. Adv.* 6, eaaz1334. doi:10.1126/sciadv.aaz1334

Supplementary Material

1 CHANGES OF THE LND CONFIGURATION

Tab.S1 lists the changes to the LND configuration which were made on the 3rd, 4th, 5th, and 9th lunar day (counted from the landing of Chang'E 4). An unforeseen sudden drop in temperature caused mechanical stresses in detectors A, H, I, and J which unfortunately resulted in an increased noise level of these detectors. This necessitated changes 1 - 3 presented below. Furthermore, we updated the onboard software to improve the response to the highest-energy stopping protons as is discussed in bullet 4 beneath. Point 5 below discusses how the LND firmware accumulates data into DPS boxes. Because these had to be defined before LND could be fully calibrated, they are not placed optimally for heavy ions.

Table S1. L1 threshold Changes history of LND (upper) and other configuration changes (bottom).

Lunar day	A2H	H2	I1H	I2H	J1
3rd	200 keV	42 keV	96 keV	300 keV	128 keV
4th	400 keV				
9th		300 keV			
5th	Disable A2 in L3 logics: LET and charged particles		Raise L3 threshold of detector I from 50 keV to 400 keV		

1. The stress-induced increase in the noise level of the affected detector segments were partially compensated by adjusting the thresholds of the affected segments, as shown in Tab. S1.
2. We disabled the A2 channel in the L3 logic of LET and stopping particles to further reduce the impact of the increased noise on the LET spectra. LND triggers on the B detector which is also used for determining the LET spectrum. If the signal in detector A is also above threshold, then the appropriate LET channel is augmented. Thus the increased noise in A2 resulted in a corrupted LET spectrum which was fixed by disabling the A2 channel in the L3 logic. Disabling A2 in the level-3 logic dramatically changed the geometry factors and path length of LET spectra. An updated version of Table 4 in (Wimmer-Schweingruber et al., 2020) regarding the parameter of various LET spectra is given in Tab. S2
3. In the fifth lunar day we uploaded commands to raise the threshold of detector I in L3 trigger logic from 50 keV to 400 keV. The data products of penetrating particle were changed mostly as shown in panel (b) of Fig. 2, since we filtered many minimum ionizing protons that deposited

Det.	# bins	$\langle L \rangle$ [μm]	\hat{L} [μm]	$\text{var}(L)$ [μm]	g [mm^2sr]
1 $A \cdot B \cdot C \cdot I$	64	523	523	54	33
2 $\bar{A} \cdot B \cdot I \cdot J$	64	615	588	14896	2098
3 $A \cdot B \cdot I \cdot J$	8×64	511	513	1178	79
4 $2 \cup 3 \approx B \cdot J$	64	611	584	14774	2177
5 $1 \cup 3 \approx A \cdot B$	64	514	515	881	112

Table S2. Properties of the various LET spectra after disabling A2 in LND. This is thus an updated version of Table 4 in Wimmer-Schweingruber et al. (2020)

energy less than 400 keV in detector I. These missing particles mainly populate in the left half of penetrating panels of Xmas plots in DPS box H12 and H10. Luckily the detector response of the albedo particles, which are also in the left half, did not change as its energy deposition in the front detectors are much higher than the level 3 threshold of detector I.

4. Protons stopping in the I detector deposit different energy in it than our initial simulations had predicted. This means that the H9 DPS box is not correctly placed and therefore only has a reduced geometry factor compared to the analytical value of $0.275 \text{ cm}^2\text{sr}$. The correct value is given in Tab. S3.
5. Because of an error in the calculation of the locations of the DPS boxes for heavy ions they do not reflect the real positions of heavy ions in the Xmas plot. Thus, the DPS heavy ions should not be used for analysis. Also, because of the very low fluxes of heavy ions, the better time resolution of the DPS boxes of heavy ions is not needed and the data provided by the Xmas plot (at 1 hour time resolution) is more than adequate. The positions of the DPS boxes have not been corrected.

Those changes in the LND configuration were successful in salvaging the primary data products of LND. The quality of LND's data continues to be excellent thanks to the redundant design of LND.

2 UPDATED RESPONSE FUNCTIONS FOR PROTONS

Figure 3 (a) shows the geometry factors for the different DPS channels. The lower and upper limits in energy of the proton DPS boxes are fairly sharp for stopping particles (DPS boxes H1 - H9), but are not as clearly delineated for penetrating particles, as is to be expected. In other words, the geometry factors are not purely geometric quantities, but energy dependent response functions. We give the updated boundaries at the 50%-level (a kind of FWHM) in the second column of Tab. S3. For the lowest energy bin (H1), we used the 10%-level for the lower boundary, for H10 we used the 10% boundary for the upper limit.

Because of the sometimes broad energy response (e.g., for H10 or H11) variations of the primary particle spectrum will result in different counts rates in these DPS channels even if the total number of particles remains the same. The count rate is determined by integrating the product of the geometry factor and the primary particle spectrum. This results in a small, but in some cases non-negligible variation of the geometry factor. This is shown in columns three and four of Tab. S3 for a logarithmically flat (power-law exponent $\gamma = -1$) and the solar-minimum 24/25 CREME96 model. The calculation was performed as shown in eq. S1,

$$\bar{G} = \frac{\int_0^{inf} f(E) g dE}{\int_{E_{min}}^{E_{max}} f(E) dE}, \quad (\text{S1})$$

where $f(E)$ is the input spectrum and the g are the (energy-dependent) geometry factors as shown in Fig. 3 (a).

Fig. 2 (a) shows that the proton DPS boxes are contaminated (primarily) by heavier ions. We account for this by a fixed correction factor for each DPS channel which is given in columns 5 and 6 for the CREME96 and BON14 models (again computed for solar minimum 24/25). These corrections can be substantial for some channels, as can be seen in the table.

The last column of Tab. S3 gives the numerical values of the LND data points shown in Fig. 5 together with their uncertainties.

Table S3. Weighted geometry factors and energy bins of primary and albedo protons, correction factors caused by other particles for CREME96 and BON14 case, and the averaged GCR and albedo proton fluxes.

Name	Energy(MeV)	GF($cm^2 sr$) ($\gamma = -1$)	GF($cm^2 sr$) (CREME)	Correction (CREME)	Correction (BON14)	GCR Flux ($cm^2 sr s Mev$) $^{-1}$
H1	9.18, 10.73	0.29	0.30	0.95	0.87	$4.66 \pm 0.28 \times 10^{-5}$
H2	10.73, 12.90	0.28	0.31	0.97	0.94	$3.96 \pm 0.21 \times 10^{-5}$
H3	12.90, 15.96	0.29	0.32	0.96	0.94	$4.22 \pm 0.18 \times 10^{-5}$
H4	15.96, 18.65	0.27	0.27	0.98	0.97	$4.90 \pm 0.23 \times 10^{-5}$
H5.	18.65, 21.17	0.26	0.28	0.97	0.96	$5.29 \pm 0.24 \times 10^{-5}$
H6.	21.17, 29.73	0.27	0.28	0.96	0.96	$7.60 \pm 0.15 \times 10^{-5}$
H7	29.73, 31.50	0.28	0.27	0.98	0.97	$8.38 \pm 0.37 \times 10^{-5}$
H8	31.50, 33.36	0.25	0.29	0.82	0.78	$7.96 \pm 0.34 \times 10^{-5}$
H9	33.17, 34.14	0.17	0.20	0.79	0.76	$9.13 \pm 0.61 \times 10^{-5}$
H10	139.2, 368.4	0.11	0.095	0.98	0.98	$4.74 \pm 0.01 \times 10^{-4}$
H11	42.3, 139.2	0.28	0.30	0.36	0.35	$1.98 \pm 0.01 \times 10^{-4}$
H14	34.94, 41.76	0.28	0.35	0.75	0.72	$1.54 \pm 0.02 \times 10^{-4}$
Albedo	64.7, 76.7	0.18	-	-	-	$1.12 \pm 0.09 \times 10^{-4}$

REFERENCES

Wimmer-Schweingruber, R. F., Yu, J., Böttcher, S. I., Zhang, S., Burmeister, S., Lohf, H., et al. (2020). The Lunar Lander Neutron and Dosimetry (LND) Experiment on Chang'E 4. Space Science Reviews 216, 104. doi:10.1007/s11214-020-00725-3

QUIET-TIME LOW ENERGY ION SPECTRA OBSERVED ON SOLAR ORBITER DURING SOLAR MINIMUM

With the launch of the Solar Orbiter (SolO) on February 10, 2020, we have further expanded our measurement ability of energetic particles in the new era of space observations and the inner heliosphere. This is achieved by the Energetic Particle Detector (EPD) onboard SolO, measuring particles in the energy range over several orders of magnitude from keV to GeV.

In the first year of its mission, SolO has observed numerous events and structures associated with solar eruptions. Gómez-Herrero et al. (2021) reported the first near-relativistic solar electron events observed by EPD on July 2020. The solar origin and the interplanetary transport condition of those particles are investigated. Later, Kollhoff et al. (2021) analyzed the first widespread solar energetic particle (SEP) of Solar Cycle (SC) 25 that occurred on November 29, 2020. Mason et al. (2021c) analyzed the heavy ion properties of this event. Besides, Mason et al. (2021a) reported the observations of five impulsive SEPs during the first perihelion movement of SolO. Those events have low intensity and are undetectable at one au, indicating the special advantage of SolO and PSP in the inner heliosphere. Furthermore, SolO also observed the energetic particles associated with the corotating interaction regions (CIRs) (Allen et al., 2021b), stream interaction regions (SIRs) (Aran et al., 2021) and an interplanetary coronal mass ejections (ICMEs) (Kilpua et al., 2021).

Additionally, the second half of the solar activity minimum provides a valuable quiet period in 2020. This period is characterized by the absent or rare occurrence of SEPs, interplanetary shocks, and other related activities, apart from the above-mentioned events. Therefore, studying the ion spectra and their variation in the inner heliosphere during this period is an excellent opportunity to understand anomalous cosmic rays (ACRs), galactic cosmic rays (GCRs), and properties of quiet time spectra. This work attempts to answer the first two questions we asked in Sec. 1.2: "How do the ACRs and GCR behave during the most recent solar activity minimum and the onset phase of solar cycle 25?" and "What is the difference between the current solar cycle and the previous one?"

The overview of the publication

Below we list the main observations from Mason et al. (2021b).

- The quiet-time ion spectra observed by the Suprathermal Ion Spectrograph (SIS) and the High Energy Telescope (HET) during the solar minimum between Feb 2020 and Jan 2021 are shown. The spectra are comprised of protons, helium-4, helium-3, oxygen, carbon, and iron and include ACRs, GCRs, and lower energy particles from impulsive SEP. The energy range spans a few tens of keV/nuc - \sim GeV/nuc,

- Super-quiet periods are defined, and the corresponding spectra are derived. The overall shape and intensity are similar to the quiet time spectra except that the lower energy helium-4 spectrum extends to ~ 300 keV/nuc before the intensity rises.
- The radial dependence of 4.4 Mev/nuc He and O during this period was first derived. The gradient has considerable uncertainty but is consistent with a positive small O gradient.

The following article is reproduced from Mason et al. (2021b) with permission from *Astronomy & Astrophysics*, ©ESO:

QUIET-TIME LOW ENERGY ION SPECTRA OBSERVED ON SOLAR ORBITER DURING SOLAR MINIMUM

Mason, G. M., G. C. Ho, R. C. Allen, **Z. G. Xu**, N. P. Janitzek, J. L. Freiherr von Forstner, A. Kohllhoff, D. Pacheco, J. Rodríguez-Pacheco, R. F. Wimmer-Schweingruber, G. Bruce Andrews, C. E. Schlemm, H. Seifert, K. Tyagi, W. J. Lees, J. Hayes, R. Gómez-Herrero, M. Prieto, S. Sánchez-Prieto, F. Espinosa Lara, I. Cernuda, P. Parra Espada, O. Rodríguez Polo, A. Martínez Hellín, C. Martin, S. Böttcher, L. Berger, J. C. Terasa, S. Boden, S. R. Kulkarni, A. Ravanbakhsh, M. Yedla, S. Eldrum, R. Elftmann, and P. Kühl, *Astronomy & Astrophysics*, 656, page L5 (2021), doi: 10.1051/0004-6361/202140540

Own contribution: 25%

LETTER TO THE EDITOR

Quiet-time low energy ion spectra observed on Solar Orbiter during solar minimum

G. M. Mason¹, G. C. Ho¹, R. C. Allen¹, Z. G. Xu², N. P. Janitzek³, J. L. Freiherr von Forstner², A. Kohlhoff², D. Pacheco², J. Rodríguez-Pacheco⁴, R. F. Wimmer-Schweingruber², G. Bruce Andrews¹, C. E. Schlemm¹, H. Seifert¹, K. Tyagi^{1,5}, W. J. Lees¹, J. Hayes¹, R. Gómez-Herrero⁴, M. Prieto⁴, S. Sánchez-Prieto⁴, F. Espinosa Lara⁴, I. Cernuda⁴, P. Parra Espada², O. Rodríguez Polo⁴, A. Martínez Hellín², C. Martín^{2,6}, S. Böttcher², L. Berger², J. C. Terasa², S. Boden^{2,7}, S. R. Kulkarni^{2,8}, A. Ravanbakhsh^{2,9}, M. Yedla^{2,9}, S. Eldrum², R. Elftmann², and P. Kühl²

¹ Johns Hopkins Univ. Applied Physics Laboratory, Laurel, MD, USA
e-mail: glenn.mason@jhuapl.edu

² Institut für Experimentelle und Angewandte Physik, Christian-Albrechts-Universität zu Kiel, Kiel, Germany

³ ESA-ESAC, Madrid, Spain European Space Agency (ESA/ESAC), Villafranca del Castillo, 28692 Madrid, Spain

⁴ Space Research Group, Universidad de Alcalá, Alcalá de Henares, Spain

⁵ Now at Univ. Colorado/LASP, Boulder, CO, USA

⁶ Now at: German Aerospace Center (DLR), Dept. of Extrasolar Planets and Atmospheres, Berlin, Germany

⁷ Now at: DSI Datensicherheit GmbH, Rodendamm 34, 28816 Stuhr, Germany

⁸ Now at: Deutsches Elektronen-Synchrotron (DESY), Platanenallee 6, 15738 Zeuthen, Germany

⁹ Now at: Max-Planck-Institute for Solar System Research, Justus-von-Liebig-Weg 3, 37077 Göttingen, Germany

Received 11 February 2021 / Accepted 16 March 2021

ABSTRACT

Context. The Solar Orbiter spacecraft cruised in the inner heliosphere during Feb. 2020 – Jan. 2021, moving between \sim 0.5–1.0 au radial distance. The Energetic Particle Detector suite operated continuously during this period.

Aims. The Suprathermal Ion Spectrograph and High Energy Telescope observations made during intervals in between transient intensity increases were used to determine the low energy ion spectra and composition during quiet times.

Methods. Energetic particle spectra and major ion components, including ^3He , were measured over the range \sim 0.1–100 MeV nucleon $^{-1}$. The radial dependence of 4.4 MeV nucleon $^{-1}$ ^4He and O was measured. A short interval of extremely low intensities (“super-quiet”) was also studied.

Results. Spectra measured during the quiet period showed transitions, including galactic cosmic rays (> 50 MeV nucleon $^{-1}$), anomalous cosmic rays (a few to \sim 50 MeV nucleon $^{-1}$), and a steeply rising “turn-up” spectrum below a few MeV nucleon $^{-1}$ whose composition resembled impulsive, ^3He -rich solar energetic particle events. The radial dependence had large uncertainties but was consistent with a small gradient. During the super-quiet interval, the higher energy components remained similar to the quiet period, while the approximately flat low energy ^4He spectrum extended downward, reaching \sim 300 keV nucleon $^{-1}$ before transitioning to a steeply rising spectrum.

Key words. acceleration of particles – Sun: abundances – Sun: particle emission – interplanetary medium – cosmic rays

1. Introduction

During so-called quiet periods when transient solar particle events, interplanetary shocks, and other activity is absent, low energy ion spectra in the interplanetary medium near 1 au are formed of three components, as illustrated in Fig. 1: From high energy to low energy, these are galactic cosmic rays (GCRs), anomalous cosmic rays (ACRs), and a “turn-up” spectrum below a few MeV nucleon $^{-1}$ that increases with decreasing energy. While the GCRs and ACRs vary with solar cycle timescales, the turn-up spectrum is variable on shorter timescales and may be dominated by remnant solar energetic particles, stream interaction, and shock-accelerated particles, as well as more local sources such as comets or planetary upstream magnetospheric

events (e.g., overviews by Klecker et al. 1977; Reames 1999; Desai et al. 2008; Dayeh et al. 2009; Mason & Gloeckler 2011).

Anomalous cosmic rays originate from interstellar neutrals entering the outer heliosphere, followed by ionization and acceleration that is presumably in association with the termination shock, and penetrate into the inner heliosphere where their intensity is reduced by solar modulation (e.g., Klecker 1999; Cummings et al. 2002; McComas & Schwadron 2006). Although well studied at 1 au and beyond, there have been very few observations of ACRs inside 1 au. Solar Orbiter offers the opportunity to study this component in detail inside Earth’s orbit.

The variable turn-up spectrum at low energies has been investigated to ascertain whether these particles have a solar origin or are modulated GCRs (Krimigis et al. 1973; Zamow 1975),

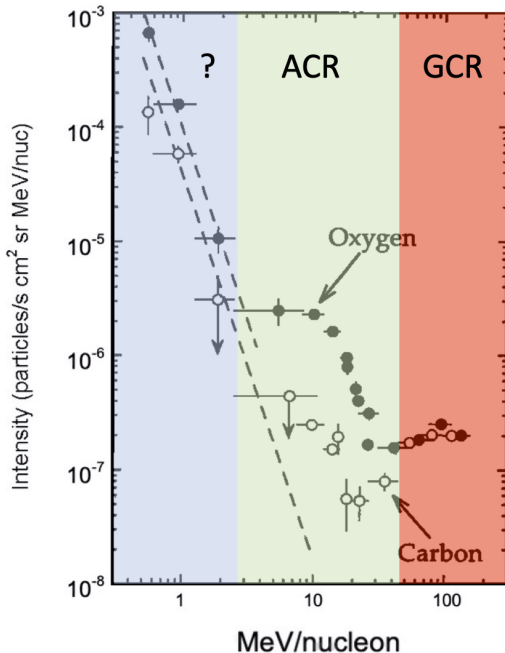


Fig. 1. Quiet-time energy spectra observed near solar minimum at 1.0 au on the Solar, Anomalous, and Magnetospheric Particle Explorer (SAM-PEX) satellite in 1992–1993; colored shading approximately separates three energy regimes and their associated spectra. *Left:* low energy “turn-up” spectra of undetermined origin. *Center:* anomalous cosmic ray O and C. *Right:* modulated GCRs. The figure is adapted from Mewaldt et al. (1993).

accelerated solar wind, or some other steady emission from the Sun (Fisk & Gloeckler 2006; Mason & Gloeckler 2011). Characterizing this population is important for determining the characteristics of the inner heliosphere suprathermal ion pool, which provides an important seed population for energetic particles energized by interplanetary shocks (Kahler & Ling 2019). Solar Orbiter has the potential to distinguish between different models for this component by determining, for example, whether it is more or less intense closer to the Sun or at latitudes off the ecliptic plane. In this Letter we present the first observations from Solar Orbiter that address these questions.

2. Observations

The particle observations reported here were made on the Solar Orbiter spacecraft (Müller et al. 2020) with the Suprathermal Ion Spectrograph (SIS) and High Energy Telescope (HET) which are part of the Energetic Particle Detector (EPD) suite (Rodríguez-Pacheco et al. 2020). The SIS is a time-of-flight mass spectrometer that measures ion composition from ~ 0.1 – 10 MeV nucleon $^{-1}$, and HET is a dE/dx versus E telescope that measures particle composition from ~ 10 to several hundred MeV nucleon $^{-1}$. For the SIS observations, the background was suppressed by requiring consistency between the instrument’s two independent mass measurements.

2.1. Selection of time intervals

The definition of quiet time at energies below a few MeV nucleon $^{-1}$ is subjective because there is no identifiable

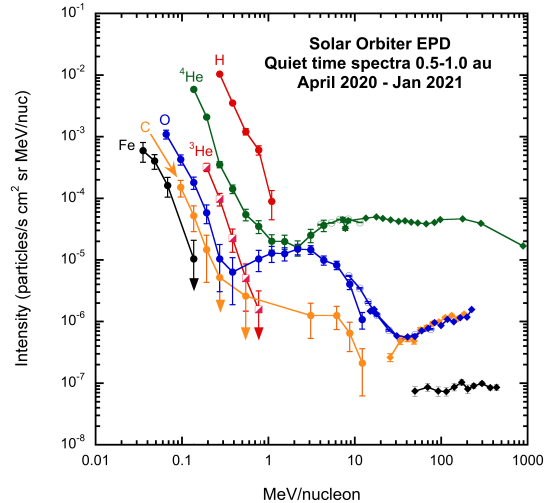


Fig. 2. Quiet-time spectra observed on Solar Orbiter between 0.5 and 1.0 au by EPD/SIS (filled circles and half-filled squares), EPD/HET (filled diamonds), and ACE at 1 au (open circles). Downward pointing arrows signify one-count upper limits.

minimum count rate at these energies, rather a continuous range of intensity values whose lower limit depends on many factors, such as instrument energy threshold, background and/or sensitivity (e.g., Dayeh et al. 2009; Richardson et al. 1990), as well as activity levels in interplanetary space. This Letter analyzed two intervals: first, a “quiet” interval where obvious increases in the hourly averaged 273 keV nucleon $^{-1}$ H and He intensities showed the presence of transient events that were removed from the analysis (see Allen et al. 2021; Mason et al. 2021). The quiet period has 2386 hours of collection time from April 2020 through January 2021 and is used for the observations in Figs. 2 and A.1.

Second, we selected a “super-quiet” interval, the quietest multiday interval during the study, in order to measure the residual spectra at the lowest levels below 1 MeV nucleon $^{-1}$ (e.g., Mason et al. 1979; Mason & Gloeckler 2011). Appendix B describes the identification of this 192-hour super-quiet interval, which is used for Fig. 3.

2.2. Anomalous cosmic rays and low energy turn-up in the quiet-time interval

Figure 2 shows the quiet-time EPD spectra, with small coverage gaps in He and O covered by quiet data from the Advanced Composition Explorer (ACE) Solar Isotope Spectrometer. The ACR O in Fig. 2 rises from the GCR spectrum at ~ 30 MeV nucleon $^{-1}$, similar to the 1992–1993 spectra in Fig. 1. However, the 1992–1993 ACR spectrum flattens around 10 MeV nucleon $^{-1}$, although the wide energy bin from 2.5–10 MeV nucleon $^{-1}$ might conceal more detail. In any case, the 2020–2021 ACR O keeps rising, with a peak near 4 MeV nucleon $^{-1}$ that is about five times higher than the Fig. 1 spectrum; this spectrum was measured somewhat before solar minimum but reached levels near that shown in Fig. 2 by 1994 (Klecker et al. 1998). The ACR O in Fig. 2 decreases from this local maximum then transitions to the turn-up at about 300 keV nucleon $^{-1}$, about a factor of ten lower energy than the start of the turn-up in the 1992–1993 data. In the range ~ 10 – 100 MeV nucleon $^{-1}$, the ^4He intensity of $\sim 4 \times 10^{-5}$ ($\text{s}^{-1} \text{cm}^2 \text{sr MeV nucleon}^{-1}$) is similar to previously measured spectra near

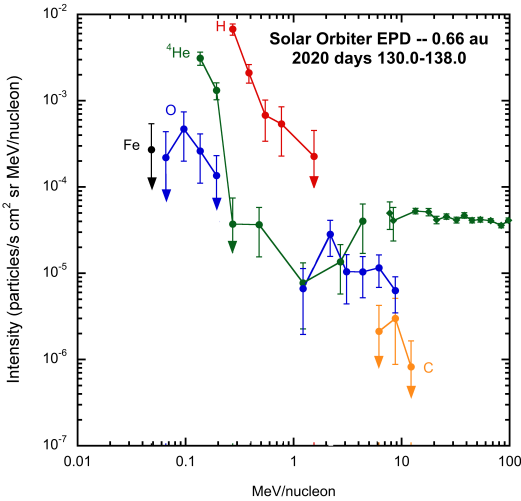


Fig. 3. Low energy spectra during the super-quiet period; symbols are the same as in Fig. 2.

solar minimum (Garcia-Munoz et al. 1977; Reames et al. 1997). The radial gradient in ${}^4\text{He}$ and O near the peak of the spectrum is discussed in Appendix A.

2.3. Low energy spectra in a super-quiet period

In order to further explore the turn-up spectra, we studied a super-quiet interval selected as described in Appendix B. Figure 3 shows the super-quiet period particle spectra. In the low energy turn-up portion the intensities are about half that shown in the period in Fig. 2. Above 1 MeV nucleon $^{-1}$, the He and O flatten due to ACRs. Although ${}^3\text{He}$ was present in Fig. 2, it is absent here. Examining the spectral shapes in Fig. 3, the ${}^4\text{He}$ spectrum is consistent with the higher energy ACRs down to about 300 keV nucleon $^{-1}$, although the statistical uncertainties are large. Below 300 keV nucleon $^{-1}$, there is a large increase in intensity for both ${}^4\text{He}$ and O. Although the data in Fig. 3 are at the limits of the instrument sensitivity, they are consistent with an ACR ${}^4\text{He}$ source down to 300 keV nucleon $^{-1}$. However, the errors are large enough that other possibilities cannot be ruled out.

3. Discussion and conclusions

The ACR spectra shown in Fig. 2 are similar to observations in prior solar cycles. However, they also show the ACR O spectrum with a local maximum at $\sim 2\text{--}4$ MeV nucleon $^{-1}$, rather than a plateau, and a small decrease below ~ 4 MeV nucleon $^{-1}$. Since most prior ACR measurements start at several MeV nucleon $^{-1}$ this feature cannot be compared with the earlier work. In the range 8–27 MeV nucleon $^{-1}$ Mewaldt et al. (1993) reported very similar maximum ACR O intensities in the 1972, 1987, and 1993 solar minima, where in each case the intensity decreased by an order of magnitude when modulation reached solar maximum values. They pointed out that this closely repeatable level at solar minimum is also mirrored in much higher energy neutron monitor data. Jokipii et al. (1977) showed that ACRs enter the heliosphere either drifting along the neutral sheet, or flowing down the solar polar regions to the equatorial region, depending on the 22-year polarity of the solar cycle. The current solar minimum corresponds to the $A > 0$ drift condition, where ACRs

drift in from the polar regions and, therefore, a positive latitudinal gradient is predicted, which has been observed beyond 1 au (Cummings et al. 1995; McKibben 1989). As Solar Orbiter reaches higher latitudes later in the mission the polarity of the current cycle predicts a positive gradient, although close to the Sun the effect may be small.

We now consider the turn-up spectra, first for the quiet time. The spectra and composition, especially with the high ${}^3\text{He}/{}^4\text{He}$ ratio, are consistent with impulsive solar energetic particle (SEP) material. Previously, Richardson et al. (1990), Desai et al. (2006), and Dayeh et al. (2009) found high ${}^3\text{He}/{}^4\text{He}$ in quiet periods during solar maximum, with the ${}^3\text{He}$ nearly disappearing during solar minimum. The present solar minimum quiet time has ${}^3\text{He}/{}^4\text{He} \sim 20\%$ below 1 MeV nucleon $^{-1}$, considerably higher than the previous results. This might be due to a combination of the observations being closer to the Sun, where the impulsive SEP intensities are higher and a lower general level of corotating interaction region (CIR) intensities, which fall off strongly inside 1 au (Allen et al. 2021). Where comparisons can be made, the overall intensity levels in Fig. 2 are generally similar to the earlier surveys. Below 1 MeV nucleon $^{-1}$, the H and ${}^4\text{He}$ power-law spectral slopes are -2.8 and -3.1 , respectively, and are similar to the H and He spectral slopes < 10 MeV nucleon $^{-1}$ summarized by Richardson et al. (1990).

Considering the super-quiet period, the H and He turn-up spectra in Fig. 3 are about one-half the intensity of the previously reported super-quiet periods in 1977 and 2008–2009 (Mason & Gloeckler 2011). Given the large variability of intensities observed at low energies, it is surprising that the present H and ${}^4\text{He}$ intensities are so similar to those reported earlier. For H and ${}^4\text{He}$, the measurements are statistically accurate, so for these species instrument sensitivity is not a limiting factor. The proton spectral slope is -2.5 .

A basic question is whether when SEPs and other transients are removed, there remains a continuous source of energetic ions in the interplanetary medium, for example, from either heated solar material or cooled GCRs. The presence or lack of such energized ions can provide insights into possibly new acceleration processes in the interplanetary medium or solar corona. In the super-quiet period at 0.66 au, between 300 keV nucleon $^{-1}$ and a few MeV nucleon $^{-1}$, the ${}^4\text{He}$ is consistent with an extension of the ACR spectrum to lower energies, but the lack of observations of heavier elements in this range leaves the source properties ambiguous. However, we find the turn-up spectra still present, with protons extending to ~ 1 MeV, but with ${}^4\text{He}$ showing a sharp drop-off above 200 keV nucleon $^{-1}$. The difference between the H and ${}^4\text{He}$ drop-off energies may be a clue for the accelerating mechanism. At even lower energies down to the solar wind peak, other sources, such as inner source material or continuously heated solar wind, may be critically important (e.g., Gloeckler & Geiss 1998; Fisk & Gloeckler 2006).

The super-quiet turn-up spectra reported here need to be examined in the context of multiple sources that contribute to the suprathermal ion pool within 1 au. Intensities as shown in Fig. B.1 make it clear that during solar minimum energetic particles associated with solar wind streams are the most common population to dominate intensities, followed by SEP events. During solar active periods this situation is reversed as SEPs become more common. The surveys of Desai et al. (2006) and Dayeh et al. (2009) showed, however, that impulsive ${}^3\text{He}$ -rich SEP events dominate, apparently since their frequency of occurrence compensates for their smaller size compared to large gradual events (see also Wiedenbeck et al. 2005; Wang et al. 2012).

Considering regions closer to the Sun than 0.5 au, where the bulk of energetic particles may be accelerated in large-scale shock-associated events, the mix of quiet-time particles may change. The stream-associated events important inside 1 au show a large negative gradient (Allen et al. 2021, and references therein) and may therefore be much less important close to the Sun. Additionally, the impulsive ^3He -rich material reported here in the quiet turn-up very possibly is not coming directly from active regions on the Sun, but rather is remnant material from earlier events that finds its way into the inner heliosphere: This can be tested in future Solar Orbiter observations as the perihelion decreases later in the mission and the solar activity cycle progresses.

Acknowledgements. The Suprathermal Ion Spectrograph (SIS) is a European facility instrument funded by ESA. The SIS instrument was constructed by the JHU/Applied Physics Lab. and CAU Kiel. We thank the many individuals at ESA and within the Energetic Particle Detector team for their support in its development. Post launch operation of SIS at APL is funded by NASA contract NNN06AA01C, and we thank NASA headquarters and the NASA/GSFC Solar Orbiter project office for their continuing support. The UAH team acknowledges the financial support by the Spanish Ministerio de Ciencia, Innovación y Universidades FEDER/MCIU/AEI Projects ESP2017-88436-R and PID2019-104863RB-I00/AEI/10.13039/501100011033. The CAU Kiel team thanks the German Federal Ministry for Economic Affairs and Energy and the German Space Agency (Deutsches Zentrum für Luft- und Raumfahrt, e.V., (DLR)) for their unwavering support under grant numbers 50OT0901, 50OT1202, 50OT1702, and 50OT2002; and ESA for supporting the build of SIS under contract number SOL.ASTR.CON.00004, and the University of Kiel and the Land Schleswig-Holstein for their support of SIS. We acknowledge data from the ACE web site from the Caltech Solar Isotope Spectrometer instrument and SWICS solar wind instrument.

References

- Allen, R. C., Mason, G. M., Ho, G. C., et al. 2021, [A&A, 656, L2](#) (SO Cruise Phase SI)
- Cummings, A. C., Mewaldt, R. A., Cummings, J., et al. 1995, [Geophys. Res. Lett., 22, 341](#)
- Cummings, A. C., Stone, E. C., & Steenberg, C. D. 2002, [ApJ, 578, 194](#)
- Dayeh, M. A., Desai, M. I., Dwyer, J. R., et al. 2009, [ApJS, 693, 1588](#)
- Desai, M. I., Mason, G. M., Mazur, J. E., & Dwyer, J. 2006, [ApJ, 645, L81](#)
- Desai, M. I., Mason, G. M., Müller-Mellin, R., et al. 2008, [J. Geophys. Res., 113, 8103](#)
- Fisk, L. A., & Gloeckler, G. 2006, [ApJ, 640, L79](#)
- Garcia-Munoz, M., Mason, G. M., & Simpson, J. 1977, [ApJ, 213, 263](#)
- Gloeckler, G., & Geiss, J. 1998, [Space Sci. Rev., 86, 127](#)
- Jokipii, J. R., Levy, E. H., & Hubbard, W. B. 1977, [ApJ, 213, 861](#)
- Kahler, S. W., & Ling, A. G. 2019, [ApJ, 872, 89](#)
- Klecker, B. 1999, [Adv. Space Res., 23, 521](#)
- Klecker, B., Hovestadt, D., Gloeckler, G., & Fan, C. Y. 1977, [ApJ, 212, 290](#)
- Klecker, B., Mewaldt, R. A., Bieber, J. W., et al. 1998, [Space Sci. Rev., 83, 259](#)
- Krimigis, S. M., Armstrong, T. P., & Kohl, J. W. 1973, [ICRC, 13, 1656](#)
- Marquardt, J., Heber, B., Potgieter, M. S., & Strauss, R. D. 2018, [A&A, 610, A42](#)
- Mason, G. M., & Gloeckler, G. 2011, [Space Sci. Rev., 98](#)
- Mason, G. M., Gloeckler, G., & Hovestadt, D. 1979, in [ICRC 16, 1, 259](#)
- Mason, G. M., Ho, G. C., Allen, R. C., et al. 2021, [A&A, 656, L1](#) (SO Cruise Phase SI)
- McComas, D. J., & Schwadron, N. A. 2006, [Geophys. Res. Lett., 33, 4102](#)
- McKibben, R. B. 1989, [J. Geophys. Res., 94, 17021](#)
- Mewaldt, R. A., Cummings, A. C., Cummings, J. R., et al. 1993, [Geophys. Res. Lett., 20, 2263](#)
- Müller, D., Cyr, O. C. S., Zouganelis, I., Gilbert, H. E., & Marsden, R. 2020, [A&A, 642, A1](#)
- Rankin, J. S., McComas, D. J., Leske, R. A., et al. 2021, [ApJ, 912, 139](#)
- Reames, D. V. 1999, [ApJS, 518, 473](#)
- Reames, D. V., Barbier, L. M., & von Rosenvinge, T. T. 1997, [Adv. Space Res., 19, 809](#)
- Richardson, I. G., Reames, D. V., Wenzel, K., & Rodriguez-Pacheco, J. 1990, [ApJ, 363, L9](#)
- Rodríguez-Pacheco, J., Wimmer-Schweingruber, R. F., Mason, G. M., et al. 2020, [A&A, 642, A7](#)
- Wang, L., Lin, R. P., Krucker, S., & Mason, G. M. 2012, [ApJS, 759, 69](#)
- Wiedenbeck, M. E., Mason, G. M., Cohen, C. M. S., et al. 2005, in [ICRC 29, 117](#)
- Zamow, R. 1975, [ApJ, 197, 767](#)

Appendix A: ACR radial gradient inside 1 au

Figure A.1 shows the ${}^4\text{He}$ and O intensities near 4.4 MeV nucleon $^{-1}$ for three radial distances. The combination of a low count rate along with small Δr leads to large uncertainties,

but it is consistent with the small positive O radial gradient observed on Helios and Parker Solar Probe (Marquardt et al. 2018; Rankin et al. 2021), as well as over larger distances beyond 1 au (Cummings et al. 1995).

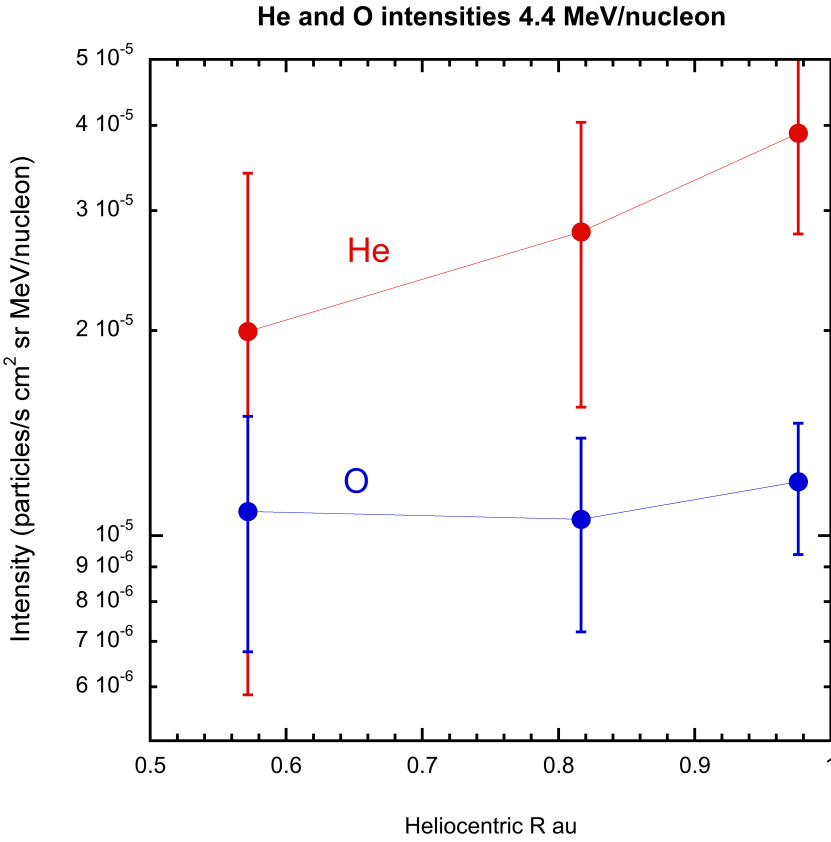


Fig. A.1. Quiet-time interval He and O intensities observed near the peak of the low energy ACR spectra near 4.4 MeV nucleon $^{-1}$ vs heliocentric radius.

Appendix B: Selection of super-quiet interval

To select a super-quiet interval, we first selected intervals where suprathermal H and He intensities were noticeably lower than their values between intra-event peaks elsewhere. Figure B.1 shows three such areas in shaded yellow labeled (a)–(c) (e.g., compare days 130–138 with days 210–215). Summing over these three intervals yielded spectra similar to the low energy portions of Fig. 2, but at somewhat lower intensities. In particular the ${}^3\text{He}/{}^4\text{He}$ ratio was $(15 \pm 5)\%$, indicating an impulsive SEP source. Looking in more detail, we found that the arrival time of the ${}^3\text{He}$ showed that almost all of the counts arrived in a short period on day 164.9 in interval (c). The source of these particles might have been AR12765, which was in the Southern hemisphere at Carrington Longitude 113° when viewed from Earth on day 165. Additionally, it was seen that during interval (b) the H and He intensities rose towards the end. Interval

a did not show any such variations; rather, the intensities were low and did not show any obvious time variations. Interval (a) (2020 days 130.0–138.0) was therefore selected as the super-quiet interval, and the other two were set aside. During the super-quiet interval the Solar Orbiter separation angle from Earth was only about 9° , and so images from the Solar Dynamics Observatory (SDO) at L1 show the solar disc practically as viewed by Solar Orbiter. On NOAA reports for day 138, there were no plages or active regions, and the solar synoptic analysis was featureless except for small coronal holes. Solar Wind Ion Composition Spectrometer (SWICS) data from the ACE Science Center indicated slow (~ 280 – 350 km s^{-1}) solar wind speeds over the nine-day period (solar wind data from Solar Orbiter were not available). Thus, this extremely quiet period was associated with very low magnetic and solar wind activity. The interval was 192 hours long, and the average radial distance was 0.66 au.

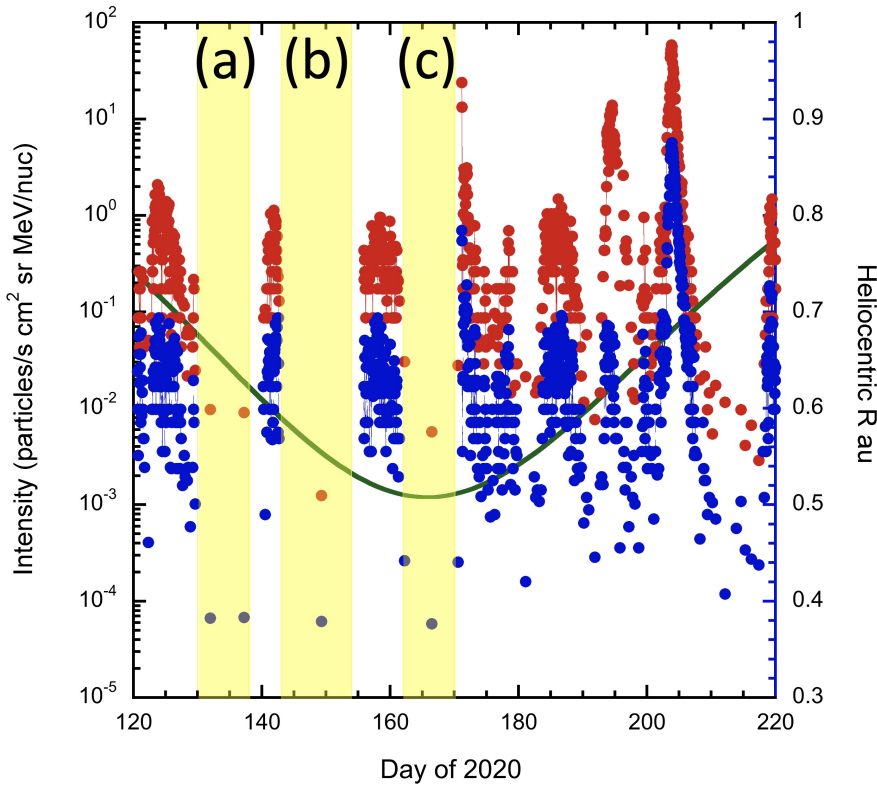


Fig. B.1. Intensities of 273 keV nucleon $^{-1}$ H (red filled circles) and He (blue), for mid-2020 showing heliocentric distance and yellow intervals (a)–(c) with low intensities. Large intensity increases in the figure are associated with CIRs and SEP events. The text describes residual time variations in intervals (b) and (c) that led them to be disqualified, leaving interval (a) as the super-quiet interval.

OBSERVATION OF ANOMALOUS COSMIC RAYS IN THE INNER HELIOSPHERE

At the end of section 6, Mason et al. (2021b) reported the radial gradient of anomalous cosmic ray (ACR) oxygen and helium-4 with energies of 4.4 MeV/nuc within 1 au. The analysis was based on the measurements from the Suprathermal Ion Spectrograph (SIS) instrument in 2020, and particle intensities were plotted as a function of three radial locations. Due to limited counting numbers, the flux uncertainties of flux were relatively significant. However, the results still indicate a positive and small gradient for oxygen compared to the observations from Helios and Parker Solar Probe (PSP) (Marquardt et al., 2018; Rankin et al., 2021).

As of 2023, the changing solar activity and the solar modulations have also influenced ACRs in the inner heliosphere as they propagate inward and diffuse throughout the heliosphere. Those changes are reflected in the variation of ACR intensities and potentially in that of the radial gradient. Meanwhile, the Solar Orbiter (SolO) has completed its fifth orbit and continues its journey in the inner heliosphere. The High Energy Telescope (HET) on board SolO, which has been measuring helium of tens of MeV/nuc during the last two years, witnessed the change of solar activity and solar modulation.

Therefore, in this chapter, we investigate new ACR observations in the inner heliosphere and in the new solar cycle, utilizing new data from HET on board SolO. We present the spectra and radial gradient of ACR helium in the inner heliosphere between 2020 and 2022, taking into account possible interruptions such as solar energetic particles (SEPs), periodically occurring corotating interaction regions (CIRs) and long-term solar modulation. Preliminary results indicate the consistent helium measurements of HET and other instruments, for example, the Solar and Heliospheric Observatory (SOHO)/Electron Proton Helium Instrument (EPHIN). The radial gradients of helium-4 agree well within the large uncertainties with previous results from PSP. The variation of the helium radial gradient in the early phase of solar cycle 25 is also discussed.

The details of the data analysis and results are given below. It is worth noting that results have not yet been published. We plan to continue this analysis and prepare a final publication to be submitted to *Astronomy and Astrophysics* soon.

7.1 INTRODUCTION

ACRs are accelerated interstellar pick-up ions characterized by the abundance of singly ionized atomic nuclei widespread in the heliosphere and predominant in the energy range of tens of MeV/nuc. They originate from the interstellar neutral particles, which are ionized by the solar wind via the charge exchange process when they flow into the heliosphere. Once they become ionized, the solar wind carries these charged particles to the outer heliosphere, where particles gain

energy. One source of ACRs is believed to be the blunt termination shock located at the boundary of heliosphere (McComas and Schwadron, 2006). Since the ACRs were first discovered in 1970, scientists have confirmed the observations of ACR helium, oxygen, neon, and also protons in the outer heliosphere (Garcia-Munoz et al., 1973; Hovestadt et al., 1973; McDonald et al., 1974; Potgieter, 2013).

Generally, the transport of the cosmic rays in the heliosphere are described by the interaction between charged particles and the interplanetary magnetic field embedded in the solar wind. The different physical processes that affect the propagation of particles are (a) diffusion caused by the irregular magnetic field, (b) adabatic energy loss and convection due to the expanding solar wind, and (c) gradient and curvature drifts in the heliospheric magnetic field. Though the cosmic ray transport equations describe and model those basic processes (Parker, 1965; Jokipii et al., 1977; Jokipii and Thomas, 1981; McDonald et al., 2001) in general, the detailed roles of each component interacting with the varying solar magnetic field in the inner heliosphere. i.e., within 1 au, still need to be fully understood. New measurements by PSP indicate that the radial gradient of the lower energy cosmic rays within 1 au is inconsistent with the model prediction (Rankin et al., 2021).

The spatial gradients, including both radial and latitudinal gradients, provide valuable insights into the variation of drift effects of charged particles during the different solar cycles. As elucidated by Jokipii et al. (1977), Jokipii and Kopriva (1979), and Potgieter (2013), the drift direction of energetic particles differs with the polarity of the Sun's magnetic field, which alternates approximately every 11 years and results in the formation of a 22-year variation. The recent solar activity minimum in 2020 denotes positive polarity (A+). Consequently, the positively charged ions drift inward from the south and north pole regions while moving outward along the equatorial plane through the current sheet. Conversely, during the opposite polarity (A-) period, ions drift inward from the equator and exit through the poles. The drift direction of electrons is opposite to that of ions. These drift effects are manifested in spatial gradients. Previous observations from the Voyager and the Pioneer missions have indicated that the latitudinal gradient changes sign between two consecutive solar cycles belonging to different polarities, in agreement with predictions from transport models (McKibben et al., 1979; Cummings et al., 1987; Christon et al., 1986). Moreover, the magnitude of the radial gradient varies between different solar cycles of opposite polarity (Rankin et al., 2021, 2022; Giacalone et al., 2022; Webber and Lockwood, 1981; Marsden et al., 1999).

According to Rankin et al. (2021), the radial gradient of cosmic rays can be expressed as:

$$g_r = \frac{1}{f} \frac{\partial f}{\partial r} = \frac{\partial \ln f}{\partial r} , \quad (5)$$

where g_r denotes the differential radial gradient component under the assumption that the latitude gradient is negligible. The gradient represents the change of the differential flux, f with respect to radial distance r . The radial gradient can be obtained by fitting the data to a linear equation using the least square method.

Benefiting from its unique orbits, which have the closest perihelion distance of 0.28 au, SolO, launched on Feb 10, 2020, have provided valuable measurements of cosmic rays during the quiet time, shedding light into the transport effects of cosmic rays in the inner heliosphere by deriving the radial gradient of those particles. In Fig. 17, we present the orbit information of SolO from Feb 2020 to May 2023. The top three panels display the radial distance of SolO to the Sun, Carrington longitude, and Carrington latitude of SolO. As depicted in the top panel, SolO has completed five orbits and is moving away from the Sun after passing its sixth perihelion. The closest distance to the Sun was achieved during the fifth orbit in September of 2022. The Carrington longitude of SolO indicates its movement relative to a fixed longitude line on the Sun. Originally defined from Earth's perspective, with a mean synodic period of approximately 27.2753 days, the Carrington system and its origin point are applied to the SolO coordinate system. Due to the greatly varying radius of the orbit, orbital periods of SolO Carrington rotations range between 26.6 and 35.8 days, slightly differing from the period of Earth. Currently, the latitude of SolO is constrained within a range of $\sim \pm 8$ degrees. In addition, we provide the radial distance and the longitudinal separation between SolO and Earth to illustrate the relative positions.

To better visualize and understand SolO's movement in the inner heliosphere and its relation to the Sun and Earth, we depict the orbit track of SolO in two coordinate systems in Fig. 18. The top panel shows the orbit in the heliocentric coordinate system, where the mean equinox is used as the reference direction of x-axis. In this coordinate system, SolO's orbit exhibits an elliptical shape. Similarly, the bottom panel of Fig. 18 presents the trajectory in a heliographic coordinate system, with the Sun fixed in the center and the Earth positioned at 1 au, marked as the blue dot. The x-axis is aligned to the Sun - Earth direction. In this coordinate system, orbits appear twisted and undergo changes in shape.

The color bars in both panels indicate the time sequence from February 2020 to May 2023. The numbers of Carrington rotations are marked at the beginning of each rotation and labeled next to the orbit track. The moving direction of the spacecraft can be inferred from changes in the numbers and colors.

7.2 INSTRUMENTS AND DATA EMPLOYED IN THIS STUDY

The charged particle measurements reported in this study are from HET onboard SolO, which could measure charged particles in the energy range from tens of MeV/nuc to a hundred MeV/nuc. Specifically, we focus on helium particles within the energy range of 10 - 50 MeV/nuc, which are the HET stopping particles measured in detector C. During quiet times, the predominant particles are ACRs in this energy range. Further details regarding the HET measurement principle can be found in section 3.2 and Rodríguez-Pacheco et al. (2020).

Similar to the analysis by Mason et al. (2021b) for SIS, our analysis of the helium radial gradients measured by HET is also constrained by the counting statistics due to the limited geometry factor of HET and the low helium intensities in space. In order to derive radial gradients with better accuracy, we employ two methods to increase count statistics and hence reduce uncertainties of gradients. In the

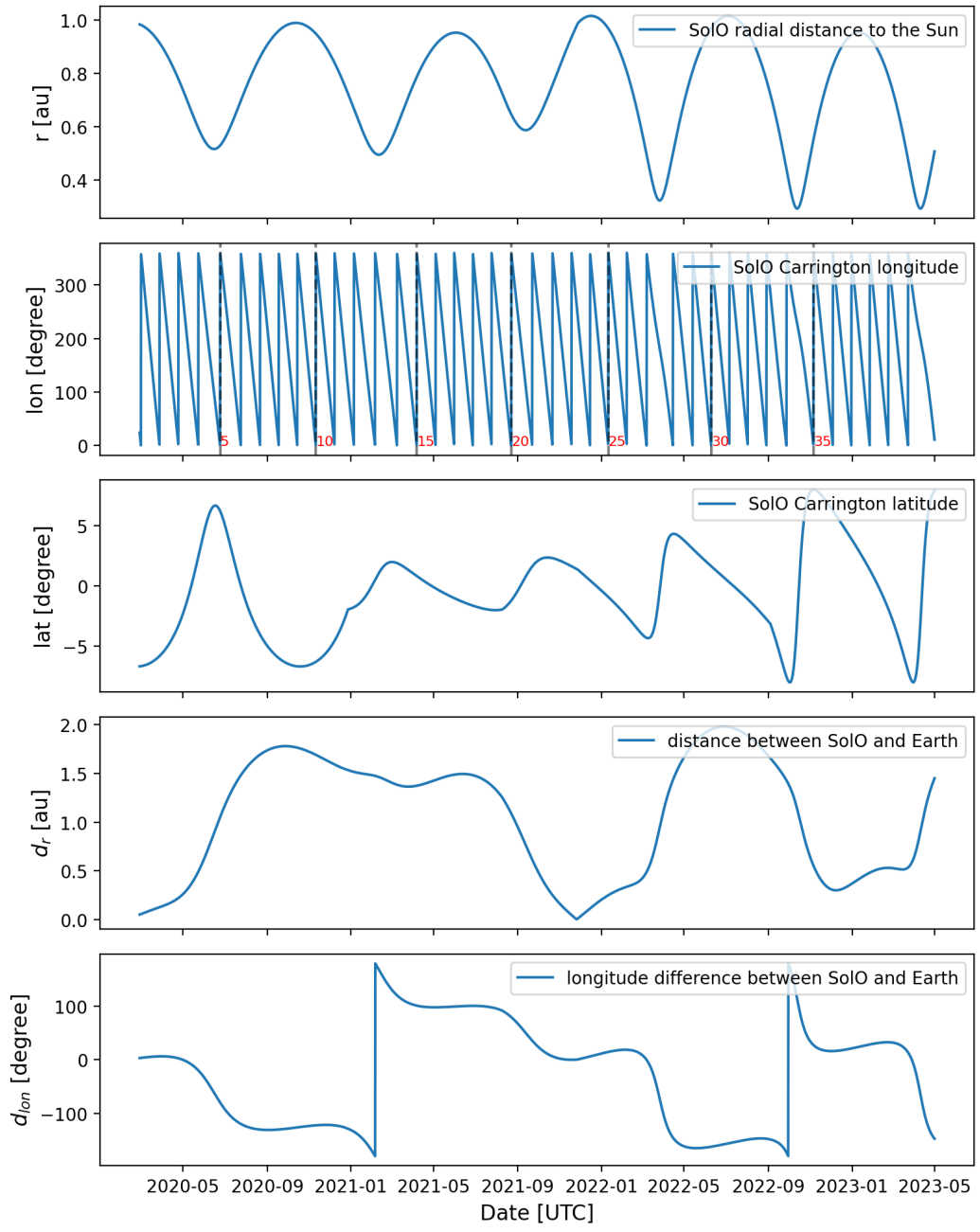


Figure 17: (From top to bottom) The variation of SolO's radial distance, Carrington longitude, Carrington latitude as well as the distance and longitude separation between SolO and SOHO. The period covered in the figure ranges from February 2020 to May 2023.

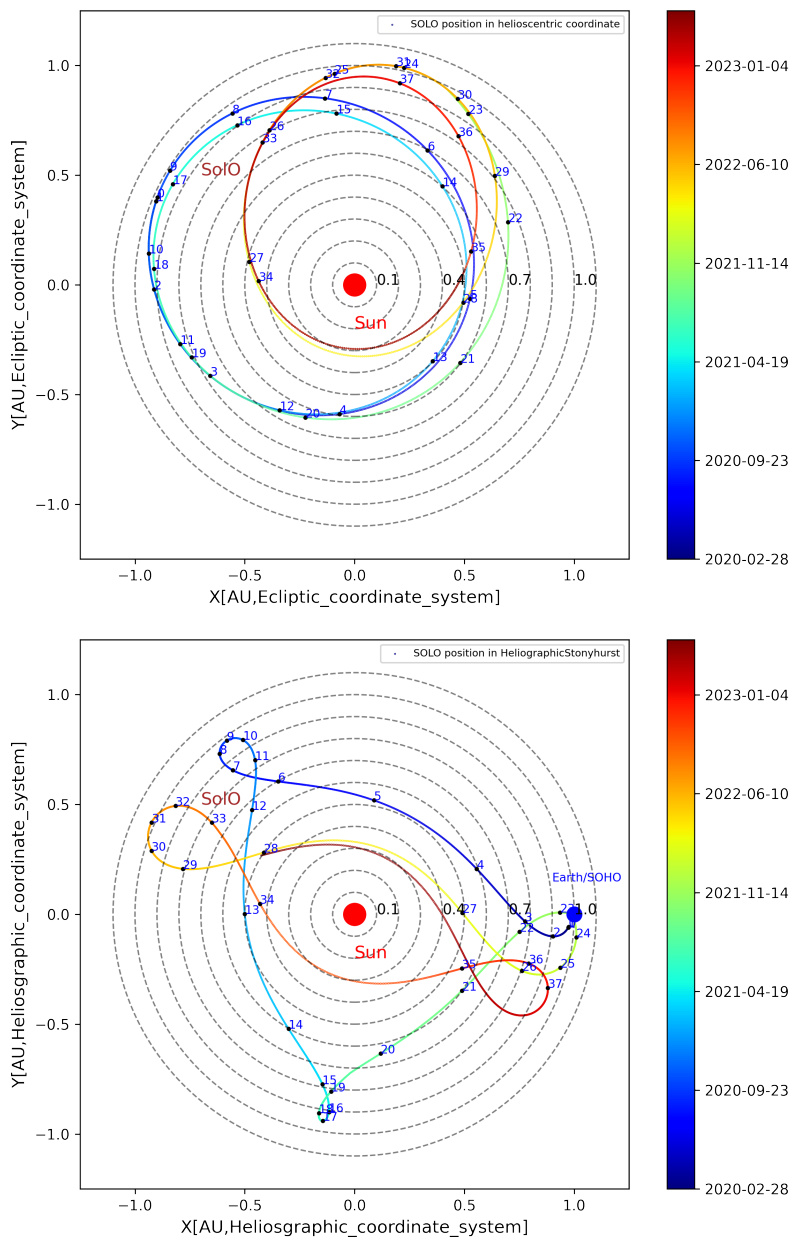


Figure 18: Top: The orbit track of SolO in the heliocentric mean ecliptic coordinate system where the origin is the center of the Sun, and x-axis points to the mean equinox and the xy - plane is the ecliptic plane. Bottom: The orbit track of SolO in the Stonyhurst coordinate system. Earth is fixed at 1 au and is marked with a solid blue circle. The other measurements from SOHO/EPHIN, ACE/CRIS/SIS and LND are from locations near Earth. The numbers next to the dashed circle lines indicate the distance from the Sun to 1 au. The blue dots along the track indicate the start of each Carrington rotation of SolO. About 37 Carrington rotations are used in this study, as the numbers next to the tracks show. The period ranges from February 2020 to May 2023.

first method, we calculate a summation of count rates measured by four HET apertures. There are two sets of Electron Proton Telescope (EPT)/HET telescopes mounted perpendicularly on the SolO, with each measuring stopping particles from two ends. Hence, SolO/HET can provide helium flux measurements from sunward, anti-sunward, southward, and northward directions. In the following analysis, we simply use the averaged helium intensity from four directions as the measurement of SolO. By doing so, we can reduce the uncertainties of helium intensity to half. Secondly, we rebinned the fine energy channels of HET and reconstructed four energy channels in the energy range of 11.1 - 19.4 MeV/nuc, 19.4 - 29.5 Mev/nuc, 29.5 - 41.2 Mev/nuc, 41.2 - 49.0 Mev/nuc, to further increase the counting statistic of each channel.

In addition to the nominal data products, designed for scientific purposes and measuring the flux of different charged particles of different energies, we also take advantage of one type of housekeeping data as an indicator of SEP events. This housekeeping data registers every particle that can trigger two solid state detectors (SSDs) (A and B) in coincidence but without resolving the particle species and their primary energies. This counter also has a larger field of view (FOV). Therefore, it has more significant counting statistics than the nominal scientific data products, which can better determine the onset and the end of the SEP events. In Fig. 22, we present the hourly count rate of two multiple detector counters. One is from the sunward telescope, named HET_any (a1,b1i), and the other is from the anti-sunward telescope, named HET_any(a2,b2i). Later in Sec. 7.4, we explain how to use these counters to filter the SEP events.

Apart from HET, we also used the observations from instruments or space-craft close to Earth for comparison. We use helium and heavy ion measurements from the Solar Isotope Spectrometer (SIS) and the Cosmic Ray Isotope SpectrometerCosmic Ray Isotope Spectrometer (CRIS) onboard the Advanced Composition Explorer (ACE), helium measured by Solar and Heliospheric Observatory/Electron Proton Helium Instrument and helium intensity measured by Lunar Lander Neutron and Dosimetry Experiment on the lunar far-side surface. Low-Energy Telescope (LET) provides helium measurements with energy below 10 MeV/nuc from the Solar Terrestrial Relations Observatory (STEREO)-A space-craft. But only SOHO/EPHIN is used as the baseline of the long-term trend of helium-4 anomalous cosmic rays.

7.3 OVERVIEW OF OBSERVATIONS BETWEEN 2020 AND 2022 AND THE CROSS-CALIBRATION BETWEEN FOUR INSTRUMENTS

Comparison of spectra between HET and other instruments

Before deriving radial gradients of helium, it is necessary to provide an overview of the HET observations of heavier ions, such as helium, carbon, nitrogen, and oxygen. Fig. 19 illustrates the averaged spectra between 2020 and 2022 after removing possible SEP periods.

The HET measurements are represented by diamonds of various colors, with red for helium-4, orange for carbon, green for nitrogen, and blue for oxygen. The

helium spectrum spans a wide energy range and consists of particles stopping in detector B (< 10 MeV/nuc), stopping in detector C ($10 - 100$ MeV/nuc), and penetrating particles (> 100 MeV/nuc). The analysis of ACR helium radial gradients is based only on measurements of helium-4 stopping in detector C. Although they are not used in this study, it is worth noting that the intensities measured by two channels around 100 MeV/nuc are a few times higher than those in the nearby channels. The reason for these abnormal increases is yet unknown. Besides, when converting counts to fluxes in the galactic cosmic ray (GCR) spectrum, geometry factors of fully penetrating particle channels, i.e., the last three channels, are calculated based on the 4π simulation. That is because HET could not distinguish incident directions of those fully penetrating particles, which are mainly GCR. Unlike SEP, GCR are nearly isotropic in the heliosphere.

In Fig. 19, ACE measurements are plotted as circles, including filled circles representing SIS and empty ones for CRIS. Unfortunately, at the moment, helium measurements from ACE are available only below 15 MeV/nuc. Hence, we use helium data from SOHO/EPHIN which are shown as purple squares, to calculate radial gradients of ACR helium. Besides, LND-measured helium-4 is also shown as brown triangles. EPHIN covers the ACR energy range of $10 - 50$ MeV/nuc while LND covers the energy range of $10 - 35$ MeV/nuc.

Fig. 19 reveals a general agreement of the averaged spectra of four particle species, though measurements come from different instruments and distinct positions. Furthermore, the flat helium spectra between 10 MeV - 50 MeV/nuc and the peak intensity of oxygen and nitrogen at 10 MeV/nuc demonstrate the presence of the ACR components in the inner heliosphere.

Fig. 20 focuses on the helium-4 spectra based on the measurements when SolO was positioned between 0.95 and 1 au, after subtracting measurements of SEP. The periods when SolO was close to 1 au in the last two years are given in Tabel 2, which consists of start times, end times, and the relative distance from SolO to Earth. The averaged spectrum of EPHIN and HET helium at energies above 10 MeV/nuc are comparable. Therefore, we utilize the EPHIN and HET helium measurements within the energy range of 10 to 50 MeV/nuc in the subsequent analysis. A discrepancy between the spectra appears in energy channels below 10 Mev/nuc where intensities of SIS and HET are about two times higher than those of EPHIN. Besides, the LND spectrum appears generally higher than the other measurements and has larger error bars. The more significant uncertainties are due to the limited operation time on the lunar surface (see section 3.1). The spectra don't agree for quiet times, which may be due to different background levels of the instruments.

Temporal variation of helium-4 intensity

Fig. 21 presents intensity profiles of helium from February 2020 to October 2022 from HET, EPHIN, LND, and LET. The energy ranges of reconstructed channels are labeled in the corresponding legends. The bottom panel shows the distance of SolO from the Sun.

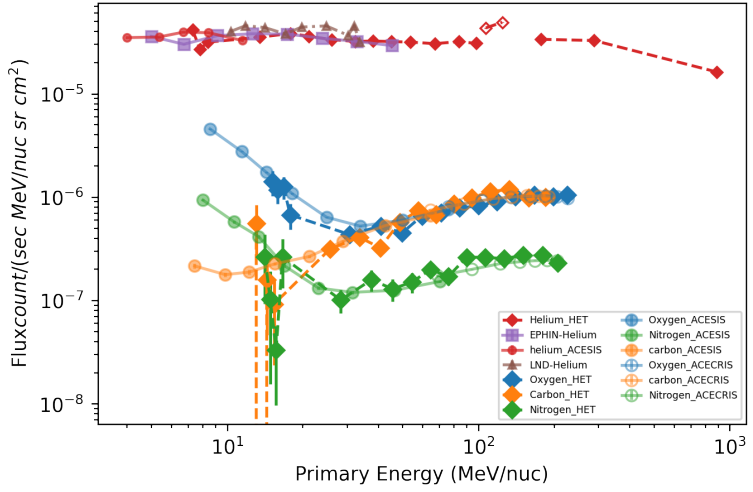


Figure 19: The helium-4 (red, brown, purple), carbon (orange), nitrogen (green), and oxygen (blue) spectra averaged between 2020 and 2022. SEP events have been removed. The data used in this figure covers observations from SolO/HET, SOHO/EPHIN, ACE, and LND.

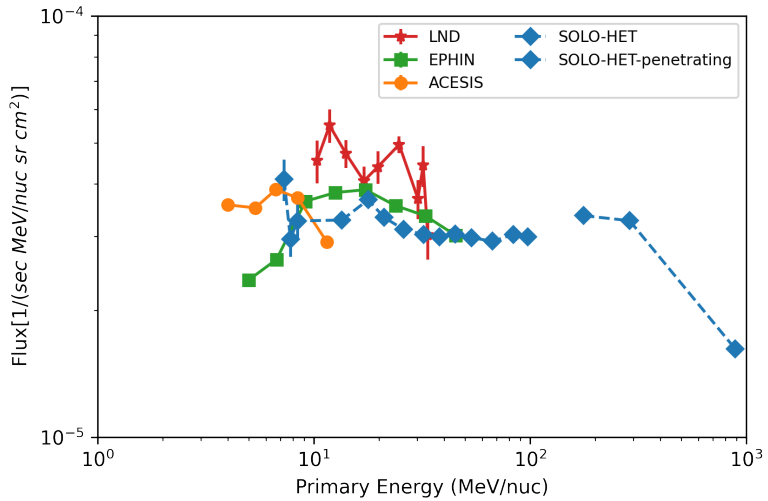


Figure 20: The helium-4 spectra of SolO/HET, SOHO/EPHIN, ACE/SIS and Chang'4/LND when SOLO was between 0.95 and 1AU. SEP events have been removed according to the SEP list in Appendix B.

Figure 21 clearly shows that helium fluxes are relatively stable from 2020 to the middle of 2021, dominated by cosmic rays; only one large SEP event occurred at the end of 2020 (Kollhoff et al., 2021). Since the second half of 2021, more SEPs have been observed and were measured by different instruments, for instance, HET and EPHIN, as shown in the top two panels of Fig. 21. Those large and intense SEPs significantly disturb the time profile of the ACR background and, consequently, must be removed before we calculate the ACR radial gradient. Of

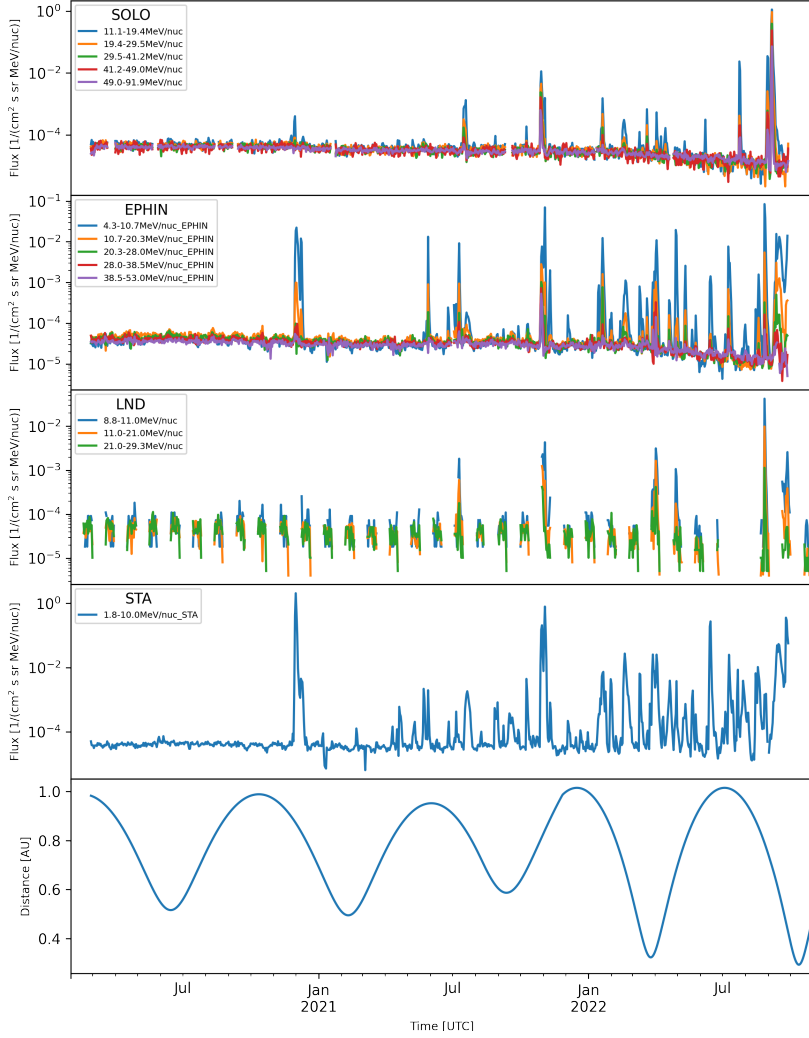


Figure 21: From top to the bottom: The daily averaged helium flux measured by SolO/HET, SOHO/EPHIN, Chang'E-4/LND, and STEREO-A/LET over 2020.2 - 2022.10. The bottom plot shows the radial distance of SolO from the Sun.

note, the energetic helium arrives differently at SolO, SOHO, and STEREO-A. The discontinuities of LND measurements are due to the hibernation of LND during the local night on the Moon's far-side surface.

In addition to the intermittently occurring SEPs, a long-term decrease is also clearly seen in the HET and EPHIN time profiles from 2020 to the end of 2022. This decrease is caused by the enhanced solar modulation, which significantly reduces the number of ACRs arriving at Earth and in the inner heliosphere within one astronomical unit. We expect a further decrease of the ACR intensity in the next few years before the solar activity reaches its next maximum.

In contrast to the transient variation from SEPs and 11-year variation attributed to the large-scale solar modulation, the intensities of cosmic rays are additionally influenced and modulated by recurring, compressed structures that are formed by the interaction between fast and slow solar wind stream emitted from the solar corona. These compressed structures, known as stream interaction regions

or corotating interaction regions, periodically enhance the pressure and density of the plasma and corotate with the Sun, aligned with the Sun's rotation (Burlaga, 1974; Gosling et al., 1976; Richardson, 2004). Those changes in local conditions modify the transport of cosmic rays, resulting in decreases of the intensity of the order of 1 - 5 % (Richardson, 2004, 2018), which are not as significant as those induced by SEPs and overall solar modulations.

Table 2: A list of time periods when SolO is between 0.95 and 1 au. The distances between SolO and Earth are also given.

number of period	start time	end time	distance to Earth (au)
1	2020-02-28	2020-03-16	0.07
2	2020-09-14	2020-11-10	1.76
3	2021-05-27	2021-06-09	1.49
4	2021-11-21	2022-01-15	0.13
5	2022-06-05	2022-08-02	1.96
6 (not used)	2023-01-04	2023-01-17	0.41

7.4 AVERAGED HELIUM INTENSITY PROFILE BETWEEN 2020 AND 2022

Solar energetic particle events list

As previously mentioned, SEP events significantly disturb the ACR background. Therefore, it is crucial to have a complete and properly defined list of SEP periods. This section describes the methodology and data products we used to determine the SEP periods. The SEP lists are determined separately for SolO and SOHO/EPHIN since SEPs arrived differently at SolO and at Earth.

To thoroughly remove SEPs and mitigate the presence of residual particles that may not be directly recognized from intensity profiles, we use different data products to identify SEPs rather than relying solely on helium data.

The multiple detector counters of HET sunward and anti-sunward telescope are employed to determine SEP observed by SolO. As shown in Fig. 22, the hourly counts of two counters range from approximately 600 to 800 during quiet time. When SEP occurred, both counters increased significantly and exceeded the background, though the peak values of two counters might differ depending on the pitch angle distribution of SEPs. We use the sunward measurements to determine the SEP periods. For SEPs reaching Earth, we utilize the time profile of protons in the energy range below 10 MeV observed by EPHIN to determine SEPs. The corresponding proton profiles are displayed in Fig. 23

The durations of SEP events are determined using the 3σ method, supplemented by eye inspection. Here, σ is the standard deviation of background measurements taken during pre-event quiet periods. SEP periods are defined as consecutive time intervals when the flux exceeds three times the standard deviation above the background. This method is commonly used to determine the

onset time of SEP events and is valid for those SEPs with clear onset and sharp increase.

However, if the background is unclear and the increase of the temporal profiles is slow, the determination of the onset and end of the event might have a larger uncertainty. In this case, we check the results manually and determine the boundaries of the SEP periods by eye. As a result, the SEP periods that we determined are illustrated as the magenta-colored regions in Fig. 22 and Fig. 23. The SEP periods are listed in Table 6 and Table 7 in Appendix B.

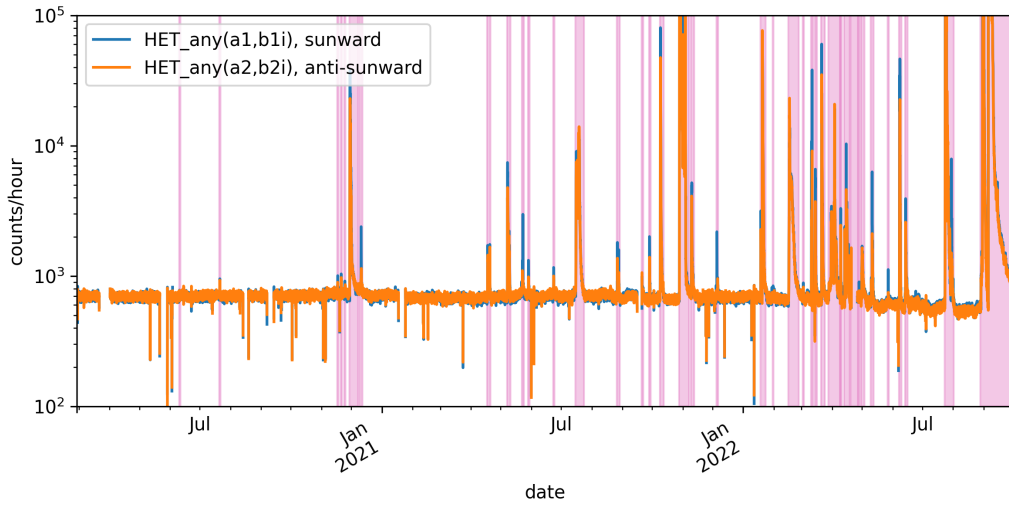


Figure 22: Hourly count rate of the HET multiple detector counters. The magenta-colored regions are the SEP periods we identified.

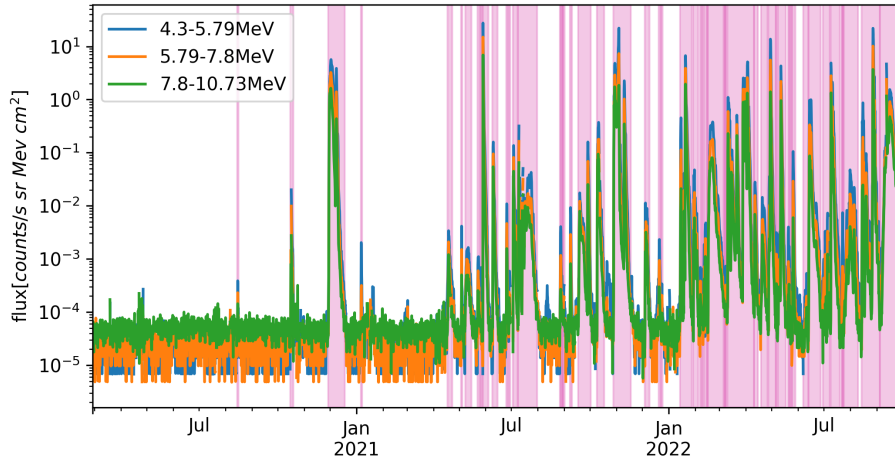


Figure 23: The proton flux measured by SOHO/EPHIN below 10 MeV. The data we used here are the level-3 proton data products generated from pha data (Kühl et al., 2020). The magenta-colored regions indicate SEPs observed near Earth.

Averaged over Carrington rotation

As mentioned earlier, transient SEPs, long-term solar modulation, SIR and quasi-periodic CIR affect the ACR intensity. In the previous section, we identified and removed SEP periods to obtain a slowly changing profile. In this section, we will further reduce the impact of recurring compressed regions by averaging the intensity profile over each Carrington rotation, as suggested by Rankin et al. (2021). One complete Carrington rotation corresponds to the period between two adjacent peaks of SolO's Carrington longitude, which is depicted in the second panel from the top of Fig. 17.

Fig. 24 displays the average helium flux from HET (orange line) and EPHIN (blue line) in four generally comparable energy bins though two different instruments from different locations measured them. Besides, both averaged fluxes decrease over time, which is noteworthy, indicating the largely increased solar modulation during the new solar cycle. The red dashed lines indicate the variation in radial distance between SolO and the Sun.

However, we could still see some discrepancies that are worth noting. During the end of 2020 and the start of 2021, the HET helium intensity is unusually higher compared to that measured by EPHIN. The discrepancies are up to 30 % and are clearly seen in all four channels. Furthermore, the bottom panel of Fig. 24 shows that before 2021, the intensities of 38.5 - 53.0 MeV/nuc helium from EPHIN are statistically lower than those from HET. After that, such a discrepancy gradually disappeared in this channel. However, such a discrepancy is unseen in lower energy channels. Currently, the reasons for these discrepancies are unclear.

Fig. 25 illustrates the helium flux within the energy range of 11.1-19.4 MeV/nuc from HET, shown as a function of the radial distance from 0.4 to 1 au. Data points of different colors represent the averaged fluxes during the Carrington rotation in different orbits, as indicated in the legends. The Carrington rotation numbers from 0 to 30 are also given. Notably, the intensity of helium at the last measurement point is about five times less than that at the beginning. Such a decrease is caused by the solar modulation. Removing this trend is discussed in the next section.

7.5 RADIAL GRADIENT OF ACR HELIUM

Deriving the slight radial gradient ($\sim 25\%/\text{au}$, Rankin et al. (2021)) from the substantially changed data is challenging, specifically when dealing with the five-fold decrease in helium intensity resulting from solar modulation. To address this challenge and obtain the radial gradient, we detrend the HET flux by using the EPHIN flux as a baseline. We assume that the solar modulation is the same for both instruments. We first calculate the ratio of HET and EPHIN and then estimate the radial gradient of different energy ACR helium using the definition in Eq. 5.

We present the temporal variation of flux ratio between HET and EPHIN for four energy channels in the first and third rows of Fig. 26. The various colored regions represent periods of different orbits. The second and fourth rows illustrate the ratio in log scale as a function of the radial distance. Here, only the data

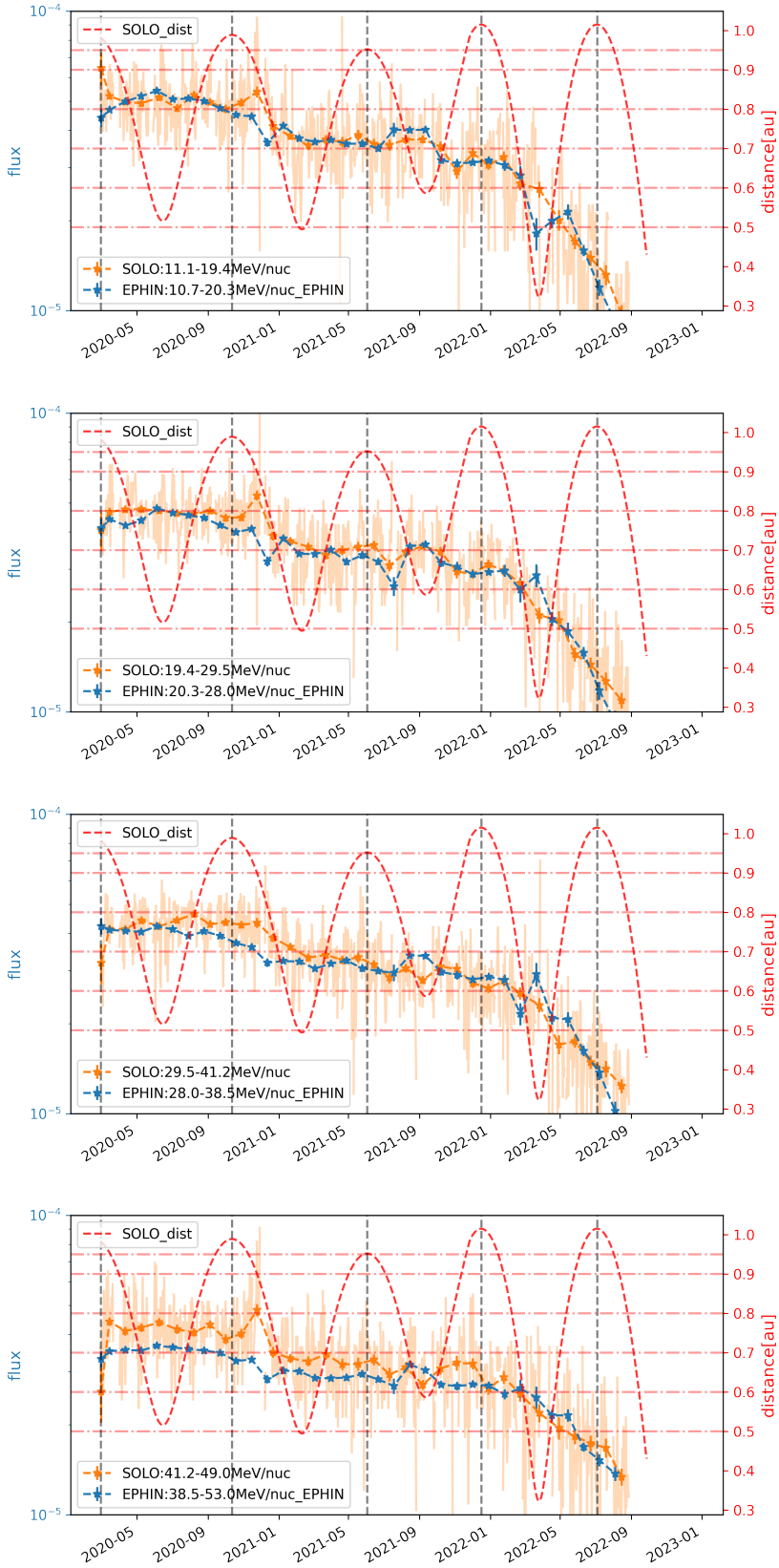


Figure 24: The flux of SolO (orange) and EPHIN (blue) averaged over the Carrington rotation periods in the energy channels of 10 - 20 MeV/nuc, 20 - 30 MeV/nuc, 30 - 40 MeV/nuc, and 40 - 50 MeV/nuc. The daily averaged HET helium fluxes are also shown in different energy channels as light orange lines. Red dashed lines are the radial distance of SolO to the Sun.

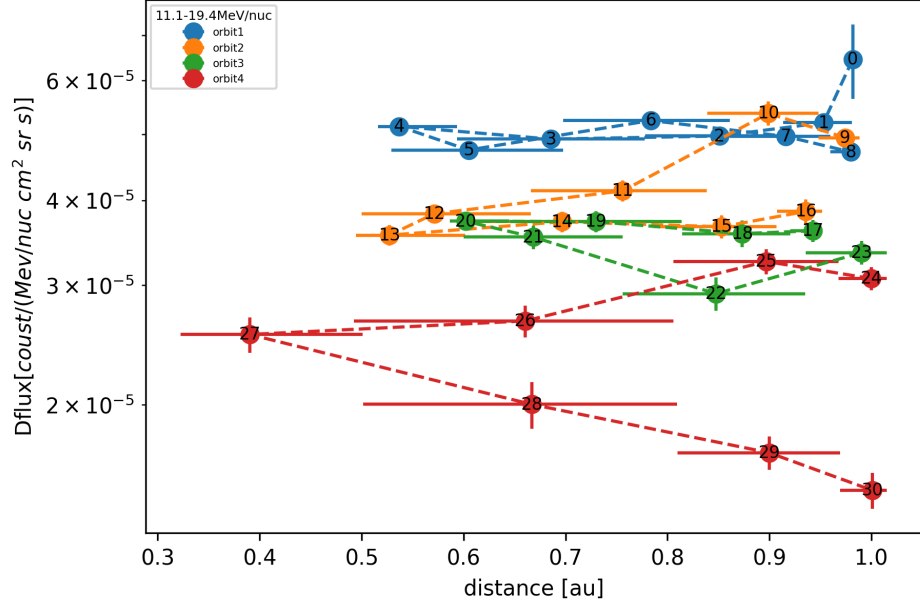


Figure 25: The change of flux of 11.1 - 19.4 MeV/nuc helium from HET with respect to the radial distance of SolO. The data for different orbits are presented in distinct colors. The numbers over data points indicate the order of time.

points from the first three orbits are shown and fitted. That is because SEPs are the dominant particles in the fourth orbit. Hence, most of the data are removed, causing considerably higher uncertainties in the result. The colored dashed lines in the figure represent the fitting results obtained for different orbits. The shaded regions surrounding these lines are the corresponding 95% confidence intervals, indicating the uncertainty of the fitting results. The averaged radial gradients of the first three orbits are depicted as black dashed lines, indicating the overall trend between 2020 and 2022. In addition, we have summarized the radial gradient of ACR helium in different energy channels and for different orbits in Table 3.

Number of Orbit	1	2	3	4	ave(1-3)
Energy (MeV/nuc)	20200228 - 20201012	20201012 - 20210602	20210602 - 20211216	20211216 - 20220704	
10 - 20	27 ± 9	38 ± 14	21 ± 19	-25 ± 22	28 ± 8
20 - 30	19 ± 9	28 ± 20	11 ± 15	33 ± 16	19 ± 08
30 - 40	5 ± 14	12 ± 14	37 ± 21	8 ± 21	10 ± 11
40 - 50	5 ± 9	27 ± 21	58 ± 19	20 ± 18	21 ± 11

Table 3: Radial gradient of helium (%/au) in different energy channels at different orbits between 2020 and 2022.

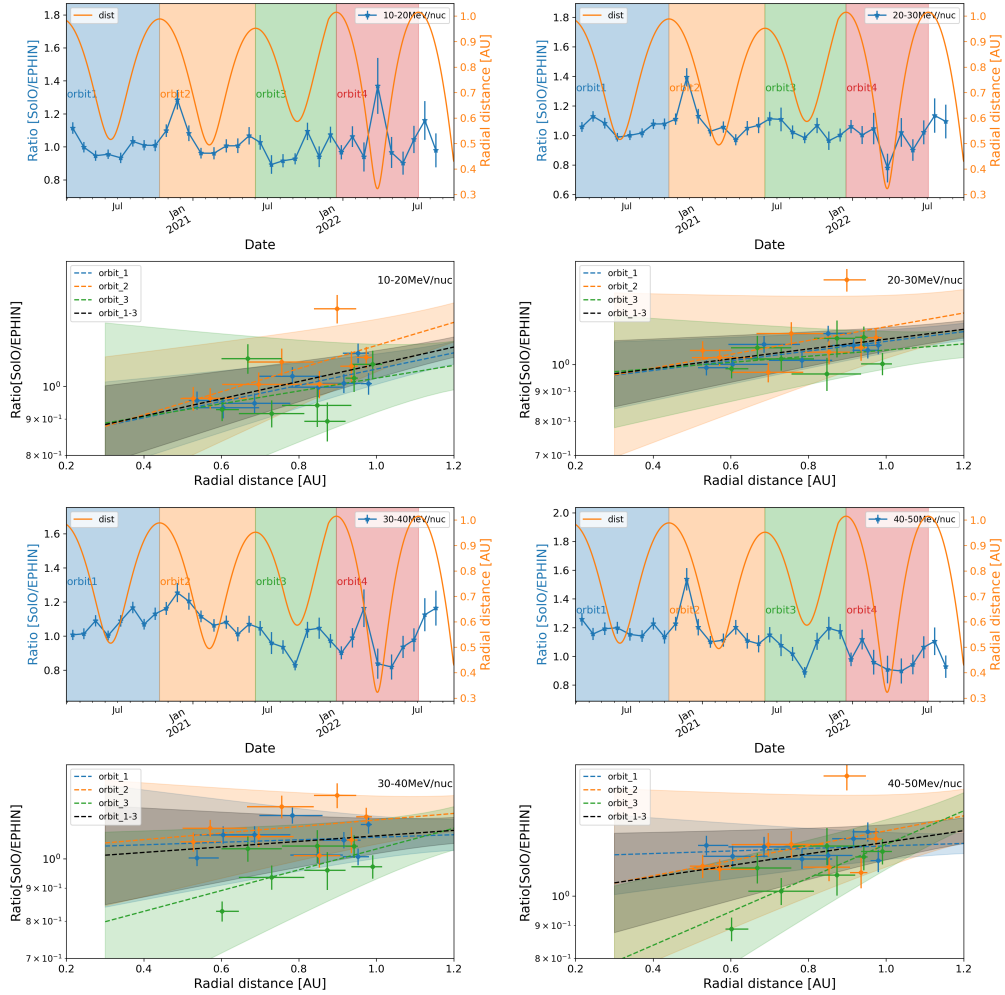


Figure 26: Row 1 and 3: The temporal variation of the helium flux ratio between HET and EPHIN measurements (averaged over their own Carrington rotation and interpolated to calculate the ratio) for different energies; Row 2 and 4: Flux ratio vs radial gradients in the first three orbits, overlay by the log-linear fitting lines.

Radial gradient of helium vs energy

Fig. 27 displays the energy dependence of the radial gradient of ACR helium measured by PSP and SolO. Despite the significant uncertainties, radial gradients of helium measured by SolO averaged over the first three orbits are shown as orange diamonds. Except for helium in the energy range of 30 - 40 MeV/nuc, which has a lower average gradient of $10 \pm 11\% / \text{au}$, we report radial gradients of $28 \pm 8\% / \text{au}$, $19 \pm 8\% / \text{au}$, and $21 \pm 11\% / \text{au}$ for helium energies of 10 - 20 MeV/nuc, 20 - 30 MeV/nuc and 40 - 50 MeV/nuc respectively. Such gradients are consistent with PSP's results within the uncertainties. To compare with PSP results derived by Rankin et al. (2021), we replot helium radial gradients as the blue circles at their energy range. PSP measurements are from 2018 to 2019 in the

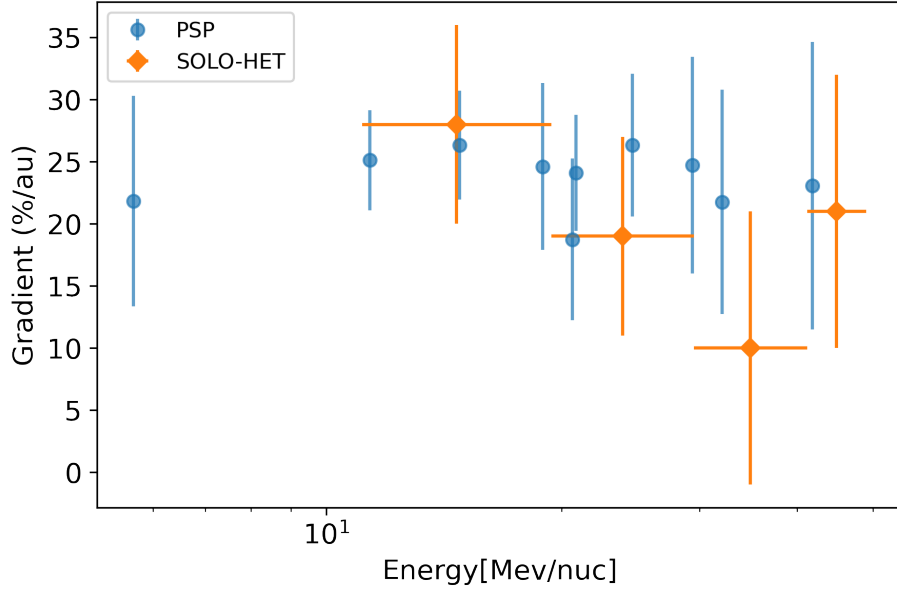


Figure 27: The radial gradient of helium measured in the ecliptic plane at different energies. The values from HET are given as orange diamonds with corresponding error bars. The multiple blue circles in the figure represent the gradient obtained from PSP (Rankin et al., 2021).

same solar activity minimum but earlier than SolO. The averaged radial gradient of helium in the energy range of 4 - 45 MeVn/nuc is about 25 ± 5 %/au.

The time variation of the radial gradient

We also present the time variation of the helium radial gradients for different energy ranges from 10 - 50 MeV/nuc in Fig. 28. The behaviors exhibited by the various energy channels are distinct, and the radial gradients show significant variations from 2020 to 2022, probably due to increased solar activity. Several intriguing features are observed in the time variation of the radial gradients, which are unexpected and hard to explain.

The peaks of radial gradients occur at different times for each energy channel. The highest radial gradient for the 10 - 20 Mev/nuc helium channel appears during the second orbit, while for the 30 - 50 Mev/nuc channels, the peaked gradients are observed in the subsequent orbit.

Furthermore, the sign of the radial gradient in the energy range of 10 - 20 MeV/nuc changes from positive to negative during the fourth orbit in 2022. This change could be attributed to the more considerable uncertainties introduced by SEPs. Because of the more frequently appeared SEP in the fourth orbit, we might remove most of the data from EPHIN measurements in one Carrington rotation; thus, the remaining days' measurements are likely not representative of the whole Carrington rotation. Consequently, the Carrington averaged EPHIN flux in the fourth orbit exhibit more fluctuations than the previous periods. An alternative explanation for the observed sign change in the radial gradient could be attributed

to the complex magnetic field structures in the inner heliosphere governed by the Sun and solar activity. For instance, near the Sun, the radial components are overwhelmed by the transverse magnetic fluctuations (Rankin et al., 2022) in the inner heliosphere below 1 au, causing a different transport environment than in the outer heliosphere. On the other hand, with the Sun becoming more active than before, the large-scale HMF might also be distorted by transient eruptions such as CMEs.

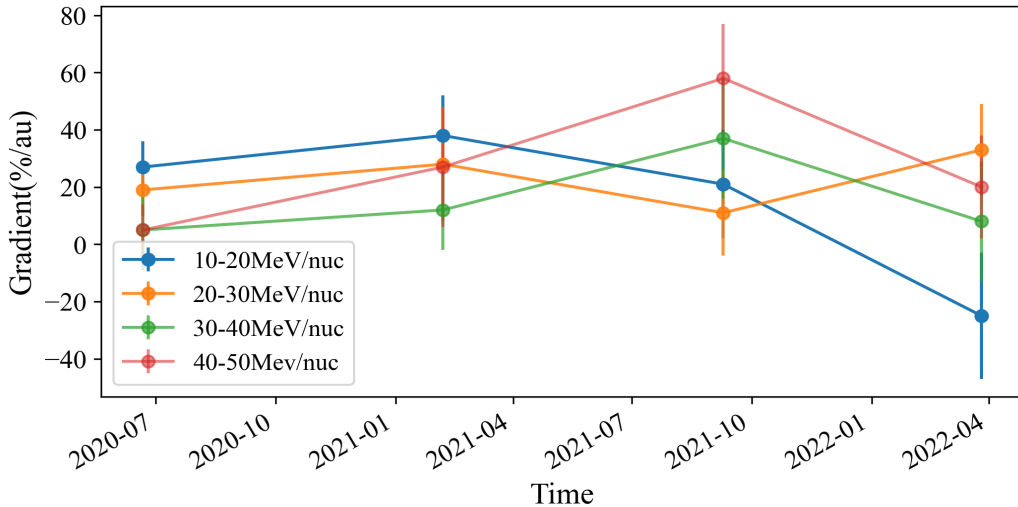


Figure 28: The time variation of the ACR helium radial gradients from 2020 to 2022.

7.6 SUMMARY AND DISCUSSION

We presented the ACR helium in the energy range of 10 - 50 MeV/nuc, measured by SolO/HET between Feb 2020 and Sep 2022. The first half of this time period was still the solar activity minimum at the end of solar cycle 24, characterized by minimal solar activity, while the second half witnessed an increasing number of SEPs. Comparisons between the helium spectra obtained by HET, EPHIN, and ACE/SIS show general agreement. Furthermore, SolO and ACE exhibit consistent measurements of carbon, oxygen, and nitrogen.

By utilizing the EPHIN measurements as a baseline, we derive the radial gradient of ACR helium in the inner heliosphere. We reduce the effects of long-term solar modulation by dividing the intensity of HET by that of EPHIN after we remove the interference by SEPs and the potential short-term variations due to CIRs. We report that the radial gradients for helium energies of 10 - 20 MeV/nuc, 20 - 30 MeV/nuc, and 40 - 50 MeV/nuc are 28 ± 8 %/au, 19 ± 8 %/au, and 21 ± 11 %/au respectively. These results are consistent with gradients obtained by PSP within the uncertainty. Interestingly, the averaged radial gradient in the energy range of 30 - 40 MeV/nuc is only half that in the other channels, about 10 ± 11 %/au. Currently, those results are very preliminary, and more investigation is needed to improve the results and explain this feature.

The analysis above shows how challenging it is to derive the radial gradient of ACR helium. In addition to the intensity decrease caused by the long-term solar modulation, the more problematic component is the remanent SEPs that may not have been recognized from the time series of the proton flux from EPHIN and the L₂ trigger rate of HET. Here, we proposed additional methods to derive cleaner ACR measurements.

The first method sets a threshold for the particle intensity that will be used to calculate the averaged flux. By doing so, the data points of intensity higher than the threshold will be filtered out. In practice, we chose the threshold of 95 % of the sum of helium accumulated in one Carrington rotation. This method is under the assumption that the highest intensity particles are from SEPs that we could not identify. As a result, the radial gradients with this extra mask are consistent with the gradients we obtained above. We derive the gradients of $27 \pm 7 \text{ \% / au}$, $16 \pm 8 \text{ \% / au}$ and $21 \pm 11 \text{ \% / au}$ for helium energies of 10 - 20 MeV/nuc, 20 - 30 MeV/nuc and 40 - 50 MeV/nuc, respectively.

Due to the high time resolution and limited FOV of HET data products, the count rates of helium measurements are discrete values and, most of the time, are zeros, as the data show. The distribution of the count rate should be described by a Poisson distribution with a parameter λ equal to the mean values. The second method assumes that the ACR background, which is unaffected by any modulation effects, has constant intensity during a specific period, for instance, one day. A mean value could represent the measurements of this background. However, when the background is interrupted by short-time structures, regardless of whether it causes the flux to increase or decrease, the Poisson distribution with mean values as λ s can not model the count rate distribution. Note that this method is only applied to disentangle short-term changes. In practice, firstly, we calculate the mean value during one day. Secondly, we estimate the probability that the measurements follow a Poisson distribution with the λ equal to the mean value. By doing so, we obtain the same table as in Table 3, and the new results are given below in Table 4. The averaged gradients over the first three orbits are 34 ± 8 , 22 ± 10 , 19 ± 11 for helium energies of 10 - 20 MeV/nuc, 20 - 30 MeV/nuc, and 40 - 50 MeV/nuc, respectively.

We agree that some other methods could also be used to derive the radial gradient of ACR helium in the future. For instance, we could use the median value rather than the mean value to represent the flux of the center Carrington rotation. The purpose of this method is that median values are less affected by outliers. Hence we could avoid the higher energy tails, if there are any, after we remove SEPs discussed before. Besides, we could also use the daily averaged flux rather than the mean value of a full Carrington rotation to calculate the ratio between HET and EPHIN.

Furthermore, as discussed in Rankin et al. (2021), the GCR helium should also be considered in the energy range of 10 - 50 MeV/nuc. According to the spectra predicted from the simulation, the GCR helium intensity increases with the energy before it peaks at a few hundred MeV. Rankin et al. (2021) found that after subtract the assumed GCR intensity, the radial gradient becomes larger. Therefore, we will

also consider this correction in future work once we find a proper way to estimate the varying GCR helium intensity.

Here, we present the result of our analysis of the radial gradient without giving any detailed explanations. Nevertheless, linking our current observations to the previous results and our present knowledge of cosmic ray transport will significantly advance our understanding of the transport of ACRs in the inner heliosphere.

Number of Orbit	1	2	3	4	ave(1-3)
Energy (MeV/nuc)	20200228 - 20201012	20201012- 20210602	20210602- 20211216	20211216- 20220704	
10 - 20	43 ± 10	21 ± 18	41 ± 13	40 ± 49	34 ± 8
20 - 30	34 ± 13	23 ± 19	-9 ± 13	-16 ± 28	22 ± 10
30 - 40	8 ± 15	19 ± 14	41 ± 22	10 ± 20	13 ± 12
40 - 50	15 ± 4	15 ± 24	55 ± 32	65 ± 33	19 ± 11

Table 4: The radial gradient of helium (%/au) in the same format as Tab. 3 but with the extra mask to remove the potential short-term variation.

8

CONCLUSION AND OUTLOOK

The main topic of this thesis is to better understand energetic particles measured by new instruments during the new solar cycle. Since they contain critical information on particles' acceleration, injection, and propagation mechanisms in space, energetic particles within the energy range of tens of MeV in the heliosphere are of great importance. Besides, the even higher energy particles (hundreds of MeV) are a potential hazard to the health of astronaut who works in deep space, especially during the period without the protection of the spacecraft hull.

Benefiting from two new instruments, the Lunar Lander Neutron and Dosimetry Experiment (LND) on board Chang'E-4 operating on the lunar surface and the High Energy Telescope (HET) on board the Solar Orbiter (SolO) orbiting and approaching the Sun, we have an excellent opportunity to improve our understanding of these energetic particles. Therefore, in this thesis, all three particle populations in the energy range between a few MeV/nuc and a few hundred MeV/nuc, including solar energetic particles (SEPs), galactic cosmic rays (GCRs), and anomalous cosmic rays (ACRs) are thoroughly investigated. We summarize the key results we obtained and link them to the scientific questions we asked in the motivation section (Sec. 1.2).

In the first publication presented in Chapter 4, we try to answer two questions regarding the SEPs: "What is the source of those energetic particles?" (S1) and "How do those energetic particles arrive at distant longitudes?" (S2)

We report the first SEP event measured on the lunar far-side surface, during which the peak energy of protons is about 20 MeV. This SEP event persists for less than one day, and the time profiles of electrons and protons show clear velocity dispersion and are anisotropic during the start of the event. We first derive the proton integrated spectrum, which is comparable with measurements from other L1 instruments. Then, we infer the release times of protons and electrons using the velocity dispersion method. We find an hour earlier injection of electrons than protons. Meanwhile, the flare originates from a distant but solitary active region on the solar disk. A slowly moving coronal mass ejection (CME) appeared in the coronagraph of SOHO after the eruption of the solar flare. This intriguing event indicates the contradiction between the in-situ and remote-sensing observations. The in-situ measurements suggest that this event should be well-connected to the particle source. However, the remote-sensing data show that the active region is located at more than 100 degrees east of the magnetic footpoint of the LND. The different release times of protons and electrons might indicate the different acceleration and transport mechanisms. After excluding the possibility of local acceleration, the flare and the CME driven shock appear to be the most credible source of these energetic particles in this event.

We propose potential transport mechanisms that could account for the traversal of protons and electrons within the lower coronal region and over the heliosphere,

such as expanding CME-driven shocks, irregular magnetic field lines, and even transport path diverging from the nominal Parker spiral field. Furthermore, the idea of the Heliospheric Current Sheet (HCS) serving as the transport bridge of energetic particles between the solar source and L1 in this special case was brought up (Battarbee et al., 2018), even though the detailed transport mechanism remains unclear and needs further investigation. By analyzing multiple spacecraft/instrument observations, we discuss the source of tens of MeV protons and a few hundred keV electrons and their possible transport in the heliosphere. Our results indicate the necessity of using multiple spacecraft/instrument observations to study the SEP events and the complexity of the SEP events.

In addition to SEPs, GCRs and secondary particles, for example, albedo protons, are also essential components of the radiation environment on the lunar surface. Therefore, in the second publication, we present the GCR proton spectrum and the intensity of albedo protons during 2019-2020. The studies of GCRs related to the question, "How do the ACRs and GCR behave during the most recent solar activity minimum and the onset phase of solar cycle 25?" (C1); "What is the difference between the current solar cycle and the previous one?" (C2), and "How does solar modulation affect the intensity of cosmic rays?" (C3). Besides, the albedo proton measurements answer the question, "How do those secondary particles induced by those cosmic rays affect the radiation environment on the lunar surface?" (C5).

Both primary and albedo proton measurements are taken by LND on the lunar surface for the first time. The primary GCR proton spectrum spans the energy range from ~ 10 to ~ 400 MeV, including both the stopping and penetrating particles of LND. However, at present, the uncertainty of the penetrating data products is still more significant than anticipated. More efforts are needed to improve these data products. The proton measurements from SOHO/EPHIN during the same periods in the energy range of 10-50 MeV are consistent with the LND measurements. Our measurements find that the intensities of lower energy GCR protons are higher than those during the prior solar activity minimum, reaching a historical record since the start of the space age, indicating the impact of solar modulation on the variability of cosmic rays.

Moreover, we obtained intensities of 65 - 76 MeV albedo protons on the lunar surface. The flux of albedo protons in this solar activity minimum is consistent with that in the previous solar activity minimum, obtained by LRO/CRaTER between 2009 - 2010 in the lunar orbit. By calculating the intensity ratio of albedo to primary protons, we confirm that below approximately 50 MeV, the albedo protons are the predominant component of the proton flux during quiet times on the lunar surface.

Meanwhile, the analysis of the quite-time measurements of protons, helium-4, helium-3, oxygen, carbon, and iron from Mason et al. (2021b) obtained the ion spectra during the solar activity minimum 24/25 between 0.5 - 1.0 au. The lower energy measurement is made by Solo/SIS, and the higher energy part is measured by HET. These spectra are comprised of the GCR components, the ACR components, and the spectrum of the low energy particles, which could be the residual particles of the preceding impulsive SEP events. These measurements

show similar characteristics of particle spectra compared to previous solar activity minimum, providing the potential answer to question C2.

Chapter 7 is a forthcoming publication focusing on heavy ions obtained from HET between 2020 and 2022. In particular, the focus is on the ACR helium and their spatial distributions, which contain transport information of cosmic rays in the inner heliosphere. This part gives the answer to question, "How do the cosmic rays distribute within the inner heliosphere?" (C4). As an ongoing project, we only report the result of data analysis here without further explanation. Using cross-calibrating methods, we find that the spectra of heavy ions derived from different instruments are consistent. The intensity time profiles of ACR helium are obtained after thoroughly removing short-term enhancement from SEPs. These profiles clearly show the decrease in the intensity of cosmic rays, which is caused by long-term solar modulation. After properly considering the possible modulation effects, which are the most challenging part of our data analysis, we derive the radial gradients of 10 - 50 MeV/nuc ACR helium that are measured by SolO/HET between 0.3 and 1 au. The radial gradients are $28 \pm 8\%$ /au, $19 \pm 8\%$ /au, $10 \pm 11\%$ /au, $21 \pm 11\%$ /au for helium energies of 10 - 20 MeV/nuc, 20 - 30 MeV/nuc, 30 - 40 MeV/nuc, and 40 - 50 MeV/nuc respectively. We also get consistent results from different methods. Such gradients are consistent with results obtained from Parker Solar Probe (PSP) measurements. We also discuss the time variation of those gradients and their implication on the change of transport conditions as the increase of solar activities. The further explanation of these intriguing results will be the focus of the next step. In the future, we plan to implement the same data analysis approach to ACR oxygen in the energy range of 5 - 25 MeV/nuc and even the GCR particles to draw a complete picture of the spatial gradients of cosmic rays in the inner heliosphere. We hope we can advance our current understanding of the transport of cosmic rays in the inner heliosphere.

In short, the excellent charged particle measurements obtained by LND and HET have improved our understanding of the relationship between the Sun and the heliosphere and are of great help in preparing for future human exploration on the Moon and in deep space. We should take good care of these fragile instruments and fully employ the fruitful data they provide to expand our knowledge of the heliosphere.

BIBLIOGRAPHY

- Adams J. H., J. et al. (1991). "The Charge State of the Anomalous Component of Cosmic Rays." In: *The Astrophysical Journal Letter* 375, page L45. doi: 10.1086/186084.
- Agostinelli, S. et al. (2003). "Geant4—a simulation toolkit." In: *Nuclear Instruments and Methods in Physics Research Section A: Accelerators, Spectrometers, Detectors and Associated Equipment* 506.3, pages 250–303. doi: 10.1016/S0168-9002(03)01368-8.
- Allen, R. C. et al. (2021a). "Energetic ions in the Venusian system: Insights from the first Solar Orbiter flyby." In: *Astronomy & Astrophysics* 656, A7, A7. doi: 10.1051/0004-6361/202140803.
- Allen, R. C. et al. (2021b). "Suprathermal particles from corotating interaction regions during the first perihelion pass of Solar Orbiter." In: *Astronomy & Astrophysics* 656, L2, page L2. doi: 10.1051/0004-6361/202039870.
- Aran, A. et al. (2021). "Evidence for local particle acceleration in the first recurrent galactic cosmic ray depression observed by Solar Orbiter. The ion event on 19 June 2020." In: *Astronomy & Astrophysics* 656, L10, page L10. doi: 10.1051/0004-6361/202140966.
- Armstrong, T. et al. (2014). "Strategies for mitigation based on increased knowledge of the solar particle radiation hazard en route to/at mars for spacecraft systems and for astronauts/cosmonauts." In: *The Particle Radiation Hazard enroute to and at Mars. Publ. Internat. Acad. Astronautics*.
- Battarbee, M., S. Dalla, and M. S. Marsh (2018). "Modeling Solar Energetic Particle Transport near a Wavy Heliospheric Current Sheet." In: *The Astrophysical Journal* 854.1, 23, page 23. doi: 10.3847/1538-4357/aaa3fa.
- Bethe, H. A. (1930). "Zur Theorie des Durchgangs schneller Korpuskularstrahlen durch Materie." In: *Ann. d. Phys.* 5, page 325.
- Bhattacharjee, P. (2000). "Origin and propagation of extremely high energy cosmic rays." In: *Physics Reports* 327, pages 109–247. doi: 10.1016/S0370-1573(99)00101-5.
- Blandford, R. D. and J. P. Ostriker (1978). "Particle acceleration by astrophysical shocks." In: *The Astrophysical Journal* 221, pages L29–L32.
- Blasi, P. (2013). "The origin of galactic cosmic rays." In: *The Astronomy and Astrophysics Review* 21, 70, page 70. doi: 10.1007/s00159-013-0070-7.
- Bloch, F. (1933). "Zur Bremsung rasch bewegter Teilchen beim Durchgang durch Materie." In: *Ann. d. Phys.* 16, page 285.
- Boschini, M. J. et al. (2018). "Propagation of cosmic rays in heliosphere: The HELMOD model." In: *Advances in Space Research* 62.10, pages 2859–2879. doi: 10.1016/j.asr.2017.04.017.
- (2019). "The HELMOD model in the works for inner and outer heliosphere: From AMS to Voyager probes observations." In: *Advances in Space Research* 64.12, pages 2459–2476. doi: 10.1016/j.asr.2019.04.007.
- (2022). "Forecasting of cosmic rays intensities with HELMOD Model." In: *Advances in Space Research* 70.9, pages 2649–2657. doi: 10.1016/j.asr.2022.01.031.
- Burlaga, L. F. (1974). "Interplanetary stream interfaces." In: *Journal of Geophysical Research* 79.25, page 3717. doi: 10.1029/JA079i025p03717.
- Bučík, R. et al. (2021). "The long period of ${}^3\text{He}$ -rich solar energetic particles measured by Solar Orbiter 2020 November 17–23." In: *Astronomy & Astrophysics* 656, L11, page L11. doi: 10.1051/0004-6361/202141009.
- Bučík, R. et al. (2023). "The first gradual solar energetic particle event with an enhanced ${}^3\text{He}$ abundance on Solar Orbiter." In: *Astronomy & Astrophysics* 669, A13, A13. doi: 10.1051/0004-6361/202245037.

- Cane, H., R. McGuire, and T. Von Rosenvinge (1986). "Two classes of solar energetic particle events associated with impulsive and long-duration soft x-ray flares." In: *The Astrophysical Journal* 301, pages 448–459.
- Cane, H. et al. (2003). "Two components in major solar particle events." In: *Geophysical research letters* 30.12.
- Chertok, I. M. (2022). "On some features of the solar proton event on 2021 October 28 - GLE73." In: *Monthly Notices of the Royal Astronomical Society* 517.2, pages 2709–2713. doi: 10.1093/mnras/stac2843.
- Christon, S. P. et al. (1986). "Differential measurement and model calculations of cosmic ray latitudinal gradient with respect to the heliospheric current sheet." In: *Journal of Geophysical Research* 91.A3, pages 2867–2878. doi: 10.1029/JA091iA03p02867.
- Cliver, E. W. et al. (1995). "Extreme "Propagation" of Solar Energetic Particles." In: *International Cosmic Ray Conference*. Volume 4. International Cosmic Ray Conference, page 257.
- Cliver, E. et al. (1982). "Injection onsets of 2 gev protons, 1 mev electrons, and 100 kev electrons in solar cosmic ray flares." In: *The Astrophysical Journal* 260, pages 362–370.
- Corti, C. et al. (2019). "Numerical Modeling of Galactic Cosmic-Ray Proton and Helium Observed by AMS-02 during the Solar Maximum of Solar Cycle 24." In: *The Astrophysical Journal* 871.2, 253, page 253. doi: 10.3847/1538-4357/aafac4.
- Cucinotta, F. A. and M. Durante (2006). "Cancer risk from exposure to galactic cosmic rays-implications for human space exploration." In: *Lancet Oncology*.
- Cummings, A. et al. (2019). "Voyager 2 Observations of the Anisotropy of Anomalous Cosmic Rays in the Heliosheath." In: *36th International Cosmic Ray Conference (ICRC2019)*. Volume 36. International Cosmic Ray Conference, 1071, page 1071. doi: 10.22323/1.358.01071.
- Cummings, A. C., E. C. Stone, and W. R. Webber (1987). "Latitudinal and radial gradients of anomalous and galactic cosmic rays in the outer heliosphere." In: *Geophysical Research Letters* 14.3, pages 174–177. doi: 10.1029/GL014i003p00174.
- Cummings, A. C. et al. (1995). "Anomalous cosmic ray oxygen gradients throughout the heliosphere." In: *Geophysical Research Letters* 22.4, pages 341–344. doi: 10.1029/94GL03343.
- Cummings, A. C. et al. (2009). "Radial and latitudinal gradients of anomalous cosmic ray oxygen in the inner heliosphere." In: *Geophysical Research Letters* 36.18, L18103, page L18103. doi: 10.1029/2009GL039851.
- Cummings, A. C. et al. (2016). "Galactic Cosmic Rays in the Local Interstellar Medium: Voyager 1 Observations and Model Results." In: *The Astrophysical Journal* 831.1, 18, page 18. doi: 10.3847/0004-637X/831/1/18.
- de Simone, N. et al. (2011). "Latitudinal and radial gradients of galactic cosmic ray protons in the inner heliosphere - PAMELA and Ulysses observations." In: *Astrophysics and Space Sciences Transactions* 7.3, pages 425–434. doi: 10.5194/astra-7-425-2011.
- Desai, M. and J. Giacalone (2016). "Large gradual solar energetic particle events." In: *Living Reviews in Solar Physics* 13, 3, page 3. doi: 10.1007/s41116-016-0002-5.
- Dobynde, M. I. and J. Guo (2021). "Radiation Environment at the Surface and Subsurface of the Moon: Model Development and Validation." In: *Journal of Geophysical Research (Planets)* 126.11, e06930, e06930. doi: 10.1029/2021JE006930.
- Dresing, N. et al. (2012). "The Large Longitudinal Spread of Solar Energetic Particles During the 17 January 2010 Solar Event." In: *Solar Physics* 281.1, pages 281–300. doi: 10.1007/s11207-012-0049-y.
- Dresing, N. (2014). "THE LONGITUDINAL DISTRIBUTION OF ENERGETIC PARTICLES IN THE INNER HELIOSPHERE- MULTIPOINT OBSERVATIONS WITH STEREO." PhD thesis. Kiel University.

- Dresing, N. et al. (2023). "The 17 april 2021 widespread solar energetic particle event." In: *A&A* 674, A105. doi: 10.1051/0004-6361/202345938.
- Elftmann, R. (2020). "The High Energy Telescope on Solar Orbiter: Development and Validation of the Onboard Data Processing." PhD thesis. URL: https://macau.uni-kiel.de/receive/macau_mods_00000608.
- Fermi, E. (1949). "On the Origin of the Cosmic Radiation." In: *Physical Review* 75.8, pages 1169–1174. doi: 10.1103/PhysRev.75.1169.
- Fisk, L. A., B. Kozlovsky, and R. Ramaty (1974). "An Interpretation of the Observed Oxygen and Nitrogen Enhancements in Low-Energy Cosmic Rays." In: *The Astrophysical Journal Letter* 190, page L35. doi: 10.1086/181498.
- Forbush, S. E. (1946). "Three Unusual Cosmic-Ray Increases Possibly Due to Charged Particles from the Sun." In: *Physical Review* 70, pages 771–772. doi: 10.1103/PhysRev.70.771.
- Forbush, S. and I. Lange (1942). "Further note on the effect on cosmic-ray intensity of the magnetic storm of march 1." In: *Terr. Magn. Atmos. Electr* 47, pages 331–334.
- Forstner, J. L. Freiherr von et al. (2021). "Radial evolution of the April 2020 stealth coronal mass ejection between 0.8 and 1 AU: A comparison of Forbush decreases at Solar Orbiter and Earth." In: *A&A*. doi: 10.1051/0004-6361/202039848.
- Forstner, J. L. Freiherr von (2020). "Multipoint observations of ICMEs in the inner heliosphere: Forbush decreases and remote sensing." en. PhD thesis. URL: https://macau.uni-kiel.de/receive/macau_mods_00001144.
- Fox, N. J. et al. (2016). "The Solar Probe Plus Mission: Humanity's First Visit to Our Star." In: *Space Science Reviews* 204.1-4, pages 7–48. doi: 10.1007/s11214-015-0211-6.
- Fu, S. et al. (2021). "Variations of the Galactic Cosmic Rays in the Recent Solar Cycles." In: *The Astrophysical Journal Supplement Series* 254.2, 37, page 37. doi: 10.3847/1538-4365/abf936.
- Garcia-Munoz, M., G. M. Mason, and J. A. Simpson (1973). "The Anomalous 1972 Low Energy Galactic Cosmic Ray Proton and Helium Spectra." In: *International Cosmic Ray Conference*. Volume 2. International Cosmic Ray Conference, page 1304.
- Giacalone, J., J. F. Drake, and J. R. Jokipii (2012). "The Acceleration Mechanism of Anomalous Cosmic Rays." In: *Space Science Reviews* 173.1-4, pages 283–307. doi: 10.1007/s11214-012-9915-z.
- Giacalone, J. et al. (2022). "Anomalous Cosmic Rays and Heliospheric Energetic Particles." In: *Space Science Reviews* 218.4, 22, page 22. doi: 10.1007/s11214-022-00890-7.
- Gieseler, J. and B. Heber (2016). "Spatial gradients of GCR protons in the inner heliosphere derived from Ulysses COSPIN/KET and PAMELA measurements." In: *Astronomy & Astrophysics* 589, A32, A32. doi: 10.1051/0004-6361/201527972.
- Gleeson, L. J. and W. I. Axford (1967). "Cosmic Rays in the Interplanetary Medium." In: *The Astrophysical Journal Letter* 149, page L115. doi: 10.1086/180070.
- (1968). "Solar Modulation of Galactic Cosmic Rays." In: *The Astrophysical Journal* 154, page 1011. doi: 10.1086/149822.
- Gleeson, L. J. and I. H. Urch (1973). "A Study of the Force-Field Equation for the Propagation of Galactic Cosmic Rays." In: *Astrophysics and Space Science* 25.2, pages 387–404. doi: 10.1007/BF00649180.
- Gloeckler, G. et al. (1995). "The Solar Wind and Suprathermal Ion Composition Investigation on the Wind Spacecraft." In: *Space Science Reviews* 71.1-4, pages 79–124. doi: 10.1007/BF00751327.
- Gómez-Herrero, R. et al. (2021). "First near-relativistic solar electron events observed by EPD onboard Solar Orbiter." In: *Astronomy & Astrophysics*. doi: 10.1051/0004-6361/202039883.

- Gopalswamy, N et al. (2013). "The first ground level enhancement event of solar cycle 24: direct observation of shock formation and particle release heights." In: *The Astrophysical Journal Letters* 765.2, page L30.
- Gopalswamy, N. (2006). "Coronal Mass Ejections and Type II Radio Bursts." In: *Geophysical Monograph Series* 165, page 207. doi: 10.1029/165GM20.
- Gosling, J. T. (1993). "The solar flare myth." In: *Journal of Geophysical Research* 98, pages 18937–18950. doi: 10.1029/93JA01896.
- Gosling, J. T., A. J. Hundhausen, and S. J. Bame (1976). "Solar wind stream evolution at large heliocentric distances: Experimental demonstration and the test of a model." In: *Journal of Geophysical Research* 81.13, page 2111. doi: 10.1029/JA081i013p02111.
- Guo, J. et al. (2021). "Radiation environment for future human exploration on the surface of Mars: the current understanding based on MSL/RAD dose measurements." In: *The Astronomy and Astrophysics Review* 29.1, 8, page 8. doi: 10.1007/s00159-021-00136-5.
- Guo, J. et al. (2023). "The First Ground Level Enhancement Seen on Three Planetary Surfaces: Earth, Moon, and Mars." In: *Geophysical Research Letters* 50.15, e2023GL103069, e2023GL103069. doi: 10.1029/2023GL103069.
- Hassler, D. M. et al. (2012). "The Radiation Assessment Detector (RAD) investigation." In: *Space Science Reviews* 170.1, pages 503–558. doi: 10.1007/s11214-012-9913-1.
- Heber, B. et al. (1996a). "Spatial variation of ζ_{106} Mev proton fluxes observed during the Ulysses rapid latitude scan: Ulysses COSPIN/KET results." In: *Geophysical Research Letters* 23.12, pages 1513–1516. doi: 10.1029/96GL01042.
- Heber, B. et al. (1996b). "Spatial variation of ζ_{40} MeV/n nuclei fluxes observed during the ULYSSES rapid latitude scan." In: *Astronomy & Astrophysics* 316, pages 538–546.
- Heber, B. et al. (1998). "Latitudinal distribution of ζ_{106} MeV protons and its relation to the ambient solar wind in the inner southern and northern heliosphere: Ulysses Cosmic and Solar Particle Investigation Kiel Electron Telescope results." In: *Journal of Geophysical Research* 103.A3, pages 4809–4816. doi: 10.1029/97JA01984.
- Heber, B. et al. (2008). "Latitudinal Gradients of Galactic Cosmic Rays during the 2007 Solar Minimum." In: *The Astrophysical Journal* 689.2, pages 1443–1447. doi: 10.1086/592596.
- Hörandel, J. R. (2003). "On the knee in the energy spectrum of cosmic rays." In: *Astroparticle Physics* 19.2, pages 193–220. doi: 10.1016/S0927-6505(02)00198-6.
- Hou, D. et al. (2020). "Removing the dose background from radioactive sources from active dose rate measurements in the Lunar Lander Neutron & Dosimetry (LND) experiment on Chang'E 4." In: *Journal of Instrumentation* 15.1, Po1032. doi: 10.1088/1748-0221/15/01/P01032.
- Hovestadt, D. et al. (1973). "Differential Energy Spectra of Low-Energy (≥ 8.5 MeV per Nucleon) Heavy Cosmic Rays during Solar Quiet Times." In: *Physical Review Letters* 31.10, pages 650–653. doi: 10.1103/PhysRevLett.31.650.
- Hundhausen, A., H. Gilbert, and S. Bame (1968). "The state of ionization of oxygen in the solar wind." In: *The Astrophysical Journal* 152, page L3.
- Huttunen-Heikinmaa, K., E. Valtonen, and T. Laitinen (2005). "Proton and helium release times in SEP events observed with SOHO/ERNE." In: *Astronomy & Astrophysics* 442.2, pages 673–685. doi: 10.1051/0004-6361:20042620.
- Iancu, O. D. et al. (2018). "Space radiation alters genotype–phenotype correlations in fear learning and memory tests." In: *Frontiers in Genetics* 9. doi: 10.3389/fgene.2018.00404.
- Jokipii, J. R. (1990). "Cosmic rays in the heliosphere: Present status and future opportunities." In: *Particle Astrophysics - The NASA Cosmic Ray Program for the 1990s and Beyond*. Edited by W. V. Jones, F. J. Kerr, and J. F. Ormes. Volume 203. American Institute of Physics Conference Series, pages 155–167. doi: 10.1063/1.39148.
- Jokipii, J. R. and D. A. Kopriva (1979). "Effects of particle drift on the transport of cosmic rays. III. Numerical models of galactic cosmic-ray modulation." In: *The Astrophysical Journal* 234, pages 384–392. doi: 10.1086/157506.

- Jokipii, J. R., E. H. Levy, and W. B. Hubbard (1977). "Effects of particle drift on cosmic-ray transport. I. General properties, application to solar modulation." In: *The Astrophysical Journal* 213, pages 861–868. doi: 10.1086/155218.
- Jokipii, J. R. and B. Thomas (1981). "Effects of drift on the transport of cosmic rays. IV - Modulation by a wavy interplanetary current sheet." In: *The Astrophysical Journal* 243, pages 1115–1122. doi: 10.1086/158675.
- Kahler, S. W. and A. G. Ling (2019). "Suprathermal Ion Backgrounds of Solar Energetic Particle Events." In: *The Astrophysical Journal* 872.1, 89, page 89. doi: 10.3847/1538-4357/aafb03.
- Kahler, S., E Hildner, and M. Van Hollebeke (1978). "Prompt solar proton events and coronal mass ejections." In: *Solar Physics* 57.2, pages 429–443.
- Kahler, S. et al. (1984). "Associations between coronal mass ejections and solar energetic proton events." In: *Journal of Geophysical Research: Space Physics* 89.A11, pages 9683–9693.
- Kallenrode, M. (2003). "Current views on impulsive and gradual solar energetic particle events." In: *Journal of Physics G: Nuclear and Particle Physics* 29.5, page 965.
- Kennedy, A. R. (2014). "Biological effects of space radiation and development of effective countermeasures." In: *Life Sciences and Space Research* 1, pages 10–43. doi: 10.1016/j.lssr.2014.02.004.
- Kerr, G. D. (1988). "Quality factors." In: *Health Physics* 55.2. URL: https://journals.lww.com/health-physics/Fulltext/1988/08000/Quality_Factors.16.aspx.
- Kilpua, E. K. J. et al. (2021). "Multi-spacecraft observations of the structure of the sheath of an interplanetary coronal mass ejection and related energetic ion enhancement." In: *Astronomy & Astrophysics* 656, A8, A8. doi: 10.1051/0004-6361/202140838.
- Klassen, A. et al. (2018). "Strong non-radial propagation of energetic electrons in solar corona." In: *Astronomy & Astrophysics* 614, A61, A61. doi: 10.1051/0004-6361/201732041.
- Klecker, B. (1995). "The Anomalous Component of Cosmic Rays in the 3-D Heliosphere." In: *Space Science Reviews* 72.1-2, pages 419–430. doi: 10.1007/BF00768815.
- Klecker, B. et al. (1980). "On the charge state of the anomalous oxygen component." In: *Geophysical Research Letters* 7.12, pages 1033–1036. doi: 10.1029/GL007i012p01033.
- Klecker, B. et al. (1995). "Charge State of Anomalous Cosmic-Ray Nitrogen, Oxygen, and Neon: SAMPEX Observations." In: *The Astrophysical Journal Letter* 442, page L69. doi: 10.1086/187818.
- Kollhoff, A. et al. (2021). "The first widespread solar energetic particle event observed by Solar Orbiter on 2020 November 29." In: *Astronomy & Astrophysics* 656, A20, A20. doi: 10.1051/0004-6361/202140937.
- Kouloumvakos, A. et al. (2022). "The first widespread solar energetic particle event of solar cycle 25 on 2020 November 29. Shock wave properties and the wide distribution of solar energetic particles." In: *Astronomy & Astrophysics* 660, A84, A84. doi: 10.1051/0004-6361/202142515.
- Kouloumvakos, A. et al. (2019). "Connecting the Properties of Coronal Shock Waves with Those of Solar Energetic Particles." In: *The Astrophysical Journal* 876.1, 80, page 80. doi: 10.3847/1538-4357/ab15d7.
- Kühl, P. et al. (2020). "The Electron Proton Helium INstrument as an example for a Space Weather Radiation Instrument." In: *Journal of Space Weather and Space Climate* 10, 53, page 53. doi: 10.1051/swsc/2020056.
- Laitinen, T. et al. (2016). "Solar energetic particle access to distant longitudes through turbulent field-line meandering." In: *Astronomy & Astrophysics* 591, A18, A18. doi: 10.1051/0004-6361/201527801.

- Laitinen, T. et al. (2023). "An Analytical Model of Turbulence in Parker Spiral Geometry and Associated Magnetic Field Line Lengths." In: *The Astrophysical Journal* 943.2, 108, page 108. doi: 10.3847/1538-4357/aca892.
- Lange, I. and S. E. Forbush (1942). "Note on the effect on cosmic-ray intensity of the magnetic storm of march 1, 1942." In: *Journal of Geophysical Research* 47.2, pages 185–186.
- Lanzerotti, L. J. and C. G. MacLennan (1995). "Anomalous cosmic ray oxygen and neon (~ 2.4 MeV/nucl) at high southern heliolatitudes." In: *Geophysical Research Letters* 22.23, pages 3353–3356. doi: 10.1029/95GL03551.
- Lario, D. et al. (2022). "Influence of Large-scale Interplanetary Structures on the Propagation of Solar Energetic Particles: The Multispacecraft Event on 2021 October 9." In: *The Astrophysical Journal* 934.1, 55, page 55. doi: 10.3847/1538-4357/ac6efd.
- Le Roux, J. A. and M. S. Potgieter (1995). "The Simulation of Complete 11 and 22 Year Modulation Cycles for Cosmic Rays in the Heliosphere Using a Drift Model with Global Merged Interaction Regions." In: *The Astrophysical Journal* 442, page 847. doi: 10.1086/175487.
- Leo, W. (1994). *Techniques for Nuclear and Particle Physics Experiments: A How-to Approach*. Springer. URL: <https://books.google.de/books?id=W7vHQgAACAAJ>.
- Li, C. et al. (2021). "Overview of the Chang'e-4 Mission: Opening the Frontier of Scientific Exploration of the Lunar Far Side." In: *Space Science Reviews* 217.2, 35, page 35. doi: 10.1007/s11214-021-00793-z.
- Manuel, R. et al. (2011). "Time-dependent cosmic ray modulation." In: *Advances in Space Research* 47.9, pages 1529–1537. doi: 10.1016/j.asr.2010.12.007.
- Marquardt, J. and B. Heber (2019). "Galactic cosmic ray hydrogen spectra and radial gradients in the inner heliosphere measured by the HELIOS Experiment 6." In: *Astronomy & Astrophysics* 625, A153, A153. doi: 10.1051/0004-6361/201935413.
- Marquardt, J. et al. (2018). "Energy spectra of carbon and oxygen with HELIOS E6. Radial gradients of anomalous cosmic ray oxygen within 1 AU." In: *Astronomy & Astrophysics* 610, A42, A42. doi: 10.1051/0004-6361/201731490.
- Marsden, R. G. et al. (1999). "On the gradients of ACR oxygen at intermediate heliocentric distances: Ulysses/Soho results." In: *Advances in Space Research* 23.3, pages 531–534. doi: 10.1016/S0273-1177(99)80007-6.
- Martucci, M. et al. (2023). "The First Ground-Level Enhancement of Solar Cycle 25 as Seen by the High-Energy Particle Detector (HEPD-01) on Board the CSES-01 Satellite." In: *Space Weather* 21.1, e2022SW003191, e2022SW003191. doi: 10.1029/2022SW003191.
- Mason, G. M. et al. (2021a). " ^3He -rich solar energetic particle events observed on the first perihelion pass of Solar Orbiter." In: *Astronomy & Astrophysics* 656, L1, page L1. doi: 10.1051/0004-6361/202039752.
- Mason, G. M. et al. (2021b). "Quiet-time low energy ion spectra observed on Solar Orbiter during solar minimum." In: *Astronomy & Astrophysics* 656, L5, page L5. doi: 10.1051/0004-6361/202140540.
- Mason, G. M. et al. (2021c). "Solar energetic particle heavy ion properties in the widespread event of 2020 November 29." In: *Astronomy & Astrophysics* 656, L12, page L12. doi: 10.1051/0004-6361/202141310.
- McComas, D. J. and N. A. Schwadron (2006). "An explanation of the Voyager paradox: Particle acceleration at a blunt termination shock." In: *Geophysical Research Letters* 33.4, L04102, page L04102. doi: 10.1029/2005GL025437.
- McComas, D. J. et al. (2015). "Local Interstellar Medium: Six Years of Direct Sampling by IBEX." In: *The Astrophysical Journal Supplement Series* 220.2, 22, page 22. doi: 10.1088/0067-0049/220/2/22.
- McComas, D. J. et al. (2019). "Termination Shock Measured by Voyagers and IBEX." In: *The Astrophysical Journal* 884.2, 145, page 145. doi: 10.3847/1538-4357/ab441a.

- McDonald, F. et al. (2001). "The Cosmic Ray Radial and Latitudinal Intensity Gradients in the Inner and Outer Heliosphere 1996-2001.3." In: *International Cosmic Ray Conference*. Volume 10. International Cosmic Ray Conference, page 3906.
- McDonald, F. B. and N. Lal (1986). "Variations of galactic cosmic rays with heliolatitude in the outer heliosphere." In: *Geophysical Research Letters* 13.8, pages 781–784. doi: 10.1029/GL013i008p00781.
- McDonald, F. B. et al. (1974). "The Anomalous Abundance of Cosmic-Ray Nitrogen and Oxygen Nuclei at Low Energies." In: *The Astrophysical Journal Letter* 187, page L105. doi: 10.1086/181407.
- McIntosh, S. W. et al. (2020). "Overlapping Magnetic Activity Cycles and the Sunspot Number: Forecasting Sunspot Cycle 25 Amplitude." In: *Solar Physics* 295.12, 163, page 163. doi: 10.1007/s11207-020-01723-y.
- McKenna-Lawlor, S. et al. (2015). "Recommendations to mitigate against human health risks incurred due to energetic particle irradiation beyond low earth orbit/bleo." In: *Acta Astronautica* 109, pages 182–193.
- McKibben, R. B. (1989). "Reanalysis and confirmation of positive latitude gradients for anomalous helium and galactic cosmic rays measured in 1975-1976 with pioneer 11." In: *Journal of Geophysical Research* 94.A12, pages 17021–17033. doi: 10.1029/JA094iA12p17021.
- McKibben, R. B., K. R. Pyle, and J. A. Simpson (1979). "The solar latitude and radial dependence of the anomalous cosmic-ray helium component." In: *The Astrophysical Journal Letter* 227, pages L147–L152. doi: 10.1086/182887.
- Mewaldt, R. A. et al. (1993). "The return of the anomalous cosmic rays to 1 AU in 1992." In: *Geophysical Research Letters* 20.20, pages 2263–2266. doi: 10.1029/93GL02493.
- Mewaldt, R. A. et al. (2001). "Long-term fluences of energetic particles in the heliosphere." In: *AIP Conference Proceedings* 598.1, pages 165–170. doi: 10.1063/1.1433995.
- Meyer, P., E. Parker, and J. Simpson (1956). "Solar cosmic rays of february, 1956 and their propagation through interplanetary space." In: *Physical Review* 104.3, page 768.
- Millikan, R. A. and G. H. Cameron (1928). "The origin of the cosmic rays." In: *Phys. Rev.* 32 (4), pages 533–557. doi: 10.1103/PhysRev.32.533.
- Miroshnichenko, L. I., E. V. Vashenyuk, and J. A. Pérez-Peraza (2013). "Solar cosmic rays: 70 years of ground-based observations." In: *Geomagnetism and Aeronomy* 53.5, pages 541–560. doi: 10.1134/S0016793213050125.
- Möller, T. et al. (2013a). "Radiation measurements on the stratospheric balloon BEXUS 13." In: *21st ESA Symposium on European Rocket and Balloon Programmes and Related Research*. ESA Special Publications. ISBN : 978-92-9092-285-8. doi: DOI:10.13140/2.1.4096.2565.
- Möller, T. et al. (2013b). "The Calibration of the Flight Radiation Environment Detector (FRED)." In: *Proc. Int. Cosmic Ray Conf.* <http://www.cbpf.br/icrc2013/papers/icrc2013-0422.pdf>.
- Müller, D. et al. (2020). "The Solar Orbiter mission — science overview." In: *A&A* 642, A1. doi: 10.1051/0004-6361/202038467.
- Nagovitsyn, Y. A. and V. G. Ivanov (2023). "Solar Cycle Pairing and Prediction of Cycle 25." In: *Solar Physics* 298.3, 37, page 37. doi: 10.1007/s11207-023-02121-w.
- Newkirk G., J. and D. G. Wentzel (1978). "Rigidity-independent propagation of cosmic rays in the solar corona." In: *Journal of Geophysical Research* 83.A5, pages 2009–2016. doi: 10.1029/JA083iA05p02009.
- O'Neill, P. M. (2006). "Badhwar O'Neill galactic cosmic ray model update based on advanced composition explorer (ACE) energy spectra from 1997 to present." In: *Advances in Space Research* 37.9, pages 1727–1733. doi: 10.1016/j.asr.2005.02.001.
- O'Neill P. M. and Golge, S. a. T. C. (2015). *Badhwar - O'Neill 2014 Galactic Cosmic Ray Flux Model Description*. Technical report.

- Palmerio, E. et al. (2022). "CMEs and SEPs During November-December 2020: A Challenge for Real-Time Space Weather Forecasting." In: *Space Weather* 20.5, e2021SW002993, e2021SW002993. doi: 10.1029/2021SW002993.
- Palmroos, C. et al. (2022). "Solar Energetic Particle Time Series Analysis with Python." In: *Frontiers in Astronomy and Space Sciences* 9, 395, page 395. doi: 10.3389/fspas.2022.1073578.
- Papaioannou, A. et al. (2022). "The first ground-level enhancement of solar cycle 25 on 28 October 2021." In: *Astronomy & Astrophysics* 660, L5, page L5. doi: 10.1051/0004-6361/202142855.
- Park, J. et al. (2013). "The Source Regions of Solar Energetic Particles Detected by Widely Separated Spacecraft." In: *The Astrophysical Journal* 779.2, 184, page 184. doi: 10.1088/0004-637X/779/2/184.
- Parker, E. N. (1965). "The passage of energetic charged particles through interplanetary space." In: 13.1, pages 9–49. doi: 10.1016/0032-0633(65)90131-5.
- Parker, E. N. (1958). "Dynamics of the interplanetary gas and magnetic fields." In: *The Astrophysical Journal* 128, page 664. doi: 10.1086/146579.
- Potgieter, M. S. (2013). "Solar Modulation of Cosmic Rays." In: *Living Reviews in Solar Physics* 10.1, 3, page 3. doi: 10.12942/lrsp-2013-3.
- Prasad, A. et al. (2023). "An Improved Prediction of Solar Cycle 25 Using Deep Learning Based Neural Network." In: *Solar Physics* 298.3, 50, page 50. doi: 10.1007/s11207-023-02129-2.
- Rankin, J. S. et al. (2021). "First Observations of Anomalous Cosmic Rays in to 36 Solar Radii." In: *The Astrophysical Journal* 912.2, 139, page 139. doi: 10.3847/1538-4357/abec7e.
- Rankin, J. S. et al. (2022). "Anomalous Cosmic-Ray Oxygen Observations into 0.1 au." In: *The Astrophysical Journal* 925.1, 9, page 9. doi: 10.3847/1538-4357/ac348f.
- Reames, D. V. (1999). "Particle acceleration at the Sun and in the heliosphere." In: *Space Science Reviews* 90, pages 413–491. doi: 10.1023/A:1005105831781.
- (2013). "The Two Sources of Solar Energetic Particles." In: *Space Science Reviews* 175, pages 53–92. doi: 10.1007/s11214-013-9958-9.
- Reames, D. V. (1988). "Bimodal Abundances in the Energetic Particles of Solar and Interplanetary Origin." In: *The Astrophysical Journal Letter* 330, page L71. doi: 10.1086/185207.
- (2021). *Solar Energetic Particles. A Modern Primer on Understanding Sources, Acceleration and Propagation*. Volume 978. doi: 10.1007/978-3-030-66402-2.
- Reinhard, R. and G. Wibberenz (1974). "Propagation of Flare Protons in the Solar Atmosphere." In: *Solar Physics* 36.2, pages 473–494. doi: 10.1007/BF00151216.
- Richardson, I. G. et al. (2014). "> 25 MeV Proton Events Observed by the High Energy Telescopes on the STEREO A and B Spacecraft and/or at Earth During the First ∼ Seven Years of the STEREO Mission." In: *Solar Physics* 289.8, pages 3059–3107. doi: 10.1007/s11207-014-0524-8.
- Richardson, I. G. (2004). "Energetic Particles and Corotating Interaction Regions in the Solar Wind." In: *Space Science Reviews* 111.3, pages 267–376. doi: 10.1023/B:SPAC.0000032689.52830.3e.
- (2018). "Solar wind stream interaction regions throughout the heliosphere." In: *Living Reviews in Solar Physics* 15.1, 1, page 1. doi: 10.1007/s41116-017-0011-z.
- Rodríguez-Pacheco, J. et al. (2020). "The Energetic Particle Detector - energetic particle instrument suite for the Solar Orbiter mission." In: *A&A* 642, A7. doi: 10.1051/0004-6361/201935287.
- Rouillard, A. P. et al. (2012). "The Longitudinal Properties of a Solar Energetic Particle Event Investigated Using Modern Solar Imaging." In: *The Astrophysical Journal* 752, 44, page 44. doi: 10.1088/0004-637X/752/1/44.

- Russell, C. T., J. G. Luhmann, and R. J. Strangeway (2016). *Space physics: An introduction.* Cambridge University Press.
- Sakao, T. et al. (2007). "Continuous plasma outflows from the edge of a solar active region as a possible source of solar wind." In: *Science* 318.5856, pages 1585–1588.
- Schrijver, C. J. et al. (2013). "Pathways of Large-scale Magnetic Couplings between Solar Coronal Events." In: *The Astrophysical Journal* 773.2, 93, page 93. doi: 10.1088/0004-637X/773/2/93.
- Schwadron, N. A. et al. (2016). "Signatures of volatiles in the lunar proton albedo." In: *Icarus* 273, pages 25–35. doi: 10.1016/j.icarus.2015.12.003.
- Shea, M. A. and D. F. Smart (2012). "Space Weather and the Ground-Level Solar Proton Events of the 23rd Solar Cycle." In: *Space Science Reviews* 171.1-4, pages 161–188. doi: 10.1007/s11214-012-9923-z.
- Shen, Z. N. et al. (2019). "Modulation of Galactic Cosmic Rays from Helium to Nickel in the Inner Heliosphere." In: *The Astrophysical Journal* 887.2, 132, page 132. doi: 10.3847/1538-4357/ab5520.
- Simpson, J. A., M. Zhang, and S. Bame (1996). "A Solar Polar North-South Asymmetry for Cosmic-Ray Propagation in the Heliosphere: The ULYSSES Pole-to-Pole Rapid Transit." In: *The Astrophysical Journal Letter* 465, page L69. doi: 10.1086/310127.
- Simpson, J. A. et al. (1995). "The latitude gradients of galactic cosmic ray and anomalous helium fluxes measured on Ulysses from the Sun's south polar region to the equator." In: *Geophysical Research Letters* 22.23, pages 3337–3340. doi: 10.1029/95GL02473.
- Slaba, T. C. and K. Whitman (2020). "The Badhwar-O'Neill 2020 GCR Model." In: *Space Weather* 18.6, e02456, e02456. doi: 10.1029/2020SW002456.
- Spence, H. E. et al. (2013). "Relative contributions of galactic cosmic rays and lunar proton "albedo" to dose and dose rates near the moon." In: *Space Weather* 11 (11), pages 643–650. doi: 10.1002/2013SW000995.
- Stone, E. C. et al. (2013). "Voyager 1 Observes Low-Energy Galactic Cosmic Rays in a Region Depleted of Heliospheric Ions." In: *Science* 341.6142, pages 150–153. doi: 10.1126/science.1236408.
- Stone, E. C. et al. (2019). "Cosmic ray measurements from Voyager 2 as it crossed into interstellar space." In: *Nature Astronomy* 3, pages 1013–1018. doi: 10.1038/s41550-019-0928-3.
- Strauss, R. D., R. A. Leske, and J. S. Rankin (2023). "The Modulation of Anomalous and Galactic Cosmic-Ray Oxygen over Successive Solar Cycle Minima." In: *The Astrophysical Journal* 944.2, 114, page 114. doi: 10.3847/1538-4357/acb53d.
- Sveshnikova, L. G. (2003). "The knee in the Galactic cosmic ray spectrum and variety in Supernovae." In: *aap* 409, pages 799–807. doi: 10.1051/0004-6361:20030909.
- Thakur, N et al. (2014). "Ground level enhancement in the 2014 january 6 solar energetic particle event." In: *The Astrophysical Journal Letters* 790.1, page L13.
- Torsti, J. et al. (1999). "Energetic (~10–65 MeV) protons observed by ERNE on August 13–14, 1996: Eruption on the solar back side as a possible source of the event." In: *Journal of Geophysical Research* 104.A5, pages 9903–9910. doi: 10.1029/1998JA900017.
- Tu, C. et al. (2005). "Solar wind origin in coronal funnels." In: *Science* 308.5721, pages 519–523.
- Tylka, A. J. et al. (1997). "CREME96: a revision of the C_ osmic R_ ay E_ffects on M_ icro-E_lecronics code." In: *IEEE Transactions on Nuclear Science* 44.6, pages 2150–2160. doi: 10.1109/23.659030.
- Vos, E. E. and M. S. Potgieter (2016). "Global Gradients for Cosmic-Ray Protons in the Heliosphere During the Solar Minimum of Cycle 23/24." In: *Solar Physics* 291.7, pages 2181–2195. doi: 10.1007/s11207-016-0945-7.

- Vos, E. E. and M. S. Potgieter (2015). "New Modeling of Galactic Proton Modulation during the Minimum of Solar Cycle 23/24." In: *The Astrophysical Journal* 815.2, 119, page 119. doi: 10.1088/0004-637X/815/2/119.
- Wang, L. (2009). "Solar Impulsive Energetic Electron Events." PhD thesis. UC Berkeley. URL: <https://escholarship.org/uc/item/33w5g946>.
- Webber, W. R. and J. A. Lockwood (1981). "A study of the long-term variation and radial gradient of cosmic rays out to 23 AU." In: *Journal of Geophysical Research* 86.A13, pages 11458–11462. doi: 10.1029/JA086iA13p11458.
- Weller, R. A. et al. (2010). "Monte Carlo Simulation of Single Event Effects." In: *IEEE Transactions on Nuclear Science* 57.4, pages 1726–1746. doi: 10.1109/TNS.2010.2044807.
- Wimmer-Schweingruber, R. F. et al. (2021). "First year of energetic particle measurements in the inner heliosphere with Solar Orbiter's Energetic Particle Detector." In: *Astronomy & Astrophysics* 656, A22, A22. doi: 10.1051/0004-6361/202140940.
- Wimmer-Schweingruber, R. F. et al. (2020). "The Lunar Lander Neutron and Dosimetry (LND) Experiment on Chang'E 4." In: *ssr* 216.6, 104, page 104. doi: 10.1007/s11214-020-00725-3.
- Wu, W. et al. (2019). "Lunar farside to be explored by Chang'e-4." In: *Nature Geoscience* 12.4, pages 222–223. doi: 10.1038/s41561-019-0341-7.
- Xu, Z. et al. (2020). "First Solar Energetic Particles Measured on the Lunar Far-side." In: *The Astrophysical Journal Letter* 902.2, L30, page L30. doi: 10.3847/2041-8213/abbccc.
- Xu, Z. et al. (2022). "Primary and albedo protons detected by the Lunar Lander Neutron and Dosimetry experiment on the lunar farside." In: *Frontiers in Astronomy and Space Sciences* 9, 974946, page 974946. doi: 10.3389/fspas.2022.974946.
- Xu, Z. et al. (2023). "Solar Orbiter EPD measurements of Anomalous cosmic ray in the inner heliosphere from 0.3 AU to 1 AU." In: manuscript in preparation.
- Zhang, S. et al. (2020). "First measurements of the radiation dose on the lunar surface." In: *Science Advances* 6.39, eaaz1334. doi: 10.1126/sciadv.aaz1334.
- Zhang, S. et al. (2021). "Radiation Dose of LND on the Lunar Surface in Two Years." In: *Chinese Journal of Space Science* 41.3, pages 439–444. doi: 10.3724/SP.J.0254-6124.2021.0311.

ACKNOWLEDGEMENTS

At this point, I want to express my gratitude to everyone who has played an important role during the course of my Ph.D. Their assistance, guidance, and support have been invaluable over the past five years. Without their help, I would not be where I am now.

First of all, I would like to thank my supervisor, Prof. Robert F. Wimmer-Schweingruber, for giving me the opportunity to join the group and work on the exciting projects - Chang'E-4/LND and SolO/EPD. He supported me in publishing these results in scientific journals and presenting them at multiple international conferences. I enjoyed discussing scientific topics with him. Those discussions inspired me and made me more productive.

I am also grateful to Prof. Jingnan Guo, who recommended me to Robert five years ago. She guided and helped me a lot on the LND projects. I hope I can have opportunities to continue our collaborations in the future. Besides, I would like to thank Prof. Dressing Nina, who provided valuable instructions and comments on the SEP paper of LND. She kindly wrote me a strong reference letter for me for the postdoc application of Caltech. That recommendation must be one of the key factors that help me to be selected from multiple candidates.

Furthermore, many thanks are given to my lovely colleagues working on LND and SOLO projects and in the Kiel group. Firstly, I would like to thank my officemate Dr. Lars Berger, for his patience and kindness every time I asked him basic and stupid questions. These discussions with him were one of the best moments that I enjoyed most. Despite that, I would like to show special thanks to him for his encouragement during finishing my thesis in the last two months. By the way, I still can not enjoy your heavy metal music. Secondly, I would like to show my appreciation to Dr. Verena Heidrich-Meisner, Dr. Patrick Kühl, and Dr. Marquardt Johannes for their proofreading of this thesis. They provided valuable suggestions and vastly improved the thesis. Next, I want to express my appreciation to my colleagues in the Kiel group for their help. They are the future Ph.D., Alexander Kollhoff, Chaoran Gu, Salman Khaksarighiri, Kröhnke Henning, as well as Dr. Daniel Pacheco, Dr. Liu Yang, Dr. Johan von Forstner, Dr. Jia Yu, and Henning Lohf.

I also want to thank my friends in Kiel, Jinru He, Lei Shao, Xuenan Li, and Xiuming Sun, who have always supported me, taken care of me, and helped me survive the tough COVID times. I remember the time that we enjoyed the fried chicken wings and played Catan all night until the following day. Thanks to those tough times, they made me stronger and more confident.

In the end, I would like to thank my parents - Aifang Wang and Fazhen Xu - for their understanding and support during my studies. Specifically, I would like to express my deepest love and gratitude to my wife, Zhenlin Zhu. She always has my back, and I am so lucky to have her in my life.

Further acknowledgments to the online tools for thesis writing and proofreading, including but not limited to Chatgpt, Grammarly, NotionAI, and DeepL. They are mighty in correcting grammar mistakes.

A

LND INSTRUMENT

This supplement chapter provides the simulation setup of Lunar Lander Neutron and Dosimetry Experiment (LND), the overview of the LND measurements in the last four years (2019 - 2023), and potential topics that worth to be investigated in the future.

LND SIMULATION SET-UP

As explained by Wimmer-Schweingruber et al. (2020), response functions of the LND to energetic particles are determined by the simulation using the Geometry and Tracking 4 (Geant4) toolkit. In this section, I explain the simulation setup of LND.

Fig. 29 shows a screenshot of the LND simulation model that we utilized. The model is a digital copy of the actual instrument based on the computer-aided design (CAD) model. The outermost lines define the space where the simulation runs, which has a size of 20cm × 20cm × 20cm. The area inside the box is the vacuum. The white structure in the middle is the housing of LND sensor heads composed of Al boards. The olive-colored layers in the sensor head are carriers of solid state detectors (SSDs) while SSDs are shown in blue color. The pink color indicated the location of Gd foils, which are used to detect thermal neutrons. Next to the central detector stacks are two printed circuit boards (PCBs) in green color.

THE OVERALL PROTON, HELIUM, AND TID VARIATION AND THE MOST UPDATED SEP LIST

Here we provide the overview of the proton, helium flux, and Total Ionizing Dose (TID) temporal variation from 2019 to Nov 29, 2022, measured by LND on the lunar far-side surface, as shown in Fig. 30. Figures are generated by the LND web plotter, a web application used to visualize LND data quickly. Currently, the webplotter is running on the server named etsasa and only be accessible to internal users. The webplotter is written in Python, and the source codes are available in the GitHub repository https://gitlab.physik.uni-kiel.de/LND/lnd_webplotter. After October 2023, this Github server is no longer served, and those codes are available via the new GitLab server, which is supported by the computer center of Kiel University.

The data gaps of LND data appear periodically every lunar night. This gap is due to the switch off of instruments in order to survive during the lunar night. The more significant data gaps are periods when the lander conducts experiments. After 2021, more solar energetic particle (SEP) events are observed by LND. Some of them even induced enhancement of TID dramatically. It is worth noting that three consecutive SEP events occurred in April of 2022, as shown in Fig. 30.

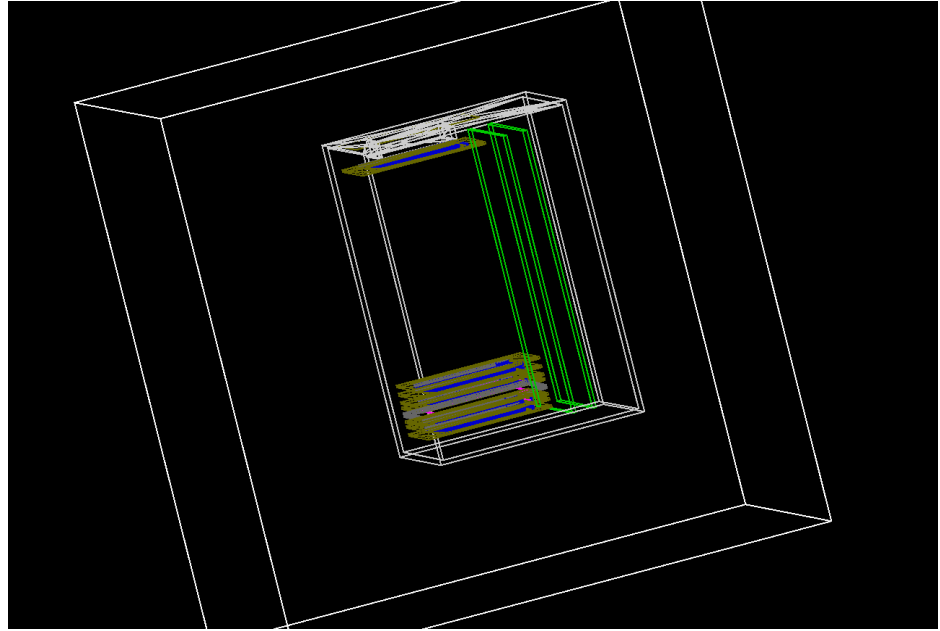


Figure 29: The inner structure of the LND sensor head that is utilized in the Geant4 simulation. The sizes of each piece of structure are taken from the CAD model of LND

The proton intensity increased after LND switched on and returned back to the background level before the end of the lunar day. The completed proton, helium, and TID time profiles are registered by LND. Therefore, these three SEP events provide an excellent opportunity to study the SEPs and its radiation impact on the lunar far-side surface.

In addition to the events that occurred on April 2022, other SEP events are listed in table 5, including the first SEP event in May 2019 and the first ground level enhancement (GLE) event at the end of 2021.

The start and end times of SEP events are determined simply by eye inspection of proton time profiles. i.e. the top panel of Fig. 30. If LND did not register the complete time profile of SEP events, the start time and end time of SEP events are simply the start and the end of the corresponding lunar day, respectively. The letters Y/N in the radiation hazard column indicate whether this event causes an increase of TID. The events of No.10, 15, and 18 are three SEP events that cause a significant increase of TID compared to others, and peak values of TID are up to $50 \mu\text{Gy}/\text{hour}$. The peak energy indicates the energy of the channel where the time profiles have clear enhancements.

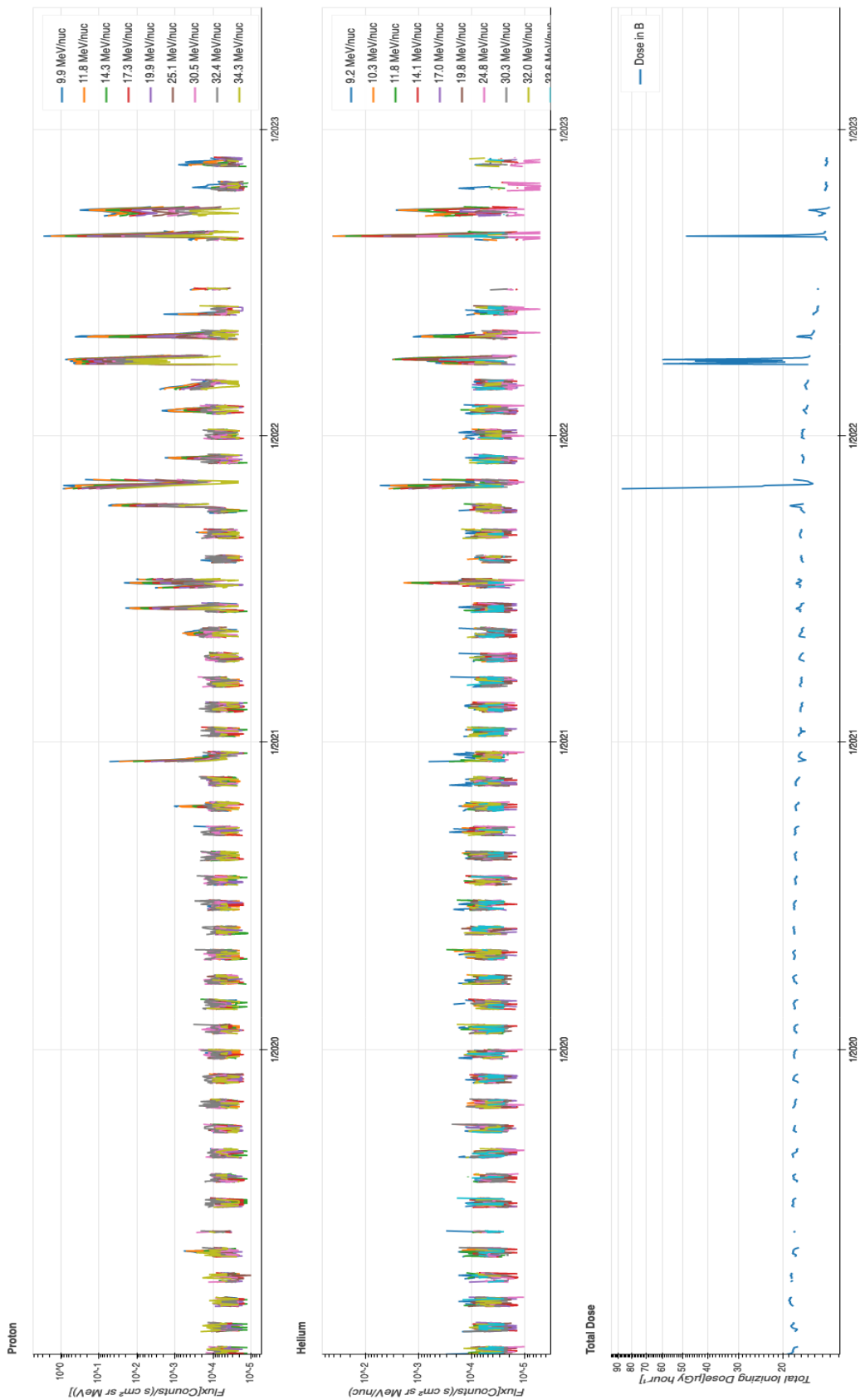


Figure 30: The proton, helium flux and TID temporal variation from 2019 to Nov 29, 2022, measured by LND on the lunar far-side surface

Table 5: A list of SEP events observed by LND between 2019 and 2022

No.	Start time	End time	Radiation hazard	Peak energy (Proton, MeV)
1	2019-05-04 12:00	05-06 00:00	N	~ 10
2	2019-05-06 06:00	05-06 18:00	N	~ 20
3	2020-10-16 18:00	10-19 00:00	N	~ 20
4	2020-12-09 06:00	12-12 00:00	N	> 35
5	2021-06-09 06:00	06-12 00:00	Y	> 35
6	2021-07-04 06:00	07-07 00:00	N	> 35
7	2021-07-09 10:00	07-12 06:00	Y	> 35
8	2021-07-13 12:00	07-15 06:00	Y	> 35
9	2021-10-09 06:00	10-12 00:00	Y	> 35
10	2021-10-30 08:00	11-06 05:00	Y(intense)	> 35
11	2021-11-09 10:00	11-10 08:00	Y	~ 30
12	2021-12-05 05:00	12-07 09:00	N	~ 30
13	2022-01-29 22:00	02-03 11:00	N	~ 30
14	2022-02-25 06:00	03-01 19:00	N	~ 30
15(a,b,c)	2022-03-28 06:00	04-07 01:00	Y(intense)	> 35
16	2022-04-28 00:00	05-04 06:00	Y	~ 30
17	2022-05-25 16:00	05-26 23:00	N	~ 20
18	2022-08-26 08:00	09-01 11:00	Y(intense)	> 35
19	2022-09-19 23:00	09-30 12:00	Y	~ 30
20	2022-11-19 10:00	11-20 10:00	N	~ 15

HOUSEKEEPING DATA OF LND

The instrument team uses the housekeeping data of LND to check the current status and health of the instrument. Here, we present the temperature, bias current, and bias voltage.

LND has six temperature sensors, monitoring the temperature variation of the sensor head (SH) and the electronic box (EB). Two temperature sensors are placed near the SSDs, one inside of the EB, and the remaining three are placed on the power board, the analog board, and the digital board. The time variations of temperature are given in panel (a) of Fig.31. These sensors only measure in the daytime. The usual working temperature is above 20 degrees and has been increasing recently. The long-term seasonal temperature variation might be due to the change in the distance between the Moon and the Sun.

The other two housekeeping data we show are the bias current and bias voltage, which indicate the status of SSDs. Usually, the current is low, and the voltage is close to -150 V. The current and voltage variations are correlated with temperature,

```

# The Awk scripts for the LND bias current and voltage
# correction
# HK_Ibias and HK_Vbias are the bias current and voltage
# measured on the LND instrument
# LVPS represents the low-voltage power supply of the LND
# instrument
# degC is the function to convert the temperature from
# Kelvin to Celsius
#=====
function Ibias() {
    a = $(HK_Ibias+3)
    if (a>4000) a = (147.3 + degC($(HK_T_LVPS+3))*0.164 - $(
        HK_Vbias+3)*0.05488) / 0.01810
    return a*0.4928
}
function Vbias() {
    return $(HK_Vbias+3)*0.05488 + $(HK_Ibias+3)*0.01810
}

```

as the measurement of the first two lunar days shows. However, as we explained in Section 3, the particle signals of detectors A, H, I, and J are dominated by a massive amount of lower energy noise. Those noises cause the increase of bias current, reaching the upper limit of this channel, 2000 nA. Therefore, the bias voltage and bias current measurements are no longer reliable. We give the scripts that can be used to correct the bias voltage and bias current of LND without any further explanation for documentary purposes. The scripts are from Stephan Böttcher (private communication), the designer of LND. Bias current >2000 nA is calculated from the bias voltage monitor by assuming a properly working power supply.

POSSIBLE RESEARCH TOPIC RELATED TO LND DATA

There are still a lot The possible future work based on the LND data includes:

- Heavy ion measurements of LND: The heavy ions are one of the crucial components of LND data products. Currently, the published data products count the C, N, and O in one channel and heavier ions in another. We can derive and create the data products of different particle species with further calibration and data analysis.
- Studying the discrepancy of TID between LND and Cosmic Ray Telescope for the Effects of Radiation (CRaTER): In Zhang et al. (2020), we have shown that the dose rate measured in two instruments are consistent during the first two lunar days. However, my preliminary results from comparing two years' data showed that the long-term variation of TID and CRaTER have different tendencies and are not consistent in the long run. This is out of our

expectations. The possible reasons include the decay of the neutral source of LND and the different responses of the two instruments.

- Albedo proton spectrum with better energy resolution: Currently, due to the counting statistic considerations, we only define albedo protons between 65 - 76 MeV as a single data point. In the future, with more than four years of data collection, data products of refined energy resolution will also be possible. Furthermore, two dimensions linear energy transfer (LET) measurement could also be used to study the albedo particles and potentially derive the dose rate of albedo particles.
- ${}^3\text{He}$ measured by LND: The reliable ${}^3\text{He}$ data products of LND should be generated, and the ${}^3\text{He}/{}^4\text{He}$ ratio in the energy range of 10 - 35 MeV/nuc should be derived.
- Instrument response of TID to SEPs: The TID could be predicted by assuming an input spectra. The analysis could help understand the instrument and relationship between SEP and TID.
- Jovian electrons.

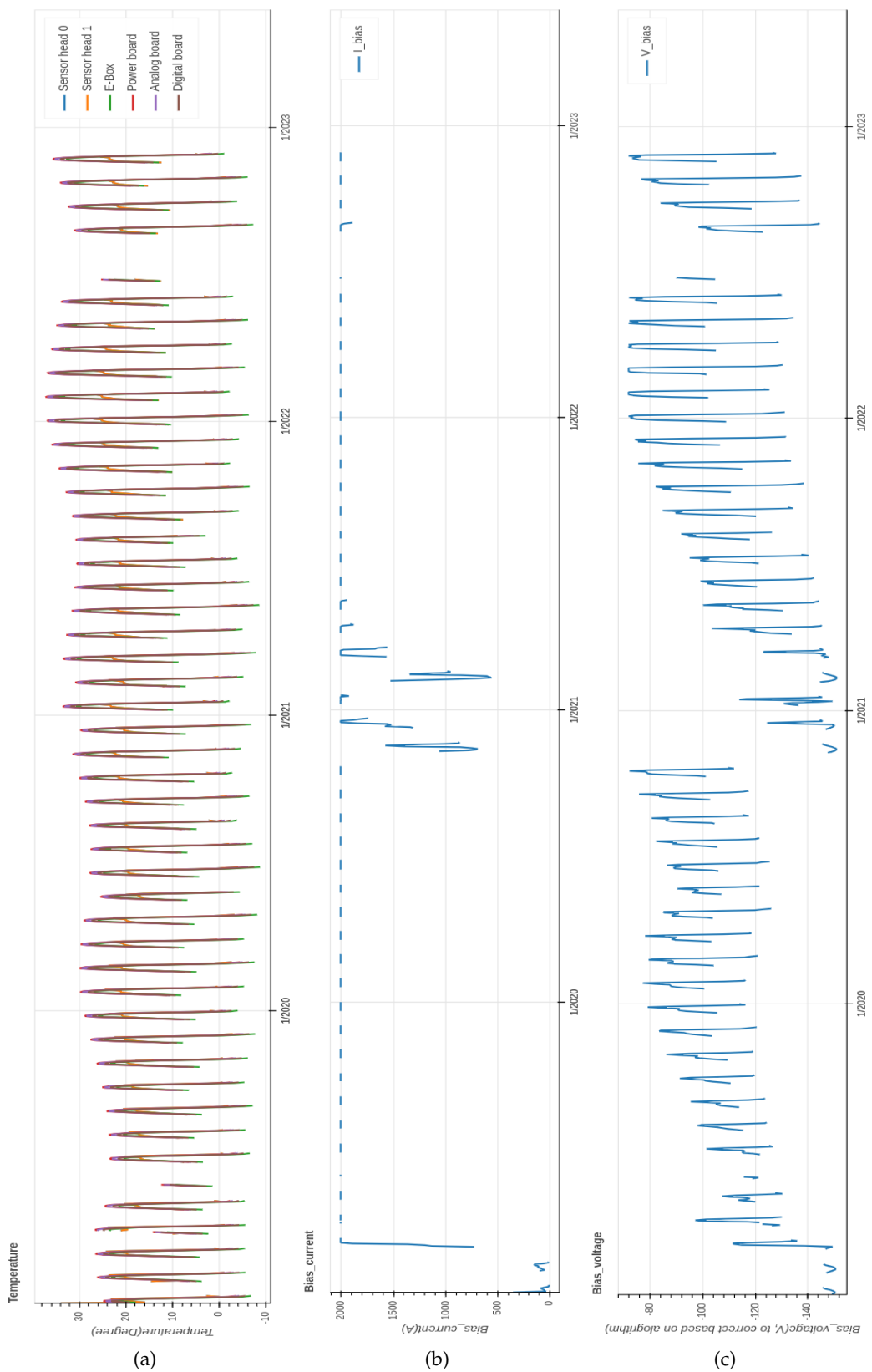


Figure 31: The variation of housekeeping data including (a) temperature, (b) bias current, and (c) bias voltage. The temperatures are measured by the sensors assembled inside of the LND sensor head and electronic box. The overview plot from 2019 to Nov 29, 2022.

B

SEPS LIST OF HET AND EPHIN MEASUREMENTS

Below are two lists of solar energetic particle (SEP) periods that we determined in Chapter 7 separately based on the High Energy Telescope (HET) housekeeping data and Electron Proton Helium Instrument (EPHIN) proton time profile. The start time and end time of SEP events indicate a longer duration of enhancement than what SEP events should be in order to get the anomalous cosmic ray (ACR) background as clean as possible. The durations of SEP events are given in units of hours.

Table 6: SEP events list and duration from SolO/HET

SEP number	Start time	End time	Duration(hours)
1	2020-06-10 08:10:18	2020-06-11 10:10:18	26.0
2	2020-07-20 18:31:24	2020-07-22 00:21:24	29.8
3	2020-11-16 19:31:41	2020-11-18 04:01:41	32.5
4	2020-11-20 08:51:41	2020-11-21 17:41:41	32.8
5	2020-11-24 03:01:42	2020-11-25 10:41:42	31.7
6	2020-11-29 01:31:42	2020-12-08 02:31:43	217.0
7	2020-12-09 10:11:44	2020-12-12 13:51:44	75.7
8	2021-04-17 05:32:03	2021-04-20 22:42:03	89.2
9	2021-05-07 08:02:05	2021-05-10 21:22:06	85.3
10	2021-05-22 09:52:08	2021-05-24 15:02:08	53.2
11	2021-05-28 11:42:08	2021-05-30 04:12:09	40.5
12	2021-06-22 23:02:12	2021-06-24 12:12:12	37.2
13	2021-07-15 10:32:15	2021-07-24 02:52:16	208.3
14	2021-08-26 06:32:21	2021-08-29 05:42:22	71.2
15	2021-09-20 07:42:25	2021-09-22 06:02:25	46.3
16	2021-09-27 19:02:26	2021-09-29 10:52:26	39.8
17	2021-10-08 18:42:28	2021-10-12 16:12:28	93.5
18	2021-10-28 03:42:31	2021-11-07 12:52:32	249.2
19	2021-11-09 05:22:33	2021-11-12 10:52:33	77.5
20	2021-12-04 20:52:36	2021-12-06 23:42:36	50.8
21	2022-01-18 06:02:43	2022-01-23 20:32:43	134.5
22	2022-01-30 16:02:45	2022-01-31 19:02:45	27.0
23	2022-02-15 14:32:47	2022-02-26 07:42:48	257.2
24	2022-03-02 06:42:49	2022-03-03 08:42:49	26.0

Continued on next page

Table 6 – *Continued from previous page*

number	Start time	End time	Duration(hours)
25	2022-03-10 09:02:50	2022-03-12 11:32:51	50.5
26	2022-03-14 05:52:51	2022-03-16 15:12:51	57.3
27	2022-03-20 17:32:52	2022-03-24 11:22:52	89.8
28	2022-03-28 00:52:53	2022-04-08 20:02:55	283.2
29	2022-04-08 23:42:55	2022-04-10 12:32:55	36.8
30	2022-04-13 01:22:55	2022-04-18 13:52:56	132.5
31	2022-04-19 17:22:56	2022-04-26 22:34:02	173.2
32	2022-04-27 15:02:58	2022-04-28 17:32:58	26.5
33	2022-04-30 05:22:58	2022-05-03 11:32:58	78.2
34	2022-05-09 20:52:59	2022-05-12 21:43:00	72.8
35	2022-05-26 21:23:02	2022-05-28 03:13:02	29.8
36	2022-06-07 07:43:04	2022-06-09 22:33:04	62.8
37	2022-06-13 12:53:05	2022-06-16 07:43:05	66.8
38	2022-07-23 10:33:10	2022-08-01 19:23:12	224.8
39	2022-08-28 18:43:16	2022-10-01 11:53:21	809.2

Table 7: SEP event list and duration from SOHO/EPHIN

SEP number	Start time	End time	Duration(hours)
1	2020-08-14 22:00:00	2020-08-16 06:00:00	32.0
2	2020-10-16 03:00:00	2020-10-19 11:00:00	80.0
3	2020-11-29 07:00:00	2020-12-18 14:00:00	463.0
4	2021-01-06 04:00:00	2021-01-07 18:00:00	38.0
5	2021-04-17 15:00:00	2021-04-22 21:00:00	126.0
6	2021-05-03 11:00:00	2021-05-04 19:00:00	32.0
7	2021-05-08 07:00:00	2021-05-15 10:00:00	171.0
8	2021-05-22 12:00:00	2021-05-25 10:00:00	70.0
9	2021-05-26 00:00:00	2021-05-28 00:00:00	48.0
10	2021-05-28 12:00:00	2021-06-04 09:00:00	165.0
11	2021-06-09 02:00:00	2021-06-14 22:00:00	140.0
12	2021-06-25 03:00:00	2021-06-27 10:00:00	55.0
13	2021-06-28 01:00:00	2021-06-29 23:00:00	46.0
14	2021-07-02 18:00:00	2021-07-08 07:00:00	133.0
15	2021-07-08 22:00:00	2021-07-31 03:00:00	533.0
16	2021-08-26 17:00:00	2021-08-30 00:00:00	79.0

Continued on next page

Table 7 – *Continued from previous page*

SEP number	Start time	End time	Duration(hours)
17	2021-08-30 09:00:00	2021-09-01 08:00:00	47.0
18	2021-09-07 15:00:00	2021-09-09 19:00:00	52.0
19	2021-09-17 06:00:00	2021-10-02 02:00:00	356.0
20	2021-10-09 00:00:00	2021-10-17 14:00:00	206.0
21	2021-10-28 05:00:00	2021-11-17 11:00:00	486.0
22	2021-12-04 01:00:00	2021-12-09 11:00:00	130.0
23	2021-12-20 01:00:00	2021-12-22 12:00:00	59.0
24	2021-12-23 08:00:00	2021-12-24 13:00:00	29.0
25	2022-01-14 02:00:00	2022-01-27 14:00:00	324.0
26	2022-01-29 13:00:00	2022-02-04 17:00:00	148.0
27	2022-02-06 09:00:00	2022-02-08 16:00:00	55.0
28	2022-02-09 00:00:00	2022-02-10 00:00:00	24.0
29	2022-02-10 21:00:00	2022-02-15 00:00:00	99.0
30	2022-02-15 16:00:00	2022-03-08 00:00:00	488.0
31	2022-03-08 03:00:00	2022-03-09 16:00:00	37.0
32	2022-03-10 11:00:00	2022-04-10 10:00:00	743.0
33	2022-04-10 19:00:00	2022-04-15 00:00:00	101.0
34	2022-04-18 12:00:00	2022-04-26 06:00:00	186.0
35	2022-04-27 06:00:00	2022-05-06 03:00:00	213.0
36	2022-05-06 05:00:00	2022-05-07 10:00:00	29.0
37	2022-05-08 17:00:00	2022-05-17 18:00:00	217.0
38	2022-05-20 02:00:00	2022-05-25 00:00:00	118.0
39	2022-05-25 09:00:00	2022-05-28 19:00:00	82.0
40	2022-06-07 00:00:00	2022-06-13 00:00:00	144.0
41	2022-06-13 03:00:00	2022-06-27 04:00:00	337.0
42	2022-06-30 03:00:00	2022-07-07 22:00:00	187.0
43	2022-07-09 02:00:00	2022-07-19 14:00:00	252.0
44	2022-07-22 00:00:00	2022-07-24 00:00:00	48.0
45	2022-07-24 10:00:00	2022-08-10 00:00:00	398.0
46	2022-08-14 03:00:00	2022-09-04 13:00:00	514.0
47	2022-09-04 14:00:00	2022-10-09 06:00:00	832.0
48	2022-10-09 20:00:00	2022-10-15 23:00:00	147.0
49	2022-10-22 06:00:00	2022-10-29 02:00:00	164.0

LIST OF PUBLICATIONS

This list shows all peer-reviewed publications that I have contributed to. Not all of these publications were included in this thesis, as they do not all fit into the logical flow of this thesis.

FIRST SOLAR ENERGETIC PARTICLES MEASURED ON THE LUNAR FAR-SIDE

Xu, Z., J. Guo, R. F. Wimmer-Schweingruber, J. L. Freiherr von Forstner, Y. Wang, N. Dresing, H. Lohf, S. Zhang, B. Heber, and M. Yang, *The Astrophysical Journal Letter*, 902, 2, page L30 (2020), doi: 10.3847/2041-8213/abbccc

Own contribution: 80%

PRIMARY AND ALBEDO PROTONS DETECTED BY THE LUNAR LANDER NEUTRON AND DOSIMETRY EXPERIMENT ON THE LUNAR FAR SIDE

Xu, Z., J. Guo, R. F. Wimmer-Schweingruber, M. I. Dobynede, P. Kühl, S. Khaksarighiri, and S. Zhang, *Frontiers in Astronomy and Space Sciences*, 9, page 974946 (2022), doi: 10.3389/fspas.2022.974946

Own contribution: 80%

QUIET-TIME LOW ENERGY ION SPECTRA OBSERVED ON SOLAR ORBITER DURING SOLAR MINIMUM

Mason, G. M., G. C. Ho, R. C. Allen, **Z. G. Xu**, N. P. Janitzek, J. L. Freiherr von Forstner, A. Kohllhoff, D. Pacheco, J. Rodríguez-Pacheco, R. F. Wimmer-Schweingruber, G. Bruce Andrews, C. E. Schlemm, H. Seifert, K. Tyagi, W. J. Lees, J. Hayes, R. Gómez-Herrero, M. Prieto, S. Sánchez-Prieto, F. Espinosa Lara, I. Cernuda, P. Parra Espada, O. Rodríguez Polo, A. Martínez Hellín, C. Martin, S. Böttcher, L. Berger, J. C. Terasa, S. Boden, S. R. Kulkarni, A. Ravanbakhsh, M. Yedla, S. Eldrum, R. Elftmann, and P. Kühl, *Astronomy & Astrophysics*, 656, page L5 (2021), doi: 10.1051/0004-6361/202140540

Own contribution: 25%

THE FIRST GROUND LEVEL ENHANCEMENT SEEN ON THREE PLANETARY SURFACES: EARTH, MOON, AND MARS

Guo, J., X. Li, J. Zhang, M. I. Dobynede, Y. Wang, **Z. Xu**, T. Berger, J. Semkova, R. F. Wimmer-Schweingruber, D. M. Hassler, C. Zeitlin, B. Ehresmann, D. Matthiä, and B. Zhuang, *Geophysical Research Letters*, 50, 15, e2023GL103069 (2023), doi: 10.1029/2023GL103069

Own contribution: 25%

ENERGETIC IONS IN THE VENUSIAN SYSTEM: INSIGHTS FROM THE FIRST SOLAR ORBITER FLYBY

Allen, R. C., I. Cernuda, D. Pacheco, L. Berger, **Z. G. Xu**, J. L. Freiherr von Forstner,

J. Rodríguez-Pacheco, R. F. Wimmer-Schweingruber, G. C. Ho, G. M. Mason, S. K. Vines, Y. Khotyaintsev, T. Horbury, M. Maksimovic, L. Z. Hadid, M. Volwerk, A. P. Dimmock, L. Sorriso-Valvo, K. Stergiopoulou, G. B. Andrews, V. Angelini, S. D. Bale, S. Boden, S. I. Böttcher, T. Chust, S. Eldrum, P. P. Espada, F. Espinosa Lara, V. Evans, R. Gómez-Herrero, J. R. Hayes, A. M. Hellín, A. Kollhoff, V. Krasnoselskikh, M. Kretzschmar, P. Kühl, S. R. Kulkarni, W. J. Lees, E. Lorfèvre, C. Martin, H. O'Brien, D. Plettemeier, O. R. Polo, M. Prieto, A. Ravanbakhsh, S. Sánchez-Prieto, C. E. Schlemm, H. Seifert, J. Souček, M. Steller, Š. Štverák, J. C. Terasa, P. Trávníček, K. Tyagi, A. Vaivads, A. Vecchio, and M. Yedla, *Astronomy & Astrophysics*, 656, A7 (2021), doi: 10.1051/0004-6361/202140803

Own contribution: 15%

FIRST YEAR OF ENERGETIC PARTICLE MEASUREMENTS IN THE INNER HELIOSPHERE WITH SOLAR ORBITER'S ENERGETIC PARTICLE DETECTOR

Wimmer-Schweingruber, R. F., N. P. Janitzek, D. Pacheco, I. Cernuda, F. Espinosa Lara, R. Gómez-Herrero, G. M. Mason, R. C. Allen, **Z. G. Xu**, F. Carcaboso, A. Kollhoff, P. Kühl, J. L. Freiherr von Forstner, L. Berger, J. Rodriguez-Pacheco, G. C. Ho, G. B. Andrews, V. Angelini, A. Aran, S. Boden, S. I. Böttcher, A. Carrasco, N. Dresing, S. Eldrum, R. Elftmann, V. Evans, O. Gevin, J. Hayes, B. Heber, T. S. Horbury, S. R. Kulkarni, D. Lario, W. J. Lees, O. Limousin, O. E. Malandraki, C. Martín, H. O'Brien, M. Prieto Mateo, A. Ravanbakhsh, O. Rodriguez-Polo, S. Sánchez Prieto, C. E. Schlemm, H. Seifert, J. C. Terasa, K. Tyagi, R. Vainio, A. Walsh, and M. K. Yedla, *Astronomy & Astrophysics*, 656, A22 (2021), doi: 10.1051/0004-6361/202140940

Own contribution: 15%

THE LUNAR LANDER NEUTRON AND DOSIMETRY (LND) EXPERIMENT ON CHANG'E 4

Wimmer-Schweingruber, R. F., J. Yu, S. I. Böttcher, S. Zhang, S. Burmeister, H. Lohf, J. Guo, **Z. Xu**, B. Schuster, L. Seimetz, J. L. Freiherr von Forstner, A. Ravanbakhsh, V. Knierim, S. Kolbe, H. Woyciechowski, S. R. Kulkarni, B. Yuan, G. Shen, C. Wang, Z. Chang, T. Berger, C. E. Hellweg, D. Matthiä, D. Hou, A. Knappmann, C. Büschel, X. Hou, B. Ren, and Q. Fu, *ssr*, 216, 6, page 104 (2020), doi: 10.1007/s11214-020-00725-3

Own contribution: 10%

FIRST MEASUREMENTS OF THE RADIATION DOSE ON THE LUNAR SURFACE

Zhang, S., R. F. Wimmer-Schweingruber, J. Yu, C. Wang, Q. Fu, Y. Zou, Y. Sun, C. Wang, D. Hou, S. I. Böttcher, S. Burmeister, L. Seimetz, B. Schuster, V. Knierim, G. Shen, B. Yuan, H. Lohf, J. Guo, **Z. Xu**, J. L. Freiherr von Forstner, S. R. Kulkarni, H. Xu, C. Xue, J. Li, Z. Zhang, H. Zhang, T. Berger, D. Matthiä, C. E. Hellweg, X. Hou, J. Cao, Z. Chang, B. Zhang, Y. Chen, H. Geng, and Z. Quan, *Science Advances*, 6, 39, eaaz1334 (2020), doi: 10.1126/sciadv.aaz1334

Own contribution: 10%

THE 17 APRIL 2021 WIDESPREAD SOLAR ENERGETIC PARTICLE EVENT

Dresing, N., Rodríguez-García, L., Jebaraj, I. C., Warmuth, A., Wallace, S., Bal-

maceda, L., Podladchikova, T., Strauss, R. D., Kouloumvakos, A., Palmroos, C., Krupar, V., Gieseler, J., Xu, Z., Mitchell, J. G., Cohen, C. M. S., de Nolfo, G. A., Palmerio, E., Carcaboso, F., Kilpua, E. K. J., Trotta, D., Auster, U., Asvestari, E., da Silva, D., Dröge, W., Getachew, T., Gómez-Herrero, R., Grande, M., Heyner, D., Holmström, M., Huovelin, J., Kartavykh, Y., Laurensen, M., Lee, C. O., Mason, G., Maksimovic, M., Mieth, J., Murakami, G., Oleynik, P., Pinto, M., Pulupa, M., Richter, I., Rodríguez-Pacheco, J., Sánchez-Cano, B., Schuller, F., Ueno, H., Vainio, R., Vecchio, A., Veronig, A. M., and Wijsen, N., *A&A*, 674, A105 (2023), doi: 10.1051/0004-6361/202345938

Own contribution: 10%

RADIAL EVOLUTION OF THE APRIL 2020 STEALTH CORONAL MASS EJECTION BETWEEN 0.8 AND 1 AU: A COMPARISON OF FORBUSH DECREASES AT SOLAR ORBITER AND EARTH

Forstner, J. L. Freiherr von, M. Dumbović, C. Möstl, J. Guo, A. Papaioannou, R. Elftmann, **Z. Xu**, J. C. Terasa, A. Kollhoff, R. F. Wimmer-Schweingruber, J. Rodríguez-Pacheco, A. J. Weiss, J. Hinterreiter, T. Amerstorfer, M. Bauer, A. V. Belov, M. A. Abunina, T. Horbury, E. E. Davies, H. O'Brien, R. C. Allen, G. B. Andrews, L. Berger, S. Boden, I. Cernuda Cangas, S. Eldrum, F. Espinosa Lara, R. Gómez-Herrero, J. R. Hayes, G. C. Ho, S. R. Kulkarni, W. J. Lees, C. Martín, G. M. Mason, D. Pacheco, M. Prieto Mateo, A. Ravankhsh, O. Rodríguez Polo, S. Sánchez Prieto, C. E. Schlemm, H. Seifert, K. Tyagi, and M. Yedla, *A&A* (2021), doi: 10.1051/0004-6361/202039848

Own contribution: 5%

RADIATION DOSE OF LND ON THE LUNAR SURFACE IN TWO YEARS

Zhang, S., D. Hou, R. F. Wimmer-Schweingruber, Y. Sun, C. Wang, Z. Chang, **Z. Xu**, G. Shen, B. Yuan, and C. Xue, *Chinese Journal of Space Science*, 41, 3, pages 439–444 (2021), doi: 10.3724/SP.J.0254-6124.2021.0311

Own contribution: 5%

THE FIRST GRADUAL SOLAR ENERGETIC PARTICLE EVENT WITH AN ENHANCED ^{3}He ABUNDANCE ON SOLAR ORBITER

Bučík, R., G. M. Mason, R. Gómez-Herrero, V. Krupar, D. Lario, M. J. Starkey, G. C. Ho, J. Rodríguez-Pacheco, R. F. Wimmer-Schweingruber, F. Espinosa Lara, T. Tadesse, L. Balmaceda, C. M. S. Cohen, M. A. Dayeh, M. I. Desai, P. Kühl, N. V. Nitta, M. E. Wiedenbeck, and **Z. G. Xu**, *Astronomy & Astrophysics*, 669, A13 (2023), doi: 10.1051/0004-6361/202245037

Own contribution: 5%

INFLUENCE OF LARGE-SCALE INTERPLANETARY STRUCTURES ON THE PROPAGATION OF SOLAR ENERGETIC PARTICLES: THE MULTISPACECRAFT EVENT ON 2021 OCTOBER 9

Lario, D., N. Wijsen, R. Y. Kwon, B. Sánchez-Cano, I. G. Richardson, D. Pacheco, E. Palmerio, M. L. Stevens, A. Szabo, D. Heyner, N. Dresing, R. Gómez-Herrero, F. Carcaboso, A. Aran, A. Afanasiev, R. Vainio, E. Riihonen, S. Poedts, M. Brüden, **Z. G. Xu**, and A. Kollhoff, *The Astrophysical Journal*, 934, 1, page 55 (2022), doi:

SUPRATHERMAL PARTICLES FROM COROTATING INTERACTION REGIONS DURING THE FIRST PERIHELION PASS OF SOLAR ORBITER

Allen, R. C., G. M. Mason, G. C. Ho, J. Rodríguez-Pacheco, R. F. Wimmer-Schweingruber, G. B. Andrews, L. Berger, S. Boden, I. Cernuda, F. Espinosa Lara, J. L. Freiherr von Forstner, R. Gómez-Herrero, J. R. Hayes, S. R. Kulkarni, W. J. Lees, C. Martin, D. Pacheco, O. R. Polo, M. Prieto, A. Ravanbakhsh, S. Sánchez-Prieto, C. E. Schlemm, H. Seifert, J. C. Terasa, K. Tyagi, **Z. Xu**, and M. Yedla, *Astronomy & Astrophysics*, 656, page L2 (2021), doi: 10.1051/0004-6361/202039870

Own contribution: 5%

FIRST NEAR-RELATIVISTIC SOLAR ELECTRON EVENTS OBSERVED BY EPD ONBOARD SOLAR ORBITER

Gómez-Herrero, R., D. Pacheco, A. Kollhoff, F. Espinosa Lara, J. L. Freiherr von Forstner, N. Dresing, D. Lario, L. Balmaceda, V. Krupar, O. E. Malandraki, A. Aran, R. Bučík, A. Klassen, K.-L. Klein, I. Cernuda Cangas, S. Eldrum, H. Reid, J. G. Mitchell, G. M. Mason, G. C. Ho, J. Rodríguez-Pacheco, R. F. Wimmer-Schweingruber, L. Berger, R. C. Allen, N. P. Janitzek, M. Laurenza, R. de Marco, N. Wijsen, Y. Y. Kartavykh, W. Dröge, T. S. Horbury, M. Maksimovic, C. J. Owen, A. Vecchio, X. Bonnin, O. Kruparova, D. Příša, J. Souček, P. Louarn, A. Fedorov, H. O'Brien, V. Evans, V. Angelini, P. Zucca, M. Prieto-Mateo, S. Sánchez-Prieto, A. Carrasco, J. J. Blanco, P. Parra, O. Rodríguez Polo, C. Martín, J. C. Terasa, S. Boden, S. R. Kulkarni, A. Ravanbakhsh, M. Yedla, **Z. Xu**, G. B. Andrews, C. E. Schlemm, H. Seifert, K. Tyagi, W. J. Lees, and J. Hayes, *Astronomy & Astrophysics* (2021), doi: 10.1051/0004-6361/202039883

Own contribution: 5%

EVIDENCE FOR LOCAL PARTICLE ACCELERATION IN THE FIRST RECURRENT GALACTIC COSMIC RAY DEPRESSION OBSERVED BY SOLAR ORBITER. THE ION EVENT ON 19 JUNE 2020

Aran, A., D. Pacheco, M. Laurenza, N. Wijsen, D. Lario, S. Benella, I. G. Richardson, E. Samara, J. L. Freiherr von Forstner, B. Sanahuja, L. Rodriguez, L. Balmaceda, F. Espinosa Lara, R. Gómez-Herrero, K. Steinval, A. Vecchio, V. Krupar, S. Poedts, R. C. Allen, G. B. Andrews, V. Angelini, L. Berger, D. Berghmans, S. Boden, S. I. Böttcher, F. Carcaboso, I. Cernuda, R. De Marco, S. Eldrum, V. Evans, A. Fedorov, J. Hayes, G. C. Ho, T. S. Horbury, N. P. Janitzek, Y. V. Khotyaintsev, A. Kollhoff, P. Kühl, S. R. Kulkarni, W. J. Lees, P. Louarn, J. Magdalénic, M. Maksimovic, O. Malandraki, A. Martínez, G. M. Mason, C. Martín, H. O'Brien, C. Owen, P. Parra, M. Prieto Mateo, A. Ravanbakhsh, J. Rodriguez-Pacheco, O. Rodriguez Polo, S. Sánchez Prieto, C. E. Schlemm, H. Seifert, J. C. Terasa, K. Tyagi, C. Verbeeck, R. F. Wimmer-Schweingruber, **Z. G. Xu**, M. K. Yedla, and A. N. Zhukov, *Astronomy & Astrophysics*, 656, page L10 (2021), doi: 10.1051/0004-6361/202140966

Own contribution: 5%

SOLAR ENERGETIC PARTICLE HEAVY ION PROPERTIES IN THE WIDESPREAD EVENT OF
2020 NOVEMBER 29

Mason, G. M., C. M. S. Cohen, G. C. Ho, D. G. Mitchell, R. C. Allen, M. E. Hill, G. B. Andrews, L. Berger, S. Boden, S. Böttcher, I. Cernuda, E. R. Christian, A. C. Cummings, A. J. Davis, M. I. Desai, G. A. de Nolfo, S. Eldrum, R. Elftmann, A. Kollhoff, J. Giacalone, R. Gómez-Herrero, J. Hayes, N. P. Janitzek, C. J. Joyce, A. Korth, P. Kühl, S. R. Kulkarni, A. W. Labrador, F. Espinosa Lara, W. J. Lees, R. A. Leske, U. Mall, C. Martin, A. Martínez Hellín, W. H. Matthaeus, D. J. McComas, R. L. McNutt, R. A. Mewaldt, J. G. Mitchell, D. Pacheco, P. Parra Espada, M. Prieto, J. S. Rankin, A. Ravanbakhsh, J. Rodríguez-Pacheco, O. Rodríguez Polo, E. C. Roelof, S. Sánchez-Prieto, C. E. Schlemm, N. A. Schwadron, H. Seifert, E. C. Stone, J. R. Szalay, J. C. Terasa, K. Tyagi, J. L. Freiherr von Forstner, M. E. Wiedenbeck, R. F. Wimmer-Schweingruber, **Z. G. Xu**, and M. Yedla, *Astronomy & Astrophysics*, 656, page L12 (2021), doi: 10.1051/0004-6361/202141310

Own contribution: 5%

THE LONG PERIOD OF ^3He -RICH SOLAR ENERGETIC PARTICLES MEASURED BY SOLAR
ORBITER 2020 NOVEMBER 17-23

Bučík, R., G. M. Mason, R. Gómez-Herrero, D. Lario, L. Balmaceda, N. V. Nitta, V. Krupař, N. Dresing, G. C. Ho, R. C. Allen, F. Carcaboso, J. Rodríguez-Pacheco, F. Schuller, A. Warmuth, R. F. Wimmer-Schweingruber, J. L. Freiherr von Forstner, G. B. Andrews, L. Berger, I. Cernuda, F. Espinosa Lara, W. J. Lees, C. Martín, D. Pacheco, M. Prieto, S. Sánchez-Prieto, C. E. Schlemm, H. Seifert, K. Tyagi, M. Maksimovic, A. Vecchio, A. Kollhoff, P. Kühl, **Z. G. Xu**, and S. Eldrum, *Astronomy & Astrophysics*, 656, page L11 (2021), doi: 10.1051/0004-6361/202141009

Own contribution: 5%

THE FIRST WIDESPREAD SOLAR ENERGETIC PARTICLE EVENT OBSERVED BY SOLAR
ORBITER ON 2020 NOVEMBER 29

Kollhoff, A., A. Kouloumvakos, D. Lario, N. Dresing, R. Gómez-Herrero, L. Rodríguez-García, O. E. Malandraki, I. G. Richardson, A. Posner, K. L. Klein, D. Pacheco, A. Klassen, B. Heber, C. M. S. Cohen, T. Laitinen, I. Cernuda, S. Dalla, F. Espinosa Lara, R. Vainio, M. Köberle, R. Kühl, **Z. G. Xu**, L. Berger, S. Eldrum, M. Brüdern, M. Laurenza, E. J. Kilpua, A. Aran, A. P. Rouillard, R. Bučík, N. Wijsen, J. Pomoell, R. F. Wimmer-Schweingruber, C. Martin, S. I. Böttcher, J. L. Freiherr von Forstner, J. C. Terasa, S. Boden, S. R. Kulkarni, A. Ravanbakhsh, M. Yedla, N. Janitzek, J. Rodríguez-Pacheco, M. Prieto Mateo, S. Sánchez Prieto, P. Parra Espada, O. Rodríguez Polo, A. Martínez Hellín, F. Carcaboso, G. M. Mason, G. C. Ho, R. C. Allen, G. Bruce Andrews, C. E. Schlemm, H. Seifert, K. Tyagi, W. J. Lees, J. Hayes, S. D. Bale, V. Krupar, T. S. Horbury, V. Angelini, V. Evans, H. O'Brien, M. Maksimovic, Y. V. Khotyaintsev, A. Vecchio, K. Steinvall, and E. Asvestari, *Astronomy & Astrophysics*, 656, A20 (2021), doi: 10.1051/0004-6361/202140937

Own contribution: 5%

EIDESSTATTLICHE ERKLÄRUNG GEMÄSS §9 DER PROMOTIONSORDNUNG

Ich versichere an Eides statt, dass die vorliegende Abhandlung – abgesehen von der Beratung durch meinen Betreuer und der angegebenen Literatur – nach Inhalt und Form meine eigene Arbeit ist.

Ich versichere, dass die Arbeit weder ganz noch zum Teil schon einer anderen Stelle im Rahmen eines Prüfungsverfahrens vorgelegen hat. Teile dieser Arbeit wurden bereits in Fachzeitschriften veröffentlicht und sind als solche gekennzeichnet. Die Quellennachweise der jeweiligen Veröffentlichungen befinden sich ausschließlich in den zugehörigen Literaturverzeichnissen und werden nicht im Literaturverzeichnis dieser Abhandlung aufgeführt.

Ich versichere, dass die Arbeit unter Einhaltung der Regeln guter wissenschaftlicher Praxis der Deutschen Forschungsgemeinschaft entstanden ist.

Ich versichere, dass von mir noch kein frühererer Promotionsversuch unternommen wurde und mir auch kein akademischer Grad entzogen wurde.

Kiel, June 2023

Zigong Xu